Transactions of the ASME

Journal of Fluids Engineering

FLUIDS ENGINEERING DIVISION
Technical Editor
FRANK M. WHITE (1984)
Executive Secretary
L. T. NELSON (1984)
Calendar Editor
M. F. ACKERSON

Associate Editors
Fluid Machinery
AWATEF A. HAMED (1985)
WILLIAM E. THOMPSON (1984)
Fluid Measurements
THEODORE R. HEIDRICK (1984)
Fluid Mechanics
SHLOMO CARMI (1984)
CHARLES DALTON (1983)
KIRTI N. GHIA (1984)
THOMAS J. MUELLER (1985)
Fluid Transients
M. HANIF CHAUDHRY (1983)
Multiphase Flow
JOHN T. JUREWICZ (1985)
OKITSUGU FURUYA (1984)
Review Articles
RICHARD A. BAJURA (1985)

FOREIGN CORRESPONDENTS
Europe and Russia
JACQUES CHAUVIN
Europe and Russia
JOHN H. HORLOCK
India and Middle East
ARUN PRASAD
Japan and China
YASUTOSHI SENOO

BOARD ON COMMUNICATIONS
Chairman and Vice President
MICHAEL J. RABINS

Members-at-Large
W. BEGELL, W. G. GOTTENBERG,
D. KOENIG, M. KUTZ, F. LANDIS,
J. W. LOCKE, J. ORTLOFF, C. PHILLIPS,
H. C. REEDER, K. REID

President, **FRANK M. SCOTT**
Executive Director
PAUL ALLMENDINGER
Treasurer,
ROBERT A. BENNETT

PUBLISHING STAFF
Mng. Dir. Publ., **J. J. FREY**
Dep. Mng. Dir. Publ.,
JOS. SANSONE
Managing Editor, **CORNELIA MONAHAN**

The Journal of Fluids Engineering (USPS 278-480) is *published quarterly for $72 per year by* The American Society of Mechanical Engineers, 345 East 47th Street, New York, NY 10017. Second class postage paid at New York, NY and additional mailing offices. POSTMASTER: Send address changes to The Journal of Fluids Engineering, c/o THE AMERICAN SOCIETY OF MECHANICAL ENGINEERS, P.O. Box 3199, Grand Central Station, New York, NY 10163.

CHANGES OF ADDRESS must be received at Society headquarters seven weeks before they are to be effective. Please send old label and new address.

PRICES: To members, $36.00, annually; to nonmembers, $72.00. Single copies, $24.00 each. Add $6.00 for postage to countries outside the United States and Canada.

STATEMENT from By-Laws. The Society shall not be responsible for statements or opinions advanced in papers or . . . printed in its publications (B7.1, Par. 3),

COPYRIGHT © 1983 by The American Society of Mechanical Engineers. Reprints from this publication may be made on condition that full credit be given the TRANSACTIONS OF THE ASME, JOURNAL OF FLUIDS ENGINEERING and the author, and date of publication be stated.

INDEXED *by the Engineering Index, Inc.*

Published Quarterly by The American Society of Mechanical Engineers

VOLUME 105 • NUMBER 4 • DECEMBER 1983

Announcements and Special Notices

Downloaded 03 Jun 2010 to 171.66.16.159. Redistribution subject to ASME license or copyright; see http://www.asme.org/terms/Terms_Use.cfm

D. Hoyniak
Graduate Research Assistant.

S. Fleeter
Professor of Mechanical Engineering.

Thermal Sciences and
Propulsion Center,
School of Mechanical Engineering,
Purdue University,
West Lafayette, Ind. 47907

Prediction of Aerodynamically Induced Vibrations in Turbomachinery Blading

To predict the aerodynamically forced response of an airfoil, an energy balance between the unsteady aerodynamic work and the energy dissipated through the airfoil structural and aerodynamic damping is performed. Theoretical zero incidence unsteady aerodynamic coefficients are then utilized in conjunction with this energy balance technique to predict the effects of reduced frequency, inlet Mach number, cascade geometry and interblade phase angle on the torsion mode aerodynamically forced response of the cascade. In addition, experimental unsteady aerodynamic gust data for flat plate and cambered cascaded airfoils are used together with these theoretical cascade unsteady self-induced aerodynamic coefficients to indicate the effects of incidence angle and airfoil camber on the forced response of the airfoil cascade.

Introduction

The structural dynamic response of turbomachinery components to aerodynamic excitations is an item of continuing concern to designers and manufacturers of gas turbine engines. The accurate first principles prediction of the aerodynamically forced response of a turbine engine blade or vane involves the following items.

Spatially periodic variations in pressure, velocity, and flow direction of the exit flow field of an upstream airfoil element appear as temporally varying in a coordinate system fixed to the downstream row. As a result, individual airfoils are subject to a time-variant periodic aerodynamic forcing function. When the forcing function frequency is equal to an airfoil natural frequency, vibrations of the airfoil result. At times these vibrations have relatively large amplitudes which induce high vibratory stress levels. Unfortunately, at present these resonant stress levels are unknown until the first testing of the blade or vane row. If stresses in excess of a predetermined allowable level result, then airfoil life considerations require that these stresses be reduced.

The prediction of the aerodynamically forced response vibratory behavior of a blade or vane row requires a definition of the unsteady forcing function in terms of its harmonics. The time-variant aerodynamic response of the airfoil to each harmonic component of this forcing function is then assumed to be comprised of two distinct but related unsteady aerodynamic parts. One is due to the harmonic forcing function being swept past the non-responding fixed airfoils – termed the gust response. The second is created by the resulting harmonic response of the airfoil – termed the self-induced aerodynamic response and, under certain conditions, also referred to as the aerodynamic damping.

Unsteady aerodynamic gust and self-induced aerodynamic response analyses are both items of fundamental research interest. Linearized unsteady compressible and incompressible small perturbation analyses for isolated and cascaded airfoils are appearing in the open literature with regularity. Of direct application to turbomachinery design are the unsteady aerodynamic analyses for cascaded airfoils. In particular, Whitehead [1] analyzed both the transverse gust response and the torsion and translation mode self-induced aerodynamic response of a cascade of flat plate airfoils in an incompressible flow. This analysis was extended to include the effects of compressibility by Fleeter [2] and Smith [3]. The effect of airfoil profile on the self-induced aerodynamic response of a cascade in an incompressible uniform flow field has been analytically predicted by Atassi and Akai [4].

There are many mathematical and physical assumptions inherent in these models. Hence, a limited number of appropriate fundamental experiments were undertaken to assess the range of validity of the analyses. Included among these are the experiments of Ostdiek [5], Henderson and Frank [6], and Fleeter, Bennett and Jay [7, 8, 9]. A complete review of research related to unsteady flows in turbomachinery, including both experimental and analytical gust response and self-induced aerodynamic response effects, is presented by Platzer in reference 10.

Generally, the aerodynamically forced response of an airfoil is predicted utilizing a classical Newton's second law forced response approach. The unsteady aerodynamic analyses are used to describe the forcing function in conjunction with a lumped parameter description of the airfoil structural dynamic properties [11]. This paper presents an alternative calculation procedure utilizing an energy balance technique. In particular, an energy balance similar to that performed by Carta [12] is conducted between the unsteady aerodynamic work and the energy dissipated by the airfoil structural and aerodynamic damping. This technique is then

---

Contributed by the Fluids Engineering Division for publication in the JOURNAL OF FLUIDS ENGINEERING. Manuscript received by the Fluids Engineering Division, October 14, 1982.

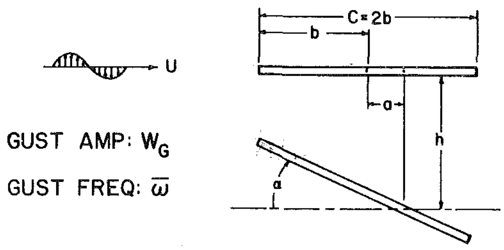

Fig. 1 Airfoil and displacement geometry and notation

applied to an airfoil cascade utilizing theoretical unsteady aerodynamic coefficients which enable the effects of reduced frequency, inlet Mach number, cascade geometry, and interblade phase angle on the aerodynamically forced response of the airfoil to be investigated. In addition, experimental unsteady aerodynamic gust data for a flat plate and a cambered airfoil cascade are used in conjunction with the theoretical zero incidence flat plate cascade unsteady self-induced aerodynamic coefficients to consider the effects of incidence angle and airfoil camber on the forced response of the airfoil cascade.

General Unsteady Aerodynamic Coefficients

Figure 1 presents a schematic representation of a two-dimensional airfoil section displaced in both torsion and translation in a uniform flow with a superimposed convected transverse sinusoidal gust. The complex, time-dependent unsteady lift and moment per unit span are written in influence coefficient form for the gust and the self-induced aerodynamic response cases in equations 1 and 2 respectively.

$$\left.\begin{aligned} L_G &= L_G{}^R + iL_G{}^I = \pi\rho b^3\bar{\omega}^2\left[A_G\left(\frac{W_G}{U}\right)\right] \\ M_G &= M_G{}^R + iM_G{}^I = \pi\rho b^4\bar{\omega}^2\left[B_G\left(\frac{W_G}{U}\right)\right] \end{aligned}\right\} \quad (1)$$

$$\left.\begin{aligned} L_{SI} &= L_{SI}{}^R + iL_{SI}{}^I = \pi\rho b^3\omega^2[A_h\, h + A_\alpha\, \alpha] \\ M_{SI} &= M_{SI}{}^R + iM_{SI}{}^I = \pi\rho b^4\omega^2[B_h\, h + B_\alpha\, \alpha] \end{aligned}\right\} \quad (2)$$

where: $h = \bar{h}\,e^{i\omega t}$; $\alpha = \bar{\alpha}\, e^{i\omega t}$; $W_G = \bar{W}_G e^{i\bar{\omega}t}$ describes the gust; (A_h, B_h), (A_α, B_α), (A_G, B_G) denote the generalized unsteady lift and moment coefficients due to airfoil translation, airfoil torsion, and the convected sinusoidal gust, respectively; ω is the airfoil natural frequency, and $\bar{\omega}$ is the gust forcing function frequency.

The total unsteady lift and moment on the airfoil are obtained by super-imposing the gust response and the self-induced unsteady aerodynamic forces and moments.

$$L(t) = L_G(t) + L_{SI}(t) = \pi\rho b^3\bar{\omega}^2\left[A_G\left(\frac{\bar{W}_G}{U}\right) + A_h\,\bar{h} + A_\alpha\,\bar{\alpha}\right]e^{i\bar{\omega}t}$$

$$M(t) = M_G(t) + M_{SI}(t) = \pi\rho b^4\bar{\omega}^2\left[B_G\left(\frac{\bar{W}_G}{U}\right) + B_h\,\bar{h} + B_\alpha\,\bar{\alpha}\right]e^{i\bar{\omega}t} \quad (3)$$

It should be noted that the airfoil response occurs at the frequency of the forcing function, hence the gust frequency, $\bar{\omega}$, has been utilized in the specification of the unsteady aerodynamic forces and moments, equation (3).

Energy Balance

The uncoupled equations of motion for the single-degree-of-freedom lumped airfoil model undergoing translation or torsion mode oscillations as depicted in Fig. 1 are given in equation (4).

$$\begin{aligned} m\ddot{h} + (1+ig)sh &= L(t) \\ I\ddot{\alpha} + (1+ig)s\alpha &= M(t) \end{aligned} \quad (4)$$

where: m denotes the airfoil mass, s is the stiffness coefficient, g is the structural damping, and I is the mass moment of inertia about the elastic axis. The uncoupled equations of motion, equation (4), represent an airfoil whose elastic axis is coincident with its center of gravity.

The response of the uncoupled single-degree-of-freedom system is determined by considering the balance between the energy input to the system and the energy dissipated by the system over one cycle of oscillation of the airfoil. The input energy to the system is obtained from a calculation of the work done by the unsteady gust forces and moments acting on the airfoil. The energy dissipated is obtained by calculating the work done by the structural damping and by the self-induced aerodynamic response (aerodynamic damping) forces and moments. For convenience, only the case of torsion mode oscillations will be considered in the following derivations. It should be noted, however, that the translation mode results can be obtained directly from those for the torsion mode by

Nomenclature

a = dimensionless distance of elastic axis aft of mid-chord
b = 1/2 airfoil chord ($C/2$)
g = structural damping coefficient
h = complex translation motion
k = reduced frequency ($k = \bar{\omega}b/U$)
m = mass of airfoil
s = stiffness coefficient
A = unsteady lift
B = unsteady moment
C = airfoil chord
I = mass moment of inertia about the elastic axis
L = unsteady lift
M = unsteady moment
S = airfoil spacing
U = free-stream velocity
W = complex transverse gust function
$\bar{W}$ = amplitude of transverse gust
α = complex torsion motion
$\bar{\alpha}$ = amplitude of oscillation in torsion
λ = phase angle between the gust and the airfoil motion
ϕ = phase angle between the gust and the resulting moment
ψ = phase angle between the unsteady moment due to the gust and the airfoil response
ρ = fluid density
σ = interblade phase angle
ω = airfoil natural frequency
$\bar{\omega}$ = frequency of the transverse gust

Subscripts

G = gust
SI = self-induced (aerodynamic damping)
h = translation
α = torsion

Superscripts

R = real part
I = imaginary part
• = derivative with respect to time

replacing I, α, and M by m, h, and L, respectively, per equation (4).

The unsteady work done per cycle of oscillation by the unsteady gust aerodynamic moment is given by the integral of the product of the real part of the unsteady moment and the resulting displacement over one cycle of motion.

$$\text{Work}_G = \oint \text{Re}[M_G(t)\, d\alpha] \tag{5}$$

where: $M_G(t) = T_0 e^{i(\bar{\omega} t + \phi)}$

$$T_0 = \pi\rho b^4 \bar{\omega}^2 \left(\frac{\bar{W}_G}{U}\right)\left[(B_G{}^R)^2 + (B_G{}^I)^2\right]^{1/2}$$

and $\phi = \tan^{-1}[B_G{}^I/B_G{}^R]$ and defines the phase angle between the gust and the aerodynamic moment due to this gust.

Carrying out the integration specified in equation (5) results in the following expression for the unsteady work due to the gust.

$$\text{Work}_G = -\pi T_0 \bar{\alpha} \sin(\lambda - \phi) \tag{6}$$

where λ denotes the phase angle between the gust and the airfoil motion. It should be noted that the quantity $(\lambda - \phi)$ is, in fact, the phase angle between the unsteady moment due to the gust and the airfoil response. It can be determined in terms of the system structural characteristics by a variety of means. For convenience herein, it is determined from the equation of motion, equation (4), per reference [11].

$$\text{Work}_G = -\pi T_0 \bar{\alpha} \sin(\lambda - \phi) = -\pi T_0 \bar{\alpha} \sin(\psi) \tag{7}$$

where:

$$\psi = \text{TAN}^{-1}\left[\frac{[gs - \pi\rho b^4 \bar{\omega}^2 B_\alpha{}^I]}{[(-I\bar{\omega}^2 + s - \pi\rho b^4 \bar{\omega}^2 B_\alpha{}^R]}\right].$$

The energy dissipated per cycle of oscillation is obtained by integrating the real part of the product of the self-induced unsteady aerodynamic response (the aerodynamic damping) moment and the airfoil displacement over one cycle of oscillation. It should be noted that although this term is written as a dissipation term, under certain conditions it can represent an energy input term.

$$\text{Work}_{SI} = \oint \text{Re}[M_{SI}(t)\, d\alpha] \tag{8}$$

This integration leads to the following expression for the energy dissipated per cycle of oscillation.

$$\text{Work}_{SI} = \pi(gs - \pi\rho b^4 \bar{\omega}^2 B_\alpha{}^I)\bar{\alpha}^2 \tag{9}$$

The balance of energy requires that the energy input to the system must be equal to that dissipated by the airfoil, i.e.,

$$\text{Work}_G = \text{Work}_{SI} \tag{10}$$

Substitution of equations (7) and (9) into this energy balance equation results in the following expression for the response amplitude of the oscillation, $\bar{\alpha}$.

$$\bar{\alpha} = \frac{T_0 \sin(\psi)}{gs - \pi\rho b^4 \bar{\omega}^2 B_\alpha{}^I} \tag{11}$$

The term sin (ψ) can be determined via application of the Pythagorean Theorem to the definition of ψ specified in equation (7) with the following result.

$$\sin(\psi) = \frac{[gs - \pi\rho b^4 \bar{\omega}^2 B_\alpha{}^I]}{[(-I\bar{\omega}^2 + s - \pi\rho b^4 \bar{\omega}^2 B_\alpha{}^R)^2 + (gs - \pi\rho b^4 \bar{\omega}^2 B_\alpha{}^I)^2]^{1/2}} \tag{12}$$

The substitution of this expression for sin(ψ) into equation (11) results in the following expression for the torsion mode amplitude of response of the airfoil to an aerodynamic excitation.

$$\bar{\alpha} = \frac{T_o}{[(-I\bar{\omega}^2 + s - \pi\rho b^4 \bar{\omega}^2 B_\alpha{}^R)^2 + (gs - \pi\rho b^4 \bar{\omega}^2 B_\alpha{}^I)^2]^{1/2}} \tag{13}$$

Unsteady Aerodynamic Forces and Moments

L_h, M_h, L_α, and M_α denote the standard form for the unsteady aerodynamic forces and moments and represent the unsteady lift and moment in translation and torsion, respectively, calculated about the airfoil 1/4 chord. These standard form 1/4 chord coefficients are related to the general unsteady aerodynamic influence coefficients through the following relationships.

$$\begin{aligned}
A_h &= L_h \\
A_\alpha &= L_\alpha - (1/2 + a)L_h \\
A_G &= L_G \\
B_h &= M_h - (1/2 + a)L_h \\
B_\alpha &= M_\alpha - (1/2 + a)(L_\alpha + M_h) + (1/2 + a)^2 L_h \\
B_G &= M_G
\end{aligned} \tag{14}$$

where a is the dimensionless distance of the torsion axis aft of the airfoil mid-chord, as depicted in Fig. 1.

The unsteady aerodynamic coefficients to be utilized in this investigation are obtained from: (1) the isolated flat plate airfoil at zero incidence in an incompressible flow field analyses of Theodorsen and Sears [13, 14]; (2) the analysis for a cascade of flat plate airfoils at zero incidence in a compressible flow field, presented in reference [2]; (3) the experimental cascade gust response data described in references [7, 8, and 9] in conjunction with the cascade self-induced response analysis of reference [2].

The isolated flat plate unsteady aerodynamic analyses, Case 1, will be utilized to verify the energy balance technique derived in the previous section. This verification will be accomplished through a comparison of the torsional response calculated by this energy balance technique and that calculated by a classical Newton's second law procedure [11].

The flat plate cascade compressible flow unsteady aerodynamic coefficients, Case 2, will be utilized to perform a parametric study on the forced response of a representative flat plate airfoil with structural characteristics based on an airfoil with a 3.18 cm chord, a thickness-to-chord ratio of 4 percent, and an aspect ratio of 2. Parameters to be varied will include the inlet Mach number, the interblade phase angle, the elastic axis location, and the cascade geometry.

The combination of the cascade analysis and the experimental gust response data, Case 3, will enable the effects of the assumptions inherent in the analyses on the response amplitude to be ascertained as well as the effects of incidence angle and airfoil camber. Experimental unsteady aerodynamic gust coefficients for flat plate and cambered airfoil cascades will be calculated from the airfoil surface unsteady pressure data presented in references [7, 8, and 9]. These experimental gust coefficients will then be utilized in conjunction with theoretical flat plate self-induced response coefficients to obtain a semi-empirical prediction of the forced response of the representative airfoil. These semi-empirical results will then be compared with corresponding forced response predictions utilizing only theoretical unsteady aerodynamics.

Results

To verify the energy balance approach for the prediction of aerodynamically induced vibrations, the uncoupled torsion

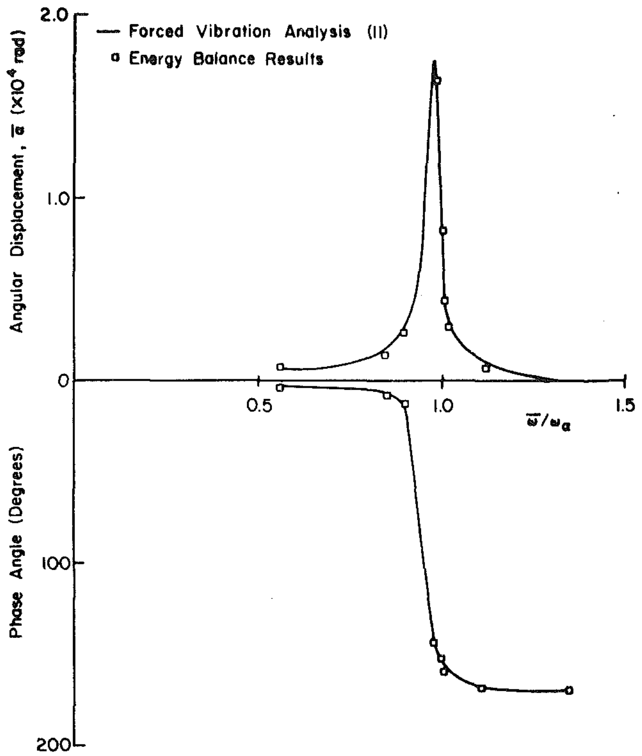

Fig. 2 Comparison of classical forced vibration results with those of the energy balance technique

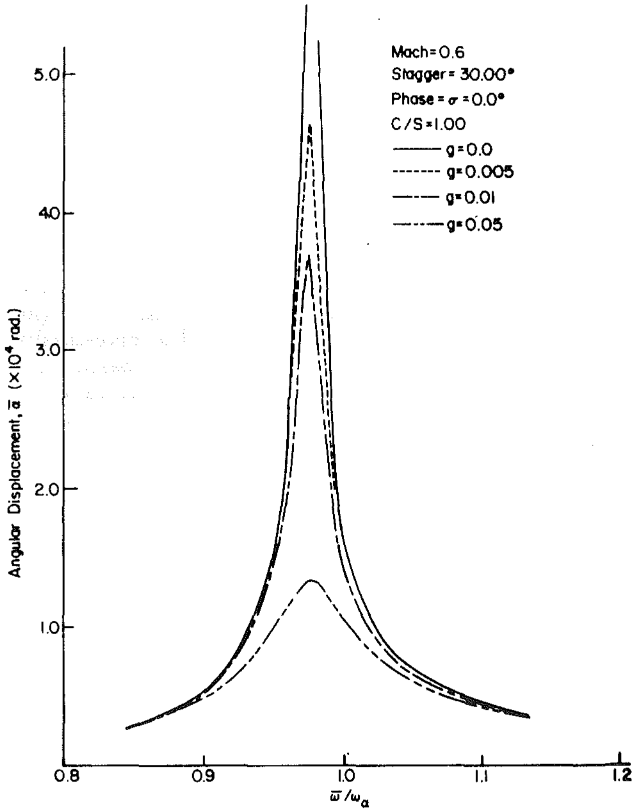

Fig. 3 Effect of damping on aerodynamic forced response amplitude

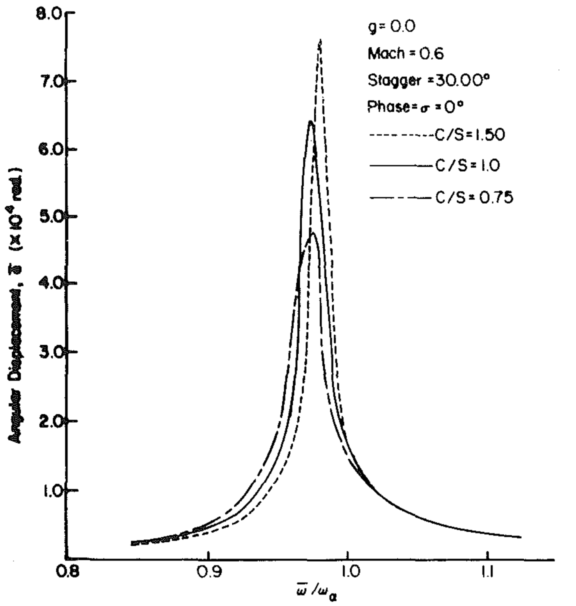

Fig. 4 Effect of cascade solidity on aerodynamic forced response amplitude

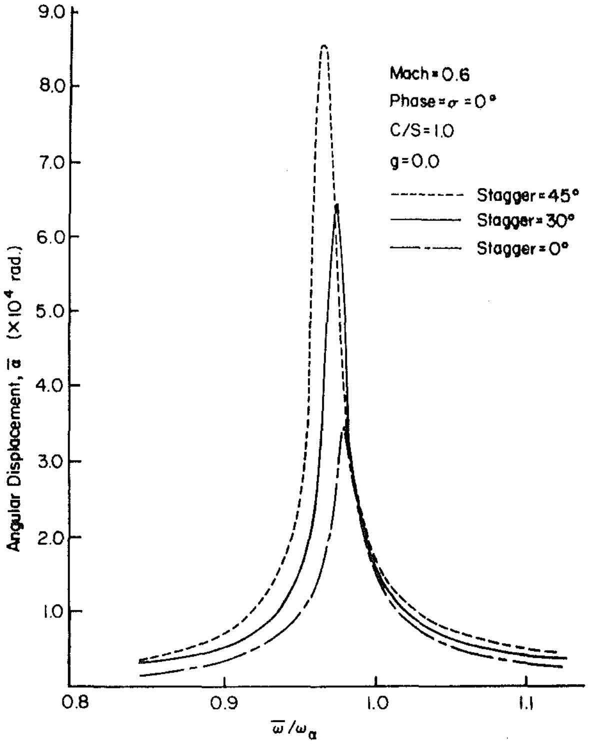

Fig. 5 Effect of Cascade stagger angle on aerodynamic forced response amplitude

mode response of the reprsentative airfoil was calculated by means of both the energy balance technique of this paper and a classical Newton's second law approach [11]. The analytical zero incidence, incompressible flow, isolated airfoil unsteady aerodynamic transverse gust and self-induced coefficients of references [13 and 14] were utilized in these calculations. Figure 2 presents the comparison of these calculation techniques in the form of the torsion mode response as a function of the ratio of the forcing function frequency to the airfoil natural frequency. As seen, the two methods yield identical results, both in terms of the amplitude and the phase of the response.

Figures 3 through 10 describe a parametric study of the aerodynamically induced uncoupled torsion mode response of the representative airfoil utilizing the theoretical flat plate cascade, compressible flow unsteady aerodynamic transverse gust and damping coefficients of reference [2]. Parameters

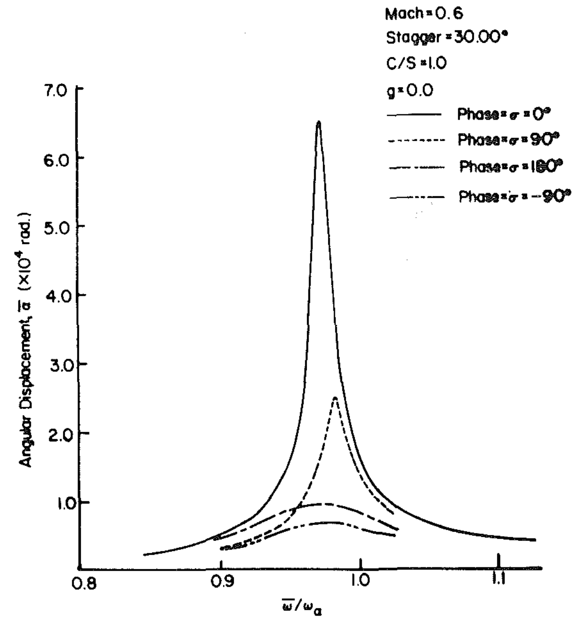

Fig. 6 Effect of interblade phase angle on aerodynamic forced response amplitude

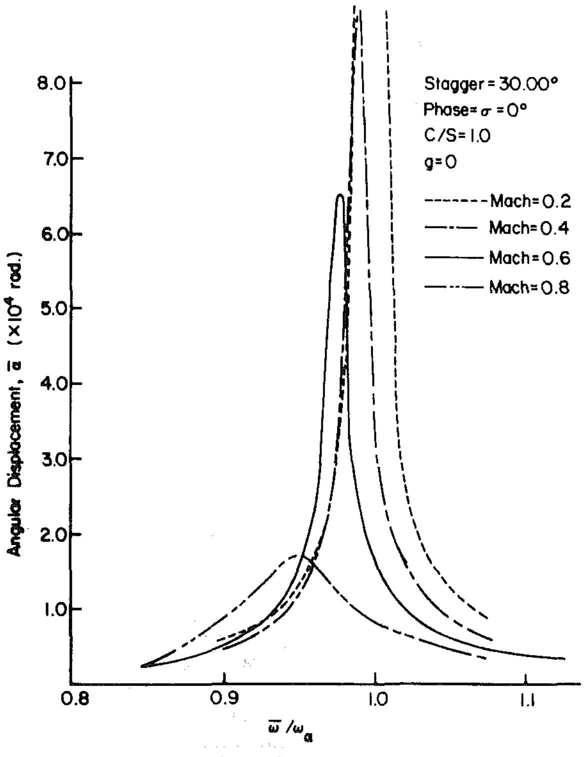

Fig. 7 Effect of inlet Mach number on aerodynamic forced response amplitude

varied include the structural damping, the cascade solidity and stagger angle, the interblade phase angle, and the inlet Mach number.

Figure 3 demonstrates the effect of structural damping on the torsional amplitude of response. Decreasing the structural damping value from 0.01 to 0.005, a factor of 2, results in approximately a 25 percent increase in the maximum response amplitude. It should be noted that the peak response amplitude does not occur when the forcing function frequency is equal to the airfoil natural frequency, even for the case of zero structural damping. This is because aerodynamic damping as well as structural damping has been considered. Thus, even when the structural damping is zero, aerodynamic damping is present in the system.

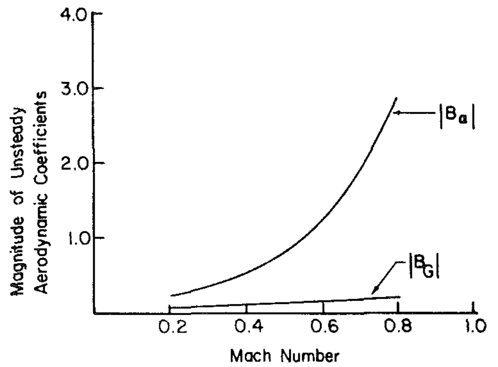

Fig. 8 Magnitude of unsteady aerodynamic coefficients as a function of inlet Mach number

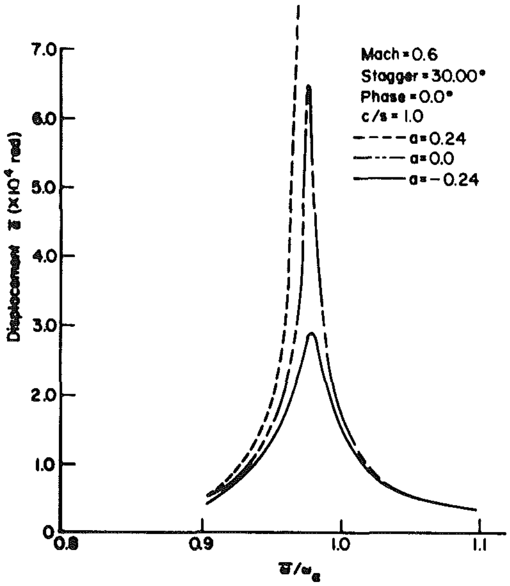

Fig. 9 Effect of elastic axis location on aerodynamic forced response amplitude

The effects of the cascade solidity and stagger angle on the amplitude of the torsional response are presented in Figs. 4 and 5, respectively. As seen, the amplitude of the response decreases as both the cascade solidity and stagger angle decrease, with the stagger angle having a much more pronounced effect.

Figure 6 demonstrates the effect of the interblade phase angle on the torsional response amplitude. The maximum response is seen to occur at an interblade phase angle of 0 deg. A change in the interblade phase angle from 0 deg to 90 deg results in a significant decrease in the maximum response amplitude. Further changes of the interblade phase angle value, to 180 and −90 deg, result in a continued decrease in the maximum response amplitude, although not nearly of the magnitude of change observed in going from 0 to 90 deg. It should be noted that in terms of a rotor-stator interaction forced response problem, the interblade phase angle represents the ratio of the number of upstream rotor blades to the number of downstream stator vanes as it describes the disturbance phase difference existing between adjacent downstream airfoils. Hence, Fig. 6 shows that minimum amplitude response is predicted when there are more rotor blades than stator vanes, with the gust representing a backward traveling wave to the stators.

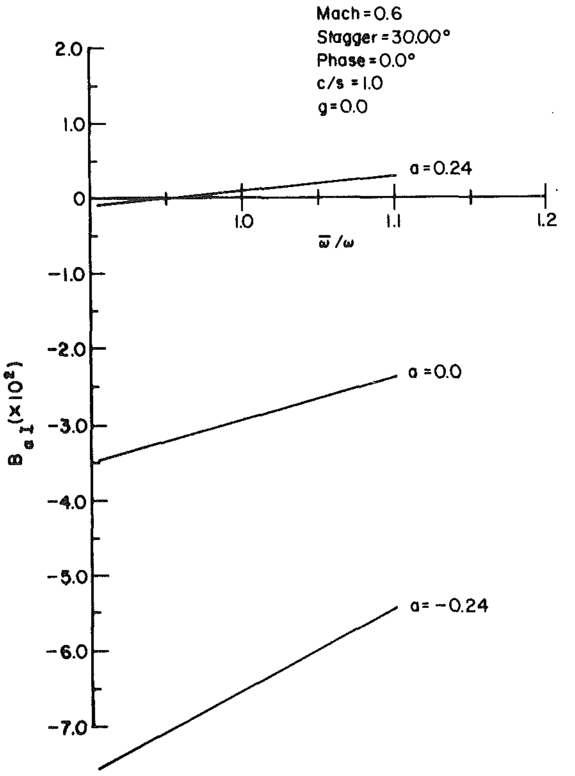

Fig. 10 Imaginary moment coefficient as a function of frequency with elastic axis location as parameter

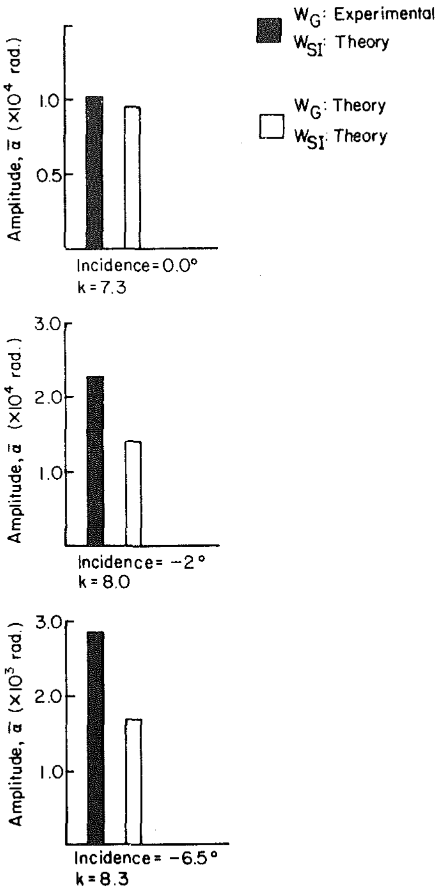

Fig. 11 Comparison of predicted aerodynamic forced response amplitude of a flat plate airfoil using semi-experimental and theoretical aerodynamic coefficients

Figure 7 shows the effect of inlet Mach number on the uncoupled torsion mode response. Increasing the Mach number results in an apparent decrease in the amplitude of response and a decrease in the value of the ratio of the gust forcing frequency to the airfoil natural frequency at which the maximum response amplitude occurs. It should be noted that the airfoil natural frequency is constant. Hence, at a constant value of $\bar{\omega}/\omega$, varying the inlet Mach number also corresponds to a variation in the reduced frequency of the airfoil ($k = \bar{\omega}b/U$). To aid in interpreting the response amplitude variations with Mach number, consider Fig. 8 which presents the magnitude of the unsteady aerodynamic gust and damping as a function of Mach number. As seen, increasing the Mach number results in an increase in the magnitudes of both the aerodynamic gust and the aerodynamic damping, with the aerodynamic damping increasing at a much greater rate. Hence, for the case considered, increasing the Mach number results in a slightly increased gust forcing function magnitude but a greatly increased level of aerodynamic damping, thereby leading to the results of Fig. 7.

Figure 9 indicates the effect that the elastic axis location has on the airfoil torsional response. In particular, this figure shows that as the elastic axis is varied from a location forward of the center of gravity to one aft, the airfoil response increases. For the example case being considered, when the elastic axis parameter, a, has a value of $+0.24$, the airfoil motion becomes unstable. This torsional instability is also demonstrated in Fig. 10 which presents the imaginary part of the unsteady torsional moment coefficient, $B_\alpha{}^1$ as a function of forcing frequency with the elastic axis location as parameter. At an elastic axis location specified by $a = +0.24$, $B_\alpha{}^1$ becomes positive, thereby indicating a flutter condition. It should be noted that varying the elastic axis location can result in a coupling of the bending and torsional modes, although only the uncoupled torsional mode of vibration has been considered herein.

To indicate the effects of incidence angle on the gust response and also the validity and usefulness of the flat plate cascade analyses, consider Figs. 11 and 12. These figures present the predicted forced torsion mode amplitude of response utilizing: (1) experimentally determined flat plate and cambered airfoil aerodynamic gust coefficients based on the data reported in references [7, 8, and 9] in conjunction with the theoretical flat plate aerodynamic damping coefficients of reference [2]; (2) theoretical flat plate aerodynamic gust and self-induced coefficients of reference [2].

For the flat plate cascade, Fig. 11, at zero incidence there is excellent agreement between the semiexperimental and the theoretical results. Decreasing the incidence angle from 0 results in increased response amplitudes as compared to the zero incidence theoretical results with the difference varying in a smooth manner. It should be noted that the reduced frequency and, hence, the unsteady aerodynamics, vary with incidence angle. Thus, these results cannot be absolutely compared to one another as a function of the incidence angle, but rather must be compared individually to the theoretical predictions.

Figure 12 compares the semiexperimental cambered airfoil cascade predictions with the corresponding flat plate theoretical predictions. As seen, the combination of a cambered airfoil at incidence angle results in a nonlinear variation of the comparison results for the response amplitude.

Summary and Conclusions

The aerodynamically forced response of an airfoil has been predicted based on an energy balance technique. In particular, an energy balance has been performed between the unsteady aerodynamic work and the energy dissipated through the

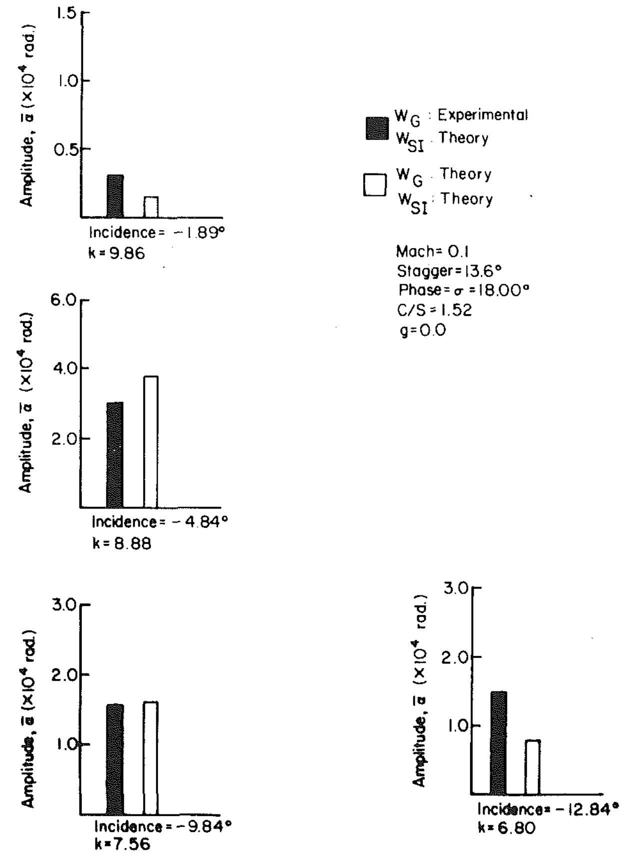

Fig. 12 Comparison of predicted aerodynamic forced response amplitude using semiexperimental and theoretical aerodynamic coefficients

airfoil structural and aerodynamic damping. A parametric study was then undertaken to investigate the effects of reduced frequency, cascade geometry, inlet Mach number, and interblade phase angle on the uncoupled torsion mode response of a representative airfoil. This study demonstrated that the torsional response amplitude decreased with:

- increased structural damping
- decreased cascade solidity
- decreased stagger angle
- increased inlet Mach number
- an interblade phase angle corresponding to a backward traveling wave
- a forward elastic axis location.

In addition, investigation of the torsional forced response of an airfoil based on experimental flat plate and cambered airfoil aerodynamic gust data revealed the following.

- The theoretical flat plate cascade aerodynamic coefficients accurately represent the physics of the problem at zero incidence angle.
- As the incidence angle is changed from a value of zero, the flat plate semiexperimental results diverge from the theoretical results, albeit in a somewhat regular manner.
- The cambered airfoil semiexperimental results differ significantly from the theoretical flat plate results, even at zero incidence.

This variation appears to be non-regular with incidence angle, thereby clearly demonstrating the need for a cambered airfoil cascade unsteady aerodynamic analysis.

Acknowledgment

This research was sponsored, in part, by the Air Force Office of Scientific Research.

References

1 Whitehead, D. S., "Force and Moment Coefficients for Vibrating Airfoils in Cascade," Aeronautical Research Council R&M3254, Feb. 1960.

2 Fleeter, S., "The Fluctuating Lift and Moment Coefficients for Cascaded Airfoils in a Nonuniform Compressible Flow," *AIAA Journal of Aircraft*, Vol. 10, No. 2, Mar. 1973.

3 Smith, S. M., "Discrete Frequence Sound Generation in Axial Flow Turbomachines," University of Cambridge, Department of Engineering Report CUED/A-Turbo/TR29, 1971.

4 Atassi, H., and Akai, T. J., "Aerodynamic and Aeroelastic Characteristics of Oscillating Loaded Cascades at Low Mach Number," ASME Paper No. 79-FT-111, Mar. 1979.

5 Ostdiek, F. R., "A Cascade in Unsteady Flow," Ph.D. thesis, The Ohio State University, 1975.

6 Henderson, R. E., and Frank, G. F., "Investigation of the Unsteady Pressure Distribution on the Blades of an Axial Flow Fan," Pennsylvania State University ARL TM 78-54, Mar. 1978.

7 Fleeter, S., Jay, R. L., and Bennett, W. A., "Rotor Wake Generated Unsteady Aerodynamic Response of a Compressor Stator," ASME *Journal of Engineering for Power*, Vol. 100, No. 4, Oct. 1978.

8 Fleeter, S., Jay, R. L., and Bennett, W. A., "The Time-Variant Aerodynamic Response of a Stator Row Including the Effects of Airfoil Camber," ASME *Journal of Engineering for Power*, Vol. 102, No. 2, Apr. 1980.

9 Fleeter, S., Jay, R. L., and Bennett, W. A., "Wake Induced Time-Variant Aerodynamics Including Rotor-Stator Axial Spacing Effects," *Symposium on Nonsteady Fluid Dynamics*, ASME, Dec. 1978.

10 Platzer, M. F., "Unsteady Flows in Turbomachines—A Review of Recent Developments," AGARD-CP-227, Sept. 1977.

11 Fung, Y. C., *An Introduction to the Theory of Aeroelasticity*, Dover Publications, Inc., 1969.

12 Carta, F. O., "Coupled Blade-Disk-Shroud Flutter Instabilities in Turbojet Engine Rotors," ASME *Journal of Engineering for Power*, Vol. 89, No. 3, July 1967.

13 Theodorsen, T., "General Theory of Aerodynamic Instability and the Mechanism of Flutter," NACA Report 496, 1935.

14 Sears, W. R., "Some Aspects of Non-Stationary Airfoil Theory and Its Practical Applications," *Journal of Aeronautical Sciences*, Vol. 8, No. 3, Jan. 1941.

Mitsukiyo Murakami
Professor,
Department of Mechanical Engineering.

Kiyoshi Minemura
Associate Professor,
College of General Education.

Nagoya University,
Nagoya, Japan

Effects of Entrained Air on the Performance of a Horizontal Axial-Flow Pump

The performance of an axial-flow pump was investigated under air-admitting conditions and the results were compared with those obtained for radial-flow pumps investigated in our previous studies. For the axial-flow pump we measured head as a function of impeller speed, liquid flow rate, and air void fraction. Flow visualization was performed and we correlated air bubble size as a function of Weber number based on mean impeller velocity. Overall flow patterns and the locations of air coalesence within the impeller were observed and diagrammed. These data contribute to earlier data obtained by ourselves and others to develop analytical models to predict pump performance degradation due to air admittance.

Introduction

Handling of air-water mixtures by centrifugal pumps is becoming increasingly important in the fields of hydraulics and in nuclear and chemical engineering. Many researchers have been working on this problem, as described for example in [1-3].

Because of the complexity of the gas-liquid flow in the pump impeller and casing, however, it has been difficult to estimate accurately the variations of pump performance due to gas content. The results [4, 5] obtained hitherto have been almost entirely qualitative, except for those of Grabovskiy [6, 7]. Recently, Wilson and his co-workers [8-10] considered this problem from a theoretical side. They analyzed the effects of admitted air and vapor on the impeller work and found that the gases did not substantially affect the impeller work if the inlet void fraction remained small. They also deduced a degradation factor for calculating the reduction of the effective pump head as a function of gas admittance. This factor, however, is valid only in a range of small void fractions. The pumps usually do work steadily with much more gas than this, but the flow pattern in the impeller differs considerably from that with small void fractions, and the foregoing factor is not justified in this case. Later researchers presented test results based on single phase similarity relations, as described by Runstadler and his co-workers [11]. Since the performance degradation of a pump under two-phase flow conditions must also depend on the pump geometry and specific speed, more reasonable models to estimate these effects are still required.

The present authors studied the same problem by using radial-flow pumps (low specific speed pumps) and found that if the performance curves under air admitting conditions were plotted as a function of a parameter, defined by the volumetric flow ratio of air to water at the pump suction, the curves were not affected by changes in air admitting conditions or by changes in pump speed or suction height [12]. It was also found that the performance change due to the air was closely related to the flow pattern change in the impeller, and experimental formulae to estimate the performance change in a range of small air quantities were obtained [13-17]. A theoretical study was also made of the motion of air bubbles in a centrifugal pump impeller and the governing factors for the motion were analyzed [18].

In this paper the applicability of the expressions which have been obtained for radial-flow pumps is tested for the axial flow-pump employed here. The performance degradation due to air admission is also related to the flow pattern in the pump.

2 Experimental Apparatus and Procedure

The pump employed in this experiment was an axial-flow type and had a horizontal shaft. The pump casing was transparent for flow visualization. Figure 1(*a*) shows the pump assembly, the specfications and the pump dimensions. Table 1 gives the geometry of the impeller blades. The experiment was carried out in a closed loop, in which the axial-flow pump, a reservoir tank for air water separation, and a Venturi-tube for flow measurements were in series, Fig. 2. Air was admitted to the suction pipe through openings at a section 1.7D upstream of the impeller eye, where D is the pipe diameter. To check the effect of different ways of air injection, air openings with small holes (diameter = 8 mm, number = 12) and also an air pipe (diameter = 16 mm, length = 90 mm) inserted vertically upward through the suction pipe were employed. The air and water discharged by the pump were separated completely in the reservoir tank. The separated air was removed from the closed pipe line by means of a vacuum pump and the water only was allowed to recirculate to the suction side of the pump through a metering Venturi-tube. The supply pressure was adjusted to various constant values by means of the vacuum pump, and cavitating

---

Contributed by the Fluids Engineering Division for publication in the JOURNAL OF FLUIDS ENGINEERING. Manuscript received by the Fluids Engineering Division, March 9, 1981.

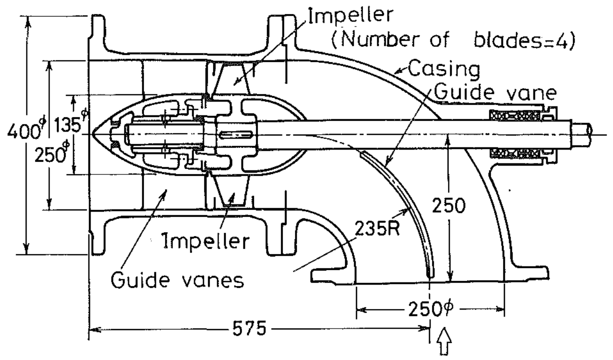

Specification
H = 3.3 m, Q = 8.8 m³/min (ϕ = 0.260), n = 1340 rpm
Specific speed = 1630 (rpm, m, m³/min)

(a) Axial-flow pump

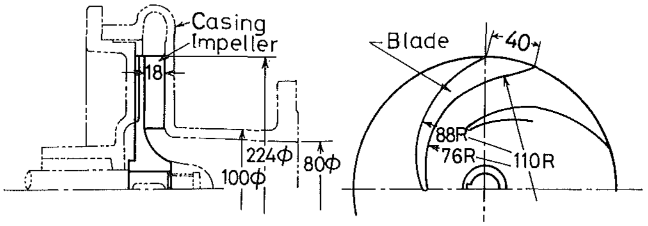

Pump performance at the maximum efficiency point

Pump	Number of blades	H (m)	Q	n rpm	Specific speed	η_{max}
P3	3	15.5	0.75(Φ_o=0.058)	1750	197	0.602
P5	5	19.3	0.89(Φ_o=0.080)	1750	179	0.665
P7	7	18.9	0.84(Φ_o=0.091)	1750	177	0.660

(Units in specific speed; m, m³/min, rpm)

(b) Radial-flow pumps

Fig. 1 Shape, dimensions and specifications of pumps

conditions of flow in the impeller were also brought about. Suction pressure at the pump inlet was read at a section 0.2D upstream of the pump inlet and the pressure elevation due to the swirling flow component generated by the impeller rotation in partial discharge was corrected as Nixon [19] and Murakami [20] describe. Discharge pressure was measured at a section 1.5D downstream of the pump outlet, where the flow was always uniform and no correction was necessary. To change the pressure in the pump system the pressure p_t on the free surface in the reservoir tank was altered. In the course of the experiment the pressure p_r for each test and the water level above the pump center line h_s were maintained at constant values. The hydro static head at the pump center height was determined by:

$$H_{sn} = (p_t - p_{an})/g\rho_w - h_s - (p_v - p_{vn})/g\rho_w \qquad (1)$$

where p_a and p_v are the atmospheric pressure and the saturated vapor pressure of water, respectively, and their subscript n denotes a standard condition (760 mmHg and 15°C). Within the range of pressure heads, $H_{sn} \geqq -1.98$ m, no appreciable cavitation effect on pump head was observed.

In order to measure the size of the air bubbles in the pump, a 35 mm camera was employed, and the motion of bubbles along the inner wall of the casing was traced. Bubble diameters were measured with a microscope on photographs enlarged about six times.

3 Equations to Predict Experimental Results

When a pump delivers water containing air bubbles, considerable energy is consumed in delivering air. This energy will be the sum of the work of discharging the air bubbles against the pressure rise in the pump and a hydraulic loss caused by the excess turbulence due to the relative motion of the bubble against the surrounding water.

Let the developed pump head without air be H_0 and that with air admittance be H. The amount of the head difference $\Delta H = H_0 - H$, will be due to the increases in hydraulic loss in the pump $\Delta h = h - h_0$ and in terms of the impeller head $\Delta H_{imp} = H_{imp} - H_{impo}$ together with the energy consumption H_a for discharging air against the presssure increase in the pump ($H_a = \int q dp/g\rho_w Q$). The impeller work in this case can be calculated by the following relations.

Nomenclature

A_2 = effective discharging area of impeller
D = diameter of suction pipe (=254 mm)
d_m = average diameter of air bubbles
g = gravitational acceleration
H = total differential head $=(p_d/g\rho_w + V_d^2/2g + Z_d) - (p_s/g\rho_w + V_s^2/2g + Z_s)$
H_{imp} = head developed by impeller {equations (2) and(3)}
H_a = head for discharging air {equation (6)}
H_{sn} = head in reservoir tank {equation (1)}
h = hydraulic loss in pump
h_s = suction height
K = numerical constant in equation (9)
L = shaft power
L_f = power loss due to bearings
l = pitch of blades
n = number of revolutions per minute
p = static pressure
p_t = static pressure on water surface in the reservoir tank
Q = volumetric flow of water
q = volumetric flow of entrained air
u_2 = peripheral velocity of impeller
V = mean flow velocity in pipes $\equiv (Q+q)/$(area)
Z = elevation of measuring point from pump center
α = inlet void fraction $\equiv q_s/(Q+q_s)$
η = pump efficiency $\equiv g\rho_w QH/L$
η_v = volumetric efficiency
ρ_w = density of water
ρ_a = density of air
σ = surface tension of water
ϕ = capacity coefficient $\equiv Q/A_2 u_2$
ψ = head coefficient $\equiv H/(u_2^2/g)$
$\Delta\psi$ = decrement of ψ due to air admission
ψ_a = dimensionless expression of H_a, $\equiv H_a/(u_2^2/g)$
ψ_{imp} = dimensionsless expression of H_{imp}, $\equiv H_{imp}/(u_2^2/g)$
$\Delta\psi_{imp}$ = increment of ψ_{imp} due to air admission
ψ_h = dimensionless expression of h, $\equiv h/(u_2^2/g)$
$\Delta\psi_h$ = increment of ψ_h due to air admission

Subscripts

s = pump inlet
d = pump outlet
0 = no air condition

Table 1 Blade profile

Radius (mm)	Chord length, c (mm)	Location of maximum camber, (% chord)	Maximum camber ratio, k/c	Location of maximum thickness, (% chord)	Maximum thickness ratio, t/c	Solidity, c/l	Stagger angle
122.25 (Tip)	108.5	40.7	0.070	41.3	0.040	0.615	64.33 deg
98.75 (Mean radius)	104.0	48.5	0.083	38.7	0.050	0.671	67.5 deg
73.0 (Nearby boss)	98.0	53.5	0.088	46.6	0.056	0.855	59.5 deg

(c = cord length, k = maximum camber, l = blade spacing, t = blade thickness)

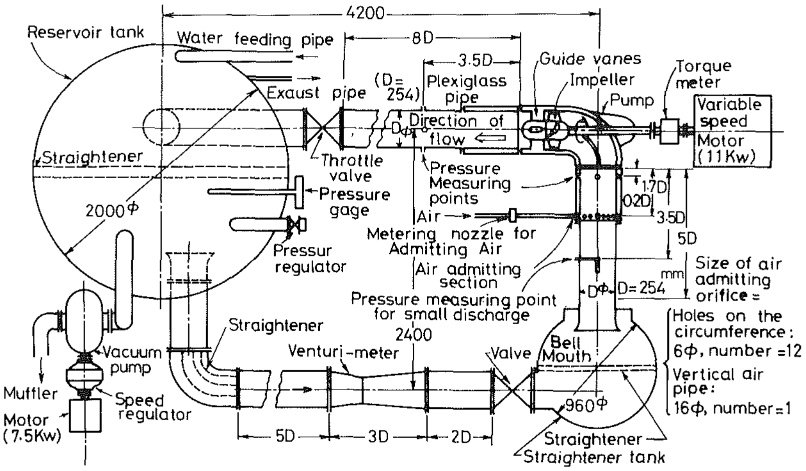

Fig. 2 General layout of experimental apparatus for axial-flow pump

$$H_0 + h_0 = H_{\mathrm{imp}_0} = \eta_{v0}(L_0 - L_{f0})/g\rho_w Q_0 \quad (2)$$

$$H + (h + H_a) = H_{\mathrm{imp}} = \eta_v (L - L_f)/g\rho_w Q \quad (3)$$

These results can be expressed as

$$\Delta H = H_a + \Delta h - \Delta H_{\mathrm{imp}} \quad (4)$$

or

$$\Delta\psi = \psi_a + \Delta\psi_h - \Delta\psi_{\mathrm{imp}} \quad (5)$$

In a radial-flow pump that has very few impeller blades, the velocity distribution in the impeller passages is very nonuniform without air, since the channel passages are unsuitably wide. This flow non-uniformity is much improved by introduction of a suitable amount of air. Hence, the impeller work is increased, namely, $\Delta\psi_{\mathrm{imp}} > 0$[14, 15, 17].

The heat required for discharging the air entrained can be estimated by the following equation when an isothermal change in the flow in the pump is assumed [12, 13]

$$H_a = (p_s q_s / g\,\rho_w Q)\,\ln(p_d/p_s) \quad (6)$$

4 Experimental Results and Discussions

4.1 Performance Curve. An example of pump performance degradation due to air admission is shown in Fig. 3, where the solid curves (marked by the letters *a-b-c*) indicate those for no air. When air is admitted at point *a* or *b*, the performance changes along the lines *a-a'* or *b-b'* as the air quantity is increased. The curves for constant inlet void fraction, α = const., are obtained by connecting the point of equal values of α for various running conditions of the pump.

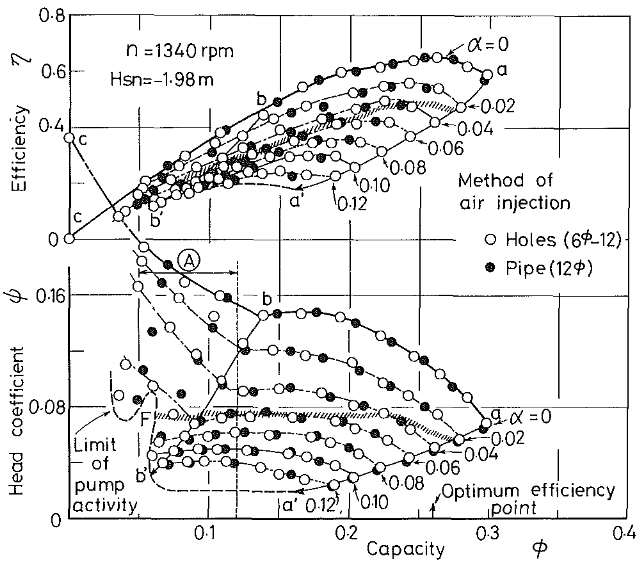

Fig. 3 Performance curves of pump (Noise and vibration occured in the region Ⓐ. Uncertainties; ϕ, $\alpha = \pm 0.0005$, $\psi = \pm 0.0009$, $\eta = \pm 0.008$)

Results showing the effect of two air injection methods are also included in the same figure, and no appreciable effects can be seen. For the sake of simplicity, only the results for the normal pump speed (n = 1340 rpm) and for suction height of H_{sn} = −1.98 m are indicated in Fig. 3, since their effects have proved to be negligible (except for extreme values) as long as the air volume is referred to the suction state [12].

The degradation ratios of head and efficiency of the pump due to air admission are shown as a function of α in Fig. 4, for the pump running near its optimum flow capacity ($\phi_0 = 0.260$). This is, the running point of the pump in this figure is varied approximately along the maximum points of the individual efficiency curves in Fig. 3. The performance degrades gradually as the air quantity increases, and the decrease is a steeper function of α within the range of $\alpha \leqq$

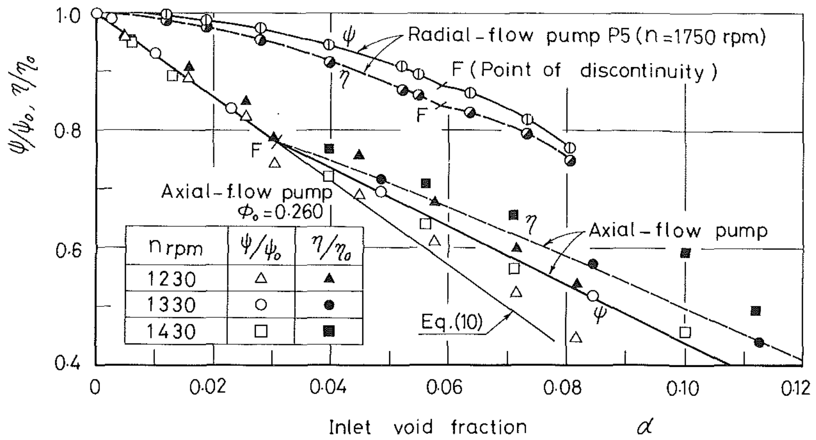

Fig. 4 Comparison of performance for radial and axial-flow pumps (Uncertainties; $\psi/\psi_0 = \pm 0.002$, $\eta/\eta_0 = \pm 0.016$, $\alpha = \pm 0.0005$)

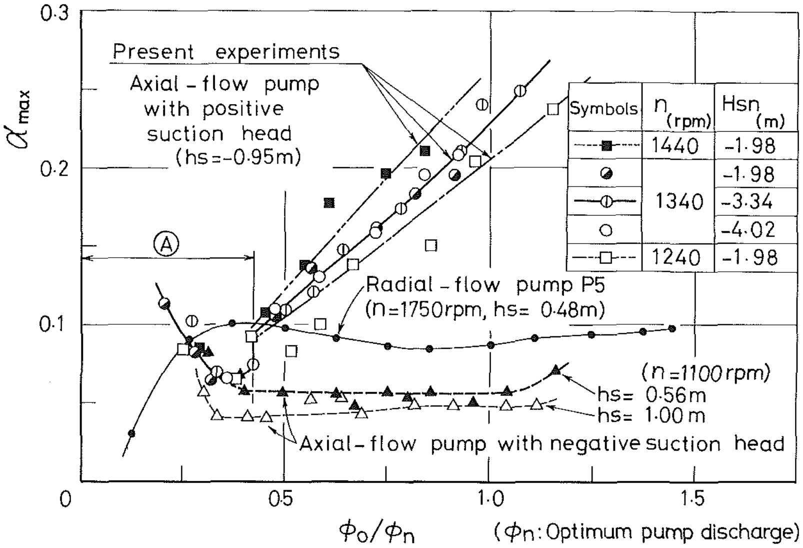

Fig. 5 Maximum possible quantities of air (Reversed flow from the pump impeller occured in the region Ⓐ. Uncertainty for α_{max} is ±0.015.)

0.03. The results for a radial-flow pump ($\psi_0 = 0.445$, $\phi_0 = 0.0080$ and $n = 1750$ rpm) [13] are also shown in the same figure. The curves for both pumps show similar gradual degradation in the range displayed.

Each performance curve in Fig. 4 shows a discontinuity F at a certain air quantity. The shaded region in Fig. 3 indicates where this discontinuity occurred for various flow capacities. At this discontinuity, the flow patterns change abruptly. We saw this behavior in our experiments with a radial-flow impeller pump [13, 14] and we saw similar flow pattern changes in this axial-flow pump, as is explained in Section 4.5.

4.2 Maximum Possible Air Quantities. When the quantity of air entrained is increased continuously, the pump ultimately loses its prime at a value of air quantity $\alpha_{\max}$. This critical value $\alpha_{\max}$ depends on the water flow rate at the beginning of air admission ϕ_0, as shown in Fig. 5. Flow of air in a suction pipe will be affected by the buoyancy of the air and hence the critical void fraction $\alpha_{\max}$ may depend on the layout of the suction pipe. The results in Fig. 5 are those for the case when the pump was tested in a pipe line (including the suction pipe) arranged in a horizontal plane.

If a suction pipe is installed in a form extending immediately downward from the pump casing, the critical void fraction $\alpha_{\max}$ becomes sensitive to the elevation of the pump above the water level of a suction well. When the water level is lower than the pump inlet ($h_s > 0$), namely, when the pump has a positive suction lift, the pump abruptly loses its prime as soon as the air volume exceeds the critical one. Results for this case, obtained from another experiment we performed, are also plotted in Fig. 5. If the water level is higher than the pump inlet ($h_s < 0$), namely, the pump is installed in a negative suction lift, the pump will be able to retain temporally its activity even when the air quantity reaches the critical value. In this case, the critical air volume, with which the pump loses it prime, is hard to determine accurately. In this critical condition, however, the gross movement of air bubbles at the pump entrance is seen to stop. The results called "present experiments" in Fig. 5 were those obtained with the pump in a relatively small negative suction lift ($h_s = -0.95$ m). The value of $\alpha_{\max}$ increases with water quantity ϕ_0 and pump speed n, within the range of $\phi_0/\phi_n \geqq 0.46$. the three sets of data in Fig. 5 for $n = 1340$ rpm confirm that $\alpha_{\max}$ is independent of the Head H_{sn}.

4.3 Size of Bubbles. The size of air bubbles entrained in the suction pipe of a pump may be greatly affected by the manner of air introduction, specifically by the dimension and position of the air admitting orifices. However, our experiments confirm that the bubbles in a rotating impeller have rather uniform size. Figure 6 shows the variation of bubble size along the flow path. Specifically, the figure displays the mean

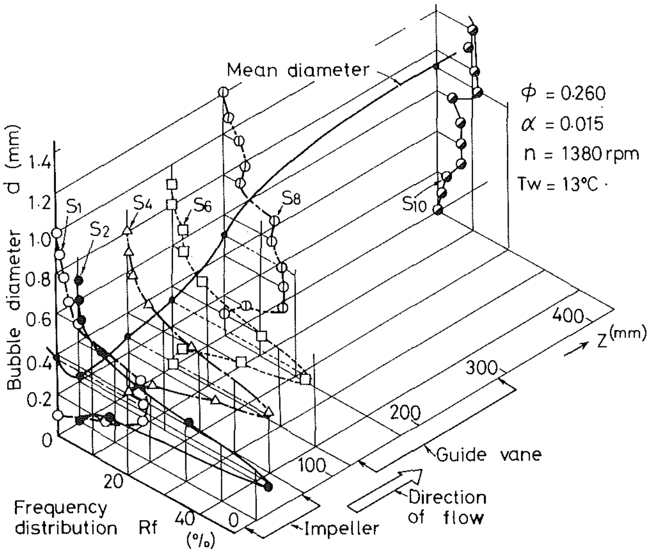

Fig. 6 Change in bubble diameter and its distribution in axial direction (Uncertainty for measured value of d is ±0.01 mm)

bubble diameter d_m and the bubble diameter frequency distribution R_f as functions of position along the flow path. The measuring sections are indicated by S1, S2, . . . , and S10 in order of flow direction. At section S1 just before the impeller inlet, the bubbles are relatively large and have a large variety of sizes. On entering the rotating impeller, however, the larger bubbles decrease remarkably in size and the bubble size become nearly uniform. From this fact, it may be concluded that a strong shear force which breaks the bubbles into finer sizes must exist in the inlet region of the impeller. As the bubbles flow through the impeller, they grow again and the diameter variety increases, since the decrease in the shear action in the downstream region causes an active coalescence of bubbles.

In the following discussion on the motion of bubbles in an impeller, the diameter at the inlet region of the impeller may be taken as representative of typical bubble dimension. The mean value of the bubble diameter d_m ranges from 0.2 mm to 0.4 mm in Fig. 6 for the normal speed of the impeller. This value changes with void fraction, impeller speed and number of impeller blades. From the experimental results in the axial-flow pump, the relationship between d_m and void fraction α can be expressed as

$$d_m/d_0 = 5.6\,\alpha + 0.44 \tag{7}$$

where d_0 denotes the values of d_m in the case of $\alpha = 0.1$. This relationship is also valid for our tests with a radial-flow pump [13, 14].

The size of air bubbles in the impeller is dependent on impeller speed and considered to be governed as well by the surface tension of the water, and hence by a Weber number. At the entrance of an impeller, where the bubbles are broken, the characteristic length and velocity for the Weber number will be the blade spacing l and the peripheral speed u of the impeller entrance. In an axial-flow pump, l and u vary along the radius of the impeller, and the values at the impeller periphery are taken as the characteristic length and speed. Mean diameters, d_m/l, and standard deviation bands of the frequency distribution for bubbles in the impeller expressed dimensionlessly are plotted against the Weber number $u^2 l \rho_w/\sigma$ in Fig. 7. The parameter $u^2 l$ is also used in the abscissa of Fig. 7 because the water temperature and hence its surface tension was kept approximately constant ($T_w = 11.5° \sim 13°C$) during the experiments. The data correlation shown in Fig. 7 are appropriate only for $\alpha = 0.02$ and it should be corrected by equation (7) for other values of α, since the bubble diameter d_m is changed by the air flow rates α as is seen in this equation.

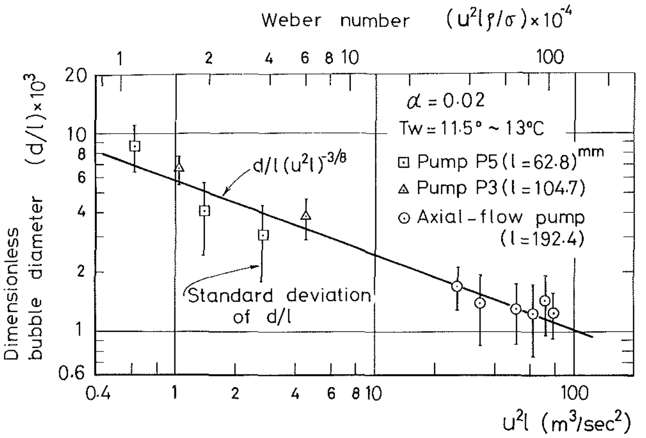

Fig. 7 Relationship between dimensionless bubble diameters and Weber numbers

Figure 7 shows that the dimensionless mean diameter of the bubbles d_m/l decreases with increase in the Weber number. In the figure, the data for the radial-flow pumps (low specific speed) with different numbers of blades, P3 and P5, are also plotted. They give substantially the same results as that in an axial-flow pump (high specific speed).

4.4 Change of Pump Head and Hydraulic Loss Due to Air Admission. The head of a pump is generally decreased by admission of air in the suction pipe. The head decrement $\Delta\psi$ is given by equation (5). When a pump is running at its optimum condition, the value of $\Delta\psi_{\rm imp}$ can be estimated by the use of equations (2) and (3) with the measured values of Q, L, and L_f, together with a volumetric efficiency η_v calculated by use of Kovats' formula [21]. The values of $\Delta\psi$, ψ_a, $\Delta\psi_h$, and $\Delta\psi_{\rm imp}$ for the axial-flow pump are plotted against α in Fig. 8, where the results of the radial-flow pump P5 are also plotted for comparison. The results in this figure correspond to tests at the maximum efficiency points as α is varied. When the air admission rate is small and $\alpha \leqq 0.035$, the head decrement $\Delta\psi$ in the axial-flow pump is larger than that in the radial-flow pump. But when the air rate α exceeds 0.035, the contrary is the case.

An increment of impeller head due to air $\Delta\psi_{\rm imp}$ remains unaltered irrespective of pump type and zero within the range of small air ratio, $\alpha \leqq 0.03$, as is indicated semi-empirically by Wilson and his co-workers [10]. If air quantity is increased gradually the curve of $\Delta\psi_{\rm imp}$ shows a discontinuity F at which the flow pattern in the impeller changes abruptly as explained below. Beyond the discontinuity point F, $\Delta\psi_{\rm imp}$ becomes negative and the impeller work reduces linearly as air increases.

The head required for discharging air ψ_a in the axial-flow pump is very small, since the rate of pressure increase in the impeller is small. The value of ψ_a can be estimated by the following equation [14] with the initial values of pressure.

$$\psi_a = \{\alpha/(1-\alpha)\}\{(p_{s0}/\rho_w u_2^2)\ln(p_{d0}/p_{s0})\} \tag{8}$$

The relationship of equation (8) is shown by line ① in Fig. 8.

The increment of the hydraulic loss $\Delta\psi_h$ is large, and it increases linearly with α when $\alpha \leqq 0.035$. When α is increased beyond this limit, $\Delta\psi_h$ takes a constant value for the axial pump, a value which is considerably smaller than that for the radial-flow pump.

The reason for this difference due to the type of pump may be explained as follows: In a radial-flow impeller the air entrained easily accumulates at the entrance of the impeller and causes a large hydraulic loss, but in an axial-flow pump this kind of accumulation is greatly reduced, since the blade

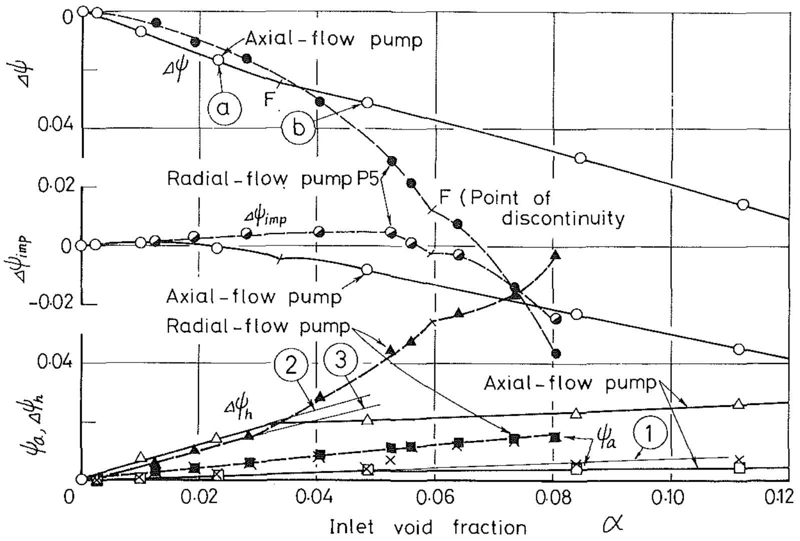

Fig. 8 Relationships between $\Delta\psi$, ψ_a, $\Delta\psi_{imp}$ and inlet void fraction α (Uncertainties; $\Delta\psi = \pm 0.002$, $\Delta\psi_{imp} = \pm 0.010$, $\Delta\psi_h = \pm 0.012$, $\psi_a = \pm 0.001$)

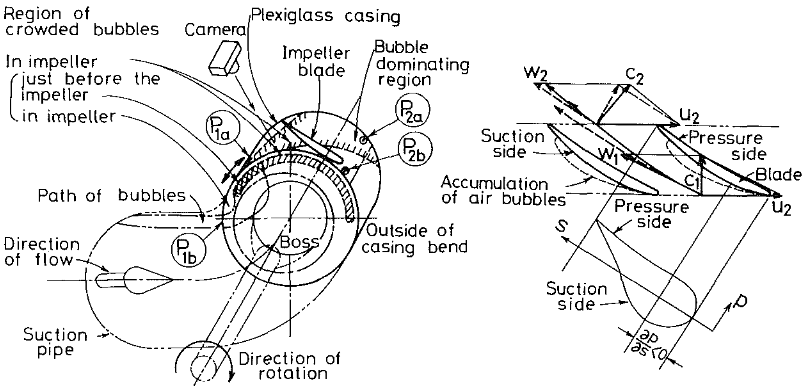

(a) Region of crowded bubbles
$P_{1a}, P_{1b}, P_{2a}, P_{2b}$: Measuring points of pressure fluctuation

(b) Pressure distribution on blade and accumulation of air bubbles

Fig. 9 Flow conditions of air bubbles in the pump

spacing at the impeller entrance is much wider. The curves of $\Delta\psi_h$ against α resembles the change of pump performance due to cavitation development with no air.

The line ② shows the following formula

$$\Delta\psi_h = K\alpha \qquad (9)$$

where K is an experimental constant and is taken to be $K = 0.60$ {the straight line ③ shows the relationship of equation (9) with the constant $K = 0.54$, found for the radial-flow pumps [13]}.

The increase in hydraulic loss due to entrained air is much larger than the value estimated with use of the friction multiplier in a stationary duct [22], because in the impeller there prevails an adverse pressure gradient, as well as centrifugal and Corioris forces, which cause a significant flow resistance and head loss.

An estimation of the performance degradation of radial-flow pumps due to air admission has been given in the previous study [14]. If the same method is applied for an estimation of the head and efficiency changes of the axial-flow pump, the following formulae result:

$$\frac{\psi}{\psi_0} = 1 - \alpha\left\{K + \frac{p_{s0}/\rho_w u_2^2}{1-\alpha}\ln\frac{p_{d0}}{p_{s0}}\right\}\frac{1}{\psi_0} \qquad (10)$$

$$\eta/\eta_0 = \psi/\psi_0 \qquad (11)$$

Equations (10) and (11) are indicated by the line in Fig. 4. These equations agree closely with the data within the range of small inlet void fraction, $\alpha \leqq 0.035$.

4.5 Change in Flow Patterns. As is seen in Figs. 4 and 8, the performance curves of the pump show discontinuity (F) at certain quantities of air. This discontinuity is attributable to an abrupt change of the flow patterns in the impeller, judged from the photographic records taken for the axial-flow pump, the flow patterns at states *a* and *b* in Fig. 8 are sketched in Fig. 9. Since the suction pipe is located horizontally, the movement of the air in the suction pipe is influenced by the buoyancy of the air. The entrained air rises up rapidly and gathers in the top of the suction pipe (unless the air bubbles have vanishingly small diameters). This accumulated air will be shifted inward, due to the centrifugal force of the flow, since the suction pipe has a curved casing in front of the impeller. Hence, the air is drawn locally into the impeller. The crowded part of air at the impeller inlet is shaded by hatched lines in Fig. 9(*a*).

Just after the impeller inlet, a favorable pressure zone exists locally, see Fig. 1(*a*), after which the air is easily accumulated. The air flow shifts to the direction of impeller rotation as it proceeds along the flow path, resulting in an oblique air flow region in the impeller as is shown in Fig. 9(*a*). The centrifugal force due to the curved motion of water in the suction bend, on the other hand, drives the crowded air bubbles towards the inside part of the pipe bend at the impeller entrance. Under the influence of these two counter forces, together with the buoyancy of air, the course of the crowded air bubbles in the impeller is changed periodically in the circumferential direction. This phenomenon occurs when the air quantity α = 0.03, corresponding to that at which the performance curves exhibit discontinuities, Fig. 8. At larger values of α, beyond these discontinuities, the region of crowded air bubbles is enlarged all over the impeller periphery outside the closed chain line in Fig. 9(*a*). In this state, a considerable amount of bubbles accumulate on the suction side of the impeller blades and this accumulation extends to the outlet side of the impeller. This flow pattern change brings about an increase of relative flow angle at the impeller outlet as shown by broken lines in Fig. 9(*b*), and decreases the peripheral component of the absolute flow velocity c_{u2} and hence, the impeller work (Fig. 8).

Corresponding to the change in flow patterns described above, the running condition of the pump becomes unstable and a slow vibration occurs. According to measurements of wall pressure inside the casing [22], the amplitude and also the period of the vibration become maximum near the point F (Fig. 8). If the air quantity α is increased beyond this maximum, the vibration amplitude decreases abruptly, and the period is also decreased to a value corresponding to the rotation period of the impeller.

The value of the void fraction α where the amplitude of the vibration becomes maximum depends on the discharge rate of water ϕ_0, since the discontinuity point F on the performance curve changes with α along the curve F-F as is seen in Fig. 3. Excitation of the vibrations due to air admission will closely relate to the characteristics of the head-capacity curve of the pump and the associated piping that surrounds the pump. A negative slope in the head-capacity curve, which normally sustains stable operation of a pump, may change to a positve slope when air is introduced (if the negative slope is appreciably small enoughh with no air condition) [22]. In turn, unstable running of the pump may result. A similar trend is also seen in the tests described by Rothe and his co-workers [23].

5 Conclusions

Effects of air entrained in the suction pipe of a horizontal type axial-flow pump were investigated experimentally and the results obtained are as follows:

(1) As air quantity increases from zero, the pump performance curve decreases continuously at first and at a certain value of void fraction α exhibits a discontinuity.

(2) An abrupt change in flow pattern was photographed at this discontinuity. Air which had accumulated locally at low void fraction dispersed over the periphery of the impeller at high void fraction.

(3) Shortly after this discontinuous change, the pump loses its prime (when the pump is operating under a positve suction lift). The maximum allowable air quantity for steady pump operation depends largely on the layout of the suction pipe.

(4) This maximum allowable air quantity increases with increase of the impeller speed, since the size of air bubbles in the impeller decreases with increase of the impeller speed, by a relationship which is given as a function of a Weber number in Fig. 7.

(5) For small air void fraction $\alpha \leq 0.04$ the performance degradation $\Delta\psi$ for the axial flow pump we tested is almost the same as that for our radial flow pump (Fig. 8). However, the degradation ratio ψ/ψ_0 between the two machines is not comparable. Both pumps exhibit gradual, rather than abrupt, degradation as void fraction increases continuously up to $\alpha = 0.08$.

Acknowledgment

The authors express their sincere thanks to Dr. Paul H. Rothe for his editorial improvements in this paper.

References

1 Stepanoff, A. J., "Flow of Gas-Liquid Mixtures," *Pumps and Blowers, Two-phase Flow*, Wiley, New York, 1964, pp. 246-274.

2 Florjancic, D., "Influence of Gas and Air Admission on the Behaviour of Single- and Multi-stage Pumps," Sulzer Research Number, 1970, pp. 35-44.

3 Arie, M., and Fukusako, S., "Performance Tests of a Centrifugal Pump," *Proceedings of the Japan-U.S. Seminar on Similitude in Fluid Mechanics*, Sept. 1967.

4 Sozzi, G. L., and Burnett, G. W., "Two-Phase Pump Performance During Steady-State Operation and During a Simulated LOCA Blowdown," Report NEDE-13239, class 1, General Electric, San Jose, Calif., Nov. 1971.

5 Olson, D. J., "Single- and Two-Phase Performance Characteristics of the Mod-1 Semiscale Pump Under Steady-State and Transient Conditions," Aerojet Nuclear Company, ANCR report 1165, Oct. 1974.

6 Grabovskiy, A. M., et al., "Relationship between specific speed and main parameters of centrifugal pumps for regulating its performance by air admission (in Russian)," I.B.Y.Z., *Energy*, Vol. 13, No. 11, Nov. 1970, pp. 91-96.

7 Grabovskiy, A. M., et al., "Estimation of main parameters when regulating the output of centrifugal pumps by air admission (in Russian)," I.B.Y.Z., *Energy*, Vol. 14, No. 12, Dec. 1971, pp. 99-104.

8 Wilson, D. G., et al. "Analytical Models and Experimental Investigation of Centrifugal Pump Performance in Two-Phase Flow," EPRI NP-170, Jan. 1977.

9 Wilson, D. G., et al., "Performance Prediction of Centrifugal Pumps in Two-Phase Flow," *Proceedings of the Joint Symposium on Design and Operation of Fluid Machinery*, ASME, Vol. 2, June 1978, pp. 81-89.

10 Mikielewicz, J., et al., "A Method for Correlating the Characteristics of Centrifugal Pumps in Two-Phase Flow," ASME JOURNAL OF FLUIDS ENGINEERING, Vol. 100, No. 4, Dec. 1978, pp. 395-409.

11 Runstadler, P. W., Jr., and Dolan, F. X., "Two-Phase Flow, Pump Data for a Scale Model NSSS Pump," *Proceedings of the Symposium on Polyphase Flow in Turbomachinery*, ASME, Dec. 1978, pp. 65-77.

12 Murakami, M., et al., "Flow of Entrained Air in Centrifugal Pumps," *Proceedings of the 13th Congress of the IAHR*, Vol. 2, 1969, pp. 71-79.

13 Murakami, M., and Minemura, K., "Effects of Entrained Air on the Performance of a Centrifugal Pump (First Report, Performance and Flow Conditions)," *Bulletin of the Japan Society of Mechancial Engineers*, Vol. 17, No. 110, Aug. 1974, pp. 1047-1055.

14 Murakami, M., and Minemura, K., "Effects of Entrained Air on the Performance of Centrifugal Pumps (2nd Report, Effects of Number of Blades)," *Bulletin of the JSME*, Vol. 17, No. 112, Oct. 1974, pp. 1286-1295.

15 Murakami, M., and Minemura, K., "Effects of Running Clearance of Semi-Open Impeller Pumps under Air Admitting Conditions," *Bulletin of the JSME*, Vol. 19, No. 136, Oct. 1976, pp. 1141-1148.

16 Murakami, M., and Minemura, K., "Flow of Air Bubbles in Centrifugal Impellers and Its Effect on the Pump Performance," *Proceedings of the 6th Australasian Hydraulics and Fluid Mechanics Conference*, Adelaide, Australia, Vol. 1, Dec. 1977, pp. 382-385.

17 Murakami, M., et al., "Effects of Entrained Air on the Performance of Centrifugal Pumps under Cavitating Conditions," *Bulletin of the JSME*, Vol. 23, No. 185, Sept. 1980, pp. 1435-1442.

18 Minemura, K., and Murakami, M., "A Theoretical Study on Air Bubble Motion in a Centrifugal Pump Impeller," ASME JOURNAL OF FLUIDS ENGINEERING, Vol. 102, No. 4, Dec., pp. 446-455.

19 Young, L., and Nixon, R. A., "Power, Flow and Pressure Measurements in Pump Testing," *Proc. Inst. Mech. Engrs.*, Vol. 174, No. 15, 1960, pp. 535-560.

20 Murakami, M., and Heya, N., "Swirling Flow in Suction Pipe of Centrifugal Pumps (First Report)," *Bulletin of the JSME*, Vol. 9, No. 34, 1966, pp. 328-337.

21 Kovats, A., *Centrifugal and Axial Flow Pumps and Compressors*, Pergamon, 1964, p. 122.

22 Murakami, M., and Minemura, K., "Effects of Entrained Air on the Performance of a Horizontal Axial-Flow Pump," *Proc. of the Symposium on Polyphase Flow in Turbomachinery*, ASME, Dec. 1978, pp. 171-184.

23 Rothe, P. H., et al., "Pump Surge Due to Two-Phase Flow," ibid., pp. 121-138.

R. E. Wilson

S. N. Walker

Department of Mechanical Engineering,
Oregon State University,
Corvallis, Oreg. 97331

Fixed Wake Theory for Vertical Axis Wind Turbines

A theory for vertical axis wind turbines has been developed using a fixed wake approach. The theory combines some of the best features of vortex and streamtube approaches. This approach accounts for flow differences between fore-and-aft-blade positions that are predicted by vortex methods while retaining the low computation costs associated with streamtube theories. The theory is applied to high tip speed ratio operation of a Darrieus Rotor where the use of linear aerodynamics results in explicit calculation of the induced velocities. Comparison to test results shows good agreement.

Introduction

Although patented in 1926, [1] the vertical axis rotor did not see extensive development until the 1970's when South and Rangi [2, 3] and later Sandia Laboratories [4] undertook the analysis, design and construction of large Darrieus Rotors. In the course of this development, many aerodynamic models for the Darrieus Rotor have been proposed [5–15]. These models vary considerably in their treatment of the flow with no single approach available that covers dynamic stall, variable induced flow, and wake crossing effects over the entire operating range of a vertical axis rotor. These models may be classified into three groups:

(a) Streamtube models [5–9]
(b) Fixed wave models [10–13]
(c) Free-vortex models [11, 14, 15]

In streamtube models the induced axial velocity is calculated at the rotor by equating the time-averaged force on the blades to the mean momentum flux through a streamtube of fixed location and dimensions. Both single and multiple streamtube approaches have been used. Most of the streamtube models predict fore-and-aft symmetry of flow quantities, however, Lapin [8] introduced the concept of using tandem actuator disks to account for the difference in the flow field between fore-and-aft parts of a streamtube. The forces are calculated from the local angle of attack and local velocity using static airfoil data for lift and drag coefficients as a function of angle of attack. The streamtube approaches have met with modest success in predicting the overall performance and windwise force of Darrieus Rotors.

The streamtube approaches can treat curved-bladed rotors and can incorporate any variation of lift coefficient with angle of attack. Additionally, the computation time needed for streamtube approaches is much less than any other approach.

The fixed wake models use a vortex sheet wake that is locally independent of time. Forces are determined from the Kutta-Joukowski law and circulation. The fixed wake analysis has a distinct advantage over streamtube methods and the computational costs are of the same order as streamtube approaches. The advantage lies in the ability to determine the differences in induced flow between the upwind and downwind blades.

The most complex and accurate method of analysis that has been developed for the Darrieus Rotor is the free vortex approach. The wake is modeled by discrete, force-free vortices convected downstream with velocity determined by induced velocities from the rest of the system.

The free vortex approach, however, has several disadvantages. These are:

1. It is quite expensive to use.
2. The values for the performance and loads are approached asymptotically. Since the wake never reaches an infinite length, the loads and performance are higher with a finite length wake than would be obtained with an infinite wake.
3. Since the wake moves very slowly at high tip speed ratios, high tip speed ratio results are not feasible with present computers.

The purpose of this paper is to demonstrate a rapid, accurate method of calculating Darrieus Rotor performance based on fixed wake concepts. A general approach is developed in this paper and applied to the high tip speed ratio operation of a Darrieus rotor. A subsequent paper will deal with the application to low tip speed ratio operation. First, the induced velocities are derived.

Induced Velocities

Consider an airfoil traversing the path shown in Fig. 1(*a*). Between A and B the airfoil moves parallel to the free stream and generates no force. At point B, the airfoil suddenly changes direction and moves across the wind, generating both lift and circulation. Again at point C, the direction of motion is changed and vorticity is again shed, although the sign of shed vorticity is opposite that shed at B. The wake system that is generated is illustrated in Fig. 1(*b*). The magnitude of the local circulation is shown and the direction is indicated by the

---

Contributed by the Fluids Engineering Division of THE AMERICAN SOCIETY OF MECHANICAL ENGINEERS and presented at the Winter Annual Meeting, Boston, Mass., November 15–19, 1983. Manuscript received by the Fluids Engineering Division, November 3, 1982. Paper No. 83-WA/FE-14.

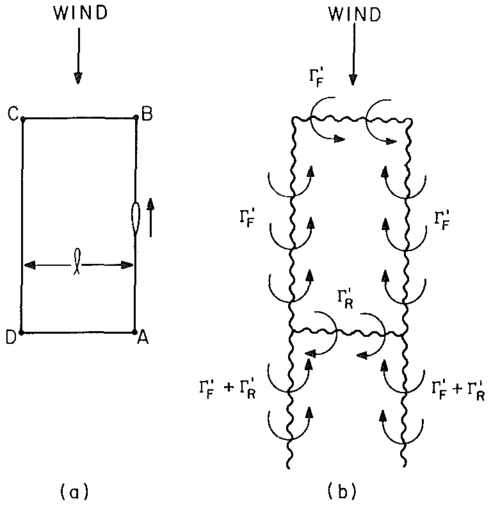

(a) (b)

Fig. 1 Airfoil and vorticity

arrows. We may take certain liberties with the illustrated path without changing the wake pattern.

In Fig. 2 the distance l has been reduced relative to the distance AB and the paths BC and DA have been made to conform with the path of a Darrieus rotor blade. Thus, we have a streamtube of a Darrieus rotor. Considering the flow in other streamtubes to be similar, we arrive at several significant observations:

1. Since the flow along BC is influenced only by the flow inside the vortex street shed by BC, the force on segment BC is not influenced by adjacent elements.
2. As the streamtube gets smaller in width the wake from BC appears as a semi-infinite vortex sheet. The resulting induced velocity at the front is due only to the semi-infinite wake of the front, i.e., $\Delta u_F \sim \Gamma'_F$ *only*. (Here the subscript F refers to the front of the streamtube.)
3. The rear station "sees" an infinite wake due to Γ'_F and a semi-infinite wake due to Γ'_R. The rear induced velocity depends upon both Γ'_R and Γ'_F.

In analytical terms we may write for the induced velocity at the front station

$$\Delta u_F \equiv a_F V = k|\Gamma'_F|$$

and for the rear station, the induced velocity is

$$\Delta u_R \equiv a_R V = k(2|\Gamma'_F| + |\Gamma'_R|)$$

In the far wake

$$\Delta u_{\text{Wake}} \equiv 2a\ V = k(2|\Gamma'_F| + 2|\Gamma'_R|)$$

Here k relates vortex spacing and strength. Thus

$$\Delta u_R - \Delta u_F = k(|\Gamma'_F| + |\Gamma'_R|) = \frac{\Delta u_w}{2}$$

or

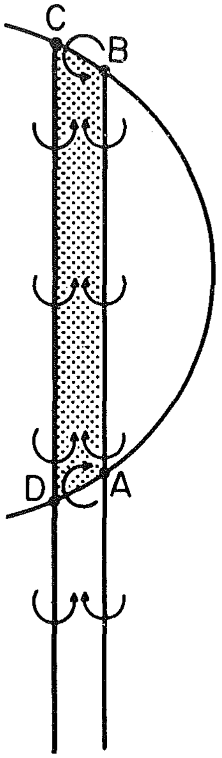

Fig. 2 Darrieus streamtube

$$a_R - a_F - a$$

and

$$\frac{\Delta u_F}{\Delta u_R} = \frac{|\Gamma'_F|}{2|\Gamma'_F| + |\Gamma'_R|} = \frac{a_F}{a_R}$$

Using uniform sign convention for Γ', positive circulation being counterclockwise, one obtains

$$\frac{a_R}{a_F} = 2 - \frac{\Gamma'_R}{\Gamma'_F} \tag{1}$$

and

$$a_R - a_F = a \tag{2}$$

Equations (1) and (2) are exactly the same as those obtained by Holme [10]. The circulation, Γ', does not include the bound circulation. For a symmetrical rotor blade that has its chord tangent to the path of rotation, the only bound circulation is the pitching circulation. Thus

$$\Gamma' = \Gamma_{\text{TOTAL}} - m\pi c^2 \Omega \cos\gamma [3/4 - x_0/c]$$

where γ is the inclination of the blade with respect to the axis of rotation, $m = (C_{L\alpha}/2\pi)$ and x_0 is the location of the blade attachment point with respect to the leading edge.

In order to determine the local induced velocities, a, a_F, and

Nomenclature

A = swept area of rotor
a = induced velocity, $-\Delta u/V$
B = number of blades
c = blade chord
C_D = blade drag coefficient
C_L = blade lift coefficient
C_P = power coefficient $P/\frac{1}{2}\rho A V^3$
C_Q = blade torque coefficient
P = power
Q = torque
r = radial position
R = Darrieus rotor maximum radius
u = wind speed at the rotor
V = free stream wind speed
W = relative velocity
X = tip speed ratio, $R\Omega/V$
z = vertical direction along axis of rotation
α = angle of attack
γ = inclination of blade element relative to z axis
Γ = circulation
θ = angular position of blade
ρ = fluid density
Ω = blade angular velocity

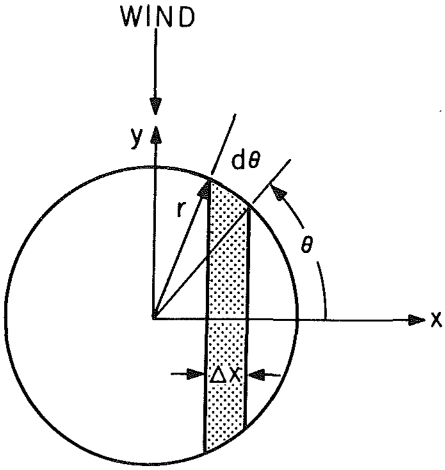

Fig. 3 Streamtube

a_R are required. Let us use a streamtube approach and equate the windwise momentum change to the mean blade force.

The streamtube is illustrated in Fig. 3 where $\Delta x = r\Delta\theta|\sin\theta|$. Equating the momentum flux in the streamtube to the blade force results in

$$a(1-a) = \frac{B}{4\pi}\frac{\Omega}{V^2}[(\Gamma_T)_F - (\Gamma_T)_R] \tag{3}$$

where B is the number of blades. Equations (1), (2), and (3) are sufficient to determine the induced velocities a, a_F, and a_R.

It has been demonstrated from a free wake analysis [15] that the power extracting loads on a Darrieus rotor blade may be closely approximated by a single force, the Kutta-Joukowski force, $\rho W\Gamma'$, where W is the local velocity relative to the blade. An iterative solution for the induced velocities is given in [16] however, for Darrieus Rotor operation at low wind speeds (high tip speed ratios) linear aerodynamics results in an explicit solution for the induced velocities.

Linear Aerodynamics

Using $C_L = 2\pi m \sin\alpha$, the circulation Γ' may be written for front or rear positions as

$$\Gamma_i' = \pi cm(W\sin\alpha)_i = \pi mcV(1-a_i)\sin\theta_i\cos\gamma \tag{4}$$

Equations (1), (2), and (3) become

$$\frac{a_R}{a_F} = 2 + \frac{1-a_R}{1-a_F} \tag{5}$$

$$a_R - a_F = a \tag{6}$$

$$a(1-a) = \frac{BcmX}{4R}\cos\gamma\sin\theta\left(1-a+\sqrt{1-2a}\right) \tag{7}$$

Equations (5) and (6) yield

$$a_F = \frac{1-\sqrt{1-2a}}{2} \tag{8}$$

$$a_R = \frac{1+2a-\sqrt{1-2a}}{2} \tag{9}$$

while equation (7) is a cubic

$$a^3 - 2a^2(1+S) + a(1+4S+S^2) - 2S = 0 \tag{10}$$

where

$$S = \frac{Bcm\Omega\cos\gamma\sin\theta}{4V}$$

Explicit solutions to equation (10) are obtainable as a function of local solidity, lift curve slope, tip speed ratio, and blade position. These equations show that for zero pitch

1. $a_{\text{MAX}} = 0.5$ occurs when $S = 0.5$
2. maximum power extraction due to lift occurs when $S = 0.229\sin\theta$.

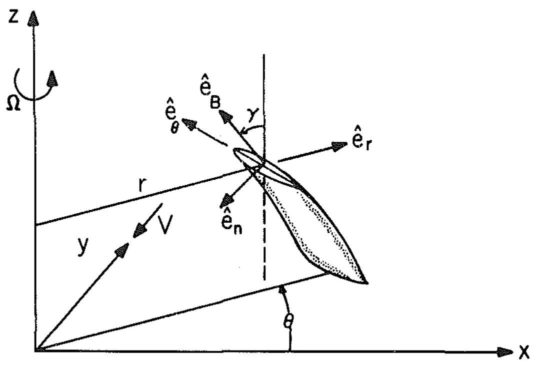

Fig. 4 Darrieus rotor blade geometry

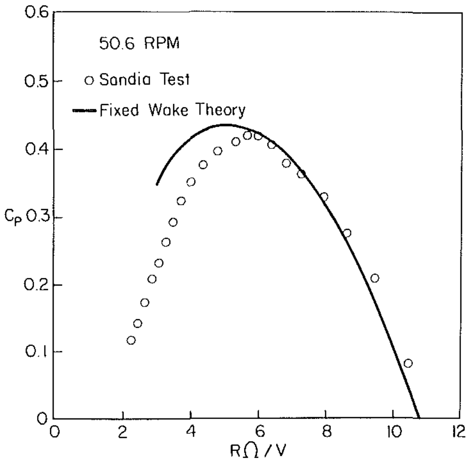

Fig. 5 Comparison of Sandia 17 m test data and fixed wake theory with linear aerodynamics. Test rpm = 50.6.

Power

The local torque developed on a Darrieus Rotor blade element is derived considering contributions from lift, drag and moment; however, the Kutta-Joukowski and drag terms are the only wake-producing terms and thus determine the power.

Consider an element of a Darrieus Rotor blade as shown in Fig. 4.

The local unit vectors may be expressed in terms of the unit vectors $\hat{i}$, $\hat{j}$, $\hat{k}$;

$$\hat{e}_r = \hat{i}\cos\theta + \hat{j}\sin\theta$$

$$\hat{e}_\theta = -\hat{i}\sin\theta + \hat{j}\cos\theta$$

$$\hat{e}_n = -\hat{e}_r\cos\gamma - \hat{k}\sin\gamma$$

$$\hat{e}_B = \hat{k}\cos\gamma - \hat{e}_r\sin\gamma$$

The blade rotates counterclockwise about the z axis. In order to determine the local effective wind on the airfoil, W_e, we define the following local velocities:

Local relative velocity due to rotation:	$-r\Omega\hat{e}_\theta$
Local wind:	$-u\hat{j}$

where $u = V(1-a_i)$, and $i = F$ or R. The relative velocity is given by

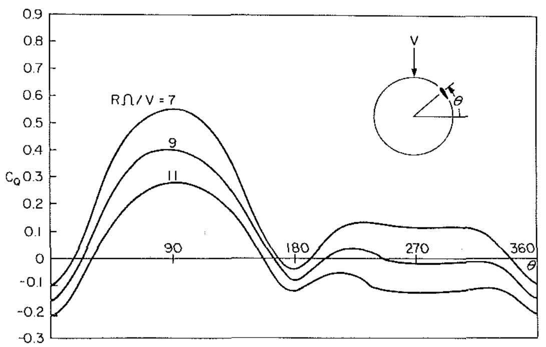

Fig. 6 Torque coefficient versus blade position for 17 m Darrieus rotor

$$\mathbf{W} = -r\Omega\hat{e}_\theta - u\hat{j}$$

The spanwise component does not contribute to the lift or drag, so

$$\mathbf{W}_e = (\mathbf{W}\cdot\hat{e}_\theta)\hat{e}_\theta + (\mathbf{W}\cdot\hat{e}_n)\hat{e}_n$$

Thus we find

$$W_\theta = r\Omega + u\cos\theta = r\Omega + V(1-a_i)\cos\theta_i$$

$$W_n = u\sin\theta\cos\gamma = V(1-a_i)\sin\theta_i\cos\gamma$$

The drag is determined from the angle of attack, α_E, which includes the pitching velocity. Thus

$$\tan\alpha_E = \frac{c\Omega\cos\gamma\left(\frac{3}{4} - \frac{x_0}{c}\right) + V(1-a_i)\sin\theta_i\cos\gamma}{r\Omega + V(1-a_i)\cos\theta_i}$$

while

$$\sin\alpha = W_n / W_e$$

where

$$W_e^2 = (r\Omega + V(1-a_i)\cos\theta_i)^2 + V^2\cos^2\gamma\,\sin^2\theta_i\,(1-a_i)^2$$

An element of blade length ds develops a torque dQ about the axis of rotation.

$$dQ = \{r\hat{e}_r \times [\hat{e}_{KJ}dF_{KJ} + \hat{e}_w dF_D]\}\cdot\hat{k}$$

where

$$\hat{e}_{KJ} = \hat{e}_n\cos\alpha + \hat{e}_\theta\sin\alpha$$

$$\hat{e}_w = \hat{e}_n\sin\alpha - \hat{e}_\theta\cos\alpha$$

The Kutta-Joukowski contribution is

$$dQ_{KJ} = \frac{1}{2}\,\rho\,W_e^2 c C_L(\alpha)\,\frac{r\sin\alpha\,dz}{\cos\gamma}$$

and the drag contribution is

$$dQ_D = -\frac{1}{2}\,\rho\,W_e^2 c C_D(\alpha_E)\,\frac{r\cos\alpha\,dz}{\cos\gamma}$$

The power is obtained from

$$P = \int_z \frac{1}{2\pi}\int_0^{2\pi} (dQ_{KJ} + dQ_D)\,d\theta$$

Comparison With Test Results

A comparison between theory and test results can be made for the Sandia National Laboratories 17 m research vertical axis wind turbine. The geometry of the 17 m machine is given in Table 1.

Aerodynamic data needed to compare theory to test results are the lift curve slope and the drag coefficient. The lift curve slope was held constant at 2π, the value given in reference [17] for the range of test Reynolds Number. Reference [17] and the results of spin tests of the Darrieus rotor [18] were used for the drag coefficient.

Table 1 17 m Geometry

Number of blades	2
Airfoil section	NACA 0015
Chord	0.610 m
R	8.277m
x_0/c	0.38
Swept area	183.3 m^2
z_{MAX}	8.090 m

Blade shape equations:

$r = 2.790 + [30.100 - z^2]^{1/2}$ $|z| \leq 4.548$ m

$r = 12.60 - 1.4826\,z$ $|z| \geq 4.548$ m

Table 2 Comparison of calculated C_p for the 17 m machine: A. Multiple streamtube theory with linear aerodynamics; *B*. Fixed wake theory with linear aerodynamics; and *C*. Fixed wake theory with nonlinear aerodynamics.

$\frac{R\Omega}{V}$	C_p (A)	C_p (B)	C_p (C)
5	0.438	0.433	0.415
7	0.371	0.376	0.362
9	0.188	0.215	0.210
11	−0.136	−0.042	−0.041

Test data used for the comparison were obtained from Sandia National Laboratories. The method of data reduction used is given by Akins [19]. The apparatus is described by Worstell [20]. Test results for operation of the 17 m machine at 50.6 rpm [21] are shown in Fig. 5.

The agreement between fixed wake theory using a linear lift relation and test data is good at high tip speed ratios. Table 2 gives a comparison of the calculated power coefficient using multiple streamtube theory and fixed wake theory. The difference between these two theories is greatest at high tip speed ratios where the difference between fore-and-aft blade induced velocities is the largest. Also given is the power coefficient calculated using the lift coefficient variation given in reference [17]. Above a tip speed ratio of 7, the difference between using a linear lift coefficient and the lift coefficient with stall is less than 3.5 percent of C_p.

Figure 6 shows the variation of the torque coefficient with blade position for the 17 m machine at various tip speed ratios. The torque coefficient, C_Q, is given by

$$C_Q \equiv \frac{\text{Blade torque}}{1/2\rho V^2 R^3}$$

Over the upwind portion of the rotor, a blade produces positive torque, however, the torque production on the lee half of the rotor is less than on the windward half of the rotor, mostly due to the lower angles of attack experienced on the lee half of the rotor. At a tip speed ratio of 11, the average torque is negative.

The analytical results were determined with and without wind shear. For the 17 m machine test site, the wind has been observed to obey a power law profile with an exponent of 0.1 [20]. The results for C_p with and without wind shear agreed to within 0.005.

Since wind shear did not influence the results, rotor symmetry allowed treatment of only half of the rotor. The rotor was divided into 5 vertical slices with 10 deg increments in the angle θ. Using a CDC CYBER 170/720, computation time was 1.4 seconds per C_p calculation.

It is concluded that fixed wake theory with linear aerodynamics provides a rapid and accurate method for predicting the high tip speed ratio performance of Darrieus rotors.

Acknowledgment

This work was sponsored by Sandia National Laboratories under Contract 37-0010.

References

1 Darrieus, G. J. M., U.S. Patent No. 1,835,018, December 8, 1931.

2 South, P., and Rangi, R., "The Performance and Economics of the Vertical Axis Wind Turbine Developed at the National Research Council, Ottawa, Canada," presented at the 1973 Annual Meeting of the Pacific Northwest Region of the American Society of Agricultural Engineers, Calgary, Alberta, Oct. 1973.

3 South, P., and Rangi, R. S., "An Experimental Investigation of a 12 ft Diameter High Speed Vertical Axis Wind Turbine," National Research Council of Canada, LTRLA166, Apr. 1974.

4 Blackwell, B. F., and Reis, G. E., "Blade Shape for a Troposkien Type of Vertical Axis Wind Turbine," Sandia Laboratories, Albuquerque, N.M., SLA74-0154, Apr. 1974.

5 Templin, R. A., "Aerodynamic Performance Theory for the NRC Vertical Axis Wind Turbine," National Research Council of Canada, LTR-160, June 1974.

6 Wilson, R. E., and Lissaman, P. B. S., "Applied Aerodynamics of Wind Powered Machines," Oregon State University, May 1974.

7 Shankar, P. N., "On the Aerodynamic Performance of a Class of Vertical Axis Windmills," National Aeronautical Laboratory, Bangalore TM AE TM-13-15, July 1975.

8 Lapin, E. E., "Theoretical Performance of Vertical Axis Wind Turbines," ASME paper 75-WA/Ener-1, presented at the ASME Winter Annual Meeting, Houston, Tex., Nov. 1975.

9 Strickland, J. H., "The Darrieus Turbine: A Performance Prediction Model Using Multiple Streamtubes," Advanced Energy Projects Department, Sandia Laboratory, SAND 75-0431, Oct. 1975.

10 Holme, Olaf, "A Contribution to the Aerodynamic Theory of the Vertical Axis Wind Turbine," International Symposium on Wind Energy Systems, Cambridge, England, Sept. 1976.

11 Fanucci, J. B., and Walters, R. E., "Innovative Wind Machines: The Theoretical Performance of a Vertical Axis Wind Turbine," p. III, 61-95, *Proceedings of Vertical Axis Wind Turbine Technology Workshop*, Sandia Laboratory, Albuquerque, N.M., SAND 76-5586, May 1976.

12 Wilson, R. E., "Vortex Sheet Analysis of the Giromill," ASME JOURNAL OF FLUIDS ENGINEERING, Vol. 100, Sept. 1978.

13 McKie, W. R., Wilson, R. E., and Lissaman, P. B. S., "Analytical Investigation of Darrieus Rotor Aerodynamics," Oregon State University, Dec. 1978, Chapter 2.

14 Strickland, J. H., Webster, B. T., Nguyen, T., "A Vortex Model of the Darrieus Turbine: An Analytical and Experimental Study," Sandia Laboratories, Albuquerque, N.M., SAND 79-7058, Feb. 1980.

15 Wilson, R. E., Lissaman, P. B. S., James, M., and McKie, W. R., "Aerodynamic Loads on a Darrieus Rotor Blade," ASME JOURNAL OF FLUIDS ENGINEERING, Vol. 105, No. 1, Mar. 1983.

16 Wilson, R. E., and Walker, S. N., "Fixed Wake Analysis of the Darrieus Rotor," Sandia Laboratories, Albuquerque, N.M., SAND 81-7026, July 1981.

17 Sheldal, Robert E., and Klimas, Paul C., "Aerodynamic Characteristics of Seven Symmetrical Airfoil Sections Through 180-Degree Angle of Attack for Use in Aerodynamic Analysis of Vertical Axis Wind Turbines," Sandia Laboratories, Albuquerque, N.M., SAND 80-2114, Mar. 1981.

18 Wilson, R. E., Klimas, P. C., and Worstell, M. H., "Drag Coefficient for the NACA 0015 Darrieus Rotor Blades," Presented at the American Solar Energy Meeting, Minneapolis, Minn., June 1983.

19 Akins, R. E., "Performance Evaluation of Wind Energy Conversion Systems Using the Method of Bins-Current Status," Sandia Laboratories, Albuquerque, N.M., SAND 77-1375, Mar. 1978.

20 Worstell, M. H., "Aerodynamic Performance of the 17-Metre-Diameter Darrieus Wind Turbine," Sandia Laboratories, Albuquerque, N.M., SAND 78-1737, Jan. 1979.

21 Worstell, M. H., "Measured Aerodynamic and System Performance of the 17 Meter Research Machine," in "Proceedings of the Vertical Axis Wind Turbine Design Technology Seminar for Industry," edited by S. Johnston, Sandia Laboratories, Albuquerque, N.M., SAND 80-0984, Aug. 1980, pp. 233-258.

Compressibility Effect in Two-Phase Flow and Its Application to Flow Metering With Orifice Plate and Convergent-Divergent Nozzle

H. Pascal
Department of Physics,
University of Alberta,
Edmonton, Alberta, Canada T6G 2J1

The effect of solution gas on the two-phase flow behavior through an orifice plate and a convergent-divergent nozzle has been investigated with regard to the flow metering of compressible two-phase mixtures. A proper thermodynamics approach to consider more accurately the compressibility effect in an accelerated two-phase flow, in particular that through an orifice and Laval's nozzle in the presence of the solution gas, has been developed. From this approach an equation of state of mixture was derived and used in determining the orifice equation. An analysis of flow behavior has been performed and several illustrative plots were presented in order to evaluate the gas solubility effect in the flow metering with an orifice plate or a convergent-divergent nozzle. A delimitation between critical and noncritical flow has been established in terms of measured parameters and a relationship between the critical pressure and gas-liquid mass ratio was also shown.

I Introduction

Previous papers on the flow behavior of compressible two phase mixtures through an orifice plate and a convergent-divergent nozzle have investigated the case in which no mass transfer between the two phases appears. For example, Tangren et al. [1] have studied the compressibility effects in an accelerated two-phase flow, in particular that through a Laval nozzle, in which the gas-liquid mass ratio was considered constant. Recently Sandhu and Jameson [2] have presented an experimental study of critical two-phase flow through a convergent-divergent nozzle. A comparison between observed flow behavior and that predicted from the homogeneous flow model in which the gas-liquid mass ratio does not depend on pressure, was made. From this comparison the limits of validity of the homogeneous model, in particular the effects of slip and non-isothermal behavior, have been emphasized. Unfortunately the comparison presented by Sandhu and Jameson [2] is limited to only the critical flow conditions in which only a small range of variables, such as mass ratio, upstream and downstream pressure, were considered. The mass transfer effect between the two phases was not considered. The case of constant mass ratio was considered by Chang and Davies [3] in their analysis to predict the pressure distribution in bubbly flow through a Venturi nozzle.

Tangren et al. [1] have assumed an adiabatic process for the mixture, while Sandhu and Jameson [2] and Chang and Davies [3] have assumed a polytropic law for gas phase; the assumptions of ideal gas and insolubility in liquid were also used. Obviously a polytropic law requires the knowledge of an empirical exponent n. However, an adiabatic process seems to be more realistic in describing the flow behavior through a Laval nozzle, in which case the adiabatic exponent in the state equation depends strongly on mass ratio and specific heat of the gas and liquid, as Tangren et al. [1] have shown.

A large class of fluids which appear currently in the oil and gas industry presents an effect of solution gas. An illustrative example is the simultaneous flow of oil and gas in which the solution gas is released from oil when the pressure is below the bubble point; in this case the gas-liquid mass ratio is a known function of pressure. The flow metering of these two-phase fluids is carried out by using the orifice plate approach or a convergent-divergent nozzle. As a result, an analysis of the accelerated two-phase flow is required in which the effects of solution gas and mixture compressibility should be considered. Until now the solution gas effect on the flow behavior has not been investigated either experimentally or theoretically.

The main objective of this investigation is to pay more attention to the compressibility effect in an accelerated two-phase flow in the presence of the solution gas. For this purpose, the approach suggested by Tangren et al. [1], will be modified in order to include the solution gas effect. Thus, the gas-liquid mass ratio will be considered as a function of pressure. The compressibility effect on the two-phase flow behavior will be illustrated with regard to the flow metering with an orifice plate or a convergent-divergent nozzle. In previous papers on this subject, the slip effect was considered

---

Contributed by the Fluids Engineering Division of THE AMERICAN SOCIETY OF MECHANICAL ENGINEERS and presented at the Symposium on Measurements on Polyphase Flows, St. Louis, Mo., June 1982. Manuscript received by the Fluids Engineering Division, June 25, 1982.

by using several empirical coefficients which are difficult to evaluate from experimental data. As a result, the slip effect on the two-phase flow behavior cannot at this time be realistically investigated. A nonslip or homogeneous flow model will be used in this investigation. A dispersed flow pattern will be considered, which may be a bubble flow when the continuous phase is a liquid and the dispersed phase is a gas, and a mist flow for an opposite situation. By introducing new devices in field operations to homogenize the mixture of gas-liquid prior to measurement with an orifice or nozzle, it is expected that the homogeneous model will become a proper tool in the metering of two-phase flow under pressure for these flow patterns.

II Equation of State for a Two-Phase Fluid

Although it is generally recognized that in an accelerated flow, in particular that through an orifice or Laval nozzle, the compressibility effect is significant factor in increasing our understanding of the two-phase flow behavior, this effect has received little attention in the literature.

Before proceeding with the derivation of an equation of state for a two-phase fluid in the presence of the solution gas, it is of particular interest to present and discuss the approach currently used in the literature for evaluating the compressibility effect in two-phase flow.

Since the volume of gas plus the volume of liquid must equal the total volume of mixture, an average density may be defined and expresssed as (Tangren et al. [1]):

$$\frac{1}{\rho_m} = \frac{\mu}{(1+\mu)\rho_g} + \frac{1}{(1+\mu)\rho_l}; \quad \mu = \frac{M_g}{M_l} \tag{1}$$

or in terms of void fraction

$$\rho_m = \beta\rho_g + (1-\beta)\rho_l \quad \beta = \frac{V_g}{V_g + V_l}. \tag{2}$$

If a polytropic process is assumed for gas phase, then the gas density may be related to pressure by relation

$$\rho_g = \rho_{g1}\left(\frac{p}{p_1}\right)^{1/n}. \tag{3}$$

For an adiabatic process $n = c_p/c_v$ and for an isothermal process $n=1$; subscript 1 refers to the value at a reference pressure p_1. Tangren et al. [1] had first shown that equation (1) or (2) is necessary but not sufficient in evaluating correctly the compressibility effect in two-phase flow. They show that the energy conservation equation, i.e., the first law of thermodynamics along with equation (1), should be used. As a result of this approach, Tangren et al. [1] have obtained for an adiabatic process the following equation of state:

$$p\left[\frac{1}{\rho_m} - \frac{1}{(1+\mu)\rho_l}\right]^{\lambda} = p_1\left[\frac{1}{\rho_{m1}} - \frac{1}{(1+\mu)\rho_l}\right]^{\lambda} = \text{constant}. \tag{4}$$

This equation was derived by assuming that the mixture is homogeneous and gas-liquid mass ratio does not depend on pressure, i.e., $\mu = \mu_0$ = constant.

Using equation (1), the state equation (4) may be rewritten as

$$\frac{1}{\rho_m} = -\frac{\mu}{(1+\mu)\rho_{g1}}\left(\frac{p_1}{p}\right)^{1/\lambda} + \frac{1}{(1+\mu)\rho_l} \tag{5}$$

in which adiabatic exponent λ in (4) and (5) is given by relation

$$\lambda = \frac{\mu c_p + c_l}{\mu c_v + c_l}. \tag{6}$$

Obviously, equation (6) shows that $\lambda \to 1$ when $\mu \to 0$ and $\lambda = c_p/c_v$ when $\mu \to \infty$. As a result, the adiabatic exponent λ may give a measure of the degree in which the two-phase mixture behaves as a gas rather than as a liquid.

If an adiabatic process is assumed, then from equations (1) and (3) one obtains

$$\frac{1}{\rho_m} = \frac{\mu}{(1+\mu)\rho_{g1}}\left(\frac{p_1}{p}\right)^{1/n} + \frac{1}{(1+\mu)\rho_l} \tag{7}$$

where $n = c_p/c_v$.

This equation is different from (5) as suggested by Tangren et al. [1]. Consequently, the compressibility effect in an accelerated flow will depend strongly on the equation of state used. However, at very high values of mass ratio μ, let us say $\mu \to \infty$, equation (6) leads to $\lambda \equiv c_p/c_v$ and in this particular case equations (5) and (7) become indentical. This result is obvious, since at high mass ratio the two phases are weakly coupled and the thermodynamic interaction effect is insignificant. At moderate values of mass ratio μ, when gas and liquid become more intimately mixed together by increasing the amount of liquid, the two phases are strongly coupled. As a result, the thermodynamic interaction effect becomes more significant. In this case, equations (5) and (7) will provide different compressibility effects, as may be seen by comparing the results obtained from (5) and (7).

The assumptions of homogeneous mixture and thermal equilibrium used by Tangren et al. [1] will also be considered in deriving the state equation. As a reuslt of these assumptions, the first law of thermodynamics for a two-phase fluid may be written as (Tangren et al. [1]) shown:

$$(M_g + M_l)dQ = (M_g c_v + M_l c_l)dT + (M_g + M_l)pd\left(\frac{1}{\rho_m}\right) \tag{8}$$

Nomenclature

c_p = specific heat at constant pressure; Kcal/Kg °C
c_v = specific heat at constant volume; Kcal/Kg °C
c_l = specific heat of liquid, Kcal/Kg °C
d = orifice diameter; m
D = pipeline diameter; m
f = cross-sectional area of orifice; m^2
M_g = mass of gas; Kg
M_l = mass of liquid; Kg
p_1 = upstream orifice pressure; Pa
p_2 = throat orifice pressure; Pa
Q_T = total gravimetric flow rate of mixture; Kg/sec
R = gas constant
T = temperature; °K
$\bar{Z}$ = compressibility factor expressed at average pressure; dimensionless
ϵ = solubility coefficent; m^2/Kg
μ_0 = free gas mass ratio; dimensionless
μ = gas-liquid mass ratio; dimensionless
ρ_m = density of the mixture; Kg/m^3
ρ_g = density of the gas phase; Kg/m^3
ρ_l = density of the liquid phase; Kg/m^3
R$_e$ = Reynolds number
$C(\mu_0, d/D, \text{R}_e)$ = orifice discharge coefficient
subscript 1 = corresponds to upstream conditions
subscript 2 = corresponds to downstream conditions

where the symbols used are listed in the nomenclature.

If a polytropic process is assumed, then

$$dQ = CdT; \quad C = \frac{\mu c + c_l}{1+\mu} \tag{9}$$

in which c is the specific heat of the gas for a polytropic process and

$$\mu = \frac{M_g}{M_l} = f(p).$$

From (8) and (9) one obtains

$$\frac{d\rho_m}{\rho_m{}^2} = (c_v - c)\frac{\mu}{1+\mu}dT \tag{10}$$

Since $p/\rho_g = \bar{Z}RT$, equation (1) may be written as

$$\bar{Z}RT = \frac{p}{\mu}\left[\frac{1+\mu}{\rho_m} - \frac{1}{\rho_l}\right] \tag{11}$$

Thus, from (10) and (11) the temperature may be eliminated and the following equation may be derived:

$$p\frac{d\rho_m}{\rho_m{}^2} = \frac{\mu}{1+\mu}\frac{c_v - c}{\bar{Z}R}\left[\frac{1+\mu}{\mu}\left(\frac{dp}{\rho_m} - p\frac{d\rho_m}{\rho_m{}^2}\right)\right.$$
$$\left.+\left(\frac{1}{\rho_l} - \frac{1}{\rho_m}\right)p\frac{d\mu}{\mu^2} - \left(\frac{\rho_{0l}}{\rho_l}\beta p + 1\right)\frac{dp}{\mu\rho_l}\right] \tag{12}$$

In deriving equation (12), it was assumed that liquid is a compressible fluid and its specific mass is a function of pressure as

$$\rho_l(p) = \rho_{l0}[1 + \beta_l(p_1 - p)] \tag{13}$$

and that the gas-liquid mass ratio μ is a function of pressure. Although the laboratory and field data show that μ is a linear function of pressure, a general relation to express the function $\mu = f(p)$ will be taken in this investigation as

$$\mu(p) = \mu_0 + \epsilon(p_1 - p)^{\alpha} \tag{14}$$

in which μ_0 is the free gas mass ratio at the reference pressure p_1 and the additional term $\epsilon(p_1 - p)^{\alpha}$ is due to the solution gas at the pressure p. As a result of equation (14), the following differential equation is obtained from (12)

$$\frac{d\rho_m}{dp} - \frac{g(p)}{\lambda}\rho_m + \frac{h(p)}{\lambda}\rho_m{}^2 = 0 \tag{15}$$

The functions $g(p)$ and $h(p)$ are given by relations

$$g(p) = \frac{1}{p} + \frac{\epsilon\alpha(p_1 - p)^{\alpha-1}}{\mu(1+\mu)} \tag{16}$$

$$h(p) = \frac{1}{\rho_l(1+\mu)}\left[\frac{1}{p} + \beta_l\frac{\rho_{l0}}{\rho_l} + \frac{\epsilon\alpha(p_1 - p)^{\alpha-1}}{\mu}\right] \tag{17}$$

in which $\rho_l(p)$ and $\mu(p)$ in (16) and (17) are expressed by relations (13) and (14) and λ in (15) is given by relation

$$\lambda = \frac{\bar{Z}c_p + (1-\bar{Z})c_v - c}{c_v - c} \tag{18}$$

derived from (12) in order to write this equation in the form (15), or

$$\lambda = (n-1)\bar{Z} + 1; \quad n = \frac{c_p - c}{c_v - c} \tag{19}$$

When an adiabatic process is considered, then $dQ = 0$ in (8). This means $C = 0$ in (9) and $c = c_l/\mu$ in (18) or (19). As a result, parameter λ in this case becomes

$$\lambda = \frac{[\bar{Z}c_p + (1-\bar{Z})c_v]\mu(p) + c_l}{c_v\mu(p) + c_l} \tag{20}$$

where $\mu(p)$ in (20) is known from (14).

Equation (15) is a differential equation of Bernoulli type and its solution may be written as

$$\frac{1}{\rho_m} = \exp\left(-\int_{p_1}^{p}\phi_0(\xi)d\xi\right)\left[\frac{1}{\rho_{m1}}\right.$$
$$\left.+\int_{p_1}^{p}\phi_1(\theta)\exp\left(+\int_{p_1}^{\theta}\phi_0(\xi)d\xi\right)d\theta\right] \tag{21}$$

in which ρ_{m1} is the specific mass of mixture expressed at the reference pressure p_1.

Since the mass ratio μ is a given function of pressure expressed by relation (14), paramteer λ for a adiabatic process will depend on pressure, as it may be seen from (20) and (14). In these circumstances functions $\phi_0(p)$ and $\phi_1(p)$ in (21) are expressed as

$$\phi_0(p) = \frac{g(p)}{\lambda(p)} \quad \text{and} \quad \phi_1(p) = \frac{h(p)}{\lambda(p)} \tag{22}$$

where $g(p)$, $h(p)$, and $\lambda(p)$ are obtained from (16), (17), and (20).

When a polytropic process is assumed, λ is a constant given by relation (19), which does not depend on the gas-liquid mass ratio. Consequently, the polytropic exponent n is unknown which should be determined experimentally. For this purpose an empirical correlation is required.

The particular case analyzed by Tangren et al. [1] may be derived from (21) assuming an adiabatic process in which mass ratio μ is constant, gas is an ideal gas and liquid is an incompressible fluid. In this situation we have $\epsilon = 0$, $\mu = \mu_0$, $\beta_l = 0$, and $\bar{Z} = 1$. As a result of these assumptions, functions $g(p)$, $h(p)$, and λ become

$$g(p) = \frac{1}{p}; \quad h(p) = \frac{1}{(1+\mu)\rho_l p} \tag{23}$$

and

$$\lambda = \frac{\mu_0 c_p + c_l}{\mu_0 c_v + c_l} \tag{24}$$

In this case, from (21) one obtains the equation of state (4). However when gas is assumed an ideal gas, i.e., $\bar{Z} = 1$, and a polytropic process is considered, equation (21) leads to the equation of state (7) in which the polytropic exponent λ is determined from (19) and expressed in (7) as

$$n = \frac{c_p - c}{c_v - c} \tag{25}$$

The previous results show that for a polytropic process in which mass ratio μ is constant the approach suggested by Tangren et al. [1] leads to an identical equation with that used in literature and it is the equation of state derived from (1) and (3). However, when the solution gas effect is considered, i.e., mass ratio μ is a function of pressure, the significant deviations between the results obtained from equations (3) and (21) are observed. Similary, the discrepancy between equations (4) and (7) is obvious. This suggests that in an adiabatic process, where mass ratio is constant, a correct equation of state for an adiabatic process may be derived provided that both the equations (1) and (8) are used.

The general case, i.e., $\epsilon \neq 0$ and $\alpha \neq 1$, requires a numerical integration to be performed in (21) for obtaining the specific mass of mixture in terms of pressure. On the other hand, a numerical procedure could be also indicated to solve the differential equation (15). However, the field and laboratory data show that mass ratio μ is a linear function of pressure so that $\alpha = 1$ in (14), (16), and (17). In these circumstances we have $d\mu/dp = -\epsilon$ and instead of equation (15) one can write

$$-\epsilon\frac{d\rho_m}{d\mu} = \phi_0(\mu)\rho_m + \phi_1(\mu)\rho_m{}^2 \tag{26}$$

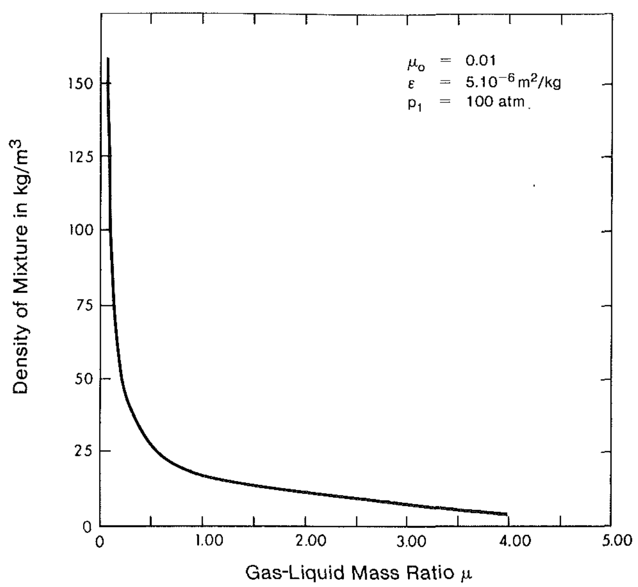

Fig. 1 Effect of solution gas on density of mixture for $\epsilon = 5.10^{-6}$ m^2/kg; adiabatic expansion of mixture

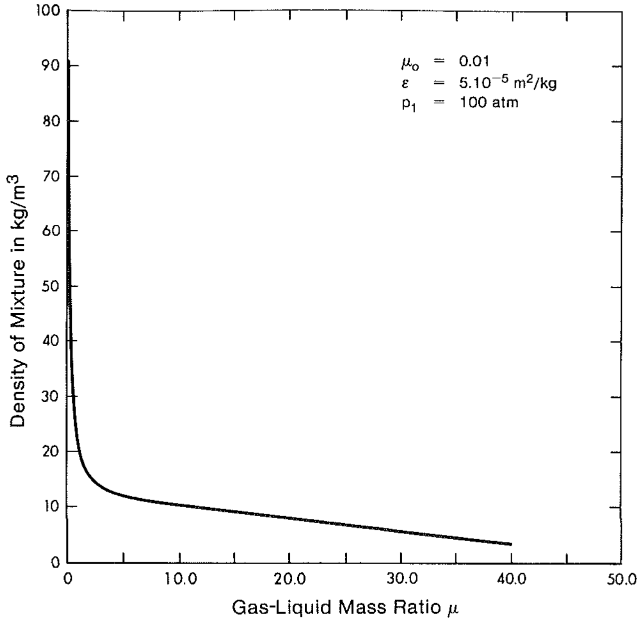

Fig. 2 Effect of solution gas on density of mixture for $\epsilon = 5.10^{-5}$ m^2/kg; adiabatic expansion of mixture

The analytical solution of this equation may be also expressed by a relation indentical to (21). However, the numerical computations have shown that an expression derived from (21) for $\alpha = 1$ may be written as

$$\frac{\rho_m(\mu)}{\rho_m(\mu_0)} = \frac{1}{U(\mu)}; \quad \mu_0 < \mu < \mu_0 + \epsilon p_1 \tag{27}$$

This equation of state may be also written as

$$\rho_m(\mu_2)U(\mu_2) = \rho_m(\mu_3)U(\mu_3) = \rho_m(\mu_0) = \text{constant} \tag{28}$$

Function $U(\mu)$ is given by relation

$$U(\mu) = \frac{\mu}{\mu_0}\left(\frac{1+\mu}{1+\mu_0}\right)^{\delta_0}\left(\frac{\alpha_0+\beta_0\mu}{\alpha_0+\beta_0\mu_0}\right)^{-\delta_1}\left(\frac{c_l+a_0\mu}{c_l+a_0\mu_0}\right)^{\delta_2} \tag{29}$$

where

$$\alpha_0 = p_1 + \frac{\mu_0}{\epsilon}; \quad \beta_0 = -\frac{1}{\epsilon};$$

$$a_0 = c_v + (c_p - c_v)\bar{z}; \quad \delta_0 = \frac{c_l - c_v}{a_0 - c_l};$$

$$\delta_1 = \frac{c_l + (\mu_0 + \epsilon p_1)c_v}{c_l + (\mu_0 + \epsilon p_1)a_0};$$

$$\delta_2 = \frac{c_l\left(1 - \frac{c_v}{a_0}\right)}{a_0\epsilon\left(p_1 + \frac{\mu_0}{\epsilon} + \frac{1}{\epsilon}\frac{c_l}{a_0}\right)} - \frac{a_0 - c_v}{a_0 - c_l}. \tag{30}$$

On the other hand, equation of state (27) may be expressed in terms of pressure by using the relation

$$\frac{p}{p_1} = 1 - \frac{\mu - \mu_0}{\epsilon p_1} \tag{31}$$

derived from (14) when $\alpha = 1$.

Discussion of Results and Conclusions

By using the equation of state (27), it is of interest to illustrate the solution gas effect on the specific mass of mixture. For example, Fig. 1 shows the specific mass variation expressed in terms of mass ratio μ when the solubility coefficient is $\epsilon = 5.10^{-6}$ m^2/Kg while Fig. 2 shows what happens when $\epsilon = 5.10^{-5}$ m^2/Kg. These figures allow a comparison which indicates that the solution gas effect is significant. The following physical data were used:

$$\begin{array}{l} c_p = 0.531 \\ c_v = 0.405 \\ c_l = 0.45 \end{array} \left\{ \frac{\text{K cal}}{\text{Kg grad}} \right.$$

To evaluate the compressibility effect in an accelerated two-phase flow we will consider the classical problem of flow through an orifice plate. For this purpose, the nonslip flow model along with the equation of state (5) will be used. As a result, the total dimensionless gravimetric flow rate may be expressed in terms of measured flow parameters p_2/p_1 as follows:

$$Q_T^* = \frac{\left[\frac{2\lambda}{\lambda-1}\mu_0(1+\mu_0)R(X^{2/\lambda} - X^{1+1/\lambda}) + 2(1+\mu_0)(X^{2/\lambda} - X^{1+2/\lambda})\right]^{1/2}}{\mu_0 R + X^{1/\lambda}} \tag{32}$$

Equation of state (27) was derived from (26) assuming the adiabatic process and $\alpha = 1$ in (14), (16), and (17). This expresses a relationship between the specific mass and gas-liquid mass ratio μ by taking into account the solution gas effect.

where λ is a given function of mass ratio μ_0 expressed by relation (24) and Q_T^* one obtains from

$$Q_T^* = \frac{Q_T}{fC\left(\mu_0, \frac{d}{D}, \text{Re}\right)\sqrt{\rho_l p_1 g}};$$

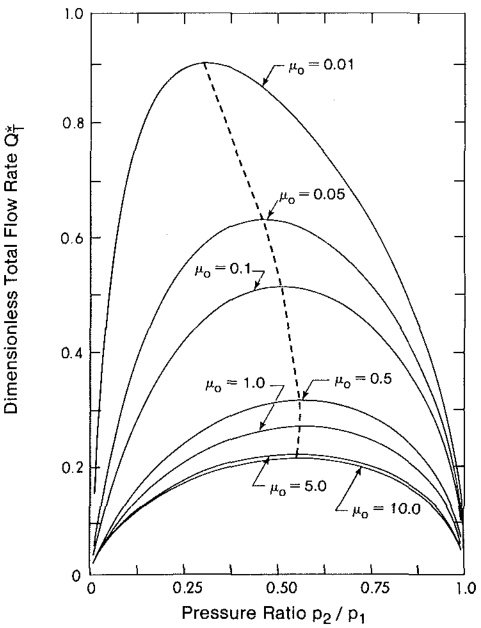

Fig. 3 Effect of gas-liquid mass ratio μ_0 on flow behavior through an orifice; adiabatic expansion of mixture for $R = 10$

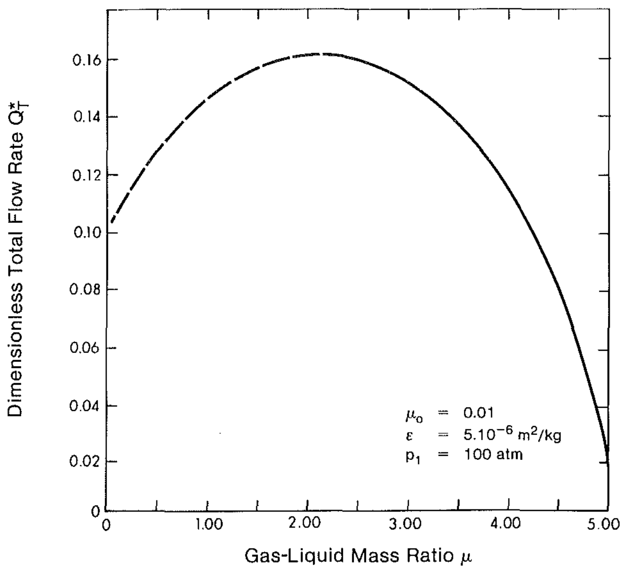

Fig. 4 Effect of solution gas on flow behavior through an orifice for $\epsilon = 5.10^{-6}$ m^2/kg; adiabatic expansion of mixture

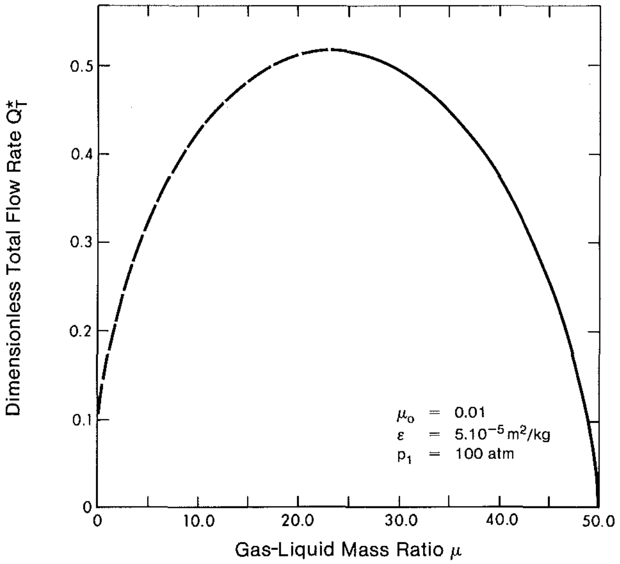

Fig. 5 Effect of solution gas on flow behavior through an orifice for $\epsilon = 5.10^{-5}$ m^2/kg; adiabatic expansion of mixture

$$X = \frac{p_2}{p_1}\,; \quad R = \frac{\rho_e}{\rho_{g1}} \tag{33}$$

As in single phase flow metering with an orifice plate, the discharge orifice coefficient in two-phase flow must be determined experimentally. However, the determination of this coefficient will be more complex since in two-phase flow we should expect that its value will depend on the gas-liquid mass ratio. Obviously, for this situation an empirical correlation to express the functional dependence of the discharge coefficient in terms of μ_0, d/D and Reynolds number will be required. Unfortunately, the literature to date on this matter does not offer such correlations for the two-phase flow of compressible mixtures. Taking into account the difficulties arising in an accelerated two-phase flow, in particular through an orifice, it is not yet possible at this time to know the function $C(\mu_0, d/D, \mathrm{Re})$ from a theoretical analysis, so that, as in single phase flow, it must be considered as a fitting parameter to be determined from laboratory experiments, using a fitting technique between the observed and predicted data.

The total dimensionless flow rate derived from (32) is expressed in terms of pressure ratio p_2/p_1 and plotted in Fig. 3 for various μ_0 values. The physical data were identical to those used in Figs. 1 and 2. The broken line in Fig. 3 shows the delimitation between the critical and noncritical flow. However, it should be noted that the portion of the curves to the left of the critical pressure ratio does not exist in practice, since the flow reaches sonic velocity at the critical pressure. In this situation, the orifice is "choked," the mass flow rate remaining constant for pressure ratios less than the critical values. The curves $\mu_0 > 10$ correspond to the case in which adiabatic exponent λ does not depend on the gas-liquid mass ratio as it may be seen from (24). In our example, illustrated in Fig. 3, this situation corresponds at $\lambda = c_p/c_v = 1.31$. As a result, for $\mu_0 > 10$ the equation of state (5) becomes identical with (7) where $n = c_p/c_v$. For $\mu_0 < 10$, Fig. 3 indicates the deviations which appear between the flow behavior by using the equations of state (5) and (7). For example, Fig. 3 reveals that deviation is more significant when the two phases are strongly coupled. Another important result derived from Fig. 3 is that the critical pressure ratio depends on the mass ratio μ_0. Thus, in the range $0.01 < \mu_0 < 0.5$ the critical pressure is a monotonically increasing function with regard to the mass ratio, While for $0.5 < \mu_0 < \infty$ an opposite situation appears. As a result of this fact, the sonic velocity will behave in an opposite situation as compared with critical pressure.

From the illustrative example shown in Fig. 3, it is obvious that the equations of state (7) is of limited applicability and its validity is restricted only to high mass ratio, i.e., $\mu_0 > 10$, where the adiabatic exponent λ does not depend on μ_0 and liquid specific heat, as it may be seen from (24).

In order to evaluate the solution gas effect on the flow rate behavior through an orifice plate, equation of state (27) should be used in deriving the orifice equation. When this is done, the following equation is obtained

$$Q_T^* = \sqrt{\frac{2[\tau(\mu_2) - \tau(\mu_1)]}{U^2(\mu_2)}} \tag{34}$$

where the function $\tau(\mu)$ is

$$\tau(\mu) = \int_{\mu_0}^{\mu} U(\xi) d\xi; \quad \mu_0 < \mu < \mu_0 + \epsilon p_1 \tag{35}$$

and the dimensionless gravimetric total flow rate of the mixture is expressed in (34) as

$$Q_T^* = \frac{Q_T \sqrt{\dfrac{\epsilon g}{\rho_m(\mu_1)}}}{fgC\left(\mu_1, \dfrac{d}{D}, \mathrm{Re}\right)}. \tag{36}$$

The subscript 1 corresponds to upstream orifice, and 2 to throat conditions. In terms of measured flow parameters, as p_1 and p_2, μ_1 and μ_2 are determined from (31).

Equation (34) was plotted in Figs. 4. and 5 in which the dimensionless total flow rate Q_T^* is expressed in terms of gas-liquid mass ratio. Figure 4 corresponds to the case when solubility coefficient is $\epsilon = 5.10^{-6} \mathrm{m}^2/\mathrm{kg}$ while Fig. 5 corresponds to $\epsilon = 5.10^{-5} \mathrm{m}^2/\mathrm{kg}$. From these figures a comparison between the two cases may be made. For example, Fig. 4 shows that the maximum flow rate, i.e., critical flow, appears at $\mu = 2.06$ and the corresponding critical pressure ratio, obtained from (31), will be $(p_2/p_1)_{\mathrm{critic}} = 0.59$, while from Fig. 5 we have $\mu = 23.1$ and $(p_2/p_1)_{\mathrm{critic}} = 0.54$. The results derived from Fig. 3, or equation (32), show that in the absence of the solution gas effect, i.e., $\epsilon = 0$, we have $(p_2/p_1)_{\mathrm{critic}} = 0.55$ when $\mu_0 = 2.06$ and $(p_2/p_1)_{\mathrm{critic}} = 0.544$ when $\mu_0 = 23.1$. As a result of this fact, it is obvious that a significant effect of the solution gas occurs at $\mu = 2.06$, where the coupling effect between the two phases is more important compared with the case $\mu = 23.1$. For example, at high mass ratio, i.e., $\mu > 20$, the mixture behaves as a gas, as may be seen from Fig. 3 and equation of state (5). The previous relations may also be expressed in terms of quality instead of gas-liquid mass ratio. For this purpose, the following relation should be used

$$\mu = \frac{x}{1-x}$$

or

$$x = \frac{\mu}{1+\mu}$$

in which x is the quality.

Acknowledgments

The author wishes to acknowledge the financial support by a grant from Alberta Oil Sands and Research Authority.

References

1 Tangren, R. F., Dodge, C. H., and Siefert, H. S., Compressibility Effects in Two-Phase Flows, *Journal of Applied Physics*, Vol. 20, 1949, pp. 637–645.

2 Sandhu, M., and Jameson, G., "An Experimental Study of Choked Foam Flows in a Convergent-Divergent Nozzle. *Int. J. Mutiphase Flow*, Vol. 5, 1979, pp. 39–58.

3 Chang, N. T., and Davis, M. R., "Pressure Distribution in Bubbly Flow Through Venturies," *Int. J. Multiphase Flow*, Vol. 7, 1981, pp. 191–210.

4 Wallis, G. B., *One Dimensional Two-Phase Flow*, McGraw-Hill, 1969, New York.

G. L. Chahine
Hydronautics, Incorporated,
Laurel, Md. 20707

Ph. F. Genoux
Direction des Recherches Etudes
et Techniques,
Paris, France 75015

Collapse of a Cavitating Vortex Ring

Introduction

Vortex rings have been a subject of interest for quite a long time. Smoke rings are good examples of a common amusing observation of this phenomenon. The recent increasing interest in large coherent structures in turbulence, for instance in the axisymmetric shear layer of circular jets, makes the study of such ring vortices even more attractive. In 1971, Crow and Champagne [1] reported a remarkable change of an air-jet structure when very slightly excited periodically at certain frequencies, *f*, by a loud-speaker. A perfect structuring of the jet (diameter *d*, velocity *V*) into discrete ring vortices was observed when the Strouhal number, $S_d = fd/V$, approached 0.3, or one of its first integer multiples. At Hydronautics Johnson recognized that this phenomenon should have an application in improving the performance of cavitating submerged jets [2]. Underwater cavitating jets were excited and the aspect of the cavitation field in their shear layer was observed to be modified from scraggly random quasilinear vapor vortices to structured well-organized ring vortex cavities moving along the jet periphery (Fig. 1). Such behavior appeared with transducer-excited CAVIJET® as well as with STRATOJETS™ where the CAVIJET nozzle or the feed tube are designed to produce self-excitation [2, 3]. The behavior of these cavitating vortex rings motivated this study, the final objective being to compare the erosive power of such rings collapsing on a target with that of equivalent scraggly random vortices. Comparative testing has already shown that STRATOJETS cut rock and perform underwater cleaning more effectively than conventional cavitating jets.

Another interest in this study stems from the observation that once a strong reentrant jet has penetrated a collapsing initially-spherical-bubble the shape of the remaining compressed permanent gas, and thus of the rebounding bubble, is toroidal [4]. Also, the velocity of the reentrant jet impresses a torque on the toroidal bubble and induces a vortical motion. We suggest that, with the knowledge of the dynamics of a cavitating vortex ring in a pressure field and its dependence on the torque force, the experimental observation of the behavior of the rebounding and collapsing torus would be a means of measuring the reentering jet velocity.

Asymptotic Approach

Let us consider a toroidal bubble of overall radius, A_0, initially at equilibrium in an infinite medium where the ambient pressure at infinity is P_0. The bubble is subjected to a vortical motion of circulation Γ. The fluid is assumed to be inviscid and incompressible, and Γ remains constant in time. The bubble contains noncondensables of partial pressure P_{g0} and liquid vapor of pressure P_v, which balance the external pressure on the bubble surface and the pressure due to the surface tension, γ. Now we consider, as in the Rayleigh-Plesset problem for a spherical bubble, that the pressure at infinity (e.g., on the bubble trajectory) varies in time to take the imposed value $P_\infty(t)$, and we seek the bubble ring dynamics. If the characteristic size, R_0, of the cross-section of the ring is of the same order as its overall radius A_0, the problem is rather complicated and the equilibrium shape of the cross-section is not circular. However when

$$\epsilon = R_0/A_0 << 1, \tag{1}$$

an asymptotic theory can be developed. In this case, a circular equilibrium cross-section shape of the torus is obtained in first approximation, considerably simplifying the problem. The existence of two length scales R_0 and A_0 will allow the use of the method of matched asymptotic expansions which further simplifies the problem. In the "outer region" (macroscale A_0) the torus appears, in the most complicated case, as a distribution of singularities on a moving circle of radius $A(t)$. In the "inner region" (microscale R_0) the torus is reduced to a

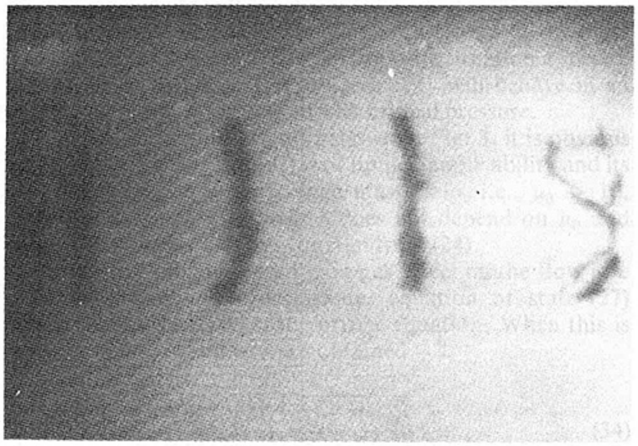

Fig. 1 Cavitating vortex rings around SERVOJET. $V \simeq 125$m/s, $\sigma \simeq 0.94$, $F \simeq 14$ kHz, $s_d = 0.59$

Contributed by the Fluids Engineering Division for publication in the JOURNAL OF FLUIDS ENGINEERING, and presented at the Cavitation and Multiphase Flow Forum, St. Louis, Missouri, June 1982. Manuscript received by the Fluids Engineering Division, November 29, 1982.

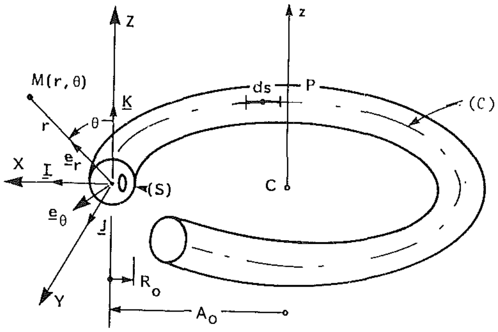

Fig. 2 Schematic of the bubble ring and coordinate axes

cylinder of variable section $R(t)$. At high orders of approximation deviation from the circular symmetry would also appear. In this paper, we will limit ourselves to the first order of approximation, where the deformation of the torus is limited to a variation of the cross-section radius $R(t)$. The motion of the vortex ring and the modification of its overall radius $A(t)$ appear only at the following orders.

Discussion of the Model

The main assumptions for the model of the behavior of a toroidal bubble in a pressure field are that the fluid is inviscid and incompressible and that diffusion phenomena can be neglected. Such assumptions are common in the study of spheroidal cavities and have been shown to be valid at least until the final stages of bubble collapse (see reference [5] for a review study, and reference [6] for a discussion of these assumptions). Here, with an inviscid fluid we must impose the additional condition that the circulation, Γ, is a constant. In a real fluid this assumption is valid as long as the time scale for the diffusion of viscosity, let us say R_0^2/ν, is small compared with the characteristic time of collapse of the toroidal cavity (given in equation (12)). For a pressure drop of one atmosphere and for water, the assumption turns out to be valid as long as the vapor core radius is greater than 0.1μm.

The assumption of small vaporous core to ring radius ratio ($\epsilon << 1$) in interesting for several practical and physical situations. It corresponds to most cases of the observed occurrance of distinct jet structuring and also to the practical range of functioning of submerged jets in deep hole drilling where the cavitation number, σ, is high and where the challenge is to induce cavitation by fluctuating the jet flow. In that case, σ varies about the cavitation inception value and the size of the vaporous ring core is small compared to the jet radius. When ϵ grows, the model loses its validity, not only because of the subsequent complex geometry of the torus involved (i.e., big deformations of the vaporous section are expected), but also because of the increased interaction with neighboring rings in the jet.

We have limited this study to the first order approximation in powers of ϵ, in which the variation of the core radius and thus of the ring volume is the predominant effect. In another study [7] we have shown that the translation velocity is given by the expression,

$$V_t = \frac{\Gamma}{4\pi R_0}\left\{\epsilon\left[\text{Log}\frac{8}{\epsilon} - \frac{1}{2} + \frac{W_e^{-1}}{\Omega}\right]\right\},$$

where W_e^{-1} and Ω are defined below in equation (10). This velocity is of order ϵ Log $8/\epsilon$, while the collapse velocity is of the order of unity which explains why in first approximation, the ring section remains circular and the bubble center does not move.

Similar expressions, not containing the Weber number term, have been obtained by Tung and Ting [8] and Moore and Safman [9, 10] for viscous rings. In these expressions ϵ is replaced by the ratio of the viscous core to the ring radius. Tung and Ting [8] used a matched asymptotic approach similar to that presented here, while Moore and Safman [9] used the Biot and Savard law with a cutoff to remove the singularity. These approaches differ only in the value of the constant 1/2 which appears in the expression of V_t, this being due to different evaluations of the viscous core size. Here no such problem exists since the core is well defined as the vaporous part of the fluid.

In the same reference quoted above [7] and in a doctoral thesis to be presented by the second author [11] the stability of the circular shape has been demonstrated. The development of non-axisymetric waves on the ring and their eventual instability, which has been observed experimentally is not considered here and should be the subject of further investigation.

Bubble Ring Dynamical Equation

With the above assumptions the flow is potential, and to study the bubble ring dynamics one has to solve in the liquid the Laplace equation subjected to the boundary conditions at infinity and on the torus wall. In the asymptotic approach the cross section of the ring is circular in first approximation, and of center 0. In addition the boundary conditions at the bubble wall are to be satisfied only in the "inner region," while the boundary conditions at infinity apply only to the "outer region." The matching of the two solutions (one in each "region") provides the missing condition for the outer region. In the "inner problem" the kinematic and dynamical conditions on the bubble surface, which is reduced to the cylinder $r = R(t)$, can be written (see Fig. 2):

$$\underline{\nabla \phi}_{\text{in}} = \dot{R}\underline{e}_r + \Gamma/2\pi R\underline{e}_\theta, \tag{2}$$

$$\rho(\dot{\phi}_{\text{in}} + |\underline{\nabla \phi}_{\text{in}}|^2/2) = P_\infty(t) - P_v - P_g + \gamma/R, \tag{3}$$

where dots denote time derivatives and ϕ_{in}, the "inner" velocity potential. Once $\phi_{\text{in}}(R,t)$ is known, (3) determines the torus dynamics.

In the "outer problem" the collapsing vortex ring appears, in first approximation, as a repartition of sources and vortices on a fixed circle of constant radius R_0. If the unknown linear strength of the sources is $q(t)$ and ω the unknown intensity of the vortices, the "outer" velocity potential, ϕ_{out}, is determined at the point M by:

$$4\pi \cdot \phi_{\text{out}}(M,t) = \int_C \frac{-q(t)}{|PM|}\,\text{ds} - \omega \iint_S \frac{PM \cdot n}{|PM|^3}\,d\sigma \tag{4}$$

where S is any surface containing the circle C, and P a field point on S or C. No additional terms are to be added to the expression (4) of ϕ_{out}, since

$$\lim_{M \to \infty} \phi_{\text{out}} = 0. \tag{5}$$

Now, matching ϕ_{out} and ϕ_{in} will allow us to determine $q(t)$, ω as well as the needed boundary condition at infinity for ϕ_{in}. The matching condition states that the behavior of ϕ_{out} when the distance OM normalized with A_0 goes to zero, is identical to the behavior of ϕ_{in} when the distance OM normalized with R_0 goes to infinity. After using equation (4) to evaluate ϕ_{out} and its limit when OM goes to zero, one obtains:

$$\begin{gathered} q(t) = 2\pi R\dot{R}, \\ \omega = \Gamma; \end{gathered} \tag{6}$$

and more interesting the velocity potential in the "inner region" is determined to have as leading terms:

$$\phi_{\text{in}} = R\dot{R}\left(\text{Log}\frac{r}{A_0} + \text{Log}\frac{\epsilon}{8}\right) + \frac{\Gamma}{2\pi}\theta. \tag{7}$$

The Log ϵ term comes from the contribution of the whole ring

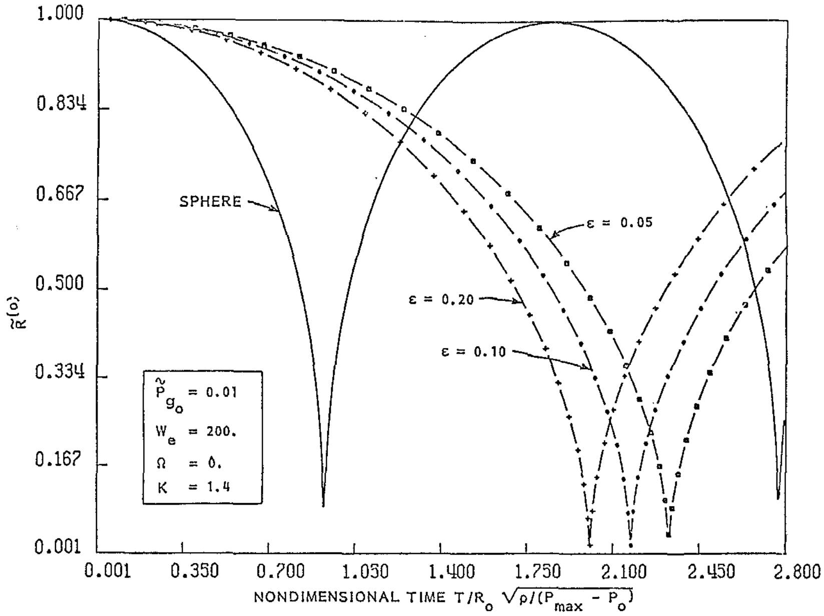

Fig. 3 Comparison of collapse times for spherical and toroidal bubbles

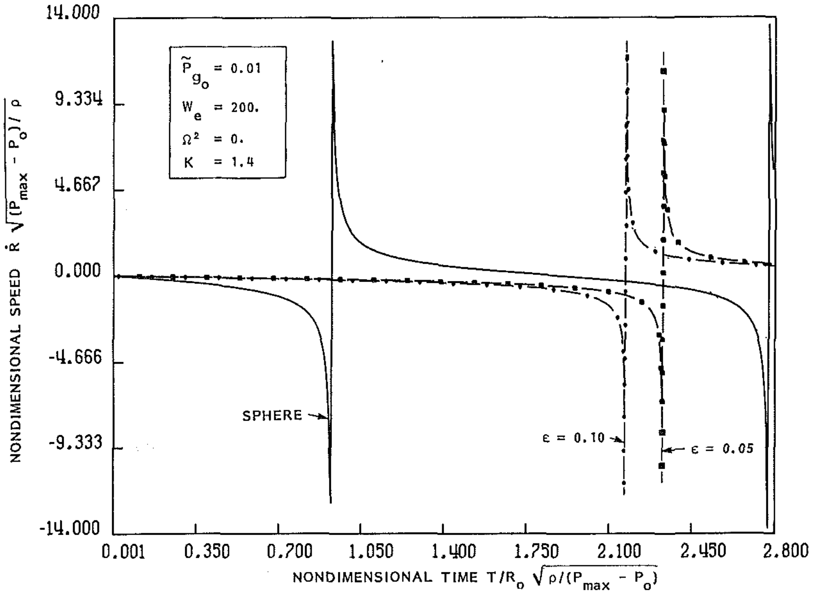

Fig. 4 Comparison of collapse speed of spherical and toroidal bubbles

to the behavior of the cylindrical portion centered at 0. Now, taking into account (7) and (2), ϕ_{in} and its derivative can be eliminated in (3) to give a differential equation for $R(t)$ which defines the bubble-ring equation. One obtains

$$(R\ddot{R}+\dot{R}^2)\text{Log}\,\frac{R}{8A_0}+\frac{1}{2}\dot{R}^2$$

$$=\frac{1}{\rho}\left[P_\infty(t)-\frac{\rho}{2}\left(\frac{\Gamma}{2\pi R}\right)^2-P_v-P_{g_0}\left(\frac{R_0}{R}\right)^{2k}+\frac{\gamma}{R}\right],\quad (8)$$

where k is the polytropic constant defining the behavior of an ideal gas in the ring bubble.

Characteristic Collapse Time of a Bubble Ring

The torus dynamical equation (8) can be written in nondimensional form by normalizing R by R_0, the pressures by $\Delta P = P_{\max} - P_o$, and time by the unknown collapse time of the bubble ring, T. Equation (8) becomes then:

$$(\tilde{R}\ddot{\tilde{R}}+\dot{\tilde{R}}^2)\text{Log}\,\frac{\epsilon\tilde{R}}{8}+\frac{1}{2}\dot{\tilde{R}}^2$$

$$=\frac{T^2\Delta P}{\rho R_0^2}\left[\tilde{P}_\infty(t)-\frac{\Omega}{2\tilde{R}^2}-\frac{\tilde{P}_{g0}}{\tilde{R}^2 k}+\frac{\text{W}_e{}^{-1}}{\tilde{R}}\right]\quad (9)$$

where tildes denotes nondimensional variables and

$$\begin{aligned}\tilde{P}_\infty(\tilde{t})&=(P_\infty(t)-P_v)/\Delta P,\\ \tilde{P}_{g_0}&=P_{g_0}/\Delta P,\\ \text{W}_e^{-1}&=(\gamma/R_0)/\Delta P,\\ \Omega&=(\rho\Gamma^2/4\pi^2 R_0{}^2)/\Delta P.\end{aligned}\quad (10)$$

$\tilde{P}_{g0}$ is a measure of the ratio of the initial gas pressure to the dynamic pressure; W_e, the Weber number, meaures the influence of the surface tension, while Ω defines the amount of the pressure drop due to the vortical motion relative to the dynamic pressure. If the normalization is correct all the

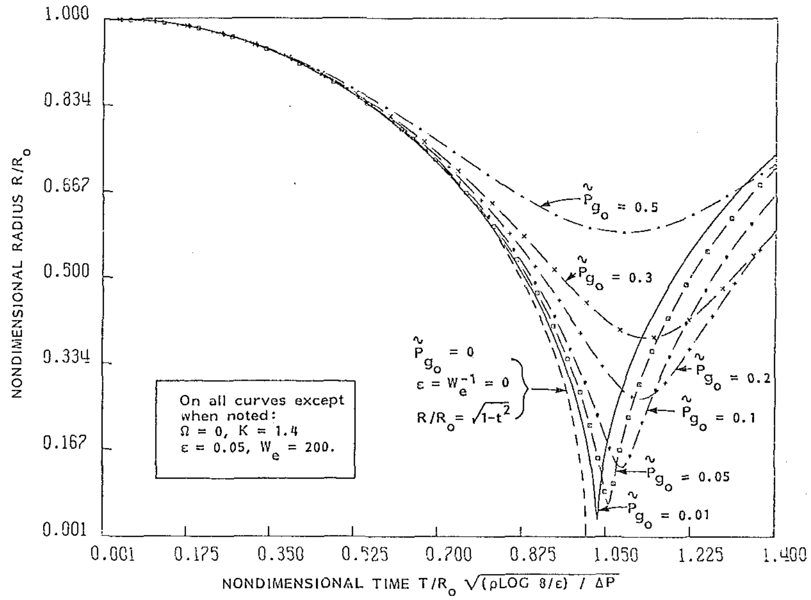

Fig. 5 Influence of gas content on toroidal bubble collapse

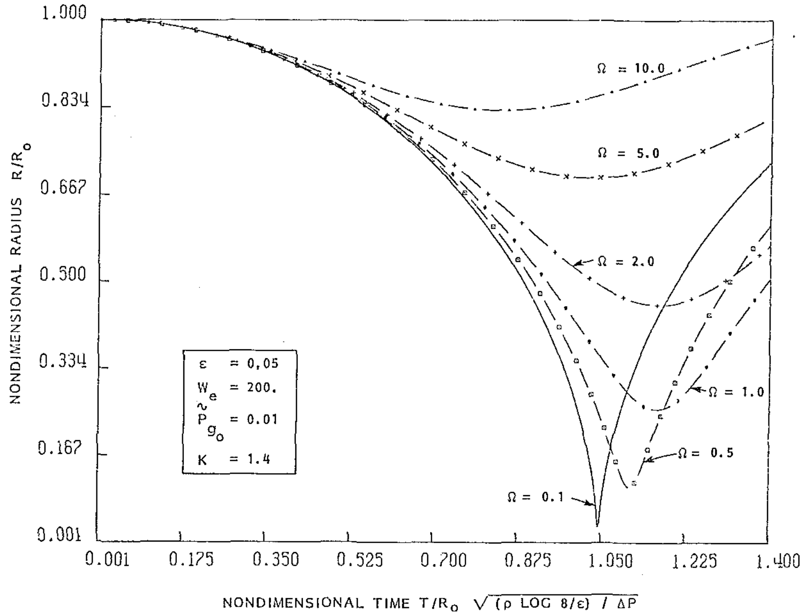

Fig. 6 Vortex strength influence on bubble ring collapse

nondimensional terms are of order unity, and as long as (Log ϵ) is of the same order as one, the equality (9) holds if $T^2\Delta P$ is of the same order of $\rho R_0{}^2$. However when ϵ goes to zero the term on the left-hand side of (9) containing Log ϵ is predominant and balances the right-hand side only if

$$T^2\Delta P/\rho R_0{}^2\text{Log}(8/\epsilon)=0(1). \qquad (11)$$

The preceding reasoning shows that for all small values of ϵ the characteristic time of the collapse is given by:

$$T\sim R_0(\rho/\Delta P)^{1/2}(\text{Log } 8/\epsilon)^{1/2} \qquad (12)$$

which differs from the Rayleigh time by a factor of (Log $8/\epsilon)^{1/2}$, indicating a longer collapse time for a ring than for a bubble having the same diameter as the cross-section of the ring. We will see below, with the numerical solution, that this is the case and that (12) gives the proper time scaling. With this choice for T, equation (9) becomes:

$$(\tilde{R}\ddot{\tilde{R}}+\dot{\tilde{R}}^2)+\left(\tilde{P}_\infty(t)-\frac{\Omega}{2\tilde{R}^2}-\frac{\tilde{P}_{g0}}{\tilde{R}^{2k}}+\frac{\text{W}_e{}^{-1}}{\tilde{R}}\right)$$

$$=\left(\text{Log}\frac{8}{\epsilon}\right)^{-1}\left(\text{Log}\tilde{R}(\tilde{R}\ddot{\tilde{R}}+\dot{\tilde{R}}^2)+\frac{1}{2}\dot{\tilde{R}}^2\right). \qquad (13)$$

When ϵ goes to zero the right-hand side becomes negligible and the left side gives the equation of the collapse of a cavitating vortex line. If, in addition, ϵ, Ω, P_{g0} and $\text{W}_e{}^{-1}$ are equal to 0 and $P_\infty(t)$ is a sudden pressure step, there is an analytical solution $\tilde{R}(\tilde{t}) = (1-\tilde{t}^2)^{1/2}$.

Numerical Solutions and Discussion

Equations (8), (9), or (13) can be solved numerically using a Runge-Kutta procedure. We present here a summary of the results obtained for various values of $\tilde{P}_{g0}$, ϵ, and Ω, when the cavitating bubble ring is subjected to a sudden increase of the pressure at infinity. For all the cases presented the polytropic constant of compression is taken equal to 1.4 and the Weber number is 200. The results are compared with those of a sphere of the same initial radius.

In Fig. 3, the collapse of the torus in absence of vortical motion and for different values of the ratio ϵ between R_0 and A_0 is compared with that of a sphere with initial radius R_0. Nondimensional curves of R/R_0 versus time normalized by the Rayleigh collapse time, $R_0(\rho/\Delta P)^{1/2}$, show the variation of the toroidal bubble lifetime with ϵ. This indicates the need for a new characteristic time, T, different from the Rayleigh time, T_R. When the same curves are redrawn with T defined by (12) they all collapse for given values of $\tilde{P}_{g0}$, K, and W_e.

Figure 4 shows, in the same conditions as in Fig. 3, the nondimensional variations of the bubble speed, $\dot{R}$, versus t/T_R. Both Fig. 3 and 4 show a slower and less intense collapse of the torus relative to the sphere. This effect increases as ϵ is decreased. However it would be erroneous to conclude that the torus erosive effect would be less intense, since a torus of initial cross section radius R_0 and a sphere of the same radius subjected to the same ΔP do not have the same initial potential energy. One ought thus to compare both bubble shapes for the same initial volume, and account for the difference in the surface of the areas subjected to the erosive power in each case. The radius of a sphere having the same volume as the torus (R_0, A_0) is

$$R_s = \left(\frac{3}{2}\pi\epsilon^{-1}\right)^{1/3} R_0, \tag{14}$$

and the ratio of the influenced surfaces is of the order

$$\frac{A_T}{A_S} \simeq \frac{4\pi R_0 A_0}{\pi R_s^2} = 4\epsilon^{-1/3}\left(\frac{3}{2}\pi\right)^{-2/3}. \tag{15}$$

One can see from equation (15) and Fig. 4 that, while the velocity of the collapse is slightly lower for the torus (about 90%) the influenced area essentially compensates for this difference: the torus influenced area is 3 times greater for $\epsilon = 0.1$ and 4 times for $\epsilon = 0.25$. One might then expect a higher erosive power with the bubble ring collapse.

The influence on the collapse of $\tilde{P}_{g0}$, the initial gas pressure of the bubble, can be seen in Fig. 5. Normalized values of R versus normalized time are represented, for the same values of ϵ, Ω, K, and W_e. We observe the same influence of P_{g0} on the torus collapse as on the spherical bubble collapse. Small values of P_{g0} slightly increase the collapse time. However, higher values completely modify this time indicating the need for a correction of the characteristic time which should account for P_{g0} in addition to ΔP. In the same Fig. 5, we have drawn the analytical asymptotic solution $(1-t^2)^{1/2}$, corresponding to $\Omega = \epsilon = W_e^{-1} = P_{g0} = 0$, as well as a comparative numerical solution for $\Omega = W_e^{-1} = P_{g0} = 0$ and $\epsilon = 10^{-8}$. We can see that the latter curve is much closer to the numerical curves for $P_{g0} = 0$ than for the asymptotic solution. This occurs because of the very slow divergence of Log ϵ when ϵ goes to zero, which indicates that the right-hand side of (13) should always be considered of the same order as the left-hand side for any practical values of ϵ.

The effect of the rotation of the ring on its collapse is illustrated in Fig. 6. The vortical motion has the same effect on the torus behavior as the noncondensible gas. Although perhaps unexpected, this result is logical once we consider equation (9). It is seen that changing P_{g0} or Ω has a comparable effect, and for $K = 1$ (isothermal compression) the two parameters, P_{g0} and Ω, can be combined into a single variable. Physically this is understandable since increasing Ω implies decreasing the local ambient pressure at the torus boundary and thus reducing the driving collapse pressure. The same remark applied for P_{g0}, since increasing the initial gas pressure, while keeping the ambient pressure constant will also reduce the driving pressure for the implosion. This observation on the influence of Ω has important consequences. For example, when attempting to increase the erosion caused by a jet we see that increasing Ω has two opposite effects: (*a*) cavitation inception will appear earlier, and (*b*) the collapse is damped. This indicates the existence of an optimum Ω for given conditions and the need for an in-depth examination of the criterion required to determine this optimum value.

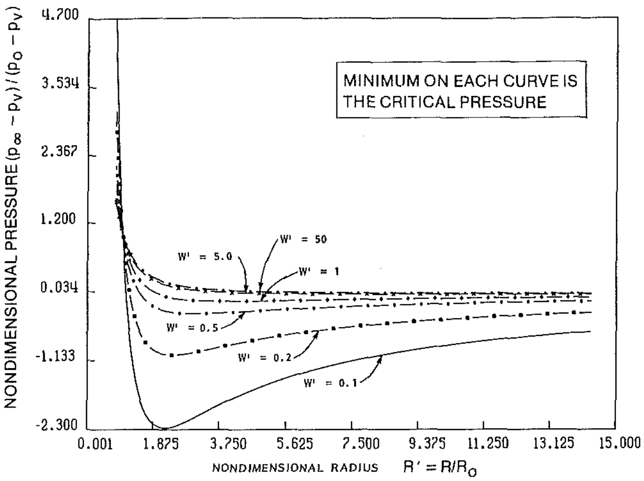

Fig. 7 Static equilibrium curves for vortex bubble rings

Finally, Fig. 7 gives the static equilibrium curves of a torus bubble. These curves allow the determination, for a given initial radius of the bubble, of the critical pressure below which an explosive growth (thus cavitation) is expected to occur. It is convenient to utilize a nondimensional representation with $P' = (P_\infty - P_v)/(P_0 - P_v)$ as the ordinate and $R' = R/R_0$ as the abscissa. The equilibrium equation is then, with an isothermal compression law ($K = 1$),

$$P' = (\Omega' + P'_{g0})/R'^2 + 1/W_e' R', \tag{16}$$

where

$$\begin{aligned} \Omega' &= (\rho\Gamma^2/4\pi^2 R_0^2)/(P_0 - P_v) \\ P'_{g0} &= P_{g0}/(P_0 - P_v), \\ W_e' &= (\gamma/R_0)/(P_0 - P_v). \end{aligned} \tag{17}$$

With the initial nondimensional condition:

$$1 = \Omega' + P'_{g0} + 1/W_e', \tag{18}$$

the static equilibrium equation becomes:

$$P' = (1 - W_e'^{-1})/R'^2 + W_e'^{-1}/R'. \tag{19}$$

We see that a unique parameter, W_e', is capable of representing all cases provided that the gas compression law is isothermal, which is consistent with quasistatic modifications of the equilibrium state. Figure 7 shows P' versus R' for a series of values of W_e'.

Conclusion

We have developed in this paper an asymptotic theory for the behavior of a bubble ring in a variable pressure field. A dynamical equation for the oscillations of the cross section radius of the torus was developed when the ratio, ϵ, between this radius and the overall radius is small. Static equilibrium curves of the torus were drawn which account for surface tension, noncondensible gas and vortical motion of the bubble ring.

Numerical solutions of the vaporous torus collapse due to a sudden ambient pressure increase are presented which show the influence of ϵ, the gas content and the circulation around the torus. A characteristic time for the collapse is derived and the importance of the various parameters is discussed. These results indicate that a bubble ring collapse should be more erosive than that of an equivalent (same initial potential energy) spherical bubble. The vortical motion is seen to induce an earlier cavitation inception while simultaneously damping the collapse. An optimum value of the circulation should therefore be sought.

Acknowledgments

This work was supported in part by the U.S. Department of Energy, Division of Geothermal Energy, under SANDIA Laboratories Contract No. 13-5129; support by the Authors organizations, Hydronautics, Incorporated and Direction Recherches Etudes Techniques, has also been provided for this study.

References

1 Crow, S. C., and Champagne, F. H., "Orderly Structure in Jet Turbulence," *Journal of Fluid Mechanics*, Vol. 48, Part 3, Aug. 1971, pp. 547-591.

2 Johnson, V. E., Jr., Lindenmuth, W. T., Conn, A. F., and Frederick, G. S., "Feasibility Study of Tuned-Resonator, Pulsating Cavitating Water Jet for Deep-Hole Drilling," HYDRONAUTICS, Incorporated Technical Report 8001-1, May 1981.

3 Johnson, V. E., Jr., Chahine, G. L., Lindenmuth, W. T., Conn, A. F., Frederick, G. S., Giacchino, G. J., Jr., "Cavitating and Structured Jets for Mechanical Bits to Increase Drilling Rate," ASME Paper No. 82-Pet-13, 1982.

4 Shutler, N. D., and Mesler, R. B., "A Photographic Study of the Dynamics and Damage Capabilities of Bubbles Collapsing Near Solid Boundaries," Dept. of Chemical and Petroleum Engineering, University of Kansas Report, Apr. 1964.

5 Plesset, M. S., and Prosperetti, A., "Bubble Dynamics and Cavitation," *Annual Review of Journal Fluid Mechanics*, Vol. 9, 1977, pp. 145-185.

6 Chahine, G. L., "Interaction Between an Oscillating Bubble and a Free Surface," ASME JOURNAL OF FLUIDS ENGINEERING, Vol. 99, 1977, pp. 709-716.

7 Genoux, Ph.F., and Chahine, G. L., "Equilibre Statique et dynamique d'un tore de vapeur," to appear *Journal de Mécanique*, 1983.

8 Tung, C., and Ting, L., Motion and Decay of a Vortex-Ring," *Journal Physics of Fluids*, Vol. 10, Vol. 5, 1967, pp. 901-910.

9 Safman, P. G., "The Velocity of Viscous Vortex-Rings," *Studies Applied Mathematics*, Vol. 49, 1970, pp. 371-380.

10 Moore, D. W., and Safman, P. G., "The Motion of a Vortex Filament with Axial Flow," *Phil. Trans.*, Vol. 272A, 1972, pp. 403-429.

11 Genoux, Ph. F., "Etude Asymptotique de mouvement et des Oscillations d'un Tore de Vapeur. Modélisation d'un Jet Cavitant Oscillant," Thèse de Docteur-Ingénieur, Universite Paris VI, 1984.

Measurements of the Spray Angle of Atomizing Jets

K.-J. Wu
Graduate Student.

C.-C. Su
Graduate Student.

Department of Mechancial and
Aerospace Engineering,
Princeton University,
Princeton, N. J. 08544

R. L. Steinberger
Assistant Professor,
Department of Mechanical Engineering,
Bucknell University,
Lewisburg, Pa.

D. A. Santavicca
Research Engineer.

F. V. Bracco
Professor.

Department of Mechanical and
Aerospace Engineering,
Princeton University,
Princeton, N.J. 08544

Liquid jets are considered issuing from single-hole, round nozzles into quiescent gases under conditions such that they break up into a well defined conical spray immediately at the nozzle exit plane. The initial angles of such sprays were measured at room temperature by a spark photography technique. Water, n-hexane, and n-tetradecane at pressures from 11.1 MPa to 107.6 MPa were injected into gaseous N_2 at pressures from 0.1 MPa to 4.2 MPa through sixteen nozzles of different geometry. Under the test conditions, the spray angle is found to be a strong function of the nozzle geometry and the gas-liquid density ratio and a weak function of the injection velocity. The measured trends are then discussed in the light of possible mechanisms of the breakup process and shown to be compatible with the aerodynamic theory of surface breakup if modified to account for nozzle geometry effects.

Introduction

The subject of this paper is very narrow: the initial angle of the sprays that are formed in Diesel and stratified-charge engines when fuel is injected directly into the compressed air in their combustion chambers through cylindrical holes. This angle is important because it influences the axial and radial distributions of the fuel and, ultimately, efficiency and emissions. Of interest is the dependence of the angle on the geometry of the nozzle, and the dynamic and thermodynamic states of liquid and gas at the moment of injection.

Typically, the injector head is made up of a group of straight, round holes (shower head) 200 to 600 μm in diameter with length-to-diameter ratios between 2 and 8. The pressure difference is greater than 10 MPa, and in some designs is even higher than 100 MPa, so that the resulting initial jet velocity is greater than 10^2 m/s. The outer surface of such jets is observed to break up into drops 1 to 10 μm in diameter within distances from the nozzle exit also of the order of 1 to 10 μm. This is only one of many modes in which liquid jets break up into drops and has been labelled [1] the atomization regime on account of the minute drops formed.

Obviously the initial angle of the spray is only one of the quantities of interest in IC engine applications. The initial distributions of drop radii and velocities are also very important. But the small size, high speed, and high drop number density of atomizing jets make drop size and velocity measurements very difficult, even at the outer edge of the spray, and no technique seems to have been found to probe the jet inner structure.

On the other hand, the measured dependency of the spray angle on various parameters can be a clue to the mechanism of atomization, and if such mechanism is identified, predictions may be possible of the quantities that are difficult to measure.

An atomizing jet is shown in Fig. 1. In earlier work [1–3], in the atomization regime, the measured spray angle was found to follow the simple relationship,

$$\tan\frac{\theta}{2} = \frac{1}{A}\,4\pi\left(\frac{\rho_g}{\rho_l}\right)^{1/2}\frac{\sqrt{3}}{6} \qquad (1)$$

where θ is the spray angle, ρ_g the density of the gas, ρ_l the density of the liquid, and A is a constant for a given nozzle geometry. Although the range of parameters was rather broad (see Table 1), only water-glycerol mixtures were used, the exit diameters of all nozzles were approximately equal and cavitation was present in all tests. Finally, even though nine nozzle geometries were explored, all had sharp exit edges. Thus in the present work we explored a broader range of density ratios, and used different liquids, cavitation-free nozzles, and nozzles of different diameters, different length-to-diameter ratios, and with rounded outlets. We also ex-

---

Contributed by the Fluids Engineering Division and presented at the Winter Annual Meeting, Boston, Mass., November 14–18, 1983, of THE AMERICAN SOCIETY OF MECHANICAL ENGINEERS. Manuscript received by the Fluids Engineering Division, December 3, 1981. Paper No. 83-WA/FE-10.

Table 1 Summary of test parameters

	References [1-3]	Present work
Test liquid	Water, glycerol, and their mixtures	Water, n-hexane, and n-tetradecane
ρ_l (g/cm^3)	0.998 - 1.261	0.665 - 0.998
P_l (MPa)	3.9 - 18.0	11.1 - 107.6
μ_l (g/s•cm)	0.010 - 17.596	0.0032 - 0.0218
σ_l (dyne/cm)	63.0 - 72.8	18.4 - 72.8
T_l (K)	room temp.	room temp.
Ambient Gas	N_2, He, and Xe	N_2
$\rho_{g\times 10^3}$ (g/cm^3)	1.1 - 51.5	1.2 - 48.7
P_g (MPa)	0.1 - 4.2	0.1 - 4.2
$\mu_{g\times 10^4}$ (g/s•cm)	1.70 - 2.26	1.70
T_g (K)	room temp.	room temp.
Nozzle geometries	9	13
d (μm)	343	254, 343, and 660
L/d	0.5 - 85	$\approx$ 0 - 50
Argument of f	1.3×10^{-4}-1.6×10^3	0.4 - 420
$\rho_g/\rho_l\times 10^3$	1.1 - 51.6	1.8 - 73.2

tended the measurements to higher injection pressures (up to 107.6 MPa). The narrower objective was to test the range of validity of equation (1), the broader one was to collect additional information about the mechanism of atomization.

This paper is organized as follows. First, experimental apparatus and procedure are described, then the range of the parameters explored and the measured spray angles are reported, and finally the possible implications of the measurements with respect to the mechanism of atomization are discussed.

Apparatus and Procedure

The experimental rig consisted of a spray chamber, a liquid pressurization system, a nozzle assembly, and instrumentation. Only a summary of the apparatus and the experimental procedure is given here. Details are available in [4].

Spray Chamber. The spray chamber was a cylindrical steel container, 19 cm ID and 48 cm in length, with four circular windows 10 cm in diameter. It was designed to withstand pressure up to 7.0 MPa at 750 K but the reported experiments were all conducted at room temperature. The liquid injections were along the axis of the chamber. The chamber was filled with Liquid Carbonic high purity nitrogen at the desired pressure. The gas density at all pressures was calculated based on the data in [5].

Pressurization System. Two techniques were used to pressurize the liquid. For liquid pressures up to 38.0 MPa, a

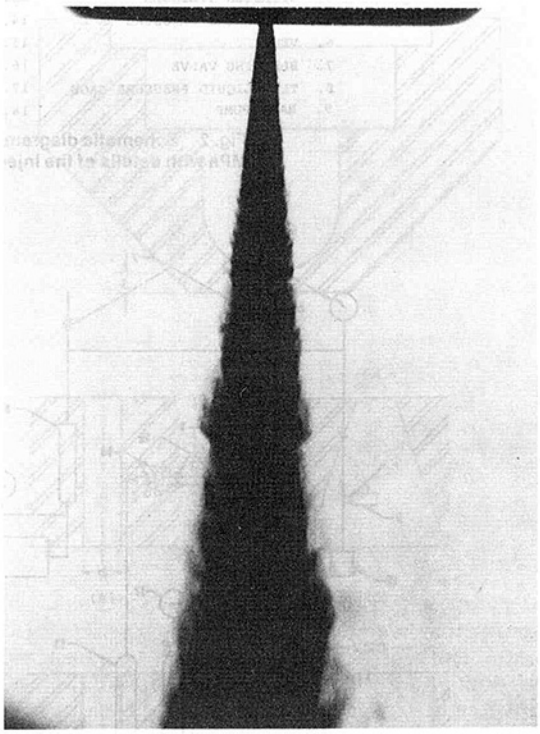

Fig. 1 Typical atomizing jet

Nomenclature

A = dimensionless nozzle constant in equations (1) and (2)

d = nozzle diameter, μm

f = function of $\frac{\rho_l}{\rho_g}\left(\frac{\text{Re}_l}{\text{We}_l}\right)^2$, [8]

K = cavitation number, $\frac{P_l-P_g}{P_g-P_v}$

L = nozzle passage length, μm

P_g,P_l = pressure of gas and liquid, MPa

P_v = vapor pressure of liquid, kPa

r = radius of curvature of nozzle exit edge, μm

Re_l = Reynolds number, $\frac{\rho_l U_{\text{vol}} d}{\mu_l}$

T = test liquid injection duration, s

T_g,T_l = temperature of ambient gas and test liquid

U_{ideal} = ideal jet velocity, cm/s

U_{vol} = volumetric averaged velocity of jet, cm/s

We_l = Weber number, $\frac{\rho_l U_{\text{vol}}^2 d}{\sigma_l}$

α = nozzle inlet approach angle, degree

Δp = effective injection pressure, P_l-P_g, MPa

θ = spray full angle, degree

μ_g,μ_l = dynamic viscosity of gas and liquid, $\frac{\text{dyne•s}}{\text{cm}^2}$

ρ_g,ρ_l = density of gas and liquid, $\frac{g}{\text{cm}^3}$

σ_l = gas-liquid surface tension, dyne/cm

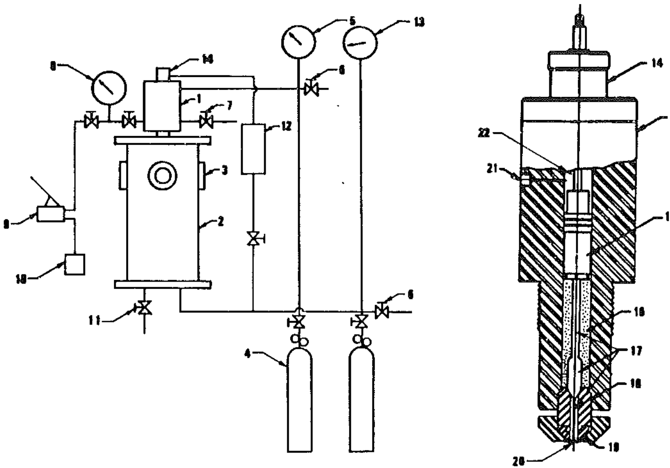

1. INJECTION CYLINDER
2. SPRAY CHAMBER
3. WINDOW
4. NITROGEN CYLINDER
5. DRIVER GAS PRESSURE GAGE
6. VENT
7. BLEEDING VALVE
8. TEST LIQUID PRESSURE GAGE
9. HAND PUMP
10. TEST LIQUID TANK
11. DRAIN
12. PRESSURE AMPLIFIER
13. CHAMBER GAS PRESSURE GAGE
14. HYDRAULIC POWER CLAMP
15. PISTON
16. TEST LIQUID RESERVOIR
17. VALVE
18. VALVE SEAT
19. NOZZLE PIECE
20. NOZZLE
21. DRIVER GAS PORT
22. DRIVER GAS

Fig. 2 Schematic diagram of the system for liquid pressures up to 38.0 MPa with details of the injection cylinder

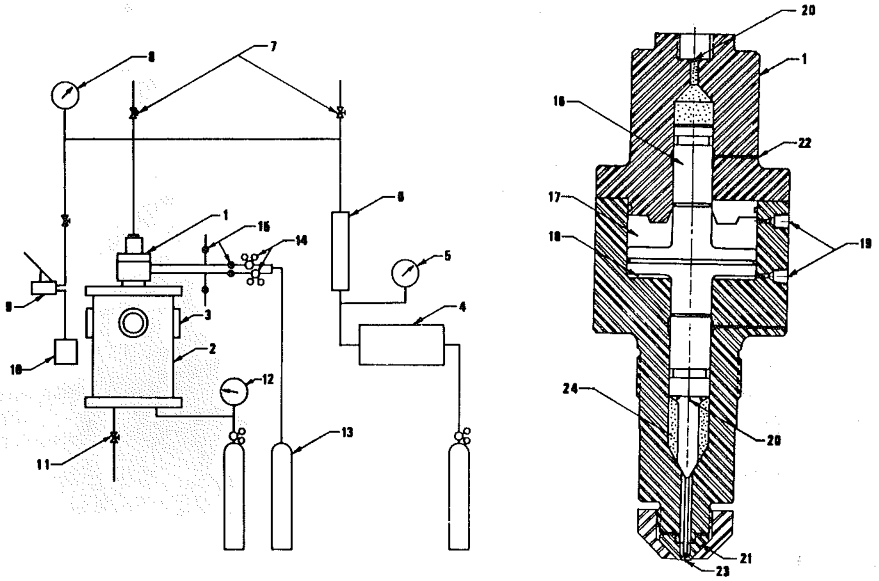

1. INJECTION CYLINDER
2. SPRAY CHAMBER
3. WINDOW
4. PRESSURE INTENSIFIER
5. DRIVER LIQUID PRESSURE GAGE
6. LIQUID RESERVOIR
7. BLEEDING VALVES
8. TEST LIQUID PRESSURE GAGE
9. HAND PUMP
10. TEST LIQUID TANK
11. DRAIN
12. CHAMBER GAS PRESSURE GAGE
13. NITROGEN CYLINDER
14. REGULATORS
15. SOLENOID VALVES
16. VALVE UNIT
17. UPPER CONTROL GAS CHAMBER
18. LOWER CONTROL GAS CHAMBER
19. CONTROL GAS PORTS
20. TEST LIQUID CONDUIT
21. NOZZLE PIECE
22. LEAK OFF
23. NOZZLE
24. TEST LIQUID

Fig. 3 Schematic diagram of the system for liquid pressures between 38.0 and 207 MPa with details of the injection cylinder

local liquid reservoir was used with a valve mechanism (Fig. 2) that allowed a constant pressure, essentially motionless liquid, to be kept upstream of the nozzle. 41 MPa nitrogen gas from Matheson, after proper regulation with a Matheson model 3075 regulator, was used to pressurize the test liquid. The valve system included a solenoid controlled pressure amplifier, a hydraulic power clamp, and a valve rod. O-rings made of neoprene from Sandem Industries were used between the valve rod and the liquid reservoir for the sealing; a hand-lapped metal-to-metal seal was used between the valve rod and the valve rod seat. The solenoid controlled pressure amplifier was driven by the gas from the pressurized nitrogen tank and created high oil pressure to operate the hydraulic power clamp which in turn lifted the valve rod off its seat.

Table 2 Nozzle geometries

Nozzle	Class	Description d (μm)	L/d	r	α(degree)
I	Constant diameter tube	254	4.0	–	180
II(a), (b), and (c)	Constant diameter tube	343	4.0	–	180
III	Constant diameter tube	660	4.0	–	180
IV(a) and (b)	Rounded outlet	343	4.0	½d	180
V	”	343	4.0	d	180
VI	Straight sided diverging nozzle	343	0	–	180
VII	Straight sided converging nozzle	343	0	–	90
VIII	Constant diameter tube	343	1.0	–	180
IX	”	335	2.0	–	180
X	”	335	4.0	–	180
XI	”	330	10	–	180
XII	”	330	20	–	180
XIII	”	330	50	–	180

When the nitrogen gas in the pressure amplifier was vented, the spring in the hydraulic power clamp forced the valve rod back to its seat.

For pressure between 38.0 MPa and 207 MPa the liquid reservoir was not immediately upstream of the nozzle and the test liquid flowed to the nozzle during the experiment through conduits of inner diameter no less than 6.9 times that of the nozzle (Fig. 3).

Test liquid was pumped into the liquid reservoir and the injection cylinder with a hand pump. Liquid and trapped air bubbles were bled out through two bleeding valves which were above any part of the liquid conduits, and the liquid inlet and outlet valves were closed, thus isolating the test liquid. Test liquid was then pressurized by the driver liquid (diesel oil) which was in turn driven by a Miller Fluid Power H66R pressure intensifier.

A valve unit, housed in the injection cylinder, controlled the initiation and termination of injection. A hole of 0.635 cm diameter through the valve unit allowed the pressurized liquid to flow through. A piece of rubber was glued on the lower end of the valve unit and sealed the nozzle very well.

Nitrogen gas was used to control the movement of the valve unit. Initially, the upper control gas chamber was filled with nitrogen gas at about 1.0 MPa, thus keeping the valve unit in the closed position. The valve unit opened when nitrogen gas at higher pressure was introduced into the lower control gas chamber. As the gas in the lower control gas chamber was vented, the valve unit was forced back to its seat and stopped the injection.

Nozzle Assembly. Sixteen injection nozzles with thirteen different geometries, as listed in Table 2, were used in the experiments. The geometries could be divided into four groups: constant diameter tube with L/d ratio between 1 and 50, rounded outlet nozzle, straight sided diverging nozzle, and straight sided converging nozzle. The details of the geometries are shown in Fig. 4, and the reasons for selecting these geometries will be discussed later.

All the nozzles were made of AISI 303 stainless steel. The diameter of the orifices ranged from 254 to 660 μm which is within the range of sizes used in Diesel engines.

For nozzles with L/d less than 10, the orifice was drilled directly into the nozzle piece under an optical microscope with a microdrilling machine from National Jet.

Nozzles XI and XII were prepared in a different way due to the difficulty in drilling long holes. For these two nozzles, a piece of 304 stainless steel hypodermic tubing with 330 μm I.D. and 635 μm O.D. from Small Parts was soldered into the nozzle piece and served as the nozzle passage. Both ends of the tubing were then carefully cleaned under microscope.

Nozzle XIII was also made from stainless steel hypodermic tubing except that the tubing was first soldered into a Swagelok brass pipe plug since the length of the orifice appeared to be too long for the interchangeable nozzle piece. The lower end of the nozzle piece was drilled and tapped so the brass plug could fit into it. With this design a sharp nozzle entrance was obtained.

Also, the entrance and exit of the nozzles were examined under a scanning electron microscope from different angles to assure that the desired sharpness (or roundness as may be the case) was obtained in the machining and not altered during the tests. The surface roughness was observed to be less than 5

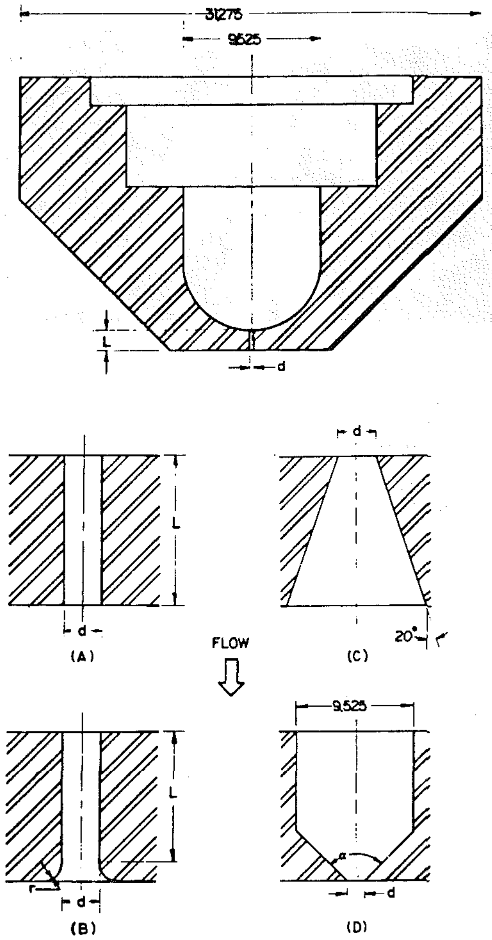

Fig. 4 Nozzle piece with details of nozzle geometries, unit: mm
(A) constant diameter tube nozzle: I, II(a), II(b), II(c), III, and VIII - XIII.
(B) rounded outlet nozzle: IV(a), IV(b), and V
(C) straight sided diverging nozzle: VI
(D) straight sided converging nozzle: VII

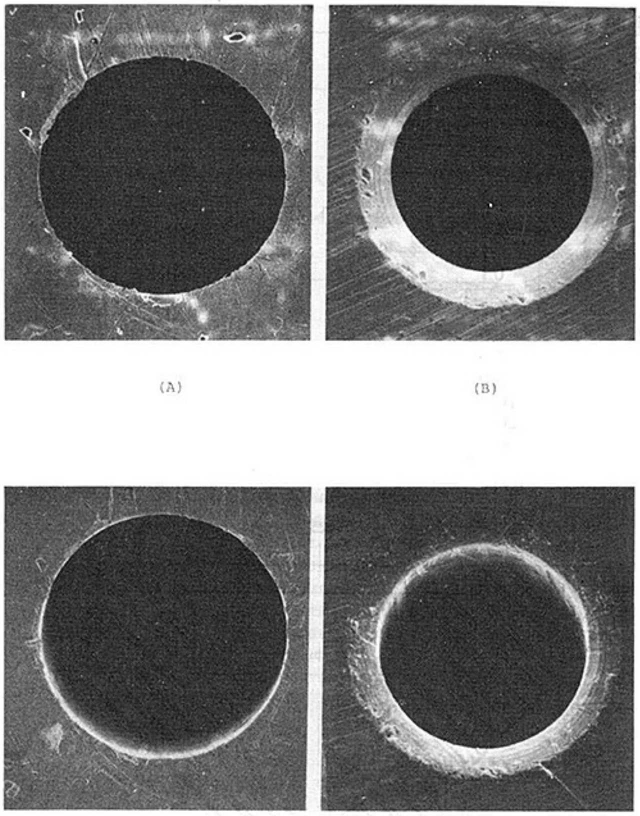
(A) (B)

(C) (D)

Fig. 5 Typical electron microscope photographs of entrance and exit of nozzle IV(*b*) before and after high liquid pressure tests:
(A) entrance, before any test
(B) exit, before any test
(C) entrance, after $P_l = 91.8$ MPa tests
(D) exit, after $P_l = 91.8$ MPa tests

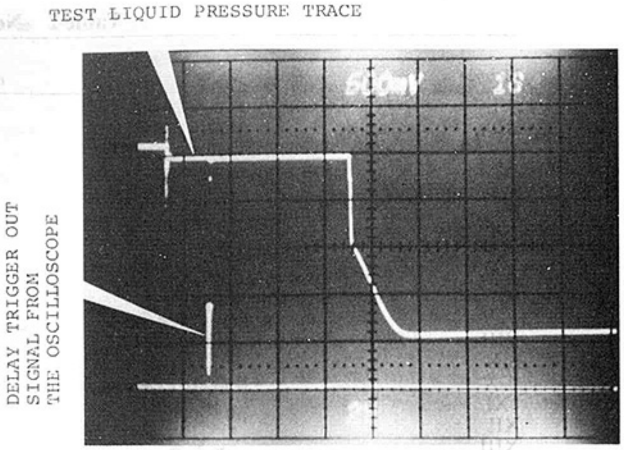

Fig. 6 Pressure trace of test liquid and delay trigger out signal from the oscilloscope

percent of the diameter. Typical photographs of a nozzle are shown in Fig. 5.

Instrumentation and Accuracy. For the low liquid pressure apparatus, the driver nitrogen gas pressure was measured with a Heise-17555 gage, and chamber gas pressure was measured with a US Gage USG-132603 gage. The accuracy of the Heise gage was ±0.2 MPa and that for the chamber gas gage was ±0.03 MPa.

In the ultra-high liquid pressure tests, the driver liquid pressure was measured at the pressure intensifier with a Heise-17555 gage having ±0.2 MPa accuracy. Test liquid pressure was read from an AMINCO 47-18340 gage whose accuracy was ±0.3 MPa.

In every test, the test liquid pressure during injection was also measured by a Kistler Model 307A pressure transducer, and Kistler Model 504 charge amplifier and the signal recorded by a Tektronix model 7313 oscilloscope with plug-in units 7A18 and 7835A. Figure 6 shows a typical photograph of the liquid pressure trace taken from the screen of the oscilloscope. The delay trigger out function of the oscilloscope was used to trigger the spark light after the liquid pressure had reached a steady value.

The sprays were illuminated by a high intensity short flash duration Xenon Model N-789B Nonolamp; a quartz lens was placed between the Nanolamp and the window on the spray chamber to collimate the light beam. The camera was an aluminum tube 107 cm long and was equipped with a Takumar 200 mm, f/3.5 lens, a mechanical shutter, and a Polaroid film back. The magnification of this system was about 5.6 and the field of view was about 1.5 cm × 2.0 cm. The film used was Polaroid type 57 film. During the experiment, the Nanolamp was actuated by a preset delay trigger out signal from the oscilloscope. The time delay between valve opening and light flash was between 0.5 to 1.0s as shown in Fig. 6. The shutter was opened manually before the light flash and the exposure time of the back lighted photographs was determined by the flash duration of the Nanolamp, which was about 20 nanoseconds.

Water, n-hexane, and n-tetradecane were used as test liquids. Their sources and properties, obtained from [6] are listed in Table 3.

Spray angles were derived from photographs for each condition. The accuracy of the measurement was within 0.5 deg. The arithmetic average of spray angles was calculated. The standard deviation of each condition is normally less than 3 percent but in some cases it was as large as 7 percent.

Measured Spray Angles

The conditions of all tests are summarized in Table 1 and details are given in reference [4].

High Density Ratio, Surface Tension, Nozzle Diameter. As pointed out in the introduction, earlier work [1-3] had indicated that, for a given nozzle geometry the spray angle is a function primarily of the density ratio (equation (1)). However, even though viscosity and pressure of the liquid, pressure and density of the gas and nozzle geometry were varied over broad ranges, nozzle diameter, liquid density, and surface tension were not varied. Thus the first priority of this work was to assess the validity of equation (1) over a broader range of density ratios and by varying the liquid surface tension and the nozzle diameter while keeping the same nozzle length-to-diameter ratio. The results of Fig. 7 show that equation (1) continues to be valid even for density ratios between 26×10^{-3} and 73×10^{-3} and that surface tension and nozzle diameter have no discernable effect on the initial angle of the spray.

High Injection Pressure. A recent trend in the design of diesel injectors is toward the use of very high injection pressures, up to 207 MPa instead of the more traditional maximum pressures of 35 MPa. Thus it is of practical interest to know whether equation (1) continues to hold at the higher injection pressures. The results of Fig. 7 (nozzles II(*b*) and II(*c*)) show that it does at least up to pressures of 107.6 MPa. (To make sure that the high injection pressures had not altered the nozzle, besides taking the standard electron microscope

Table 3 Test liquids and their properties

	Water	n-Hexane	n-tetradecane
Manufacturer and catalogue number	Tap water	Fisher Scientific Co. H-291	Eastman Kodak Co. 13090
Density ρ_l	0.998	0.665	0.763
Surface tension σ_l	72.8	18.43	26.7
Viscosity μ_l	0.010	0.0032	0.0218
$\left(\frac{\sigma_l}{\mu_l}\right)^2 \times 10^{-6}$	53.0	33.0	1.5
Vapor pressure P_v	2.34	16.5	less than 0.14

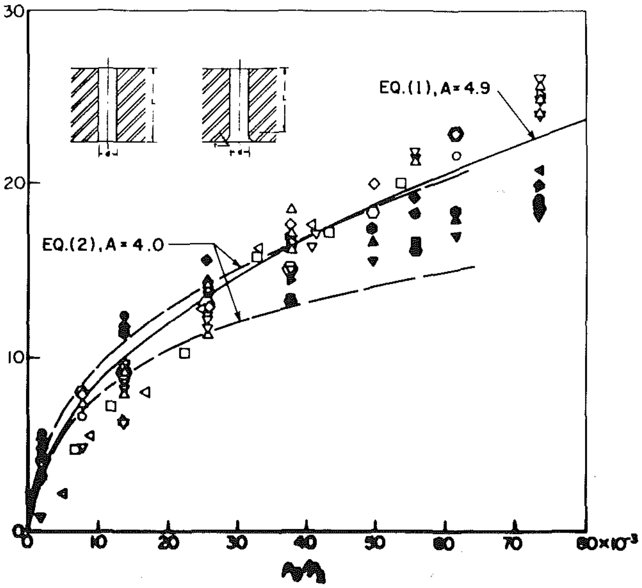

Fig. 7 Spray angle versus density ratio for constant diameter and rounded-outlet nozzles and for different nozzle diameters, test liquids, and injection velocity. Open symbols refer to lower, and closed symbols to higher, injection velocities (symbol, nozzle, liquid, U_{vol}(m/s)): ○, III, *n-h*, 126; △, II(*a*)-II(*b*), *n-h*, 108–182; ▽, IV(*a*)-IV(*b*), *n-h*, 124–146; ◁, II(*a*), H_2O, 103–106; ▷, *V*, *n-h*, 101–126; □, II(*a*), *n-t*, 106–122; ◇, II(*a*), *n-h*, 99–111; ⬡, I, *n-h*, 113–127; ●, IV(*b*), *n-h*, 350–358; ▲, II(*c*), *n-h*, 222; ▼, II(*c*), *n-h*, 311; ◀, IV(*b*), *n-h*, 217–230; ▶, II(*b*), *n-h*, 217–230; ■, II(*b*), *n-h*, 291–300; ◆, IV(*b*), *n-h*, 291–300; ⬢, II(*b*), *n-h*, 350–358; ⬢, II(*c*), *n-h*, 407.

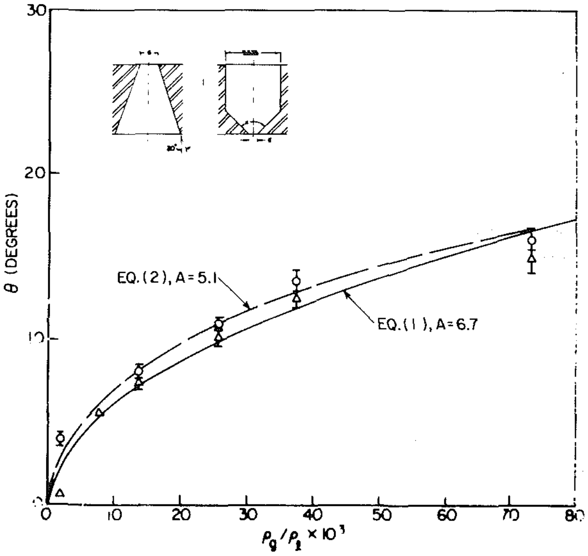

Fig. 8 Spray angle versus density ratio for cavitation-free nozzles: Test liquid: n-hexane; Δp: 11.0 MPa; △ : nozzle VI; ○ : nozzle VII

pictures of the nozzle entrance before and after the tests, the spray angle from low pressure injections was also measured before and after the high pressure ones, and no changes were found as shown in Fig. 7.)

Rounded-Outlet Nozzles. One parameter of the nozzle geometry that had not been previously tested for its possible effects on the spray angle is the radius of curvature of the exit edge of the nozzle (the radius of curvature of the entrance edge of the nozzle was tested and found to be very influential for sufficiently small L/d). Thus three nozzles (nozzles IV(*a*), IV(*b*), and V) with different exit geometries were employed and they gave the same spray angles as those with sharp outlets (Fig. 7).

Cavitation-Free Nozzles. Another important question that had not been addressed directly by the earlier work is whether cavitation alone could be responsible for atomization, since nozzle designs and operating conditions were such that some degree of cavitation was expected to be present in all tests. To see whether cavitation can be the only mechanism of atomization, it was necessary to use cavitation-free nozzles. Nozzles VI and VII are expected to be cavitation-free and produced atomized jets as shown in Fig. 8. Thus cavitation cannot be the only mechanism of atomization. The angle of the sprays from these nozzles continue to follow equation (1), but the value of constant A differs from that for the other nozzles.

Length-to-Diameter Ratio of Nozzles. Spray angles were measured for nozzles with similar diameter but L/d ranging from 1 to 50 at a fixed density ratio and results are shown in Fig. 9 together with data from references [3 and 7]. All data show that for L/d greater than 20 (nozzles XII and XIII), the spray angle decreases with increasing L/d. As L/d decreases from 20 (nozzles VIII, IX, X, and XI), the present data indicates an increase of the spray angle up to a maximum at L/d around 10 and then a decrease for L/d smaller than 10. Hiroyasu et al. [7] found the same trend but a maximum at around 20 whereas the earlier data of Reitz and Bracco [3] indicated that the angle may increase monotonically with decreasing L/d. Thus it is clear that the initial angle of the spray depends on the geometry of the nozzle. But the mechanism of this dependence is not known and even the trends are not yet fully established. The scatter may be due to sensitivity of the angle to upstream flow and to details of nozzle geometry and roughness directly for short nozzles and indirectly, through transition to turbulence, for long ones [1].

Discussion

The data of this and earlier publications are valuable in that they can be used directly to predict the injection spray angle in diesel engines. These steady state data are entered using the

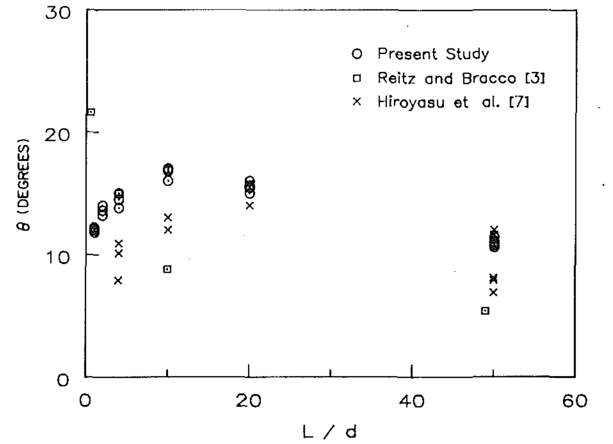

Fig. 9 Spray angle versus *L/d* for constant diameter nozzles: test liquid: *n*-hexane; Δp: 11.0 MPa; ρ_g/ρ_l: 0.0346

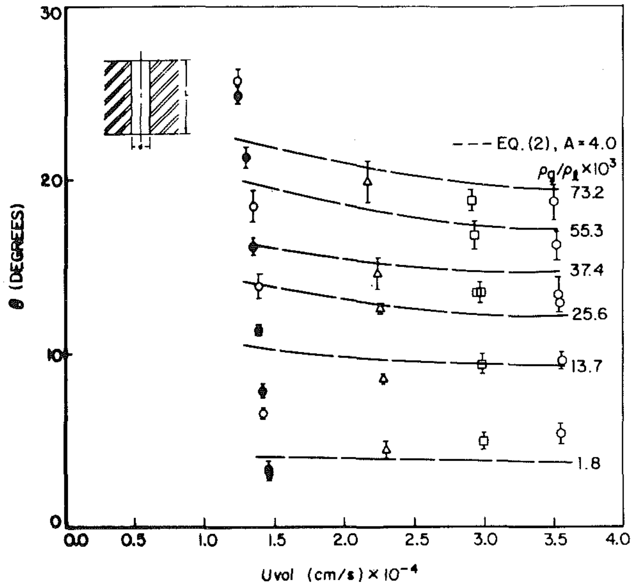

Fig. 10 Spray angle versus injection velocity for different density ratios: test liquid: n-hexane; nozzle: II(*b*); ○: $P_l = 15.3$ MPa, before $P_l = 91.8$ MPa tests; ●: $P_l = 15.3$ MPa, after $P_l = 91.8$ MPa tests; △: $P_l = 38.0$ MPa; □: $P_l = 64.9$ MPa; ⬡: $P_l = 91.8$ MPa.

instantaneous nozzle upstream and downstream conditions during injection. This use of steady data in an unsteady application is acceptable because the residence time of the liquid within the nozzle generally is less than 10^{-5} s, the initial breakup near the exit of the nozzle occurs in about 10^{-6} s, and the characteristic time for change of conditions in diesel injections is no less than 10^{-4} s [2].

The same data can also provide insight into the mechanism of disruption of the outer surface of the jet. However, this is a difficult step that requires assumptions that appear reasonable but cannot be fully supported. The first of such assumptions is that the larger the initial angle of the spray the more unstable is the outer surface of the jet. The statement is true in the limit, in that a jet that exhibits zero angle near the nozzle is stable there.

With the above assumption, in earlier work, it was concluded that each of many proposed mechanisms of breakup cannot explain the measured trends alone: if aerodynamic surface wave growth were the only mechanism, the spray angle should have been independent of nozzle geometry; if pipe turbulence were the only mechanism, jets from fully developed pipe flows should have been more unstable; if the rearrangement of the cross-section axial velocity profile of the jet were the only mechanism, then jets with laminar cores should have been more unstable; if upstream pressure oscillations were the only mechanism, then our jets should have been stable since the upstream pressure was constant in our experiments; and if wall boundary layer exit velocity profile relaxation effects were the only mechanism, then the breakup should have been independent of the gas density.

The data presented in this article further rule out cavitation as the only mechanism of breakup: if cavitation were the only agency of breakup, then nozzles VI and VII should have yielded intact jets since the flow within them was free of cavitation.

The fact that the spray angle was rather insensitive to the injection velocity is additional evidence that the disruption of the wall boundary layers at the nozzle exit is not a major factor in the atomization process. In a tubulent boundary layer, the wall stress increases roughly as the square of the flow stream velocity or, in our case, proportionally to Δp, which was varied by a factor of 9.4 (Fig. 7) with only minor effects on the spray angle. Similarly the rounding of the exit edge had no effect on the spray angle even though it is likely to have altered the rate of readjustment of the wall boundary layers.

Finally, the new data lends additional support to the hypothesis that aerodynamic interaction at the liquid-gas interface is a major component, but not the only component, of the mechanism of atomization. Indeed, for a fixed nozzle geometry, the measured spray angle behaves as predicted assuming that the aerodynamic interaction is the only mechanism of breakup.

Taylor [8] studied the rate of growth of the perturbations of planar liquid surfaces induced by gases flowing over it. He considered the limit $\rho_g << \rho_l$ and included the effects of liquid viscosity and surface tension. Ranz [9] applied Taylor's results to round jets for the limit case in which the wave length of the fastest growing perturbation is much smaller than the jet diameter, and obtained the following expression for the spray angle

$$\tan\frac{\theta}{2} = \frac{1}{A}4\pi\left(\frac{\rho_g}{\rho_l}\right)^{1/2} f\left[\frac{\rho_l}{\rho_g}\left(\frac{\mathrm{Re}_l}{\mathrm{We}_l}\right)^2\right] \qquad (2)$$

where A is a constant not determined by the linear stability analysis and f tends to $\sqrt{3}/6$ when its argument is greater than unity [9]. At this limit equation (2) reduces to equation (1).

For the data of Fig. 7, the argument of f is no smaller than 0.4 so that the spray angle should be a function mostly of the density ratio. This is seen to be the case, for a given nozzle geometry for all tested density ratios. Equations (1) and (2) reproduce the data also for different nozzle geometries provided that the constant A is given different values for different geometries. No element of the nozzle geometry enters the aerodynamic theory of Taylor and Ranz, and therefore such theory alone does not explain the process completely. The theory must be "supplemented" with a mechanism by which the nozzle geometry influences the breakup process. Such a mechanism has not yet been identified so that for the time being A must be considered an empirical constant.

Actually, there are hints that even the supplemented aerodynamic theory of atomization complies only with the most pronounced, and practically important, of the measured trends. Thus it would predict that the spray angle decreases monotonically with increasing jet velocity, tending to be independent of it in the limit:

$$\frac{\rho_l}{\rho_g}\left(\frac{\mathrm{Re}_l}{\mathrm{We}_l}\right)^2 >> 1.$$

Figure 10 shows that the measurements follow the predicted trend at sufficiently high density ratios but exhibit a mild opposite trend at lower density ratios. In fact, from Fig. 7 it can be seen that equation (2), which is the complete equation obtained from the theory, does not represent the measured trends as well as equation (1) which is an approximation to the complete equation and therefore would be expected to be less accurate.

In summary, the physical picture of atomizing jets that has emerged from this and earlier work can be stated briefly as follows. The surface of the liquid emerges from the nozzle already perturbed by events that occur within the nozzle itself and are affected by its geometry. The perturbations are selectively and rapidly amplified by the aerodynamic interaction with the gas until the outer surface of the jet breaks up into drops. The size of the drops and the intact length of the surface are much smaller than the jet diameter. The depth from the surface of the jet to which the above drop formation mechanism could possibly apply is not known. But the core eventually breaks up too since only isolated drops are found far downstream.

Progress has recently been made in computing the propagation of sprays from given nozzle exit conditions accounting also for such difficult processes as drop collisions and coalescence and the influence of drop proximity on drop drag and vaporization [10]. But the initial spray conditions that are established by the breakup process, for the most part, continue to be quantitatively unknown.

Acknowledgments

We wish to thank Mr. E. L. Griffith and Mr. J. H. Semler for their assistance in the design and the construction of the experimental apparatus.

This work was supported by the Army Research Office under Contract DAAG29-78-G-0132.

References

1. Reitz, R. D., and Bracco, F. V., "Mechanism of Atomization of a Liquid Jet," *Physics of Fluids*, Vol. 25, No. 10, Oct. 1982, p. 1730.
2. Reitz, R. D., and Bracco, F. V., "Ultra-High-Speed Filming of Atomizing Jets," *Physics of Fluids*, Vol. 22, No. 6, June 1979, p. 1054.
3. Reitz, R. D., and Bracco, F. V., "On the Dependence of Spray Angle and Other Spray Parameters on Nozzle Design and Operating Conditions," SAE Paper No. 790494, 1979.
4. Su, C. C., "Atomization of Round Liquid Jets," M.S. thesis, No. 1502-T, Dept. of Mechanical and Aerospace Engineering, Princeton Univ., 1980.
5. Thompson, P. A., *Compressible Fluid Dynamics*, McGraw-Hill, N.Y., 1972.
6. Weast, R. C., Ed., *Handbook of Chemistry and Physics*, 58th ed, CRC Press, Cleveland, OH, 1977.
7. Hiroyasu, H., Shimizu, M., and Arai, M., "The Breakup of High Speed Jet in a High Pressure Gaseous Atmosphere," ICLASS-82, Madison, Wis., June 1982.
8. Taylor, G. I., "Generation of Ripples by Wind Blowing Over a Viscous Fluid," Collected works of G. I. Taylor, Vol. 3, 1940, p. 244.
9. Ranz, W. E., "Some Experiments on Orifice Sprays," *Canad. J. Chem. Engng.*, Vol. 36, 1958, p. 175.
10. O'Rourke, P. J., and Bracco, F. V., "Modeling of Drop Interactions in Thick Sprays and Comparison with Experiments," *Proceeding of the Stratified Charge Automative Engines Conference*, The Institution of Mechanical Engineers, London, England, Publication 085298-469, Nov. 1980.

trend at sufficiently high density ratios but exhibit a mild opposite trend at lower density ratios. In fact, from Fig. 7 it can be seen that equation (2), which is the complete equation obtained from the theory, does not represent the measured trends as well as equation (1) which is an approximation to the complete equation and therefore would be expected to be less accurate.

In summary, the physical picture of atomizing jets that has emerged from this and earlier work can be stated briefly as follows. The surface of the liquid emerges from the nozzle already perturbed by events that occur within the nozzle itself and are affected by its geometry. The perturbations are selectively and rapidly amplified by the aerodynamic interaction with the gas until the outer surface of the jet breaks up into drops. The size of the drops and the intact length of the surface are much smaller than the jet diameter. The depth from the surface of the jet to which the above drop formation mechanism could possibly apply is not known. But the core eventually breaks up too since only isolated drops are found far downstream.

Progress has recently been made in computing the propagation of sprays from given nozzle exit conditions accounting also for such difficult processes as drop collisions and coalescence and the influence of drop proximity on drop drag and vaporization [10]. But the initial spray conditions that are established by the breakup process, for the most part, continue to be quantitatively unknown.

Acknowledgments

We wish to thank Mr. E. L. Griffith and Mr. J. H. Semler for their assistance in the design and the construction of the experimental apparatus.

This work was supported by the Army Research Office under Contract DAAG29-78-G-0132.

References

1. Reitz, R. D., and Bracco, F. V., "Mechanism of Atomization of a Liquid Jet," *Physics of Fluids*, Vol. 25, No. 10, Oct. 1982, p. 1730.
2. Reitz, R. D., and Bracco, F. V., "Ultra-High-Speed Filming of Atomizing Jets," *Physics of Fluids*, Vol. 22, No. 6, June 1979, p. 1054.
3. Reitz, R. D., and Bracco, F. V., "On the Dependence of Spray Angle and Other Spray Parameters on Nozzle Design and Operating Conditions," SAE Paper No. 790494, 1979.
4. Su, C. C., "Atomization of Round Liquid Jets," M.S. thesis, No. 1502-T, Dept. of Mechanical and Aerospace Engineering, Princeton Univ., 1980.
5. Thompson, P. A., *Compressible Fluid Dynamics*, McGraw-Hill, N.Y., 1972.
6. Weast, R. C., Ed., *Handbook of Chemistry and Physics*, 58th ed, CRC Press, Cleveland, OH, 1977.
7. Hiroyasu, H., Shimizu, M., and Arai, M., "The Breakup of High Speed Jet in a High Pressure Gaseous Atmosphere," ICLASS-82, Madison, Wis., June 1982.
8. Taylor, G. I., "Generation of Ripples by Wind Blowing Over a Viscous Fluid," Collected works of G. I. Taylor, Vol. 3, 1940, p. 244.
9. Ranz, W. E., "Some Experiments on Orifice Sprays," *Canad. J. Chem. Engng.*, Vol. 36, 1958, p. 175.
10. O'Rourke, P. J., and Bracco, F. V., "Modeling of Drop Interactions in Thick Sprays and Comparison with Experiments," *Proceeding of the Stratified Charge Automative Engines Conference*, The Institution of Mechanical Engineers, London, England, Publication 085298-469, Nov. 1980.

DISCUSSION

C. Sorusbay[1] and H. Binark[1]

Although atomization of liquid jets has received a considerable interest over many years, there are still some aspects which influence the atomization process that has not yet gained certainty. In this study the authors present valuable new data for the understanding of the mechanism of atomization which has been examined in view of the factors that effect the spray angle in liquid jets.

A previously obtained equation by the authors for spray angle, which is mainly based on the theory of Ranz [9], has been tested over a range of dynamic and thermodynamic states of liquid and gas and also for different nozzle geometries. Nozzle geometry has not been considered in the theory of Ranz and unfortunately it has not been included in the given expression, although it has been found to influence the initial spray angle strongly. Only adjustments are made for nozzle geometry by introducing empirical constants for different L/d ratios.

Nozzle dimension has been considered in the prediction of spray angle by Sitkei [11] where

$$\theta = 3.10^{-2} \left(\frac{L}{d}\right)^{-0.3} \left(\frac{\rho_l}{\rho_g}\right)^{-0.1} \mathrm{Re}_l^{\,0.7}$$

expressed in the notation of the present study. Here, the injection velocity seems to affect the angle of spray in an opposite manner than the results of Ranz and the present study. Also, the contradictions of Schweitzer's data [12] to the theory of Ranz has been reported previously by Ranz.

In view of the contradictions and shortcomings of the present theory, further investigations on parameters effecting the initial spray angle are required in future to be able to provide generalized expressions more accurately and discussions on these aspects from the authors would make further contributions to the present literature.

Additional References

11 Sitkei, G., *Kraftstoffaubereitung und Verbrennung bei Dieselmotoren*, Springer Verlag, 1964.
12 De Juhasz, K. J., et al., Bulletin No. 40, Eng. Exp. Stat., Pennsylvania State Col., 1932.

Authors' Closure

In Fig. 9 we give the spray angle, measured in the immediate vicinity of the nozzle exit, versus the nozzle length-to-diameter ratio. If we curve-fitted those data and included the curve fit in equation (1), we would have an equation that accounts also for the nozzle L/d. But we prefer not to do so. For applications, most people can read data off charts just as easily as they can program simple equations.

From the point of view of the fundamentals, we intend to underscore that for a fixed nozzle geometry the interpretation of the Taylor-Ranz theory seems to be reasonable but that there is no understanding at present of how the geometry of the nozzle changes the outcome of the gas-liquid interaction.

We tend to believe that the contradictions that may exist among available curve fits are due to different authors taking data in different regimes,[2] or using different techniques, e.g., steady pressure versus engine fuel pumps, or measuring the spray angle at different axial locations (irrespective of their initial values, all angles tend to the same value at sufficient distance from the nozzle), or to combinations of those factors.

---

[1] Technical University of Istanbul, Department of Mechanical Engineering, Gumussuya, Istanbul, Turkey.

[2] Reitz and Bracco, *Physics of Fluids*, Vol. 25, Oct. 1982, p. 1730.

A Theory of the Wilson Line for Steam at Low Pressures

R. A. Dobbins
Professor of Engineering,
Division of Engineering,
Brown University,
Providence, R.I. 02912
Mem. ASME

An algebraic method for determining the onset of condensation – the position of the Wilson line on a Mollier diagram – in steam at low pressures is presented. The method is based on the assumptions that the exponent of the nucleation rate expression is large and that the nucleation pulse duration is small. Under these conditions the growth integrals can be evaluated for specific rate expressions for the formation of stable droplets and their subsequent growth. The onset of condensation for a specified expansion rate is then determined by the solution to a system of algebraic equations. The method is illustrated using the classical nucleation rate and the droplet growth rate expression of Gyarmathy. The analytical solution agrees well with a published exact numerical solution by Gyarmathy. An extensive comparison of the predictions of the present method with the experimental results of Yellot (1933), Gyarmathy and Meyer (1965), Barschdorff (1965), and Moses and Stein (1978) is presented. The favorable comparison suggests that the method provides an efficient means for predicting the onset of condensation for various initial states and various expansion rates. The predictions of the theory on the role of the expansion rate, the initial stagnation conditions, and the history of the expansion are discussed.

Introduction

The point of occurrence of the condensation of supersaturated steam in turbines has been described for many years in terms of the Wilson line on the Mollier diagram whose earliest origin was essentially empirical. In recent years the existence of a high degree of supersaturation has been seriously challenged by a number of important studies conducted on operating turbines in various locations. These recent studies require a re-examination of the process of condensation in turbines and its relationship to laboratory studies conducted in converging-diverging nozzles. In spite of these developments, an understanding of the significance of the Wilson line will prove to be important to the understanding of the actual condensation processes that occur in operating turbines, in converging-diverging nozzles, and in a variety of flow devices in which an expansion process results in the buildup of supersaturation and the sudden development of condensation.

The occurrence of condensation in an expanding vapor was first calculated by Oswatitsch [1] who devised the formulation that has been widely used since that time. See, for example, Gyarmathy and Meyer [2], Hill [3], Wegener [4], Barschdorff [5], and Gyarmathy [6, 7]. The method of Oswatitsch involves solving by numerical means a system of differential and integral equations that describe the flow of the condensing vapor through a specified nozzle geometry.

An advantage of numerical solutions is their readiness to accept a large amount of detail such as the variation of properties with temperature. Regrettably our lack of knowledge of many details of the rates of nucleation and growth of clusters does not appear to justify this amount of detail at this time. A more serious disadvantage to numerical analyses is their well-known inability to provide an understanding into the dominant physical effects when many interacting phenomena are present. The present study seeks a more global view of the events which make up the early stage of the condensation process where nucleation and droplet growth are the dominant effects. Ultimately it would appear that the two procedures – the numerical method of Oswatitsch and the method described herein – have the potential of supplementing one another in important ways.

I Rate Relationships in Flows With Condensation

Early investigations of the onset of condensation appear to attribute a purely thermodynamic character to the formation of the liquid phase at elevated supersaturations. Yellot [8], showed that condensation could be represented as occurring along a line corresponding to a constant wetness fraction on the enthalpy-entropy diagram displaying the properties of steam in thermodynamic equilibrium. This concept was considerably improved when Gyarmathy and Meyer [2] showed unambiguously that the position of this line – the Wilson line – was a function of the expansion rate that is defined by

$$\dot{P} = -\frac{1}{p}\frac{dp}{dt} \tag{1}$$

and which is externally imposed by the nozzle geometry. It is understood that dp/dt in the above definition is the Eulerian

---

Contributed by the Fluids Engineering Division and presented at the Winter Annual Meeting, Washington, D.C., November 15–20, 1981, of THE AMERICAN SOCIETY OF MECHANICAL ENGINEERS. Manuscript received by the Fluids Engineering Division, June 29, 1982.

derivative equal to $u\,dp/dx$ in the case of a steady flow that is of interest in the nozzle geometry. The time derivative will prove more appropriate in applying our results to a wide variety of nozzle geometry and length scales.

The initial superheated state of the vapor will be specified by the stagnation conditions p_{01} and T_{01} (see Fig. 1). The expansion process will be assumed to be lossless and therefore will take place at constant entropy to a state on the vapor saturation line designated by p_2 and T_2. We assume the vapor to be in thermodynamic equilibrium prior to arrival at state 2 when metastable equilibrium develops in which condensation is delayed but vapor-phase internal degrees of freedom remain in equilibrium. Time $t=0$ will be chosen upon passage through state 2 when the supersaturation ratio first begins to exceed unity. We assume that the density of the vapor is low enough so that the vapor is thermally perfect,

$$p=\rho RT \tag{2}$$

Caloric imperfection will be included by allowing for the known temperature variation of the specific heat at constant pressure. The details of the treatment of the temperature dependence of various properties are given in Appendix A.

Following the recommendations of Hill [3], Barschdorff [5], Gyarmathy [6, 7], and Moses and Stein [9], we will use the classical nucleation rate. In the Volmer-Frenkel form this rate is expressed as

$$I=A\exp(-B\eta) \tag{3}$$

where

$$\eta=\frac{1}{T^3\ln^2 S} \tag{4}$$

$$A=\frac{\rho}{\rho_l}\sqrt{\frac{2\sigma}{\pi m_v^3}} \tag{5}$$

and

$$B=\frac{16\pi\sigma^3}{k(\rho_l R)^2} \tag{6}$$

Notwithstanding the widely acknowledged criticism of classical theory, see for example Springer [10], it is currently considered the most appropriate of the various theoretical expressions to describe the condensation of water vapor.

The variation of the vapor pressure will be represented by a polynomial of the form

$$\ln p_s=A_0-\frac{A_1}{T}-\frac{A_2}{T^2} \tag{7}$$

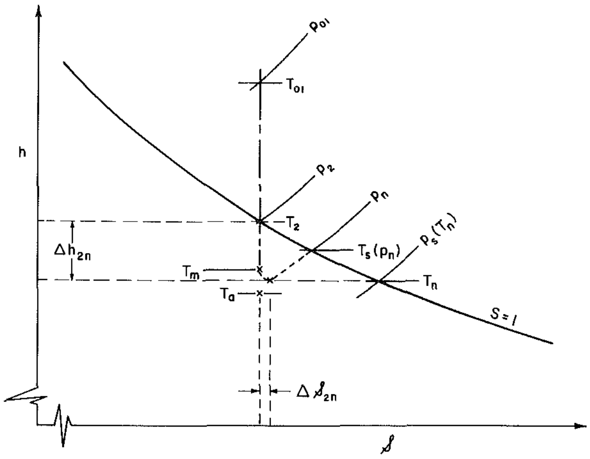

Fig. 1 The Mollier diagram for the onset of condensation in a vapor at low pressure (schematic)

Accordingly the quantity $\ln S$ where S is the supersaturation ratio is given by

$$\ln S=\ln p-A_0+\frac{A_1}{T}+\frac{A_2}{T^2} \tag{8}$$

During an expansion process below the vapor saturation line the value of S builds up counteracting the decreasing temperature until the nucleation rate given by equations (3) and (4), becomes significant.

The rate of growth of droplets is the remaining pertinent rate expression. We use the general growth rate by Gyarmathy [7] as a point of departure,

$$\frac{dr}{dt}=\frac{\lambda_g\Delta T}{\rho_l L}\,\frac{1-\dfrac{r_*}{r}}{1+1.59\dfrac{\bar{\lambda}}{r}} \tag{9}$$

where the subcooling ΔT is defined by

$$\Delta T=T_s(P)-T$$

The retarding influence of the r_*/r term in equation (9) is confined to the very early history of droplet growth and can be ignored when the droplet size is large compared with r_*. Furthermore, the growth period presently of interest is such that $r<<\bar{\lambda}$ and the expression for dr/dt becomes independent

Nomenclature

A = pre-exponential factor of the nucleation rate defined by (5) ($\mathrm{kg}^{-1}-\mathrm{s}^{-1}$)
$A_c(x)$ = area of nozzle as a function of axial position x(m^2)
a_{th} = thermal accommodation coefficient
B = constant defined by (6) which appears in the nucleation rate exponent
c_g = droplet growth rate constant given by (11) (m/s)
$c_n(t_n)$ = number of particles per unit volume at time t_n(m^{-3})
c_p = specific heat at constant pressure (J/kg-K)
$D_{32}(t_n)$ = volume surface mean diameter (μm)
I = gravimetric nucleation rate or number of particles formed per unit mass of vapor per unit time ($\mathrm{kg}^{-1}-\mathrm{s}^{-1}$)
k = Boltzmann constant (J/K)
J = volumetric nucleation rate or number of particles formed per unit volume per unit time ($\mathrm{m}^{-3}-\mathrm{s}^{-1}$)
L = latent heat of vaporization (J/kg)
$m(x_1,x)$ = the mass of particles at position x which were nucleated upstream at position x_1 (kg)
$\dot{m}$ = mass flow rate of vapor and condensate (kg/s)
M_a = Mach number at state a if metastable equilibrium were to persist until time t_n
m_v = mass of vapor molecule (kg)
p = pressure (kPa)
$\dot{P}$ = expansion rate (s^{-1})
Pr = Prandtl number of vapor
$p_s(T)$ = saturation pressure corresponding to temperature T(kPa)
r = Droplet radius (μm)
$r(t_n,t_1)$ = radius of droplet nucleated at time t_1 at present time t_n (μm)
r_* = critical size droplet (μm)

of r. Kinetic theory provides a relationship between the absolute viscosity μ and the molecular mean free path $\bar{\lambda}$,

$$\mu = \frac{2p\bar{\lambda}}{3\sqrt{RT}} \tag{10}$$

Combining (9) and (10), we find for $r_* << r << \bar{\lambda}$,

$$\frac{dr}{dt} = c_g = \frac{\rho c_p \Delta T}{2.4\rho_l L Pr}\sqrt{RT} \tag{11}$$

The nucleation and growth rates which we use are those that are favored by experimental studies in recent years but clearly much detailed physics remains to be clarified. We consider the recommended rate expressions to be tentative in nature and use them by way of illustration. The more important conclusions of the present study are not dependent upon the specific rate expressions which are employed.

II The Dynamics of the Nucleation Process

The collapse of metastable equilibrium can be envisioned schematically by referring to Fig. 2. Following Gyarmathy [7] we define the "onset of condensation" to be the moment t_n at which the nucleation rate is a maximum. This moment will correspond to the minimum value of $B\eta$ which will occur when the time derivative of η is zero, $\eta_n' = 0$. The temperature decreases from the value T_2 at $t=0$ and would reach a value T_a if metastable equilibrium persisted until time t_n. The vapor at state T_a would have the same value of entropy as states 01 and 2 as shown in Fig. 1. However, the growth of droplets formed at earlier times releases significant latent heat to cause a perceptable departure from isentropic behavior at time t_m when the temperature is T_m. The temperature will continue to decrease from T_m to some minimum value slightly later than t_n. The temperature T_n and the pressure p_n define the location of the onset of condensation and the Wilson point. The nucleation rate is finite but small when the vapor saturation line is first traversed but increases at a catastrophic rate near $t=t_n$ when the heat released by droplets formed at $t<t_n$ is sufficient to retard the further buildup of supersaturation. The effect of the heat release is to quench the nucleation rate which reaches its maximum value at $t=t_n$. The duration of the nucleation pulse, i.e., its half width when $I=e^{-1}I_n$, is given the symbol α.

In this work we will assume that (*a*) the value of $B\eta_n >> 1$, (*b*) the value of $\alpha << t_n$ from which it follows that $\dot{P}\alpha << 1$, and (*c*) the droplet size at time t_n, which is approximately given by αc_{gn} is such that $(r_* << \alpha c_{gn} << \bar{\lambda})$. The degree to which these approximations are fulfilled is discussed below.

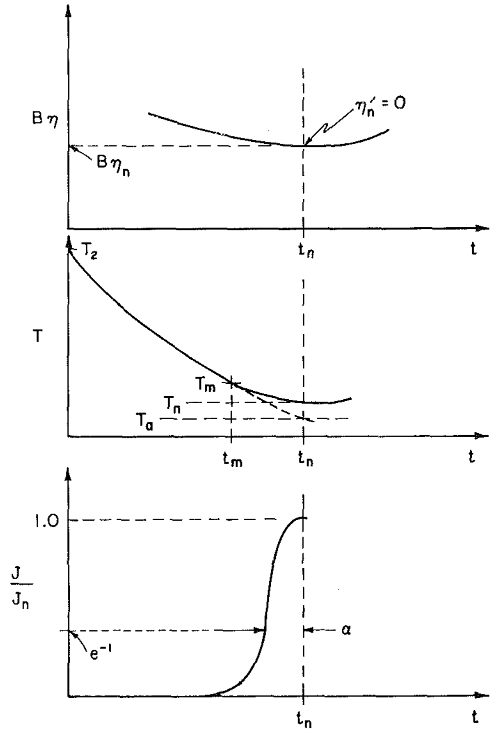

Fig. 2 Schematic curves of $B\eta$, T, and J/J_n versus t during the buildup of nucleation

III The Nucleation-Growth Integrals

The nucleation-growth integral originally formulated by Oswatitsch [1] for a steady one dimensional flow was expressed as

$$Y\dot{m} = \int_{-\infty}^{x} m(x_1, x) J(x_1) A_c(x_1) dx_1 \tag{12}$$

where $Y\dot{m}$ (the wetness fraction times the total mass flow) is the mass flow rate of the condensed phase, $J/x_1)$ the number of particles formed per unit volume per unit time, $A_c(x_1)\, dx_1$ is the local volume element, and $m(x_1, x)$ is the mass of the droplet located at the position x that was created earlier at the upstream position x_1. The total condensed phase mass flow is obtained by integrating over distance from x_1 where

Nomenclature (cont.)

R = gas constant for water vapor (J/kg-K)
S = supersaturation ratio equal to the pressure of the vapor divided by saturation pressure corresponding to vapor temperature
$\mathcal{S}$ = specific entropy (J/kg-K)
t = time (s)
T = vapor phase temperature (K)
T_c = critical temperature (K)
u = velocity (m/s)
x = nozzle axial position (m)
Y_n = wetness fraction or condensate mass fraction
α = nucleation pulse duration (s^{-1})
ΔT = subcooling equal to the saturation temperature corresponding to a given pressure minus the actual temperature (K)
$\Delta\mathcal{S}_{2n}$ = the specific entropy difference between states 2 and n (J/kg-K)
Δh_{2n} = specific enthaply difference between states 2 and n (J/kg)
γ = ratio of specific heat at constant pressure to specific heat at constant volume evaluated at T_a
$\bar{\lambda}$ = vapor molecule mean free path (μm)
λ_g = thermal conductivity of vapor (W/m-K)
μ = absolute viscosity of vapor (kg/m-s).
ρ = vapor density (kg/m^3)
ρ_l = condensate density (kg/m^3)
σ = surface tension for a flat surface (N/m)
$\Phi(D,t_n)$ = particle size distribution function at time t_n (μm^{-1})

Subscripts

$a,m,n,2,01$ = refer to quantities evaluated at thermodynamic states designated by these subscripts
m,n = refer to times t_m,t_n

nucleation occurs to x. Dividing the above integral by $\dot{m} = \rho u A_c$, we convert the volumetric nucleation rate J into a gravimetric nucleation rate, $I = J/\rho$, and convert the spatial coordinate to time $dt_1 = dx_1/u$. Specializing the time of interest to be the moment of maximum nucleation rate t_n, we find the wetness fraction at this moment to be

$$Y_n = \frac{4\pi}{3} \rho_l \int_0^{t_n} r^3(t_1, t_n) I(t_1) dt_1 \tag{13}$$

The rate of change of wetness fraction at the moment of maximum nucleation rate is the time derivative of the above expression. The result is

$$Y_n' = 4\pi\rho_l \int_0^{t_n} r^2(t_1, t_n) I(t_1) \frac{\partial r}{\partial t_1} dt_1 + \frac{4\pi}{3} \rho_l I(t_n) r_*^3 \tag{14}$$

In evaluating the integrals (13), (14) the rescaled upper limit has been set equal to infinity since $t_n >> \alpha$. This inequality implies that the droplets grow under essentially constant ambient conditions and their radius is given by

$$r(t_1, t_n) = r_* + c_{gn}(t_n - t_1) \tag{15}$$

where c_{gn} is given by equation (11) with all properties evaluated at $t = t_n$. The quantity r_* is the critical radius of the water cluster.

$$r_* = \frac{2\sigma}{\rho_l R T \ln S} \tag{16}$$

Secondly, the statement that $B\eta_n >> 1$ enables us to use the method of Laplace in evaluating the above integrals. According to this procedure the exponent of the nucleation rate is expressed as

$$B\eta = B\eta_n + B\eta_n'' \frac{(t - t_n)^2}{2} \tag{17}$$

since $\eta_n' = 0$ at $t = t_n$. Taking advantage of (15) and (17) we find, by evaluating the integrals (13) and (14)

$$Y_n = \frac{2\pi}{3} \rho_l I_n \alpha (c_{gn}\alpha)^3 [1 + g_1(\zeta)] \tag{18}$$

and

$$Y_n' = \pi^{3/2} \rho_l I_n (c_{gn}\alpha)^3 [1 + g_2(\zeta)] \tag{19}$$

where

$$g_1(\zeta) = \frac{3\sqrt{\pi}}{2} \zeta + 3\zeta^2 + \sqrt{\pi}\, \zeta^3 \tag{20}$$

$$g_2(\zeta) = \frac{4}{\sqrt{\pi}} \zeta + 2\zeta^2 + \frac{4}{3\sqrt{\pi}} \zeta^3 \tag{21}$$

and

$$\zeta = r_*/c_{gn}\alpha \tag{22}$$

Furthermore, under these circumstances the nucleation rate for $t < t_n$ is a half Gaussian curve whose $1/e$ half-width, found by integrating (3) over time using (17), is given by

$$\alpha = (2/B\eta_n'')^{1/2} \tag{23}$$

The condition for $J = J_n$ is $\eta_n' = 0$ and consequently from (4) and (8), we find the value of dT/dt at $t = t_n$ to be given by

$$T_n' = -\frac{2\, T_n}{\omega \ln S_n} f_p \dot{P} \tag{24}$$

where

$$\omega = \frac{2A_1}{T_n \ln S_n} + \frac{4A_2}{T_n^2 \ln S_n} - 3 \tag{25}$$

and $f_p \dot{P}$ represents $-(1/p)\,(dp/dt)$ evaluated at t_n. For the moment the value of f_p is unknown. We also require the value of η_n'' which is found by again using equations (4) and (8). Neglecting higher order derivatives of p, we find, after considerable manipulation.

$$\eta_n'' = \frac{\eta_n}{T_n} \omega T_n'' - \frac{2\eta_n}{\ln^2 S_n} (1 - \xi) f_p^2 \dot{P}^2 \tag{26}$$

where

$$\xi = \frac{1}{\omega^2} \left[(\omega - 3)^2 + \frac{4A_1}{T_n \ln S_n} - 12 \right] \tag{27}$$

The onset of condensation can be defined by the above equations in terms of the values of p_n, T_n, that must match the stagnation conditions.

IV Rayleigh Line Relationships

The departure of the temperature from its isentropic value results from the release of latent heat during the collapse of metastable equilibrium. The states defined by p_a, T_a, and p_n, T_n differ from one another by the release of latent heat in the amount of LY_n per unit mass and these states thus lie on a common Rayleigh line. The latter is the locus of states satisfying the continuity and momentum equations which are related by variable increments of heat addition. The usual results for the Rayleigh line can be simplified because $T_n - T_a << T_n$, etc. and we find that states n and a are related by

$$T_n = T_a \left(1 + \frac{\gamma M_a^2 - 1}{M_a^2 - 1} \frac{LY_n}{c_{pa} T_a} \right) \tag{28}$$

and

$$P_n = P_a \left(1 + \frac{\gamma M_a^2}{M_a^2 - 1} \frac{LY_n}{c_{pa}\, T_a} \right) \tag{29}$$

where

$$M_a^2 = \frac{2}{\gamma R T_a} \int_{T_a}^{T_{01}} c_p(T)\, dT \tag{30}$$

Since states a and 01 are isentropically related, it follows that

$$\frac{P_a}{P_{01}} = \exp\left[-\frac{1}{R} \int_{T_a}^{T_{01}} \frac{c_T(T)\, dT}{T} \right] \tag{31}$$

With the above expressions, (28) and (29), the entropy increase associated with the passage from state n to a is readily found to be

$$\mathcal{S}_n - \mathcal{S}_a = \frac{LY_n}{T_a} \tag{32}$$

Equation (28) relates the amount of heat released to the temperatures T_a and T_n at $t = t_n$. A second condition that must be fulfilled at this moment relates to the derivative of temperature. By differentiating (28), we find the rate of change of wetness that is necessary to change dT/dt from its value at $t = t_m$ to its value T_n' at $t = t_n$. The result is

$$Y_n' = \frac{R T_a \dot{P} (M_a^2 - 1)(1 - \phi)}{L(\gamma M_a^2 - 1)} \tag{33}$$

where ϕ, which remains to be determined, is defined by

$$\phi = \frac{\kappa}{\gamma - 1} f_p \tag{34}$$

and

$$\kappa = \frac{2\gamma}{\omega \ln S_n} \tag{35}$$

By differentiating (29) we obtain

$$f_p = \frac{M_a^2 - 1}{(\gamma - \kappa) M_a^2 - 1} \tag{36}$$

Table 1 Comparison of two methods of solution for conditions at the Wilson point

T_{01} = 413.15 K $\quad$ P_{01} = 100 kPa $\quad$ $\dot{P}$ = 3000 s^{-1}

(c_p = 1880 J/kgK, A_0 = 24.22, A_1 = 4745.6, A_2 = 0)

	Numerical Solution (Gyarmathy [7])	Present Method
$\log_{10}[J_n(m^{-3}s^{-1})]$	22.2	22.01
p_n/p_{01}	0.28	0.281
ΔT_n(K)	37.0	36.75
u_n(m/s)	640	644

Table 2 Dependence of Wilson point on initial conditions

	$\dot{P}$ = 3000 S^{-1}		
(C_p = 1880 J/kg-K	A_0 = 24.22	A_1 = 4745.6	A_2 = 0)
P_{01}(kPa)	100	350	1000
T_{01}(K)	413.15	561.91	727.09
T_2(K)	356.65	356.65	356.65
M_a^2	2.253	5.281	8.638
$\log[J_n(m^{-3}s^{-1})]$	22.01	22.02	22.02
T_n(K)	302.77	302.73	302.72
S_n	5.455	5.461	5.462
p_n(kPa)	28.079	28.048	28.042
Δh_{2n}(kJ/kg)	101.3	101.4	101.4

The relations (33) through (36) are derived in detail in Appendix B.

Finally we relate T_n'' to T_n and T_a by expanding $T(t)$ in a Taylor series about t_n both along the adiabatic path from T_m to T_a and also along the diabatic path from T_m to T_n. Noting that T_m' is $\dot{P}T_m(\gamma-1)/\gamma$ at t_m where expansion remains momentarily isentropic, we find

$$T_n - T_a = \frac{\left[\dfrac{\gamma-1}{\gamma}\dot{P}T_m(1-\phi)\right]^2}{2T_n''} \tag{37}$$

The second derivative of temperature at t_n is found by solving (37) and eliminating $T_n - T_a$ using (28),

$$T_n'' = \frac{(M_a^2-1)}{c_{pa}LY_n(\gamma M_a^2-1)}[\dot{P}RT_m(1-\phi)]^2 \tag{38}$$

V The System of Equations and Their Solution

Equations (2), (3), (8), (11), (18), (19), (23), (26) (28), (29), (30), (31), (33), and (38) together with the definitions for A, $B, f_p, r_*, \omega, \xi, \phi, \eta$ constitute fourteen equations in as many primary unknowns; $p_n, T_n, \rho_n, S_n, T_a, p_a, M_a, I_n, \alpha, Y_n, Y_n'$, T_n'', c_{gn}, η_n''. In addition there are four temperature dependent properties σ, c_p, L, and μ. The nonequilibrium state n is defined most conveniently on a Mollier diagram in terms of state 2 using T_n, T_a, and Y_n in the relationships

$$\Delta h_{2n} = \int_{T_n}^{T_2} c_p(T)dT \tag{39}$$

and

$$\Delta S_{2n} = \frac{LY_n}{T_a} \tag{40}$$

States 2 and 01 are related by the isentropic relationship

$$\int_{T_2}^{T_{01}} \frac{c_p(T)}{T}dT = R\ln\frac{p_{01}}{p_2} \tag{41}$$

and the saturation line relationship for state 2

$$\ln p_2 = A_0 - \frac{A_1}{T_2} - \frac{A_2}{T_2^2} \tag{42}$$

The latter two transcendental relations for p_2, T_2 are readily solved by the Newton-Raphson method.

The solution of the above system of equations by an iterative technique to an accuracy in T_n of 10^{-3}K is described in Appendix C.

Table 1 provides a comparison of the present method of the determining the Wilson point with a graphical presentation of an exact numerical solution by Gyarmathy [7] for a nozzle geometry specified by the value of $\dot{P}$. A calorically perfect gas is assumed with Gyarmathy's values for the vapor pressure and specific heat data. It should be emphasized that the present method gives only the conditions at the Wilson point whereas Gyarmathy's implementation of the numerical method of Oswatitsch provides the more complete history of the growth of condensation. In Table 1 we compare those quantities which can be read with reasonable accuracy from the graphical presentation [7]. The comparison shows good agreement between the exact numerical method and the algebraic solution for the case of $\dot{P}$ = 3000 s^{-1}. Thus we find that a model that assumes the droplets to grow at constant ambient conditions gives adequate agreement with an exact numerical solution that includes the influence of the time dependent ambient conditions on c_{gn}, r_*, and also includes the r_*/r term in the droplet growth equation.

The dependence of the Wilson point on the stagnation conditions is readily investigated by means of the algebraic formulation. We choose three disparate stagnation conditions which result in a transition of the vapor saturation curve at T_2 = 356.65 K. The properties at the Wilson point for the three initial states are shown in Table 2 where we find that J_n, T_n, p_n, S_n, and Δh_{2n} are essentially identical regardless of the large differences in kinetic energy at the moment of onset. The displacement along the Rayleigh line is small and identical for all three initial conditions. These calculations confirm the experimental finding of the early investigations; for a specified value of initial entropy, the history of the expansion prior to achievement of $S>1$ does not influence the thermodynamic conditions at the onset of condensation. Although the location of the Wilson point on the Mollier diagram is independent of the initial pressure for specified entropy, the character of the flow downstream is, of course, strongly influenced by the Mach number at the Wilson point [7].

Comparison With Experiments. A number of measurements of the onset of condensation at low pressures are available to provide a further test of the algebraic formulation for the Wilson line. The nozzle geometries used by the various investigators are summarized in Table 3 where we include the nozzle wall curvature and the range of p_n and $\dot{P}$ that result.

An early extensive set of measurements of he onset of condensation was conducted by Yellot in 1934 [8]. He used the visual detection of carbon arc light scattered from condensed particles to detect the onset of condensation. The experimental work went far beyond the theoretical understanding of that day when the importance of $\dot{P}$ as a controlling variable was not appreciated or reported. We have calculated $\dot{P}$ in Yellot's experiments from the geometry he

Table 3 Nozzle geometries used for determination of Wilson lines by various investigators

	Throat Area (mm^2)	Wall Curvature (mm)	P_n (kPa)	$\dot{P}$ (s^{-1})
Yellot (8;1934)	323	19.05	20-200	20,000 to 75,000 (See Note 2)
Gyarmathy & Meyer (6,7;ca 1970)	140 410 1400	(See Note 1)	10-200	1000 2900 8300
Barschdorff (1971) [Quoted by Gyarmathy (6,7;1976)]	323	584	20-80	2000 to 5000
Moses & Stein (9;1978)	100	686	2 to 20	10,500 to 12,000 (See Note 2)

1. Nozzle contour designed to produce a constant $\dot{P}$ throughout the diverging supersonic section.
2. These values are based on nozzle geometry and are uncorrected for boundary layer effects.

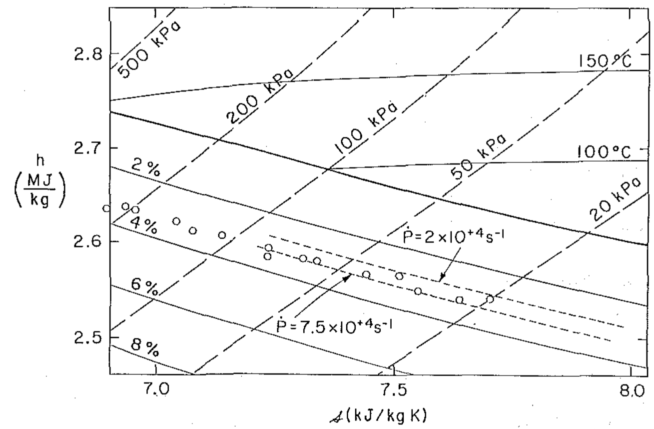

Fig. 3 A comparison of the Wilson lines predicted by the algebraic formulation with measured Wilson points by Yellot (1934). The heavy line is the vapor saturation line, short dashed line represents the Wilson lines for specified $\dot{P}$

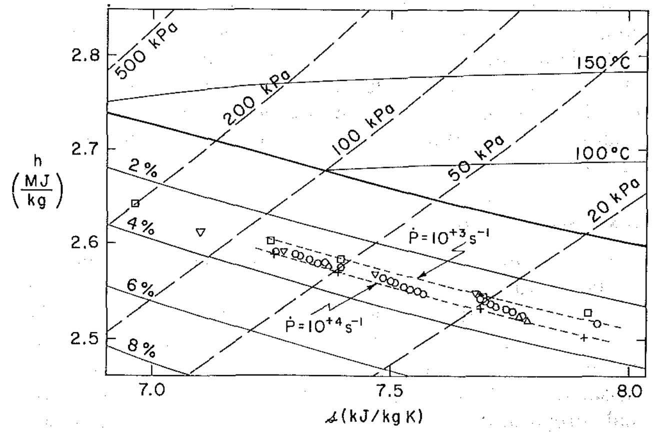

Fig. 4 A comparison of the Wilson line predicted by the algebraic formulation with the measured Wilson points from Gyarmathy and Meyer (ca. 1970) and Barschdorff (1971) as quoted by Gyarmathy (1976). The heavy line is the vapor saturation line, short dashed line represents the Wilson lines for specified $\dot{P}$.

used and find that it ranged from about 20,000 to 75,000 s^{-1} because of the high nozzle curvature. This estimate neglects the boundary layer influence on $\dot{P}$.

The experiments of Gyarmathy and Meyer [2] reported in 1965 employed three nozzles designed to produce $\dot{P}$ = constant throughout the supersonic portion. The values of $\dot{P}$ were measured and the influence of the viscous boundary layers was thereby included in the reported values given in Table 3. The onset of condensation was determined as the point where the pressure profile deviated from the adiabatic shape. The experiments were repeated in the early 1970's with improved instrumentation and these results were reported [6] and [7] with attribution to Gyarmathy and Meyer.

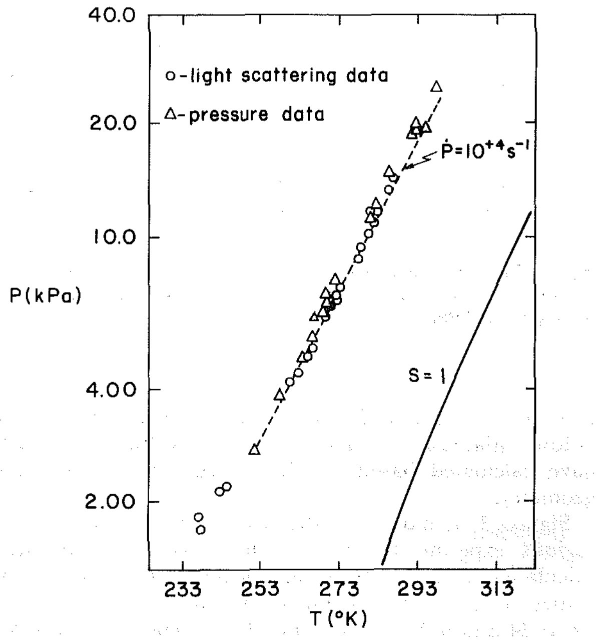

Fig. 5 A comparison of the curve of p_n versus T_n predicted the algebraic formulation with values measured by Moses and Stein (1978)

Barschdorff [5] conducted a set of experiments to test the ability of the classical nucleation rate to predict the profiles of temperature, pressure, density, etc. The onset of condensation was defined by examination of the pressure profile. Barschdorff's results are also given in [6] and [7] and the composite of his data and that of Gyarmathy and Meyer provides our best experimental knowledge of the Wilson zone in the range of expansion rate from 1000 to 8300 s^{-1} for $p_n \approx 10$ to 100 kPa.

Moses and Stein [9] in 1978 reported their observations of the onset of condensation in steam that were conducted for the purpose of comparing detection methods and also several methods of predicting the droplet growth rates. Their determination of onset was by the use of a sensitive detector of the light scattered by the growing droplets from a laser light source and also by the 1 percent deviation of the pressure

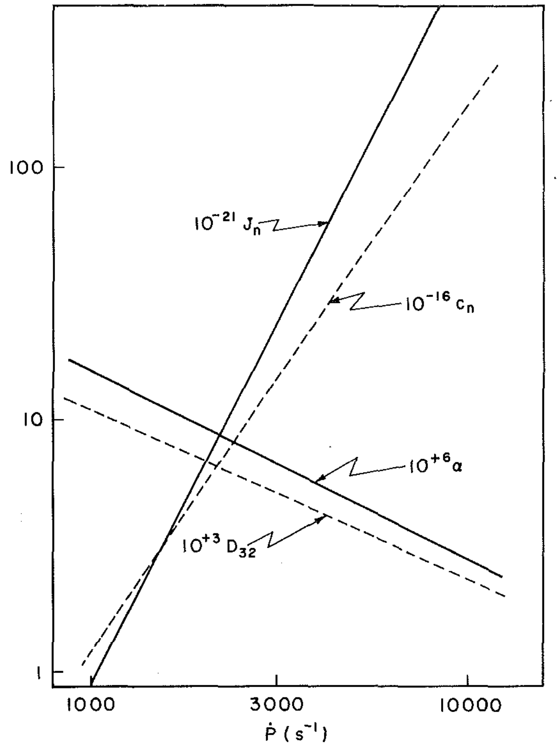

Fig. 6 The dynamics of the nucleation pulse as elucidated by the variation of J_n(m^{-3}s^{-1}), α(s), $c_n(t_n)$(m^{-3}) and $D_{32}(t_n)$ (μm) versus $\dot{P}$ for p_{01} = 120 kPa, T_{01} = 443.15°K

from its adiabatic value. Their measurements were conducted at low initial pressures and achieved the values of $\dot{P}$ which we have calculated based on their description of the nozzle geometry.

Figures 3, 4, and 5 show the measured Wilson points for the various experimental studies along with Wilson lines as calculated from the algebraic formulation of the specified values of $\dot{P}$. For all experiments the value of $B\eta$ ranged from 19 to 24 and $\alpha\dot{P}$ ranged from 0.01 to 0.06. In addition, the quantity $\zeta = r_*/c_{gn}\alpha << 1$ except for the case of a few runs at highest $\dot{P}$ and lowest p_n. With the latter exception noted, the inequalities required for the application of the algebraic method are well fulfilled. The agreement between the predicted Wilson zone and the measured Wilson points shown in Figs. 3-5 is favorable.

VIII The Dynamics of the Nucleation Pulse

The response of the nucleation process to variations in the expansion rate is illustrated in Fig. 6 which shows J_n and α versus $\dot{P}$ for given stagnation conditions. In Fig. 6 we find the peak nucleation rate ranges nearly 3 orders of magnitude in response to a 10 fold range while the nucleation pulse duration decreases by a factor of 5.6. The mean particle size is represented by the ratio of third-to-second moment of the particle size distribution function $\Phi(D,t)$,

$$D_{32} = \frac{\int_0^\infty \Phi(D,t)D^3 dD}{\int_0^\infty \Phi(D,t)D^2 dD} \qquad (43)$$

The distribution function is a semi-Gaussian curve at the Wilson point, and will develop rapidly into an asymmetric Gaussian curve as time proceeds. The value of $D_{32}(t_n)$ varies with $\dot{P}$ in a similar fashion to the nucleation pulse duration which constitutes the time period available for droplet growth. Finally, the particle number concentration at the moment of peak nucleation rate, in view of the previous results, is given by

$$c_n(t_n) = \int_0^{t_n} J(t)dt = \frac{\sqrt{\pi}}{2} J_n \alpha \qquad (44)$$

From Fig. 6 we see that $c_n(t_n)$ increases somewhat faster than $\dot{P}$ as a result of the respective variations of both J_n and α. The dependence of the mean particle diameter on the $\dot{P}$ has been the subject of discussion and experimental investigation in the past by Gyarmathy and Meyer [2], Petr [12], and Gyarmathy and Lesch [13]. The prediction of the present algebraic theory is in general agreement with the experimental observations quoted in [12] and [13]. The particle number concentration and mean size have an important bearing on the erosive power of the steam aerosol.

The behavior of the properties demonstrated by Fig. 6 allows the following interpretation of the dynamics of the nucleation pulse during the crucial interval in which J is building to its maximum value. As $\dot{P}$ increases, the supersaturation ratio assumes higher values and J_n increases dramatically. The larger concentration of droplets which results from the higher J_n causes a more rapid release of heat and thereby reduces the nucleation pulse duration. Mean particle size decreases in proportion to the decrease in nucleation pulse duration.

IX Summary

We have examined the dynamics of the nucleation pulse when $B\eta_n >> 1$ and $\alpha\dot{P} << 1$. These conditions are well fulfilled in typical nozzle experiments that have been designed to the condensation of steam in an expansion process. Using a purely algebraic formulation we find that for practical purposes the onset of condensation is (*a*) independent of the stagnation pressure for given value of stagnation entropy and (*b*) is controlled entirely by the local value of $\dot{P}$ that is determined by the local nozzle geometry. Thus the algebraic formulation is capable of defining the Wilson line for steam expansion processes of prescribed $\dot{P}$ without specifying a flow geometry or length scale. The agreement between the algebraic formulation and the corresponding exact numerical calculations is good. Nozzle experiments conducted by others also show agreement with the algebraic theory. The determination of the Wilson line for practical applications is greately facilitated by the method we have described.

Acknowledgments

The assistance of Mr. Axel zur Loye in checking algebraic results, in translating references, and in attending to various programming details is acknowledged with pleasure. The author is indebted to Professors E. A. Mason and J. Kestin of Brown University and Professor R. DiPippo of Southeastern Massachusetts University for valuable comments during the final preparation of the manuscript. This research was sponsored by the National Science Foundation under Grant CPE 26764.

References

1 Oswatitsch, K., "Kondensationserscheinungen in Überschalldüsen," *Z. Angew. Math. und Mech.*, Vol. 22, 1942, pp. 1-14.

2 Gyamathy, G., and Meyer, H., "Spontane Kondensation," VDI Forchungsheft 508, VDI Verlag, Dusseldorf, 1965.

3 Hill, P. G., "Condensation of Water Vapor During Supersonic Expansion in Nozzles," *J. Fluid Mechanics*, Vol. 25, 1966, pp. 593-620.

4 Wegener, P. P., "Gasdynamics of Expansion Flows With Condensation, and Homogeneous Nucleation of Water Vapor." Chapter 4 of *Nonequilibrium Flows*, Vol. 1, Part 1, P. P. Wegener, Editor, M. Dekker, New York, 1969.

5 Barschdorff, D., "Verlauf der Zustandsgrössen und gasdynamische Zusammehänge dei der spontanen Kondensation reinen Wasserdampfs in Lavaldüsen," *Forch. Ing. Wes.*, Vol. 37, 1971, pp. 146–157.

6 Gyarmathy, G., "Theorie de la Condensation en Cours de Detente dans les Turbines a Vapeur," *Rev. Franc. de Mech.*, Vol. 57, 1976, pp. 35–48.

7 Gyarmathy, G., "Condensation in Flowing Steam," Chapter 3 in *Two-Phase Steam Flow in Turbines and Separators*, M. J. Moore and C. H. Sieverding, Editors, Hemisphere Pub. Corp., 1976.

8 Yellot, J. J., "Superheated Steam," *Trans. ASME*, Vol. 56; 1934, pp. 411-430.

9 Moses, C. A., and Stein, G. D., "On the Growth of Steam Droplets Formed in a Laval Nozzle Using Both Static Pressure and Light Scattering Measurements," ASME JOURNAL OF FLUIDS ENGINEERING, Vol. 100, 1978, pp. 311-322.

10 Springer, G., "Homogeneous Nucleation," in *Advances in Heat Transfer*, Vol. 14, Academic Press, 1978, pp. 281-346.

11 Gyarmathy, G., "Zur Wachstumsgeshwindigkeit kleiner Flussigkeitstrophen in einer ubersättigten Atmosphare," *Z. ang. Math. Phys.*, Vol. 14, 1963, pp. 280-293.

12 Petr, V., "Measurement of An Average Size and Number of Droplets During Spontaneous Condensation of Supersaturated Steam," *Proc. Inst. Mech. Engrs.*, 1969-1970, Vol. 184, Part 3G (III), 1969, pp. 22-28.

13 Gyarmathy, G., and Lesch, F., "Fog Droplet Observations in Laval Nozzles and in an Experimental Turbine," *Proc. Inst. Mech. Engrs.*, 1969-1970, Vol. 184, Part 3G (III) 1969, pp. 29-36.

14 Schmidt, E., *Properties of Water and Steam in SI-Units*, Second Printing, Springer-Verlag, Berlin, 1979.

APPENDIX A

Representation of the Temperature Dependence of Vapor Properties

Properties excepting surface tension and vapor pressure are represented by interpolation formulae in the form of a power series in temperature which is expressed by

$$\mathcal{P}_j = \sum_{i=0}^{k} A_i^j T^i \tag{45}$$

where $\mathcal{P}_j$ refers to the property and A_i^j are the appropriate coefficients. The index $j = c$, l, and m, refer to c_p, L, and μ, respectively. The values of A_i^j (see Table IV) were obtained by fitting by the method of least squares six recognized values of each property [14] at equal temperature intervals in the range from 273 to 373 K.

Table 4 Values of temperature coefficients used for various properties

j	A_0^j	A_1^j	A_2^j	A_3^j
c	42.4594	19.7145	-0.073350	9.3201E-5
ℓ	3.03242E+6	-1586.45	1.31340	---
m	2.09434E-6	1.69259E-8	2.84996E-11	---

The surface tension was calculated from the currently recommended [14] interpolation equation

$$\sigma = c_1 \left(\frac{T_c - T}{T_c} \right)^{c_2} \left(1 + c_3 \frac{T_c - T}{T_c} \right) \tag{46}$$

where $c_1 = 0.2358$ N/m, $c_2 = 1.256$, $c_3 = -0.625$, and the critical temperature $T_c = 647.15$ K. Equation (46) gives σ within the tolerances of the IFC skeleton table.

The vapor pressure constants $A_0 = 23.24348$, $A_1 = 3757.869$, and $A_2 = 229{,}190.7$ were determined by a least squares fit for equation (7) using six IFC recommended values of vapor pressure [14] in the temperature range 273 to 373 K. These values were used in our calculations of the Wilson lines shown in Figs. 3-5. We used values of A_0, A_1, and A_2 shown in Tables 1 and 2 from [7] for the comparisons shown therein.

APPENDIX B

Derivation of Equations for Y_n' and fp From Rayleigh Line Relationships

The release of latent heat in the amount LY per unit mass of vapor causes a departure of temperature and pressure from their isentropic values. For $Y << 1$ as is applicable during the early stage of condensation, the expressions for T and p are found from the equations of conservation of mass, momentum, and energy in one dimension and the equation of state. The results, which apply throughout the interval $t_m < t < t_n$, are

$$T = T_a \left(1 + \frac{\gamma M_a^2 - 1}{M_a^2 - 1} \frac{LY}{c_{pa} T_a} \right) \tag{47}$$

$$p = p_a \left(1 + \frac{\gamma M_a^2}{M_a^2 - 1} \frac{LY}{c_{pa} T_a} \right) \tag{48}$$

All quantities in (47) and (48) are time dependent although γ, c_{pa}, and L will vary so slightly in the temperature interval between T_m and T_n that they may be treated as constants even for the calorically imperfect gas. The Mach number depends upon the enthalpy increment and its variation is also small during $t_m < t < t_n$. The time-dependent quantities in these equations are therefore Y, T, T_a, p, and p_a. Equations (47) and (48) yield (28) and (29), respectively, when $t = t_n$.

We differentiate (47) with respect to time and specialize the result for $t = t_n$. Since $\dot{P}$ is constant during the adiabatic portion of the expansion, it follows that

$$\left. \frac{dT_a}{dt} \right|_{t_n} = -\frac{\gamma - 1}{\gamma} T_a \dot{P} \tag{49}$$

With the latter relation and (24) we write the differentiated (47) as

$$\left(\frac{\gamma - 1}{\gamma} T_a - \frac{2\, T_n f_p}{\omega \ln Sn} \right) \dot{P} = \frac{\gamma M_a^2 - 1}{M_a^2 - 1} \frac{LY_n'}{c_{pa}} \tag{50}$$

We solve the latter for Y_n' using $T_n / T_a \approx 1$ to obtain the relationship designated as (33) with ϕ and κ defined by (34) and (35), respectively. The result is

$$Y_n' = \frac{RT_a \dot{P}}{L} \frac{M_a^2 - 1}{\gamma M_a^2 - 1} (1 - \phi) \tag{51}$$

To determine f_p we first differentiate equation (48) with respect to time, specialize for $t = t_n$, and divide the result by p_a. Since $Y << 1, p_n / p_a \approx 1$ and we find

$$\left. \frac{1}{p_n} \frac{dp}{dt} \right|_{t_n} = \left. \frac{1}{p_a} \frac{dp_a}{dt} \right|_{t_n} + \frac{\gamma M_a^2}{M_a^2 - 1} \frac{LY_n'}{c_{pa} T_a} \left(1 + \left. \frac{Y_n}{Y_n' \rho_a} \frac{d\rho_a}{dt} \right|_{t_n} \right) \tag{52}$$

From the adiabatic relationship between pressure and density it follows that

$$\left. \frac{1}{\rho_a} \frac{d\rho_a}{dt} \right|_{t_n} = + \left. \frac{1}{\gamma P_a} \frac{dp_a}{dt} \right|_{t_n} = -\frac{\dot{P}}{\gamma}$$

From equations (18) and (19) it also follows when $\zeta << 1$ that

$$\frac{Y_n'}{Y_n} = \frac{3\pi^{1/2}}{2\alpha}$$

Combining these last two relationships we find

$$\left. \frac{Y_n}{Y_n' \rho_a} \frac{d\rho_a}{dt} \right|_{t_n} = -\frac{\alpha \dot{P}}{3\pi^{1/2} \gamma} \tag{53}$$

Accordingly, we rewrite (52) for $\alpha \dot{P} << 1$ using the definitions of $\dot{P}_n$ and $\dot{P}$ as

$$\dot{P}_n = \dot{P} + \frac{\gamma M_a^2}{M_a^2 - 1} \frac{L Y_n'}{c_{pa} T_a} \tag{54}$$

Thus the quantity $f_p \equiv \dot{P}_n / \dot{P}$ is found to be

$$f_p = 1 + \frac{\gamma M_a^2}{M_a^2 - 1} \frac{L Y_n'}{c_{pa} T_a P} \tag{55}$$

Finally by eliminating Y_n' in the latter by using (51) and simplifying, we find

$$f_p = \frac{M_a^2 - 1}{(\gamma - \kappa) M_a^2 - 1} \tag{56}$$

In the calculations we present herein the quantity κ varies from 0.10 to 0.12. Using the typical values $\kappa = 0.10$ and $\gamma = 1.326$ we find f_p varies over the narrow range 0.69 to 0.82 when M_a ranged from $\sqrt{2}$ to ∞.

APPENDIX C

The Solution to the Algebraic Formulation

We combine (19) and (33) and solve for α, here designated as α_g, and find

$$\alpha_g = \frac{1}{\pi^{1/2} c_{gn}} \left\{ \frac{R T_a \dot{P} (1 - \phi)(M_a^2 - 1)}{I_n L \rho_l [1 + g_2(\zeta)](\gamma M_a^2 - 1)} \right\} \tag{57}$$

A second relationship for α, designated as α_p, is derived by combining (18), (19), (23), (26), and (38). The result can be expressed as

$$\alpha_p = b - \sqrt{b^2 - 2c} \tag{58}$$

where

$$b = \frac{3\pi^{2/3}}{16} \frac{\gamma - 1}{\gamma} \frac{\omega(1 - \phi)}{\mathcal{R}(\zeta)(1 - \zeta)} \frac{\ln^2 S_n}{f_p^2 \dot{P}}$$

$$c = \frac{\ln^2 S_n}{2 B \eta_n (1 - \xi) f_p^2 \dot{P}}$$

$$\mathcal{R}(\zeta) = \frac{1 + g_1(\zeta)}{1 + g_2(\zeta)}$$

The expression for b has been simplified by setting $T_m^2 / T_a T_n = 1$.

Equations (57) and (58) yield the same value of α when the proper values of T_n and p_n are determined and all algebraic equations enumerated above have been satisfied. Since (57) and (58) possess disparate sensitivity to T_n upon which they both primarily depend, the latter is used as the independent variable in an iterative procedure. In the zeroth iteration $T_n^{(0)}$ is chosen 45°K lower than T_2 and the quantities α_g and α_p are calculated at the temperatures $T_n^{(0)}$ and $T_n^{(0)} \pm 5$ K. The first iteration $T_n^{(1)}$ is the value of temperature for which $\log \alpha_g = \log \alpha_p$ using quadratic interpolation. In the zeroth iteration it is assumed that Y_n, ϕ, ξ, $g_1(\zeta)$, $g_2(\zeta)$ equal zero and $(\gamma M_a^2 - 1)/(M^2 - 1) = 1$ for the first three iterations. A convergence criterion of $T^{(n-1} - T^{(n)} < 10^{-3}$ K is used and convergence is achieved in five to nine iterations. Divergence is occasionally encountered and is eliminated by adjusting $T_n^{(0)}$. The various subsidiary quantities such as Δh_{2n}, ΔS_{2n}, $c_n(t_n)$, $D_{32}(t_n)$, etc. are readily calculated when p_n and T_n have been determined to the required accuracy. The position of the Wilson line on the Mollier diagram is fixed by locating state 2 on the saturation line and then applying the displacements for specific enthalpy Δh_{2n} and specific entropy ΔS_{2n}.

S. W. Webb
Thermofluid Staff Specialist.

J. L. Caves
Hydraulic Consultant.

Gilbert/Commonwealth,
Reading, Penn. 19603

Fluid Transient Analysis in Pipelines With Nonuniform Liquid Density

A fluid transient in a system with steady nonuniform liquid density can be analyzed by a single density computer program by modification of the input parameters. These changes allow the program to solve the correct characteristic equations with appropriate initial and boundary conditions. The applicability of the approach has been demonstrated by a transient analysis of a reservoir, pipeline, valve problem and comparing the results.

Introduction

The method of characteristics is widely used in computer programs for the analysis of transient fluid flow in piping systems. Many of these programs are designed for the analysis of single liquid density situations. Significant liquid density changes cannot be handled directly by these codes. Such situations are common, for example, in the heating of the boiler or steam generator feedwater in power plants which can change the liquid density by 20 percent or more from the condenser conditions. While these programs are unable to analyze the systems directly, modifications can be made to the computer model to given an accurate transient solution for situations with steady, nonuniform liquid density.

Theory

Conservation Equations. The usual conservation equations encountered in fluid transient problems with constant density must be modified when the fluid density in the system is nonuniform. The basic one-dimensional continuity equation is [1]:

$$\frac{1}{A}\frac{dA}{dt}+\frac{1}{\rho}\frac{d\rho}{dt}+\frac{\partial V}{\partial x}=0. \tag{1}$$

The area differential is concerned with the elasticity of the pipe material and may be expressed as:

$$\frac{1}{A}\frac{dA}{dt}=\frac{D}{t'E}\frac{dP}{dt}. \tag{2}$$

The density differential can be expressed as [2]:

$$\frac{d\rho}{\rho}=\frac{dP}{K}-\alpha dR, \tag{3}$$

where

$$\frac{1}{K}=-\frac{1}{v}\left(\frac{\partial v}{\partial P}\right)_R \tag{4}$$

and

$$\alpha=\frac{1}{v}\left(\frac{\partial v}{\partial R}\right)_P. \tag{5}$$

The parameter R is associated with any phenomena which causes density changes other than pressure. For example, the density changes may be caused by a heater in the system so R would be temperature. An oil piping system may operate with a number of different density fluids, so R would be concentration. Any density change phenomena can be handled in the same manner.

Using these expressions in the general continuity equation gives

$$\frac{1}{\rho}\frac{dP}{dt}+a^2\left(\frac{\partial V}{\partial x}-\alpha\frac{dR}{dt}\right)=0 \tag{6}$$

with

$$a^2=\left[\frac{K/\rho}{1+\dfrac{DK}{t'Ec}}\right], \tag{7}$$

where c has been introduced to account for the pipe support configuration. The only assumptions made in the derivation of equation (7) are that the bulk modulus (K) is constant in the range of pressure variation and that the pipe material is thin walled and behaves in a linear elastic manner with small deformations. The latter assumptions hold for metal and plastic pipes but not for highly deformable tubes as discussed by Wylie and Streeter [3].

The momentum equation for one-dimensional flow is [1]

$$\frac{1}{\rho}\frac{\partial P}{\partial x}+\frac{dV}{dt}+g\sin\theta+\frac{\tau_w P_w}{\rho A}=0. \tag{8}$$

Characteristic Equations. The usual development of characteristic equations for liquids is in terms of heads and involves, at this point, the assumption that the density is substantially constant with respect to head. The current derivation will proceed directly to characteristic equations in

---

Contributed by the Fluids Engineering Division of THE AMERICAN SOCIETY OF MECHANICAL ENGINEERS for presentation at the Winter Annual Meeting, November 15-20, 1981, Washington, D.C. Manuscript received by the Fluids Engineering Division, December 20, 1982. Paper No. 81-WA/FE-29.

terms of pressure, thereby avoiding this restriction. The momentum and continuity equations are identified as L_1 and L_2, respectively

$$L_1 = \frac{1}{\rho}\frac{\partial P}{\partial x} + \frac{dV}{dt} + g\sin\theta + \frac{\tau_w P_w}{\rho A} = 0, \qquad (9)$$

$$L_2 = \frac{1}{\rho}\frac{dP}{dt} + a^2\left(\frac{\partial V}{\partial x} - \alpha\frac{dR}{dt}\right) = 0. \qquad (10)$$

Combining these equations linearly with an unknown multiplier λ results in

$$L = L_1 + \lambda L_2 = \frac{1}{\rho}\frac{\partial P}{\partial x} + \frac{dV}{dt} + g\sin\theta + \frac{\tau_w P_w}{\rho A} + \lambda\left[\frac{1}{\rho}\frac{dP}{dt} + a^2\left(\frac{\partial V}{\partial x} - \alpha\frac{dR}{dt}\right)\right] = 0. \qquad (11)$$

Expanding the total derivatives and rearranging yields

$$L = \frac{\lambda}{\rho}\left[\frac{\partial P}{\partial t} + \frac{\partial P}{\partial x}\left(V + \frac{1}{\lambda}\right)\right] + \left[\frac{\partial V}{\partial t} + \frac{\partial V}{\partial x}(V + a^2\lambda)\right] - a^2\lambda\alpha\left(\frac{\partial R}{\partial t} + V\frac{\partial R}{\partial x}\right) + g\sin\theta + \frac{\tau_w P_w}{\rho A} = 0. \qquad (12)$$

The method of characteristics requires that the equation be expressed as an ordinary differential equation. Thus, R must either be a function of time or position, but not both.

If R is a function of time and position, a conservation equation for R must be introduced. This complication has been analyzed by Stoner [4], as reported by Wylie and Streeter [3], for the case of heat transfer in a gas pipeline. In this paper, the situation will not be addressed as the present method of characteristic codes are not able to handle the additional complication. The present analysis will investigate the situation where R is only a function of position. This condition can be approached when the fluid density change propagation is small during the course of the transient. For example, if the density change is due to a heater in the system, the speed of the temperature change is on the order of the fluid velocity. If the displacement of the density change is small compared to the system dimensions for the specific transient, a constant density at any location can be assumed. That is, the liquid density is steady but may be nonuniform, and R is only a function of position.

The combined equation, L, for this case is simplified to

$$L = \frac{\lambda}{\rho}\left[\frac{\partial P}{\partial t} + \frac{\partial P}{\partial x}\left(V + \frac{1}{\lambda}\right)\right] + \left[\frac{\partial V}{\partial t} + \frac{\partial V}{\partial x}(V + a^2\lambda)\right] - a^2\lambda\alpha V\frac{dR}{dx} + g\sin\theta + \frac{\tau_w P_w}{\rho A} = 0. \qquad (13)$$

This equation can be expressed as an ordinary differential equation if the characteristic velocities in the first two bracket terms are equal, or

$$\frac{dx}{dt} = V + \frac{1}{\lambda} = V + a^2\lambda. \qquad (14)$$

This condition is met when

$$\lambda = \pm\frac{1}{a}, \qquad (15)$$

so the combined momentum and continuity equation becomes

$$L = \frac{\lambda}{\rho}\frac{dP}{dt} + \frac{dV}{dt} - a^2\lambda\alpha V\frac{dR}{dx} + g\sin\theta + \frac{\tau_w P_w}{\rho A} = 0, \qquad (16)$$

where

$$\frac{d}{dt} = \frac{\partial}{\partial t} + \frac{dx}{dt}\frac{\partial}{\partial x}. \qquad (17)$$

Using the appropriate value of λ in each case, the characteristic equations are

C^+ equations:

$$\frac{1}{\rho a}\frac{dP}{dt} + \frac{dV}{dt} - a\alpha V\frac{dR}{dx} + g\sin\theta + \frac{\tau_w P_w}{\rho A} = 0; \qquad (18)$$

$$\frac{dx}{dt} = V + a. \qquad (19)$$

C^- equations:

$$-\frac{1}{\rho a}\frac{dP}{dt} + \frac{dV}{dt} + a\alpha V\frac{dR}{dx} + g\sin\theta + \frac{\tau_w P_w}{\rho A} = 0; \qquad (20)$$

$$\frac{dx}{dt} = V - a. \qquad (21)$$

In most practical cases, the fluid velocity is much less than the wave speed, so the fluid velocity contribution in equations (19) and (21) is neglected. This simplification gives straight characteristic lines with a resulting uniform xt grid and a more straightforward solution method. The convective acceleration

Nomenclature

a = wave speed
A = pipe flow area
c = pipe support constant
C_dA = effective valve flow area
C_H = Hazen-Williams coefficient
C_v = valve flow coefficient
C^+, C^- = characteristic equations
D = pipe diameter
E = pipe modulus of elasticity
f = friction factor
H = head
g = gravitational constant
ΔH = increase in head developed by the pump
K = isothermal bulk modulus of elasticity, head loss factor
l, L = length
L, L_1, L_2 = equation identifiers
$\dot{m}$ = mass flow rate
P = pressure, perimeter
Q = volumetric flow rate
R = density change parameter
t = time (seconds), pipe wall thickness
T = temperature
v = specific volume
V = fluid velocity
x = distance along pipe
Z = vertical distance
α = density change modulus
Δ = change in parameter
θ = angle of pipe to the horizontal
λ = multiplier for characteristic equations
ρ = fluid density
τ = shear stress, dimensionless valve position

Subscripts

a = acceleration
A, B, D = points on xt grid
d = downstream
f = friction
R = reservoir
o = value at time zero, reference value
u = upstream
w = wall

Superscripts

$'$ = model value
$-$ = average value

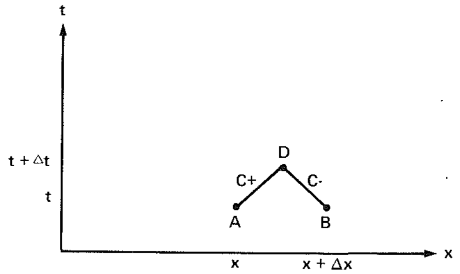

Fig. 1 *xt* grid

pressure drop is neglected by this simplification. The effect of neglecting this pressure drop is examined in Appendix A. Therefore, neglecting the velocity contribution to the characteristic speed gives

$$\frac{dx}{dt} = \pm a. \tag{22}$$

In addition, if the characteristic equations are multiplied through by the appropriate form of

$$\pm \rho a dt = \rho dx, \tag{23}$$

and the wall shear stress term is assumed to be for a circular pipe full of liquid and is rewritten as [3]

$$\frac{\tau_w P_w}{A} = \rho \frac{fV|V|}{2D}, \tag{24}$$

the equations become

C^+ equations:

$$dP + \rho a dV - a\rho V \alpha dR + \rho g \sin\theta\, dx + \rho \frac{fV|V|}{2D} dx = 0 \tag{25}$$

$$\frac{dx}{dt} = a \tag{26}$$

C^- equations:

$$dP - \rho a dV + a\rho V \alpha dR + \rho g \sin\theta\, dx + \rho \frac{fV|V|}{2D} dx = 0 \tag{27}$$

$$\frac{dx}{dt} = -a. \tag{28}$$

Integration of the C^+ equation between points A and D on the *xt* diagram in Fig. 1 gives

$$\int_A^D dP + \int_A^D \rho a dV - \int_A^D a\rho V \alpha dR + \int_A^D \rho g \sin\theta\, dx + \int_A^D \rho \frac{fV|V|}{2D} dx = 0. \tag{29}$$

The second integral can be rewritten as

$$\int_A^D \rho a dV = \rho a V \Big|_A^D - \int_A^D aV d\rho - \int_A^D \rho V da \tag{30}$$

From equation (3),

$$d\rho = \rho \frac{dP}{K} - \rho \alpha dR \tag{31}$$

so that the second and third integrals are

$$\int_A^D \rho a dV - \int_A^D a\rho V \alpha dR = \rho a V \Big|_A^D - \int_A^D \frac{\rho a V}{K} dP + \int_A^D \rho a V \alpha dR - \int_A^D \rho V da - \int_A^D a\rho V \alpha dR, \tag{32}$$

and the dR integrals cancel out.

Since $\rho VA = \dot{m}$, the total integrated C^+ equation can be simplified to

$$\int_A^D \left(1 - \frac{a\dot{m}}{KA}\right) dP + \left(\frac{a\dot{m}}{A}\right)_D - \left(\frac{a\dot{m}}{A}\right)_A - \int_A^D \frac{\dot{m}}{A} da + \int_A^D \rho g \sin\theta\, dx + \int_A^D \rho \frac{fV|V|}{2D} dx = 0. \tag{33}$$

Integration yields

$$(P_D - P_A)\left(1 - \frac{\overline{a\dot{m}}}{KA}\right) + \left(\frac{a\dot{m}}{A}\right)_D - \left(\frac{a\dot{m}}{A}\right)_A - \frac{\bar{\dot{m}}}{A}(a_D - a_A) + \bar{\rho} g (Z_D - Z_A) + \bar{\rho} \frac{fV_A|V_A|}{2D} \Delta x = 0. \tag{34}$$

In most liquid systems with or without uniform density,

$$\frac{\overline{a\dot{m}}}{KA} << 1, \tag{35}$$

and the wave speed terms can be expressed as

$$\left(\frac{a\dot{m}}{A}\right)_D - \left(\frac{a\dot{m}}{A}\right)_A - \frac{\bar{\dot{m}}}{A}(a_D - a_A) = \left(\frac{a\dot{m}}{A}\right)_D - \left(\frac{a\dot{m}}{A}\right)_A - \frac{1}{2}\left[\left(\frac{\dot{m}}{A}\right)_D + \left(\frac{\dot{m}}{A}\right)_A\right](a_D - a_A) = \frac{\bar{a}}{A}(\dot{m}_D - \dot{m}_A), \tag{36}$$

where

$$\bar{a} = \frac{a_A + a_D}{2}. \tag{37}$$

Similarly, the average value of the density can be expressed as

$$\bar{\rho} = \frac{\rho_A + \rho_D}{2}. \tag{38}$$

If the orientation of the piping system changes from point A to point D, a different average value for the elevation difference term should be defined which would be weighted by the elevation change with the associated liquid density.

The total expression for the integral becomes

$$(P_D - P_A) + \frac{\bar{a}}{A}(\dot{m}_D - \dot{m}_A) + \bar{\rho} g (Z_D - Z_A) + \bar{\rho} \frac{fV_A|V_A|}{2D} \Delta x = 0. \tag{39}$$

Nonuniform Density Equivalence. The corresponding equation for a single density situation is

$$(P_D - P_A) + \frac{a}{A}(\dot{m}_D - \dot{m}_A) + \rho g (Z_D - Z_A) + \rho \frac{fV_A|V_A|}{2D} \Delta x = 0. \tag{40}$$

In order for the single density computer program to analyze the nonuniform density situation, the terms in equations (39) and (40) must be identical. If this equivalence is achieved, the characteristic equations for the model will give a correct solution for the nonuniform density piping system. At this point, two approaches are available. Either the pressures or the heads in the system and the model can be equivalenced, but not both. The present approach equates the pressures. The heads could be made equal, but different relationships than the following would result.

Denoting the computer model values with a prime ('), the first equivalence is

$$(P_D - P_A)' = (P_D - P_A). \tag{41}$$

This equation is merely a restatement of the desired equal pressures in the system and the model.

The second equivalence gives

$$\frac{a'}{A'}(\dot{m}_D - \dot{m}_A)' = \frac{\bar{a}}{A}(\dot{m}_D - \dot{m}_A). \tag{42}$$

Equation (42) can be satisfied by using the system pipe flow area and wave speed in the model and by specifying the same mass flow rate. Note that with the same mass flow rates and areas, the liquid velocities will then not be equal, i.e., at any location, the velocities will be related as

$$V' = \frac{\rho}{\rho'} V. \tag{43}$$

The third equivalence is

$$\rho' g(Z_D - Z_A)' = \bar{\rho} g(Z_D - Z_A). \tag{44}$$

Equation (44) can be rewritten as

$$\rho' \Delta Z' = \bar{\rho} \Delta Z, \tag{45}$$

so, for equal terms,

$$\Delta Z' = \frac{\bar{\rho}}{\rho} \Delta Z. \tag{46}$$

The fourth equivalence is

$$\left(\rho \frac{f V_A \mid V_A \mid}{2D} \Delta x\right)' = \bar{\rho} \frac{f V_A \mid V_A \mid}{2D} \Delta x. \tag{47}$$

The model pipe diameter has already been made equal to the system diameter through equal flow areas. In addition, since the wave speed in the model is the same as in the system, the Δx term must also be equal in order to satisfy the characteristic velocity equation. The equivalency reduces to

$$(\rho f V_A \mid V_A \mid)' = \bar{\rho} f V_A \mid V_A \mid. \tag{48}$$

Since the mass flow rate is equal, this expression can be rewritten as

$$\left(\frac{f}{\bar{\rho}}\right)' = \frac{f}{\bar{\rho}} \tag{49}$$

or

$$f' = \frac{\rho'}{\bar{\rho}} f. \tag{50}$$

System friction factors are usually derived from a steady-state analysis and are assumed constant throughout the transient. The friction factors in the model are altered from system values according to equation (50).

Since the length and diameter are not changed, the same correction factor must be used for K factors of minor loss components, or

$$K' = \frac{\rho'}{\bar{\rho}} K. \tag{51}$$

If the Hazen-Williams [5] friction head loss equation is used, the relationship is

$$C_H' = \left(\frac{\bar{\rho}}{\rho'}\right)^{0.46} C_H. \tag{52}$$

Initial Conditions. The initial conditions in the model must also be consistent with the theory presented. Since the pressures in the model and in the system are equivalenced through the characteristic equations, the initial pressures must also be equal. Note that the hydraulic grade lines in the model and the system will not be equal for a nonuniform liquid density situation.

Boundary Conditions. The usual coordinates for a pump head-flow curve are the head difference and volumetric flow rate. If both coordinates are multiplied by the fluid density, the axes become pressure difference and mass flow rate. Since the model mass flow rate is equal to the sytem mass flow rate,

$$(\rho Q)' = \rho Q, \tag{53}$$

$$(\rho \Delta H)' = \rho \Delta H. \tag{54}$$

Therefore, the model pump curve coordinates are modified as follows:

$$Q' = \frac{\rho}{\rho'} Q, \tag{55}$$

$$\Delta H' = \frac{\rho}{\rho'} \Delta H. \tag{56}$$

Valve pressure drops are often expressed in terms of C_v through the equation [5]

$$\Delta P = \left(\frac{Q}{C_v}\right)^2 \frac{\rho}{\rho_0}. \tag{57}$$

For the same pressure drop in the model as in the system,

$$\left[\left(\frac{Q}{C_v}\right)^2 \frac{\rho}{\rho_0}\right]' = \left(\frac{Q}{C_v}\right)^2 \frac{\rho}{\rho_0} \tag{58}$$

or, since the mass flow rate and flow area are unaltered, the equation becomes

$$C_v' = \left(\frac{\rho}{\rho'}\right)^{1/2} C_v. \tag{59}$$

Similarly,

$$(C_d A)' = \left(\frac{\rho}{\rho'}\right)^{1/2} C_d A. \tag{60}$$

Other boundary conditions can be handled in a similar manner.

Verification

These relationships for the initial and boundary conditions can be easily checked by analyzing a simple steady-state flow situation. To verify the modifications to the characteristic equations, however, a transient problem must be solved. Wylie and Streeter [3] give a simple transient problem (Example 3-1) in which a pipe has a reservoir upstream and a valve downstream. The valve closes as a function of time, and the transient conditions in the line are given by Wylie and Streeter. Figure 2 depicts this problem and the appropriate parameters are listed in Table 1.

The results of this analysis were transposed into pressure and mass flow rate by assuming a liquid density of 1.0 g/cm^3

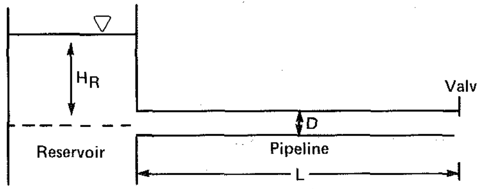

Fig. 2 Verification problem

Table 1 Verification problem parameters

	Wylie and Streeter [3]	Verification Problem
Pipe Length (L)	600 m	600 m
Pipe Diameter (D)	0.5 m	0.5 m
Friction Factor (f)	*0.018*	*0.01458*
Wave Speed (a)	1200 m/s	1200 m/s
Reservoir Head (H_R)	150 m	185.2 m
Valve (C_dA)	*0.009 m^2 (C_{vo} = 529.8)*	*0.010 m^2 (C_{vo} = 588.7)*
Fluid Density (g/cm^3)	1.0*	0.81
Valve Movement	$\tau = \frac{C_d A}{(C_d A)_O} = \frac{C_v}{C_{vo}} = (1 - \frac{t}{2.1})^{1.5}$	

* – Assumed

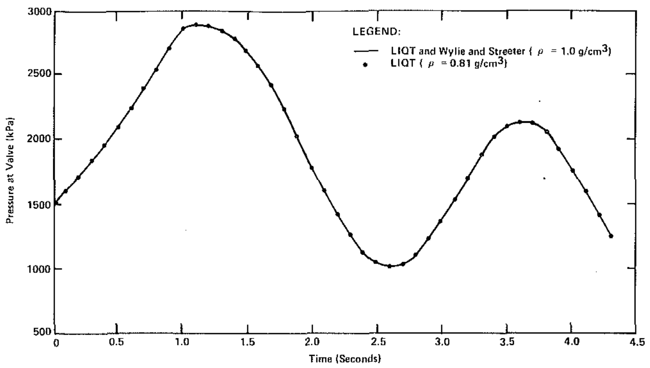

Fig. 3 Pressure response at valve versus time

in the line. This problem was analyzed by LIQT [6] with identical results. A fluid density of 0.81 g/cm^3 was then used and the appropriate parameters changed. The resulting pressure and mass flow rate at the valve are essentially identical for the two fluid densities as depicted in Figs. 3 and 4, respectively.

Summary

In order to analyze a fluid transient in a liquid system with nonuniform density with a uniform density computer code, the following modifications are necessary in constructing the model:

1) Use the actual system values for the following parameters in the model: (*a*) wave speed (average value as necessary); (*b*) pipe length, diameter (flow area); (*c*) mass flow rate (velocities and volumetric flow rates will not be equal for the model and system if the fluid densities are different) and (*d*) initial pressures (hydraulic grade lines will not be equal if the fluid densities are different).

2) Change the elevation difference by:

$$\Delta Z' = \frac{\bar{\rho}}{\rho'} \Delta Z. \tag{61}$$

3) Modify the friction head loss factors by:

$$f' = \frac{\rho'}{\bar{\rho}} f, \tag{62}$$

$$K' = \frac{\rho'}{\bar{\rho}} K, \tag{63}$$

$$C'_H = \left(\frac{\bar{\rho}}{\rho'}\right)^{0.46} C_H. \tag{64}$$

4) Alter the pump curve coordinates by:

$$Q' = \frac{\rho}{\rho'} Q, \tag{65}$$

$$\Delta H' = \frac{\rho}{\rho'} \Delta H. \tag{66}$$

5) Modify the valve coefficient by:

$$C'_v = \left(\frac{\rho}{\rho'}\right)^{1/2} C_v \tag{67}$$

or

$$(C_d A) = \left(\frac{\rho}{\rho'}\right)^{1/2} C_d A. \tag{68}$$

The transient hydraulic grade line, velocities and volumetric flow rates will not be the same in the model as in the system when the densities are different. However, the pressures and mass flow rates will be the same.

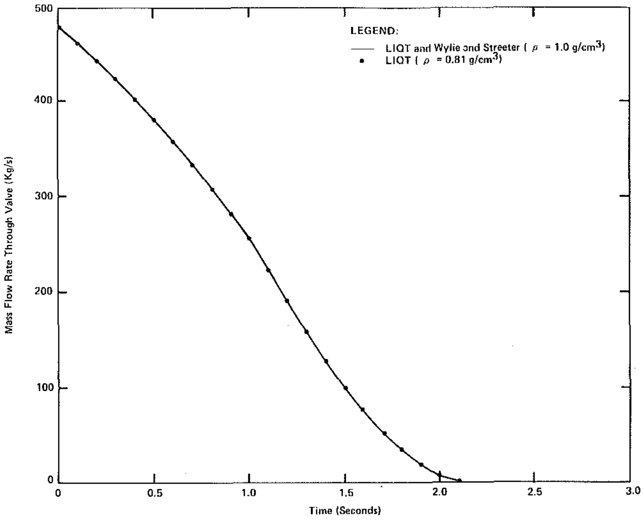

Fig. 4 Mass flow rate at valve versus time

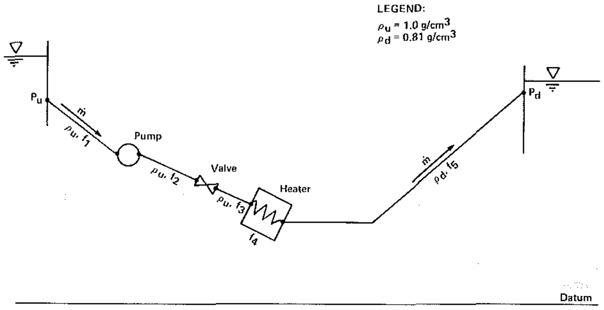

Fig. 5 Application example – piping system

Application

To illustrate how these techniques would be applied, a series-connected piping system having an in-line heater, pump and valve is considered. This system is shown in Fig. 5. Upstream from the heater, the water density is $\rho_u = 1.0$ g/cm^3. As the water passes through the heater, the density is reduced so that downstream from the heater the density is $\rho_d = 0.81$ g/cm^3.

If a transient analysis of this system is to be performed using a uniform density code, an appropriate model would be as shown in Figs. 6, 7, and 8. This model is based on a uniform density of $\rho' = \rho_d$. If ρ' was set at ρ_u or some other density, the corresponding model would not be the same, as is apparent from equations (61)-(68).

Figure 6 shows how the upstream portion of the model would differ physically from the system. Figures 7 and 8 compare the pump curves and valve curves, respectively, for the system and model.

The preceding development considers that the heater is modeled as a pipe-type component of finite length. As the liquid passes through the heater, the density changes at some finite rate. Since the heater length is often short in comparison to other pipe-segments in the system, it may be advantageous to use a lumped representation of the heater by making it a non-pipe "minor loss" type component and adding its wave travel time to an adjacent pipe, thereby permitting a larger simulation time step. The heater loss coefficient for a uniform density model would then be

$$K' = \frac{\rho'}{\bar{\rho}} K = \frac{\rho'}{\bar{\rho}} \frac{fl}{D}, \tag{69}$$

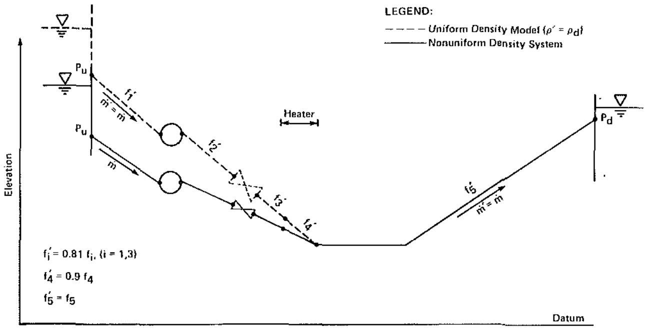

Fig. 6 Application example – comparison of system amd model elevations

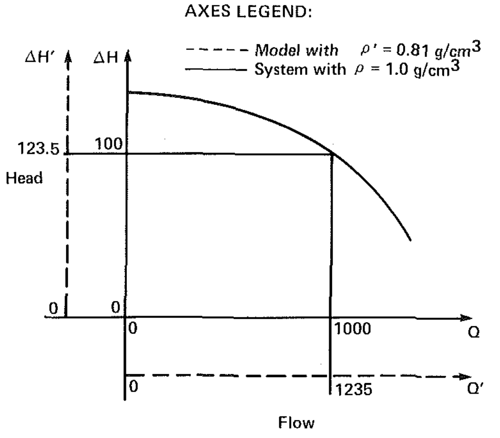

Fig. 7 Application example – comparison of system and model pump curves

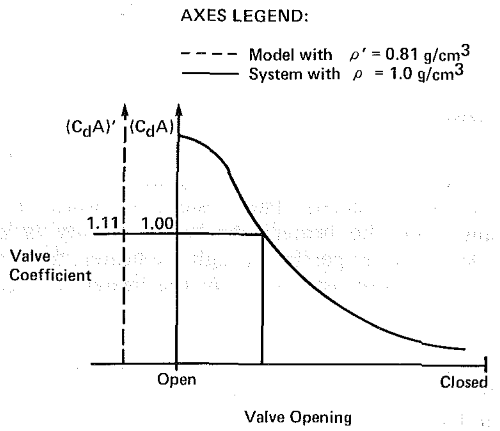

Fig. 8 Application example – comparison of system and model valve curves

where l is the heater tube length. The modified heater inlet elevation is also determined using the average density in the heater. An assessment, such as made in Appendix A, shows that the convective acceleration pressure drop associated with the momentum change between these sections is negligible compared to the friction related pressure drop. Thus, in long systems, a lumped representation can be a valid alternative for modeling the heater.

Conclusion

The proposed changes to the input parameters to the computer program have been verified by the transient analysis. Therefore, a single density computer program can be used to accurately simulate a transient in a steady nonuniform liquid density problem.

Acknowledgment

The authors appreciate the constructive reviews made by Professor E. B. Wylie at The University of Michigan and Dr. C. P. Liou at Stoner Associates, Inc., during preparation of this paper.

References

1 Streeter, V. L., and E. B. Wylie, *Fluid Mechanics*, 6th Edition, McGraw-Hill, 1975.

2 Sonntag, R. E., and G. J. VanWylen, *Introduction to Thermodynamics: Classical and Statistical*, Wiley, 1971.

3 Wylie, E. B., and V. L. Streeter, *Fluid Transients*, McGraw-Hill, 1978.

4 Stoner, M. A., "Analysis and Control of Unsteady Flows in Natural Gas Piping Systems," Ph.D dissertation, The University of Michigan, 1968.

5 *Flow of Fluids*, Crane Technical Paper No. 410, 1969.

6 LIQT Service Version 4.0 Reference Manual, Stoner Associates, Inc., Carlisle, PA, 1980.

APPENDIX A

Pressure Drop Components

The general pressure drop equation for steady-state flow from equation (8) is [3]

$$-\frac{dP}{dx} = \rho V \frac{dV}{dx} + \rho g \sin\theta + \frac{\tau_w P_w}{A} \qquad \text{(A.1)}$$

where the terms on the right-hand side are the convective acceleration, elevation and shear pressure drop components. The shear stress term for a full circular pipe can be expressed as [3]

$$\frac{\tau_w P_w}{A} = \rho \frac{fV|V|}{2D}. \qquad \text{(A.2)}$$

The friction and acceleration terms will be compared.

For constant density steady-state flow in a uniform area pipe, the change in velocity is

$$\frac{dP}{dx} + \rho a^2 \frac{dV}{dx} = 0 \qquad \text{(A.3)}$$

or

$$\frac{dV}{dx} = -\frac{1}{\rho a^2}\frac{dP}{dx} \qquad \text{(A.4)}$$

which is negligible due to the large value of the wave speed. However, if the fluid density is being changed, the velocity difference is more significant. If the fluid is being heated, the change in velocity for steady-state flow is

$$\frac{dV}{dx} = \alpha \frac{dT}{dx} - \frac{1}{\rho a^2}\frac{dP}{dx}. \qquad \text{(A.5)}$$

The ratio of acceleration to friction pressure drops is

$$\frac{\Delta P_a}{\Delta P_f} = \frac{\rho V \dfrac{dV}{dx}}{\rho \dfrac{fV|V|}{2D}}. \qquad \text{(A.6)}$$

Heater tubes are usually small in diameter and long in length to facilitate heat transfer. A typical ratio of diameter to length in a heat exchanger is about 1000 or more. The temperature induced change in outlet velocity with respect to the inlet velocity is about 20 percent at most. The turbulent friction factor is about 0.025 for the small tubes involved. Therefore, the ratio is

$$\frac{\Delta P_a}{\Delta P_f} \simeq 0.01. \qquad \text{(A.7)}$$

Thus, the convective acceleration term can be neglected for water passing through a heater. The total pressure drop is then simply the sum of the elevation and friction components.

S. R. Ahmed
Institut für Entwurfsaerodynamik,
DFVLR,
Braunschweig, West Germany

Influence of Base Slant on the Wake Structure and Drag of Road Vehicles

The time averaged wake structure of a realistically dimensioned quarter scale automobile model was studied in a wind tunnel on the basis of flow visualization, wake surveys, force and pressure measurements. Through a systematic variation of base slant angle in the range of 0 to 40 deg, the ensuing changes in the wake structure were observed and the wake structure present at lowest value of aerodynamic drag is shown. Experimental data were obtained at a model length based Reynolds number of 4.29 million. Correlation of wake structure with drag, pressure distribution, and kinetic energy content of vortex motion in wake is addressed.

1 Introduction

A possibility of reducing the aerodynamic drag of a road vehicle type bluff body by varying the base slant angle was implied in the work of Hucho [1] and Morel [2]. The mechanisms through which this drag variation occurs is however not sufficiently understood to enable a reliable prediction of the "optimum" base slant angle for given vehicle configuration. Effective experimental or theoretical procedures for drag optimisation of a vehicle configuration can be developed if the changes in velocity and pressure field around the vehicle and in the wake structure associated with a change in body geometry are known.

Much of the research on vehicle aerodynamics is restricted to force and moment studies and some surface pressure evaluations. Generality of these results is often narrowed down due to the specialised project oriented geometries investigated. Few flow field measurements are available which could serve as a basis for modelling the flow around vehicles or to gain insight into the drag creating mechanisms at work in the flow field.

As most of the road vehicles can be classified as bluff bodies which move in ground vicinity, a major contribution to the aerodynamic drag stems from pressure drag created by the low pressure prevalent in the separated flow region of vehicle base. The kinematics of flow in the wake of the vehicle are closely linked to the aerodynamic drag and govern the magnitude and disposition of the base pressure distribution.

It is evident that there is a need for detailed information about the structure of flow in the wake and its variation with changes in body geometry.

Even though the flow in wake of bluff bodies is basically unsteady the time averaged flow shows a coherent macrostructure. The large scale macrostructures appear to determine all the dynamics, pressure forces, etc. in the flow. With this in mind a systematic variation of base slant angle on a road vehicle type body was effected to experimentally study the changes in the time averaged flow structure of the wake, the surface pressure distribution and the aerodynamic drag.

2 Experimental Arrangement and Test Procedure

Wind Tunnel. Tests were conducted in the DFVLR 3 – by 3 – meters Subsonic Wind Tunnel at a wind speed of 60 m/s and a model length based Reynolds number of 4.29 million. This facility, described in [3], is an open test section closed-return wind tunnel with a working section length of 5.86 m. Turbulence intensity in the empty test section lies below 0.5 percent.

Model. The basic model configuration, Fig. 1(*a*), was a quarter scale 1.044 m long automobile model with a length: width: height ratio of 3.02: 1.16:1. The upper rear-end was interchangeable. Model undersurface had at its lowest point a ground clearance of 0.05 m. All upper and under surface details were smoothed out, edges and hood front were rounded. The model was provided with a set of 9 rear-ends with base slant angles of 0, 5, 10, 15, 20, 25, 30, 35, and 40 deg, Fig. 1(*b*). The model was instrumented with pressure taps in the longitudinal and a horizontal section of the main body. Rear-ends with base slant angles of 5, 25, and 30 deg were equipped with pressure taps on the base slant surface. Scanivalves for pressure data aquisition were installed inside the model body.

Frontal area of model including wheels was 0.1122 m^2. Engine compartment and cooling air flow path were not simulated in the model.

Test Arrangement and Wake Survey Procedure. For wake survey, the model was fixed via wheels directly on to a ground plane 3 m wide and 4.2 m long. Model was positioned 0.54 m behind ground plane leading edge leaving a ground plane

---

Contributed by the Fluids Engineering Division and presented at the Winter Annual Meeting, Washington, D.C., November 15-20, 1981, of THE AMERICAN SOCIETY OF MECHANICAL ENGINEERS. Manuscript received by the Fluids Engineering Division, April 26, 1982.

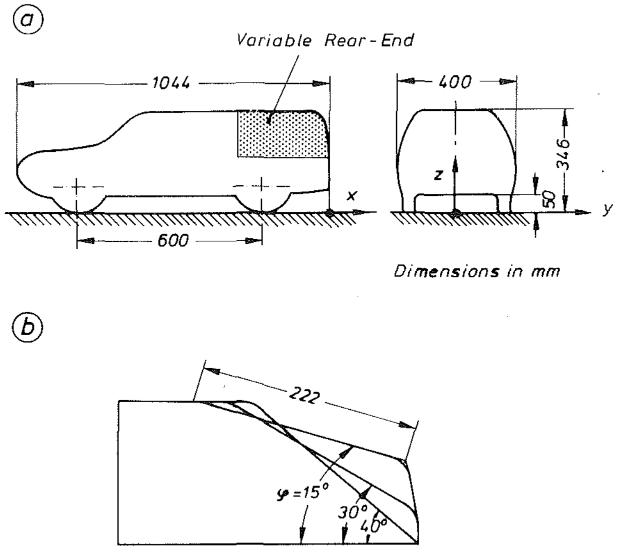

Fig. 1 **Wind tunnel model**
(a) Overall dimensions
(b) 3 Rear – ends

length behind the model of about 2.5 times model length. This was deemed necessary to avoid interference between vehicle wake and ground plane trailing edge flow [4]. The ground plane was fixed in the open test section 0.3 m above the lower edge of the 3 m × 3 m wind tunnel nozzle. Thus about 90 percent of the nozzle area was free above the ground board. Ratio of model frontal area including wheels to this area was 1.39 percent. Zero circulation on the ground board was obtained in the tunnel by adjusting the blockage on ground board undersurface till pressure from tappings situated in the upper and lower surface just aft of leading edge were balanced. Blockage on ground board undersurface was varied by mounting beams of different height across the width at model position. Boundary layer measurements in the empty tunnel on the ground board indicated a displacement thickness at model position of about 1.5 mm. This set-up permitted investigations for zero yaw flow only.

A nine-hole conical-tip yawmeter probe, used in earlier wake studies [5, 6] was used for the wake survey. The arrangement of the four orifices on the conical probe tip is such that one opposing pair is sensitive primarily to flow yaw and the other to flow incidence. The instrument is used as a null yaw reading device, in the sense that yaw rotations are imposed on the probe until the pressure in opposing pair of orifices is equalized. In this condition the tip axis is pointing nominally along the direction of local yaw. The pressure difference of the incidence-sensitive orifices is used via a calibration curve to evaluate the local flow incidence. Pressure in tip orifice and mean of the pressures in the four orifices on the tip cylindrical sleeve is a function of local total and static pressure respectively. Calibration curves are used to compute the local total and static pressure from this data. Thus magnitude and direction of local velocity vector and local static and total head are determined, given the yaw angle displacement of the probe in balanced state and the pressure values in the rest of seven orifices.

The probe was mounted on a carriage, which provided rectangular cartesian translations along the full length, width and height of the tunnel working section. All motions were effected by remotely controlled motors and measured by electronic counters. During wake survey, the probe moved continuously with a speed of 3.6 mm/s in the z-direction with x- and y-position kept fixed. The z-traverse was repeated for a new value of y which was increased in steps of 20 mm (or 40 mm) till a traverse half-plane from $y = 0$ mm to 400 mm and $z = 5$ mm to 600 mm was scanned.

Symmetry of flow in wake was checked by comparing the velocities measured on either side of the plane of symmetry. This test was done for $\varphi = 25$ deg only in the transverse plane at $x = 500$ mm. Values of V_x, V_y, and V_z measured at stations $y = \pm 20$ mm, ± 80 mm and ± 160 mm showed maximum differences of 5 percent. The distance z varied hereby from 5 mm to 400 mm.

Estimated accuracy of flow angle measurements is ± 0.3 deg. Errors of upto 1 percent of the value of free stream dynamic pressure are present in the pressures measured. More details of this experimental technique and accuracy estimates are given in [6].

Force Measurements. Force measurements were made for all nine model configurations. Only total drag values, which are of interest here are reported. The model was connected to a strain gauge balance by four cylindrical studs projecting vertically through oversize holes in the ground plane. The studs fitted into blind holes provided for in the wheels. Wheel bottom was flattened to leave an air gap of 1.5 mm above the ground plane to prevent grounding of the balance. The balance, mounted below the ground plane was screened from tunnel air flow by a casing.

Flow Visualization. Flow on model surface and wake central plane was visualised through oil film technique. To study the flow pattern in the wake, splitter plates 2 mm thick, 0.5 m high, and 1.2 m long were fixed vertically in the wake central plane on the ground board. The well-rounded up-

Nomenclature

b = model width (= 400 mm)
$c_w = W/(q_\infty F)$ = drag coefficient
$c_p = (p - p_\infty)/q_\infty$ = static pressure coefficient
c_{yz} = dimensionless kinetic energy content factor (equation (2))
W = drag force
F = projected frontal area of model (= 0.1122 m^2)
h = model height above ground (= 346 mm)
$k(y)$ = local kinetic energy factor (equation (1))
$\bar{k}(y) = k(y)/(V_\infty{}^2 h)$ = dimensionless value of k(y)
l = model length (= 1044 mm)
p, p_∞ = local and free stream static pressure
$q_\infty = (\rho/2)V_\infty{}^2$ = free stream dynamic pressure
$\mathrm{Re} = V_\infty l/\nu$ = Reynolds number based on model length
s = length measured along contour
V_x, V_y, V_z = velocity components in $x-$, $y-$, and z-directions
V_{yz} = resultant of V_y, V_z velocity components
V_∞ = free stream velocity (= – vehicle velocity)
x, y, z = rectangular road fixed coordinate system as defined in Fig. 1(a)
y_1, y_2, z_1, z_2 = coordinates of wake traverse plane edge
ν = kinematic viscosity
ρ = density
φ = base slant angle [degrees]

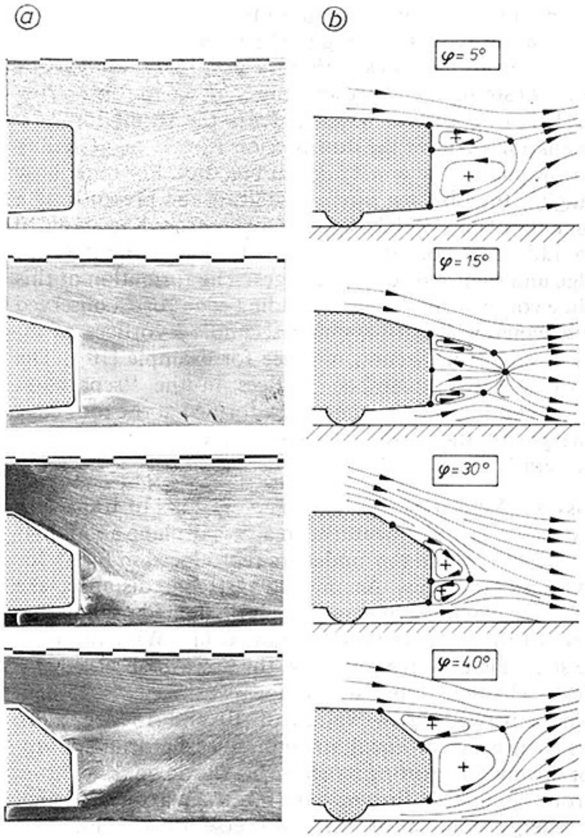

Fig. 2 **Flow pattern in wake central plane;**
(*a*) Oil flow pictures
(*b*) Stream line pattern (schematic)
• Separation or stagnation points

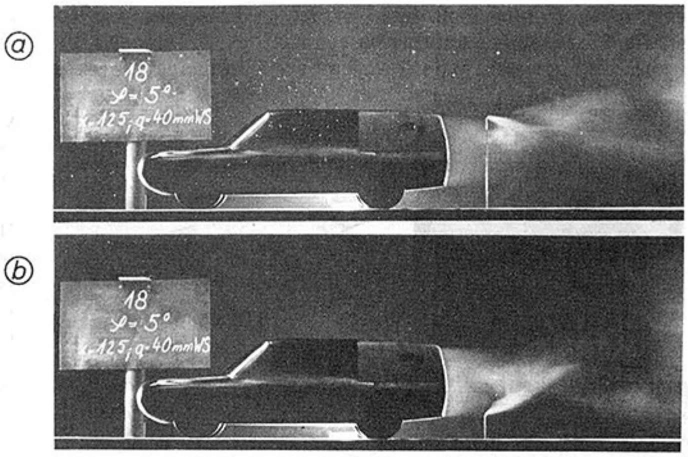

Fig. 3. Flow visualisation through smoke injection (φ = 5 deg),
(*a*) Smoke tube at wake upper "edge"
(*b*) Smoke tube at wake lower "edge"

stream edge of the splitter plate was cut out to accomodate the model rear-end leaving a gap of 25 mm between it and model surface. With this arrangement, the development of the flow in the region starting from roof rear edge, along the base slant, and into the wake could be traced. The plate surface was uniformly coated with a thin emulsion of aluminum oxide and kerosene and the wind turned on. Same technique was applied to map the flow over the rear-end surface.

As the introduction of a splitter plate in the wake central plane was expected to alter the flow pattern, the wake flow was also made visible through smoke injection to qualitatively assess the effect of splitter plate. For this purpose the splitter plate was removed and smoke was introduced at various downstream stations along the wake central plane through a thin tube of 4 mm diameter projecting vertically through the ground plane. This tube could be moved vertically and thus trace the various recirculating flow regions in wake central plane.

3 Discussion

Flow in Wake Central Plane. Flow structure in the longitudinal central plane of the wake and its variation with base slant angle is seen in the picture series of Fig. 2(*a*). These pictures were obtained by the oil flow technique described in Section 2 on a splitter plate placed in the longitudinal plane. Also shown in Fig. 2(*b*) is the schematic pattern of the streamlines derived onthe basis of the oil flow pictures. As the splitter plate upstream edge was cut out leaving a gap of 25 mm between it and model rear end-surface, the flow indicated is the one existing slightly above, behind and below the slanted, base, and undersurface of the rear-end.

The near wake exhibits in its central plane a set of contrarotating flow regions adjacent to vehicle base. The strength of these circulating flows, location of their cores and size of the region housing them is seen to be closely related to the base slant angle. For the base slant value of $\varphi = 5$ deg, the lower counter clockwise rotating flow in wake is in its extension and strength predominant. With increasing values of base slant angle, the upper, clockwise rotation flow gains on strength. For $\varphi = 15$ deg, both flows appear to be of equal strength and with $\varphi = 30$ deg, the upper flow becomes dominant. Up to this value of base slant angle, the flow seems to remain attached on major portion of the inclined rear-end surface (see also Fig. 4(*c*)). Increasing φ beyond 30 deg initiates flow separation from roof trailing edge resulting in an abrupt switch over of the wake pattern which now bears strong similarity to that observed for $\varphi = 5$ deg.

An the introduction of a splitter plate in the wake is known to alter the drag and base pressure of bluff two dimensional and axisymmetric bodies (see [7–9]) it was conjectured that in the present case of a three dimensional vehicle model, the presence of a splitter plate may cause significant changes in the wake pattern. To investigate this, the splitter plate was removed and smoke was injected in wake central plane at various downstream stations through a thin tube projecting out of the ground plane. The smoke tube could be moved vertically so as to probe the entire height of the wake. The results of wake visualization through smoke are presented in Fig. 3.

As seen in the pictures of Fig. 3, introduction of smoke at upper or lower wake edge clearly shows the presence of the two circulatory flow regions in the wake. Similar results, not shown here, were obtained for the other base slant angles investigated, which qualitatively confirm the oil flow visualization results of Fig. 2. This leads to the conclusion that the presence of the splitter plate did not basically alter the wake structure in the present case.

Flow in Vicinity of Vehicle Base. To gain a further understanding of the flow in the vicinity of vehicle base, the model rear-end was coated with kerosene and aluminum oxide emulsion as before to map the flow pattern. The results are shown in Fig. 4 together with the schematically reproduced results of Fig. (*b*) to facilitate the interpretation of the three dimensional flow field. Results of Fig. 4 were obtained with the splitter plant removed.

For base slant angle of $\varphi = 5$ deg, the flow remains attached over the inclined surface, separating later at the trailing perimeter of the base. Cross-flow over inclined side edges of the rear-end is weak. In the "separation bubble" emanating from vehicle base, a pair of horseshoe vortices situated one above another appears to exist, whereby the upper one is weak. The lower, upwash inducing vortex is responsible for the streamline pattern formed on the rear end. With increasing base slant angle, the strength of the upper horse-show vortex increases so that for $\varphi = 15$ deg both are of almost equal strength and presumably coalesce to form a ring vortex. This ring vortex, which induces the formation of a free stagnation point in the downstream flow is suggested by the oil flow picture for $\varphi = 15$ deg in Fig. 2(*a*). For other base slant angles, the oil flow pictures indicate the presence of a free stagnation line. With base slant angles exceeding about 10 deg, an additional horseshoe vortex is formed along the roof rear edge and slant rear-end side edges. The formation of this horseshoe vortex is similar to the leading edge vortex observed on delta wings with primary and secondary vortices as indicated in Fig. 4(*b*), Section AA (see for example [10]). The upper of the two horseshoe vortices in the "separation bubble" is strengthened by the vortex formed at the roof edge as a merger of these two vortices presumably takes place downstream.

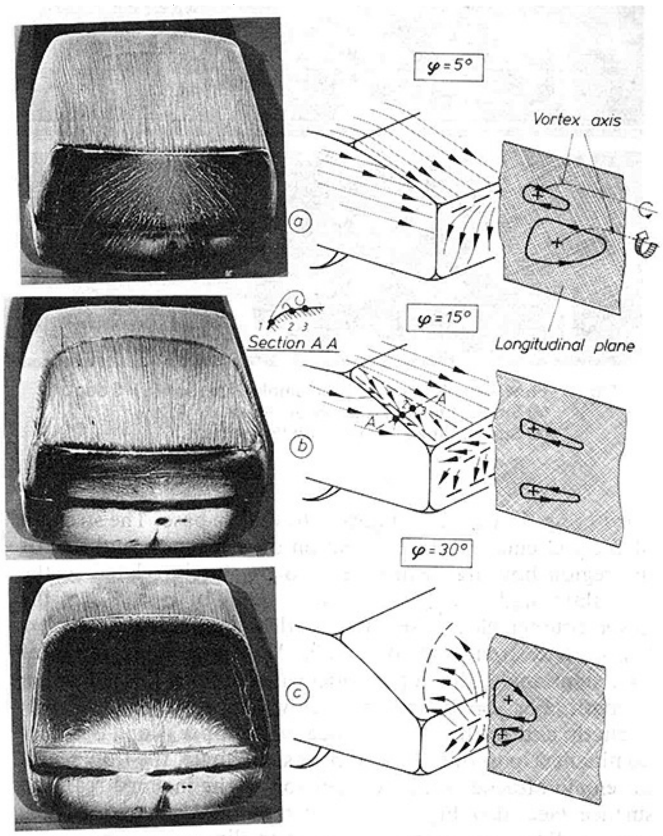

Fig. 4 Flow pattern on rear – end.
-- Stagnation or separation line

Transverse Velocity Field in Wake. Results of transverse velocity vector V_{yz}/V_∞ measured in a yz-halfplane about half a vehicle length behind the model are reproduced in Fig. 5 for four base slant angles. At this downstream distance, the weaker of the two horseshoe vortices is dissipated so that only the effect of the stronger vortex is noticeable. With variation of base slant angle from 5 to 25 deg, the upwash observed at $\varphi = 4$ deg is changed into a strong downwash at $\varphi = 25$ deg. Somewhere between φ – values of 10 and 15 deg, both vortices then being of equal strength, the characteristic upwash or downwash creating structure breaks down.

A strong circulatory flow in wake means an associated high kinetic energy content of the transverse flow field. This phenomenon is obviously associated with the aerodynamic drag of the vehicle. For base slant angle of $\varphi = 25$ deg the cross-flow velocity components reach values of upto 30 percent of the free stream value. Result of Fig. 5(*e*) bears out this observation, where the lowest value of drag c_w measured

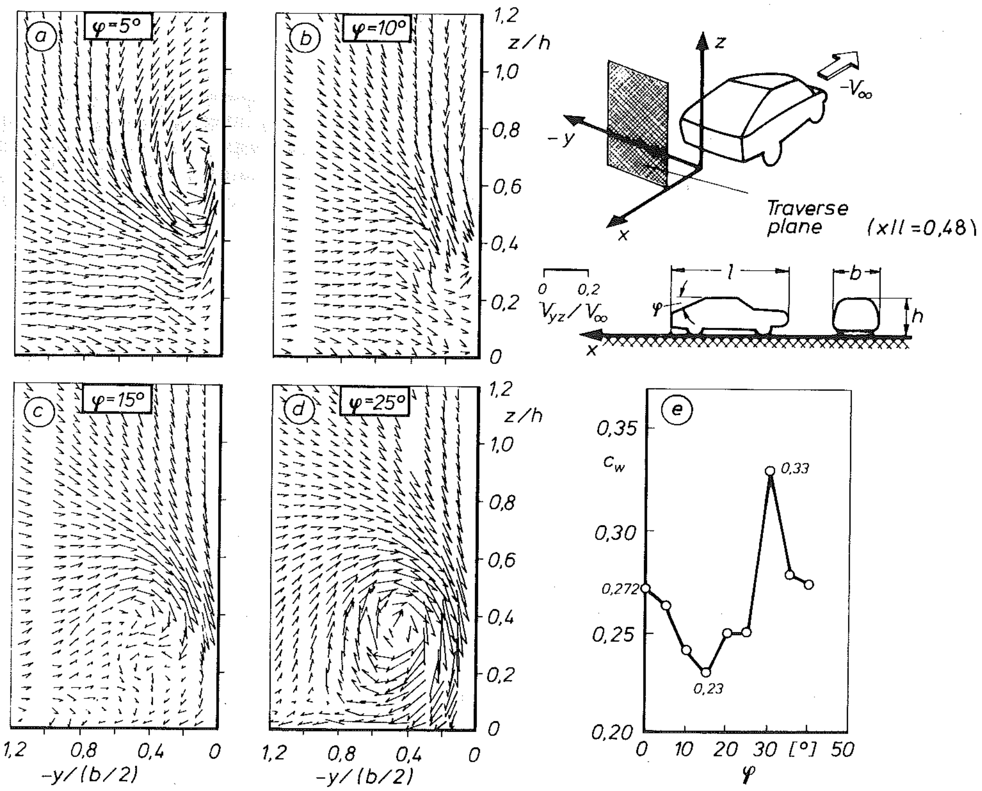

Fig. 5 (*a,b,c,d*) Transverse flow field in wake
(*e*) Drag variation with base slant angle

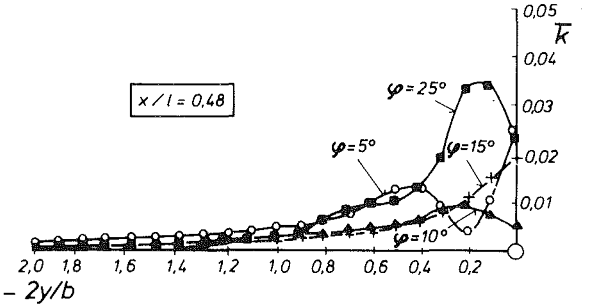

Fig. 6 Distribution of kinetic energy factor $\bar{k}$ across wake

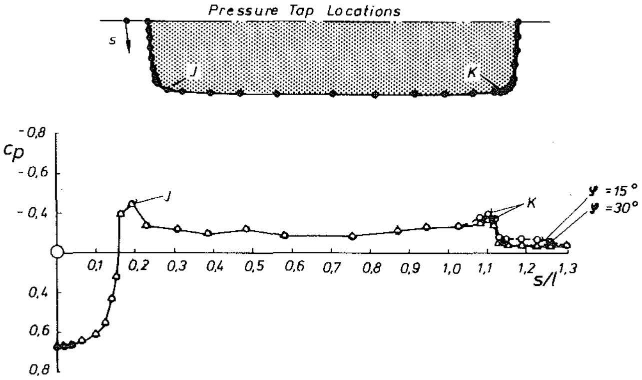

Fig. 7 Variation of wake kinetic energy content with base slant angle

corresponds to the weak transverse flow field expected in wake of a vehicle with base slant angle of about 12.5 deg.

Kinetic Energy Distribution Across Wake. A quantitative evaluation of the kinetic energy content of the wake for the base slant angles of 5, 10, 15, and 25 deg is presented in Fig. 6. At various lateral positions y = constant, the kinetic energy factor $k(y)$ was evaluated for the transverse plane situated at $x/1 = 0.48$ as

$$k(y)=\int_{z_1}^{z_2} V_{yz}{}^2dz \qquad (1)$$

Limits of integration were given by the coordinates of the traverse plane viz $z_1 = 5$ mm and $z_2 = 600$ mm. Separation of ground boundary layer from the region of interest was not attempted, as its effect on the transverse flow field was considered to be minor.

The area enclosed by the curves and the axes is a measure of the kinetic energy content of the wake transverse flow field. As such the base slant angle of 25 deg exhibits the highest kinetic energy content among the four rear-end configurations, with energy concentration towards the wake center. The area content of k-curves evaluated as

$$c_{yz}(x)=\frac{2\int_{y_1}^{y_2}k(y)dy}{V_\infty{}^2F} \qquad (2)$$

is, referred to the aerodynamic drag c_w shown in Fig. 7 for different base slant angles. This result, together with the result of Fig. 5(e) documents clearly the correlation between kinetic energy content of vehicle wake and its drag. Vehicles with low aerodynamic drag are characterised by a weak transverse flow in the wake. For the vehicle configuration under study, this optimum value lies at a base slant angle of about 12.5 deg.

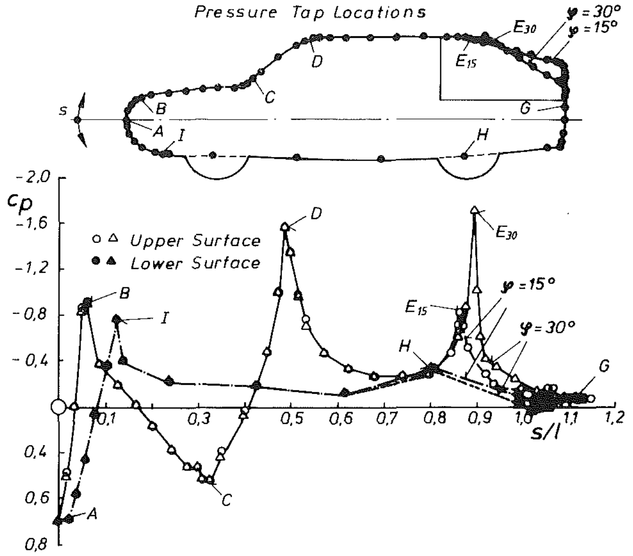

Fig. 8 Pressure distribution in longitudinal central plane

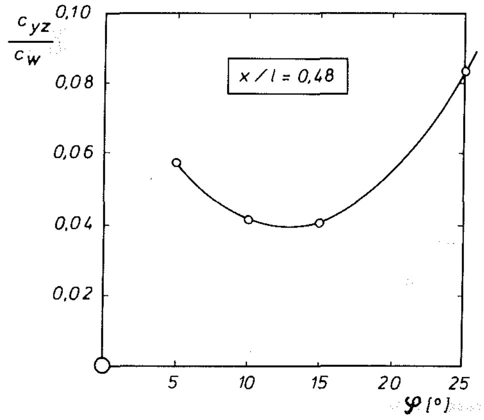

Fig. 9 Pressure distribution in horizontal plane

Pressure Distribution. The effect of base slant on the surface pressure distribution is shown by the results of Figs. 8 and 9 in which the pressure in a longitudinal and horizontal section is plotted for the base slant angles 15 and 30 deg. It is interesting to note that the upstream pressure distribution remains unaffectd by the base slant angle. Effect of base slant is confined to the rear-end surface with a sharp low pressure peak occurring just beyond the roof trailing edge. As to be expected, the pressure level on inclined surface of $\varphi = 15$ deg rear-end is higher than that of $\varphi = 30$ deg. On the lower side the opposite is true, confirming the earlier observation from oil flow pictures, that the lower, upwash creating horseshow vortex for low φ-angles predominates. Pressure distribution across the inclined rear-end surface as shown in Figs. 10 and 11 indicate a strong, from plane of symmetry laterally outwards directed flow in Section 3, just beyond the roof trailing edge. The sharply defined pressure peaks on side edges of slanted rear-end surface in sections 4 to 7 (Fig. 11) are similar to the pressure distribution over a delta wing [10] exhibiting the existence of a weak horseshow vortex for the $\varphi = 15$ deg and a strong horseshoe vortex for $\varphi = 30$ deg rear-end located along the edges of the inclined surface. Transverse flow velocity vectors in a yz-plane lying midway between roof trailing edge and vehicle base as seen in Fig. 12 also show the increased inflow towards the inclined rear-end surface with increase of base slant angle. Due to the coarse mesh of the data aquisition points and the difficulty in moving close enough to model surface, the side edge vortex could not be identified.

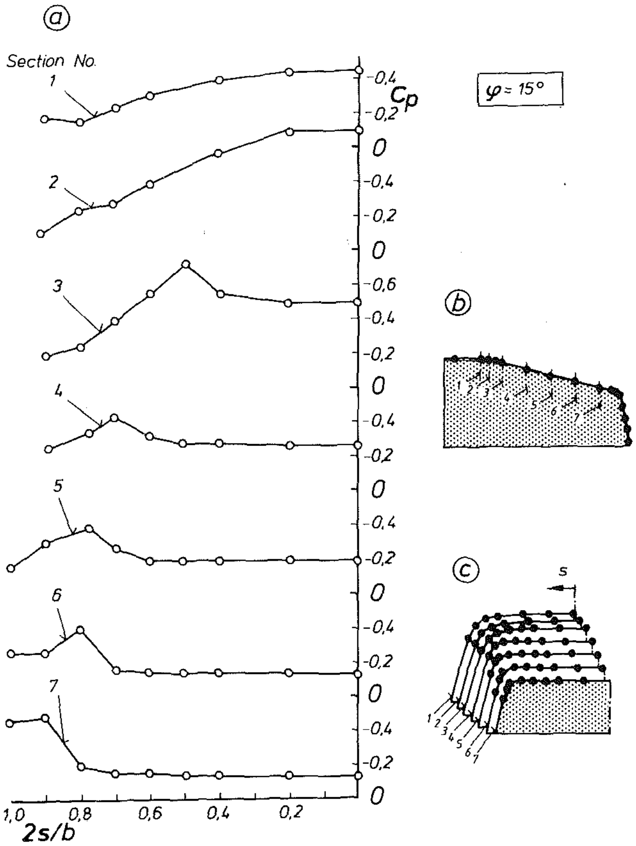

Fig. 10 (a) Pressure distribution on base slant surface (φ = 15 deg) (b) Locations of sections 1 to 7; (c) Pressure tap locations in sections 1 to 7

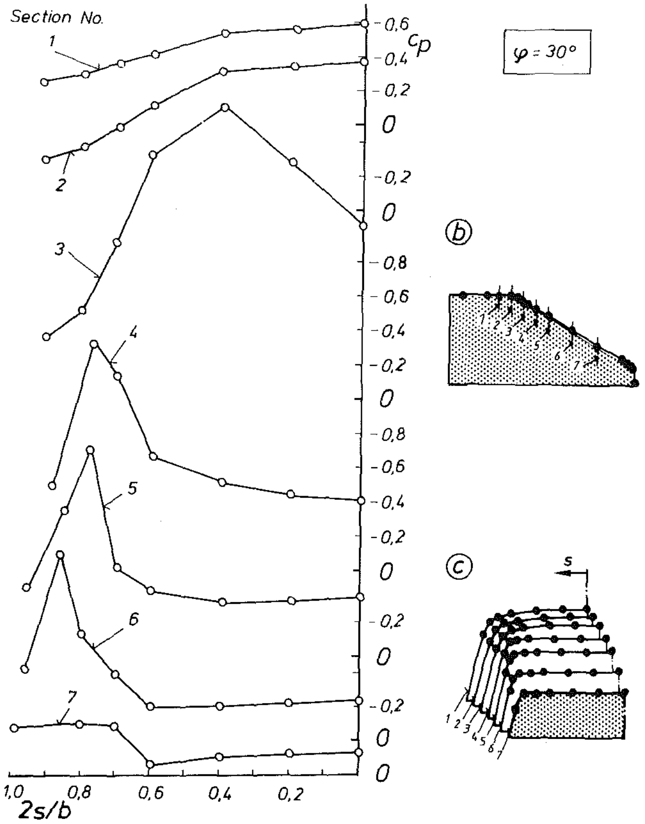

Fig. 11 Pressure distribution on base slant surface (φ = 30 deg). Legend as in Fig. 10

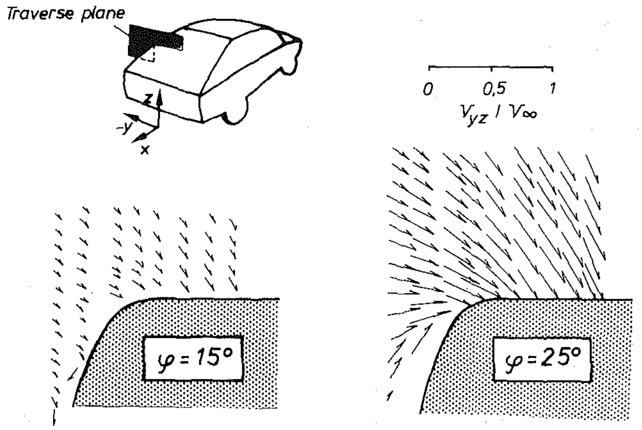

Fig. 12 Transverse flow field in vicinity of base side edge

4 Conclusions

1. The time averaged structure of the wake of a *fast-back* type road vehicle houses a pair of horseshoe vortices placed one above another in the "separation bubble" emanating from vehicle base. The trailing edges of these vortices are parallel to the longitudinal axis of the vehicle.
2. Strength and location of the horseshoe vortices is dependent upon the base slant angle.
3. The kinetic energy content of the transverse flow in wake is correlated to the aerodynamic drag of the vehicle.
4. The low drag "optimum" configuration exhibits a weak cross flow in wake where the organised upwash or downwash creating vortical motion is absent. For the configuration under study this was present at a base slant of about 12.5 deg.

References

1 Hucho, W.-H., "The Aerodynamic Drag of Cars. Current Understanding, Unresolved Problems and Future Prospects," *Proceedings of Symposium on Aerodynamic Drag Mechanisms of Bluff Bodies and Road Vehicles*, (Editors G. Sovran et al.), Plenum Press, New York, 1978, pp. 7-40.

2 Morel, T., "The Effect of Base Slant on the Flow Pattern and Drag of Three Dimensional Bodies With Blunt Ends," *Symposium Proceedings*, ref. [1], pp. 191-226.

3 Riegels, F. W. and Wuest, W., "Der 3-m-Windkanal der Aerodynamischen Versuchsanstalt Gottingen," *Zeitschrift fur Flugwissenschaften*, No. 9, 1961, pp. 222-228.

4 Ahmed, S. R., and Hucho, W.-H., "The Calculation of Flow Field Past a Van With the Aid of a Panel Method," Paper No. 770390, 1977, Society of Automotive Engineers, Inc.

5 Ahmed, S. R., and Baumert, W., "The Structure of Wake Flow Behind Road Vehicles," Symposium on Aerodynamics of Transportation, (Editors T. Morel et al.), ASME, New York, 1979, pp. 93-103.

6 Ahmed, S. R., "Wake Structure of Typical Automobile Shapes." ASME Journal of Fluids Engineering, Vol. 103, 1981, pp. 162-169.

7 Tanner, M., "Totwasserbeeinflussung bei Keilströmungen," DLR-Forschungsbericht 64-39, 1964.

8 Tanner, M., "Druckverteilungsmessungen an Kegeln," DLR-Forschungsbericht 65-09, 1965.

9 Kapoor, K., "Effect of Radial Fins on Base Drag of an Axisymmetric Body at Low Speeds," *Journal of Spacecraft*, Vol. 19, No. 1, 1982, pp. 89-92.

10 Hummel, D., "Zur Umströmung scharfkantiger schlanker Delta-flügel bei gröweren Anstellwinkeln," *Zeitschrift für Flugwissenschaften*, No. 15, 1967, pp. 376-185.

T. Motohashi[1]

R. F. Blackwelder
Professor.

Department of Aerospace Engineering,
University of Southern California,
Los Angeles, Calif. 90089-1454

Decreasing the Side Wall Contamination in Wind Tunnels

To study boundary layers in the transitional Reynolds number regime, the useful spanwise and streamwise extent of wind tunnels is often limited by turbulent fluid emanating from the side walls. Some or all of the turbulent fluid can be removed by sucking fluid out at the corners, as suggested by Amini [1]. It is shown that by optimizing the suction slot width, the side wall contamination can be dramatically decreased without a concomitant three-dimensional distortion of the laminar boundary layer.

Introduction

Operating test facilities in regimes necessary to study boundary layer transition is known to be fraught with problems. Indeed, the operating requirements are so rigid that it was only after years of wind tunnel development and testing that Schubauer and Skramstad [2] were able to identify Tollmien-Schlichting waves in a zero pressure gradient laminar boundary layer. Although present day wind tunnels are much improved, an extreme amount of diligence and care are required to establish appropriate experimental conditions such as smooth test models, low free stream turbulence, etc. However in spite of careful preparations, to study transition the facility must be operated within a Reynolds number regime where small disturbances will be amplified which makes the experimental tasks more difficult.

Usually the test model, such as a flat plate or airfoil, is attached to the side walls or other support mechanism. This almost always distorts the mean flow field and produces a turbulence region which begins at or near the corner and grows downstream. Charters [3] and others have shown that this turbulence encroaches upon the laminar flow field very rapidly downstream; i.e., it spreads typically at a 10 deg angle with respect to the downstream direction. This large growth angle severely limits the useful spanwise extent of the test model. In addition, the pressure fluctuations associated with the turbulence generated from the side walls can contaminate the remaining laminar region causing it to prematurely transition.

Amini [1] apparently was the first to attack this problem by applying suction at the corners to remove the growing turbulent regions. His test model was a 3 m long flat plate 65 cm wide with a turbulent spot generator located 30 cm downstream of the leading edge. Slots between the plate and the sidewalls were used to remove the turbulent fluid. The slots were 2 mm wide near the leading edge and decreased to 1 mm at 1.5 m downstream of the leading edge. A slight overpressure on the working side of the plate was created by a flat at the downstream end of the plate, thus removing the side wall contamination through the slots. Unfortunately, so much fluid was removed that the laminar boundary layer quickly deviated from a two-dimensional one. At 60 cm downstream from the leading edge, the laminar boundary layer displacement thickness, δ^*, at $z = \pm 24$ cm showed a significant departure from that measured along the centerline. Although Amini did notice a significant improvement in the repeatability of the generated turbulent spots, the useful streamwise extent of his model was not increased due to the departure from two-dimensionality. The present research was undertaken to determine if a more optimum distribution of the slot width could be found which would provide a larger usable area on the test model.

Experimental Conditions

The Dryden Wind Tunnel at USC was used for this investigation. This is the same tunnel used by Schubauer and Skramstad [2] and details of the tunnel configuration are found in their investigation. A 1.3 cm thick aluminum plate 550 cm long and 133 cm wide sketched in Fig. 1 was mounted horizontally in the octagonal test section. Note that the usual 10 deg side wall contamination as sketched indicates that much less than half of the plate would have a laminar boundary layer at transitional Reynolds numbers. The coordinate system has it origin on the centerline of the leading edge which had an elliptical nose. A flap having a 63 cm chord was attached to the trailing edge and was set at typically 7 and

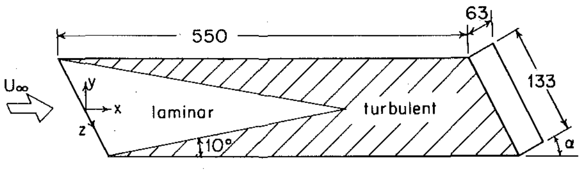

Fig. 1 Sketch of the test model showing the extent of the contaminated turbulent region due to the side wall contamination

---

[1] Assistant Professor, Department of Aerospace Engineering, Nihon University, Chiba, Japan.

Contributed by the Fluids Engineering Division for publication in the JOURNAL OF FLUIDS ENGINEERING. Manuscript received by the Fluids Engineering Division, November 24, 1982.

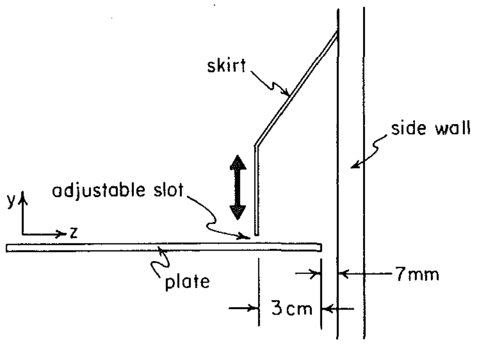

Fig. 2 Sketch of the plate, the side wall, and the adjustable skirt.

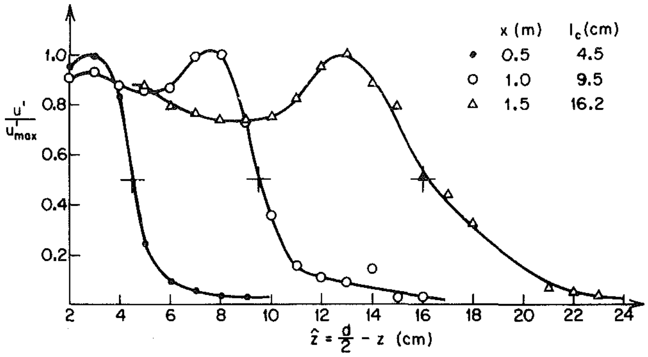

Fig. 3 The measured rms streamwise velocity fluctuations at three positions downstream

12 deg ±0.25 deg. A 6 mm × 6 mm mesh screen was positioned in the y-z plane at the end of the plate to insure a higher pressure on the working side. Forty 0.5 mm diameter pressure taps on the plate measured the pressure distribution in the x-z plane. On the working side of the plate, skirts with adjustable slots were mounted along the side walls as sketched in Fig. 2. The skirts could be raised and lowered thus forming slot openings between 0 and 6 mm along the entire length of the plate.

The velocity data were obtained using constant-temperature hot-wire anemometers described by Blackwelder and Kaplan [4]. All data were digitized at typical rates of 1000 samples/s under control of a DEC 11/55 computer and stored on either magnetic disk packs or tapes. Prior to data collection, the hot-wire sensors were always calibrated in the free stream against an MKS Baratron pressure transducer. During a data run, the hotwire was frequently moved to the free stream to determine that no drift had occurred. If errors greater than 3 percent were obtained when compared with the pressure transducer, the data were discarded, a new calibration was obtained and the experiment proceeded. The uncertainty in the mean velocity measurements was approximately 5 percent and the repeatability of the rms velocity values was roughly 8 percent. The position of the hot-wire sensors during calibration and data gathering was determined by a three-dimensional traverse under software control. The accuracy of the traverse movement in the x, y, and z directions were 0.1, 0.025 and 0.05 mm, respectively. Linearization and further data processing were accomplished using FORTRAN programs on the 11/55 computer. Data were displayed graphically on a 4010 Tektronix terminal.

Results

The location of the contamination region is characterized by a virtual origin and an angle depicting its growth rate. These parameters were determined experimentally by finding the spanwise position where the turbulent intensity decreased to half of its maximum value. A traverse in the spanwise direction at a constant elevation of 0.3 cm above the plate was taken at $U_\infty = 4.2$ m/s and the rms streamwise velocity values were recorded as shown in Fig. 3. The rms velocities are normalized with respect to their maximum values and the data are plotted versus $\hat{z} = d/2 - z$ where d is the width of the plate between the skirts. Note that the slope of $u'(z)$ decreases as the streamwise distance increases indicating that the standard deviation of the position of the laminar-turbulent interface increases downstream. At each streamwise location, the boundary of the transverse contamination region, l_c, was defined to be the position at which $u'(l_c) = 0.5u'_{\max}$. A peak in the spanwise distribution was always found nearer the sidewall, i.e., at $\hat{z} < l_c$. This is associated with the large difference in the mean values of the velocity between the laminar and turbulent boundary layers. If the position of the peaks were used to define the interface, the growth angles were the same as defined by l_c above, however, the virtual origins were different.

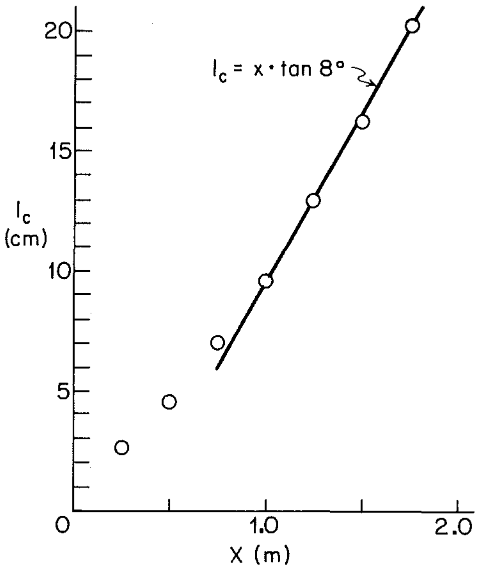

Fig. 4 Typical growth of the contaminated region with $U_\infty = 4.2$m/s and $\alpha = 7$ deg

The resultant locus of the transverse contamination region

Nomenclature

d = width of plate
l_c = spanwise length of contamination
Re = Reynolds number $U_\infty x/\nu$
u' = streamwise velocity fluctuation value
U_∞ = free stream velocity
x = distance downstream of leading edge
y = distance perpendicular to the plate
z = spanwise coordinate
$\hat{z}$ = distance from side wall
α = flap angle
δ^* = displacement thickness
θ = contamination angle
ν = kinematic viscosity

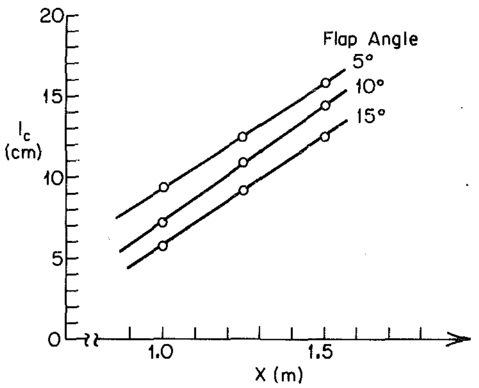

Fig. 5 The effect of the flap angle on the growth of the contaminated region. $U_\infty = 4.2$ m/s.

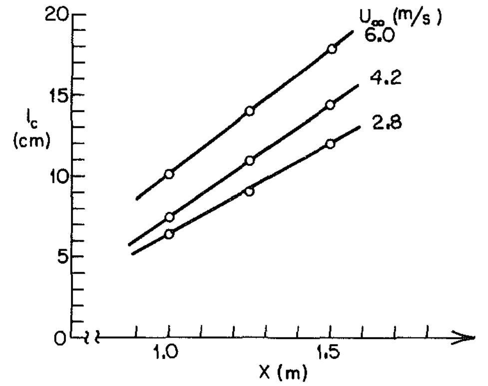

Fig. 6 The effect of the free stream velocity on the growth of the contaminated region. $\alpha = 10$ deg

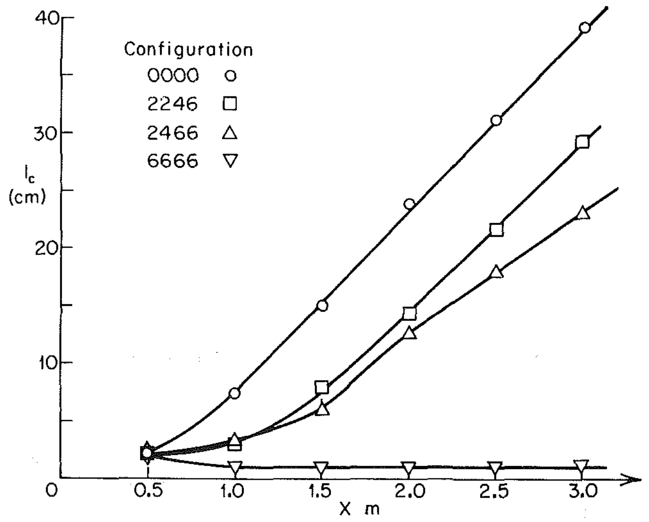

Fig. 7 The variations of the contaminated region as a function of the skirt openings. $U_\infty = 5.0$ m/s, $\alpha = 12$ deg

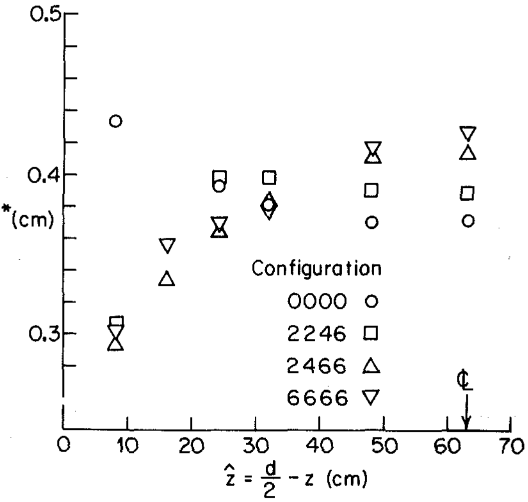

Fig. 8 Variation of the boundary layer displacement thickness for different skirt openings. $U_\infty = 5.0$ m/s, $\alpha = 12$ deg

is shown in Fig. 4 for a free steam velocity of 4.2 m/s and a flap angle of 7 deg. This base line data was obtained with the skirts completely closed. Initially the contamination grows at 5.3 deg but approaches as asymptotic value of 8 deg for $x > 0.8$ meters. Extrapolating the asymptotic value upstream yields a virtual origin at $x = 30$ cm. At this location, the Reynolds number is $U_\infty x/\nu = 85{,}000$; i.e., approximately the Reynolds number at which the flow becomes unstable to Tollmien-Schlichting waves.

The effect of the flap angle and free stream velocity on the side wall contamination are found in Figs. 5 and 6, respectively. Increasing the rear flap angle introduced a more positive pressure difference between the working and back side of the test model. This more favorable pressure difference increased the virtual origin of the contamination but did not affect its growth rate. On the other hand, increasing the free stream velocity alters both parameters. It is interesting to note that the virtual origin is typically located at $U_\infty x/\nu \sim 10^5$ near where the boundary layer first becomes unstable. The contamination angle increases from 6.4 deg to 8.7 deg as the Reynolds number (i.e., U_∞) increases. A similar increase in the asymptotic growth of turbulent spots was reported by Schubauer and Klebanoff [5].

Four different skirt configurations were tested. Each section of the skirts was 91 cm long in the streamwise direction and could be opened independently. The different configurations were denoted by a four digit number: e.g., 2466 indicated the first skirt was opened 2 mm, the second one 4 mm, etc. Beyond the fourth skirt, the remaining ones had the same opened position as the fourth one.

With $\alpha = 12$ deg and all the slots opened 6 mm, no turbulent side wall contamination was observed over the first three meters of the plate as shown in Fig. 7. At more moderate openings, intermediate contamination was found. The asymptotic growth angle was always 7-9 deg and was relatively unchanged with slot widths. However, the greatest improvement is the virtual origin of the contaminated region was moved downstream.

The two-dimensionality of the boundary layers is illustrated in Fig. 8, two meters downstream of the leading edge. With all the slots closed, the displacement thickness increased near the side wall, i.e., as $\hat{z} \to 0$, due to the turbulent boundary layers there. When all the slots were opened, a Blasius value was obtained on the centerline, but a decrease in δ^* occurs as the side walls were approached because fluid was being removed there, thus thinning the boundary layer. However, for the intermediate slot openings, δ^* only decreased 10 percent at $\hat{z} = 20$ cm at a Reynolds number of $U_\infty x/\nu = 650{,}000$. Thus a large spanwise extent over a meter wide was available for testing with less than a 10 percent deviation of the boundary layer thickness.

Conclusions

By carefully adjusting slots along the edges of a flat plate, the side wall contamination of turbulence could be reduced so that a larger region of laminar boundary layers was available for testing. The spanwise width of the laminar region was essentially doubled. The length also doubled, at least at the lower Reynolds numbers, so that the useful test area was increased by a factor of four. Thus, more comprehensive studies of transitional bounary layers at larger Re_x will be possible with this modification.

Acknowledgements

The authors thank Joe Haritonidis for overseeing the installation and instrumentation of the flat plate and the skirts. The automation of the data gathering was made possible by Dick Kaplan. The keen interest and encouragement of the late John Laufer were much appreciated. The support of the Air Force Office of Scientific Research under Contract F49620-78-C-0060 monitored by Capt. Mike Francis is gratefully acknowledged.

References

1 Amini, J., "Transition controllee en couche limite: Etude experimentale du development d' une perturbation tridimensionelle instantanee," Ph.D thesis, University of Grenoble, 1978.

2 Schubauer, G. B., and Skramstad, H. K., "Laminar Boundary Layer Oscillations on a Flat Plate," N.A.C.A. Report No. 909, 1948.

3 Charters, Alex C., "Transition Between Laminar and Turbulent Flow by Transverse Contamination," N.A.C.A. TN 891, 1943.

4 Blackwelder, R. F., and Kaplan, R. E., "On the Wall Structure in Turbulent Boundary Layers," *J. Fluid Mech.*, Vol. 76, 1976, p. 89.

5 Schubauer, G. B., and Klebanoff, P. S., "Contributions on the Mechanics of Boundary Layer Transition," N.A.C.A. Report No. 1289, 1955.

Measurement of a Recirculating, Two-Dimensional, Turbulent Flow and Comparison to Turbulence Model Predictions. I: Steady State Case

D. R. Boyle

M. W. Golay

Department of Nuclear Engineering,
Massachusetts Institute of Technology,
Cambridge, Mass. 02139

Turbulent flow measurements have been performed in a two-dimensional flow cell which is a 1/15-scale model of the Fast Flux Test Facility nuclear reactor outlet plenum. In a steady water flow, maps of the mean velocity field, turbulence kinetic energy, and Reynolds stress have been obtained using a laser doppler anemometer. The measurements are compared to numerical simulations using both the $K-\epsilon$ *and* $K-\sigma$ *two-equation turbulence models. A relationship between* $K-\sigma$ *and* $K-\epsilon$ *turbulence models is derived, and the two models are found to be nearly equivalent. The steady-state mean velocity data are predicted well through-out most of the test cell. Calculated spatial distributions of the scalar turbulence quantities are qualitatively similar for both models; however, the predicted distributions do not match the data over major portions of the flow area. The* $K-\sigma$ *model provides better estimates of the turbulence quantity magnitudes. The predicted results are highly sensitive to small changes in the turbulence model constants and depend heavily on the levels of inlet turbulence. However, important differences between prediction and measurement cannot be significantly reduced by simple changes to the model's constants.*

Introduction

In recent years interest has grown in the use of turbulent fluid dynamic simulations in engineering design analysis. In such analyses, questions regarding the universality of the turbulence model being used and the appropriateness of the numerical representation of the physical problem (e.g., spatial resolution, boundary condition treatments, and truncation error effects) often arise. A difficulty in answering these classes of questions is that the experimental data which could be used to verify the physical modelling assumptions which must be made either are not available or are derived from experiments much simpler than the case of design interest (e.g., jet boundary layer, shear layer flows, and grid-induced turbulent flows).

The work reported here was performed in the hope of improving this situation. It consists of an experimental effort resulting in a set of turbulence and mean-flow data, which may be of value for validation calculations, and a computational effort to reproduce the measured results. The latter effort illustrates some important effects, which may be of interest to engineering analysts, of the variation of the turbulence model free parameters used in a simulation. This work is reported by Boyle and Golay in greater detail elsewhere [1].

Experimental Work

This effort was performed as part of the United States Liquid-Metal-Cooled Fast Breeder Reactor (LMFBR) program. For that reason the geometry studied is a two-dimensional, greatly-simplified flow cell which preserves the important length-scale ratios of the Fast Flux Test Facility (FFTF) reactor outlet plenum. The flow cell cross section is shown in Fig. 1.

Description of the Case Measured. The test geometry was made two-dimensional (the cell is geometrically uniform in the direction (z) normal to the plane of Fig. 1 with a depth of 6.08 cm). This was done in order to provide experimental data which could be compared directly to the results of two-dimensional fluid dynamic numerical simulations. Although the use of a two-dimensional case is justified on the basis of economy, it is employed mainly because the vast majority of turbulent fluid dynamic simulations currently are performed using two-, rather than three-, dimensional codes. In the

---

Contributed by the Fluids Engineering Division and presented at the Winter Annual Meeting, Boston, Mass., November 14-18, 1983, of THE AMERICAN SOCIETY OF MECHANICAL ENGINEERS. Manuscript received by the Fluids Engineering Division, December 2, 1981. Paper No. 83-WA/FE-8.

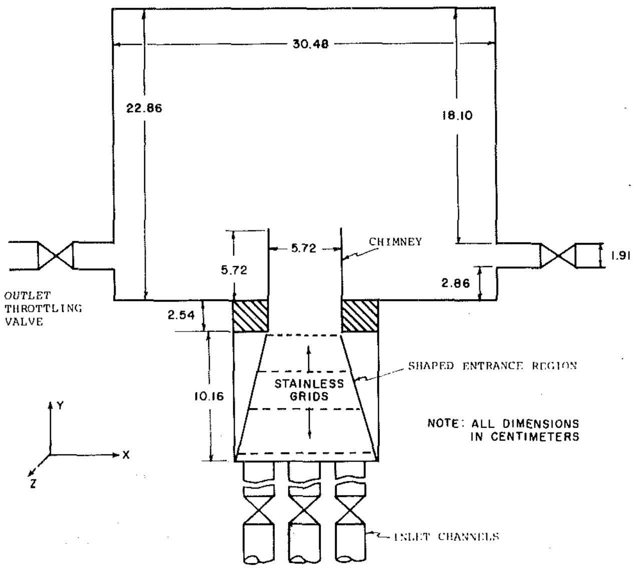

Fig. 1 Two-dimensional flow cell, 1/15 scale outlet plenum model of the Fast Flux Test Facility nuclear reactor

measurements, care was taken to ensure that data were recorded only in an asymptotic central region of the test cell where velocity gradients in the normal (z) direction were either zero or at a minimal value. Cross-cell measurements indicated that this zone occurred at the midplane, equidistant between the two faceplates throughout most of the cell.[1] All data were obtained in the cell midplane.

In the initial design of the experiment, high levels of strongly anisotropic turbulence and a spatially-peaked velocity distribution were observed at the inlet of the test cell. Figure 1 depicts the series of stainless steel screens which were subsequently installed in the inlet chimney in order to flatten the inlet velocity distribution and reduce the inlet turbulence levels. This modification provided approximately isotropic inlet turbulence and it enhanced the symmetry and two-dimensionality of the overall flow.

Experimental Apparatus and Method

In the measurements a dual-channel Laser Doppler Anemometer (LDA) observed the following turbulence quantities in a steady flow in water: two orthogonal velocity components (U and V), the turbulent kinetic energy ($K_{\text{Measured,2D}} \equiv \frac{1}{2}(\overline{u'^2} + \overline{v'^2})$),[2] and the velocity cross correlation ($\overline{u'v'}$). These quantities were measured at seventy-nine regularly spaced points on a plane centered between the two Plexiglas faceplates of the cell. Stationarity in the data was obtained by using a combination of time- and ensemble-averaging in order to provide the equivalent of 100 seconds of signal integration time for each measurement. The flow was carefully balanced to achieve symmetry so that measurements and calculations needed to be made in only half of the test cell.

Fluid Dynamic Simulation Program

The fluid dynamic simulations were performed using the computer code VARR-II [2]. It solves the incompressible mean-flow Navier-Stokes equations in two dimensions using the Simplified Marker and Cell (SMAC) algorithm [3]. Turbulent diffusion is treated using a turbulent viscosity obtained from a turbulence model. Steady flows are computed as the asymptotically-steady, long-term transient simulations, starting from arbitrary initial conditions and corresponding to steady boundary conditions. The boundary conditions and mesh configuration are described in Appendix B.

Turbulence Model Used

The main turbulence model used in this work is the two-equation $K-\sigma$ turbulence model of Stuhmiller [4] summarized in Appendix A (K is turbulence kinetic energy, and σ is turbulence viscosity). Turbulence models must use a set of closure assumptions to reduce the time-averaged turbulence conservation equations used in the model to a closed form expressible in terms of mean-flow quantities. Doing this involves using assumed relationships between averaged

---

[1] Boundary layer thickness estimations also indicate that the asymptotic region would be expected to occupy more than 85 percent of the cell thickness at any data coordinate.

[2] The quantity $K_{\text{Measured,2D}}$ defines the measured value of K obtained from the two-dimensional flow measurements. In any flow K is the quantity defined as

$$K \equiv \frac{1}{2}(\overline{u'^2} + \overline{v'^2} + \overline{w'^2})$$

The term $\overline{w'^2}$ is nonzero, although both W and all z-direction derivatives are equal to zero. In nearly isotropic turbulence (the case of this work)

$$\overline{u'^2} \cong \overline{v'^2} \cong \overline{w'^2})$$

Thus, the approximation

$$K_{\text{Measured}} \cong K_{\text{Measured,2D}} X 1.5$$

may be used. In all comparisons of data and calculations in this work the value of K_{Measured} stated is that of $K_{\text{Measured,2D}}$. However, correction of these values by the factor 1.5 may be desirable in comparisons to calculated results.

Nomenclature

$\alpha,\alpha_1,\Gamma,\Gamma_1$ = constants appearing in transport equations of $K-\sigma$ model
C_1,C_2,C_μ = constants appearing in transport equations of $K-\epsilon$ model
ϵ = turbulent energy dissipation rate
K = turbulent kinetic energy
l = length scale or Prandtl's mixing length
P = pressure
ρ = density of the fluid
σ = turbulent kinematic viscosity
σ_K,σ_ϵ = effective turbulent Prandtl numbers for transport of K and ϵ in the $K-\epsilon$ turbulence model
t = time
θ = half angle of laser beam intersection in laser doppler aneometer
U = mean velocity (vertical or X direction)
U_i = velocity component in i direction
$\overline{u'v'}$ = kinematic shear stress
u',v',w' = fluctuating velocity components
V = mean velocity (horizontal or Y direction)
W = mean velocity (normal or Z direction)
x_i,x_j = general Cartesian coordinate

Table 1 Measured mean velocity components

Position(a) I	J	$\bar{U}$ [m/s]	$\bar{V}$ [m/s]	Position(a) I	J	$\bar{U}$ [m/s]	$\bar{V}$ [m/s]
5	6	0.106	~0	14	2	0.757	0.016
	8	−0.029	−0.031		4	0.730	0.067
	10	−0.135	−0.064		6	0.164	0.024
	12	−0.255	−0.067		8	0.077	0.028
	14	−0.393	0.027		10	−0.029	0.038
	16	−0.538	0.304		12	−0.265	0.023
	17	−0.477	0.623		14	−0.499	−0.014
					16	−0.671	−0.022
6	6	0.132	~0				
	8	0.017	−0.028	16	2	0.740	0.014
	10	−0.081	−0.079		4	0.729	0.009
	12	−0.202	−0.066		6	0.156	0.029
	14	−0.387	0.036		8	0.055	0.030
	16	−0.646	0.298		10	−0.045	0.038
	17	−0.864	0.655		12	−0.297	0.031
					14	−0.471	−0.009
7.5	2	0.804	−0.006		16	−0.674	−0.011
	3	0.823	0.015				
	4	0.771	0.036	18	2	0.664	0.032
					4	0.670	0.153
8	6	0.160	−0.007		6	0.235	0.103
	8	0.078	−0.028		8	0.053	0.063
	10	~0	−0.047		10	−0.064	0.058
	12	−0.191	−0.010		12	−0.304	0.065
	14	−0.462	0.018		14	−0.406	0.032
	16	−0.759	0.072		16	−0.617	0.025
10	2	0.798	0.014	20	2	0.560	0.045
	4	0.762	0.042		4	0.603	0.204
	6	0.153	0.023		6	0.376	0.268
	8	0.092	~0		8	0.072	0.134
	10	~0	0.010		10	−0.081	0.095
	12	−0.182	0.027		12	−0.223	0.107
	14	−0.475	−0.010		14	−0.295	0.060
	16	−0.724	−0.011		16	−0.560	0.051
12	2	0.779	~0	22	2	0.449	0.048
	4	0.738	0.035		4	0.478	0.233
	6	0.155	0.008		6	0.445	0.442
	8	0.090	0.008		8	0.212	0.393
	10	0.032	0.025		10	0.030	0.258
	12	−0.251	0.015		12	−0.084	0.199
	14	−0.509	−0.021		14	−0.234	0.180
	16	−0.712	−0.028		16	−0.444	0.144

(a) Position coordinates, *I* and *J*, of the data are illustrated in Fig. B.1. In each case the data are measured at the center of the *I*, *J*-th computational cell.

turbulence quantities (e.g., *K* and Reynolds stress) and mean-flow quantities, and reduction of the number of dependent variables to that of the conservation equations. The proof of the quality of these closure assumptions is in their experimental verification. Currently the most complicated such models used for engineering analysis are two-equation models consisting of two differential turbulence quantity conservation equations; one turbulence quantity is usually *K*, and the other differs between models. Attempts at formulation of a second equation for such quantities as the turbulence length scale, *l*, [5], and the product *Kl* [6], the turbulent viscosity, σ, [4], and the turbulence dissipation rate, ϵ [7, 8], among others, are reported in the literature. Generally, the turbulence conservation equations are cast into the form of the time rate-of-change of the turbulence quantity being the net result of local source and sink terms and convective and diffusive transport (for an example, see Appendix A).

In this work the well-known $K-\epsilon$ turbulence model of Launder and associates [7, 8] was also used for numerical simulations (mainly because of the relative obscurity of the $K-\sigma$ model). It is shown in Appendix A that the two models are almost equivalent mathematically, and it is seen in the discussion of the results that they produce very similar predictions. The version of the $K-\epsilon$ model used is an equivalent form of that published in the TEACH-T fluid flow simulation computer program [9].

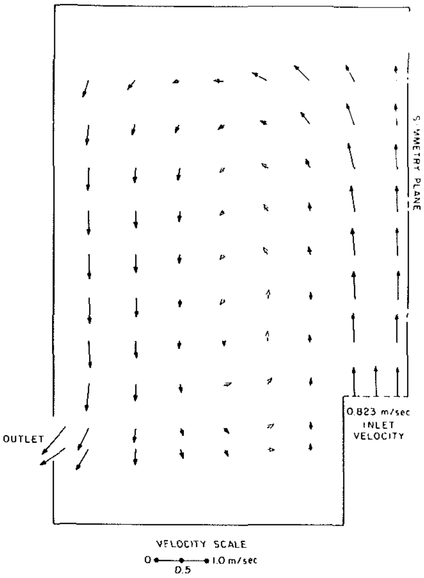

Fig. 2 Measured mean-flow velocity field

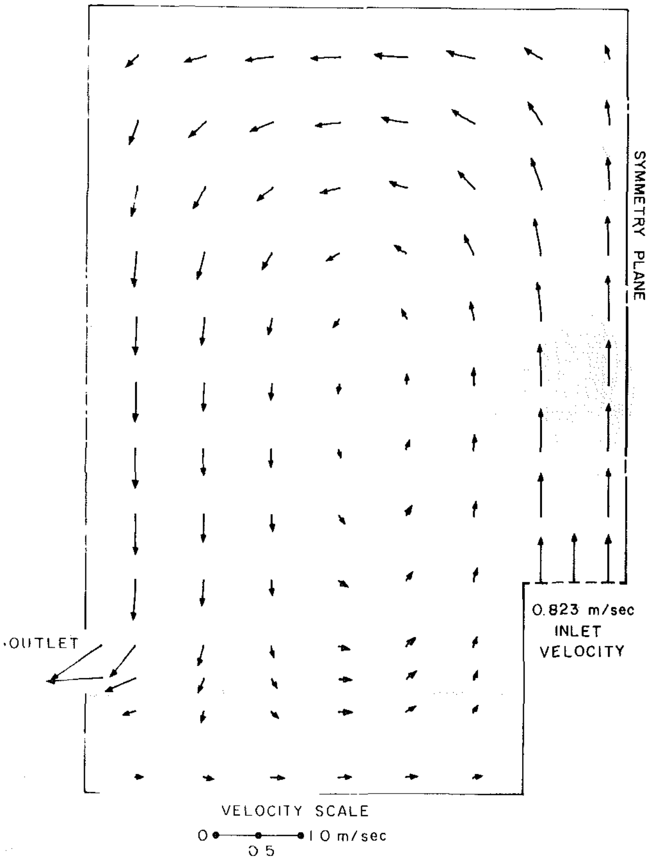

Fig. 3 Calculated mean-flow velocity field, using $K-\sigma$ turbulence model. Inlet velocity = 0.823 m/s

Discussion of Results

The steady-state, full-flow condition refers to a constant flow rate into the test cell corresponding to a Reynolds number of 70,000 based on the chimney width. Experimental errors result from the uncertainties in the LDA measurement technique and inaccuracies of the associated electronic instrumentation. The error analysis includes contributions from uncertainty in θ, broadening of the Doppler signal, and inaccuracies of individual electronic components. As is explained in detail in [1], the method of Wilson [12] is used for the compounding of errors arising from multiple sources. The resulting experimental errors are approximately 4 percent for the mean velocity, 8 percent for K, and 25 percent for the Reynolds stress.

Mean Velocity Results. The measured mean velocity vectors are plotted in Fig. 2 over one-half of the symmetrical test cell. They exhibit a recirculating flow pattern over the main body of the cell. The measured vertical and horizontal velocity components at the various measurement positions are summarized in Table 1.

The measured data were obtained at different instants at the various measurement points. As a test of the consistency of the data it was required that the inlet mass flowrate obtained from the detailed measurements agree with the independently measured flowrate in the return portion of the flow loop. An additional test of the two-dimensionality of the data is the requirement that the two-dimensional velocity field satisfy the local condition of continuity (or mass conservation). The required mass balances are obtained by computing area-weighted vertical flowrates and comparing total upflow to total downflow across each horizontal measurement plane. The relative difference between upflow and downflow is less than eight percent in each horizontal plane except those located at the vertical levels $I = 20$ and $I = 22$, as shown in Fig. B.1, where the flow differences are 12 and 43 percent, respectively. These discrepancies are readily observed in the velocity field of Fig. 2, and result from three-dimensional flow effects which occur when the inlet jet strikes the top of the cell. In this portion of the cell an asymptotic central flow region is not observed. However, over the major part of the vortex region, a good mass-flow balance obtains, and comparisons between prediction and experiment are confined to this region.

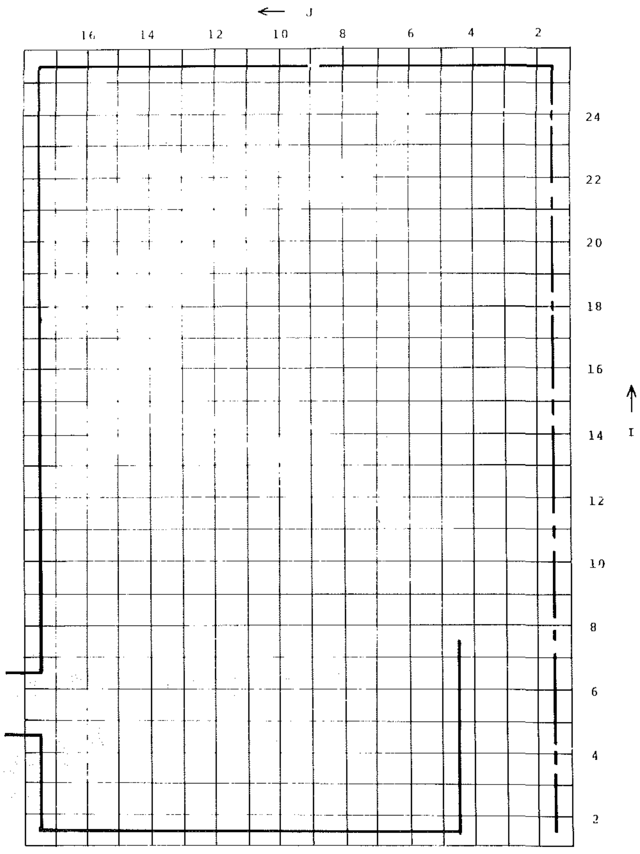

Fig. B.1 Schematic diagram of the 16 × 24 computational mesh

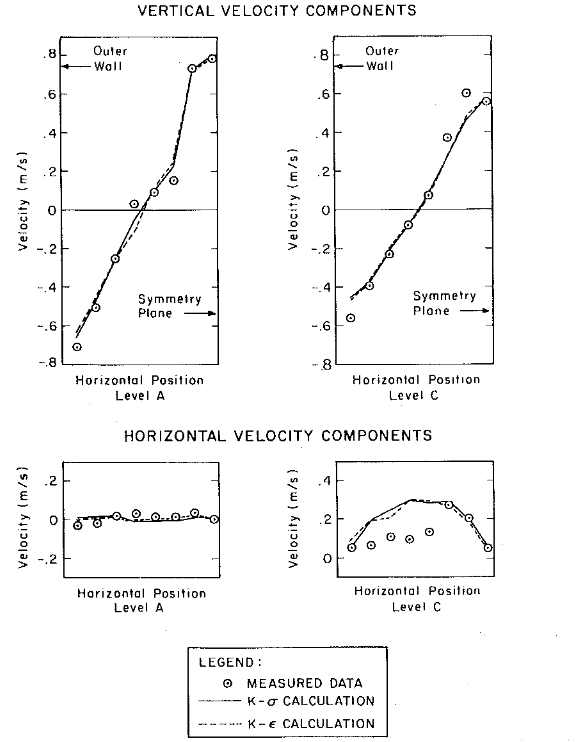

Fig. 4 Comparison of measured and calculated mean velocity components at two different vertical locations. (In Fig. B.1, $I = 12$ is level A, $I = 16$ is level B, and $I = 20$ is level C.)

Table 2 Summary of turbulence model sensitivity analysis based upon variation of model constants

Test Case No.	Turbulence model constants used α	Γ	σ	Γ_1	Decay rate of K in inlet jet	Relative magnitude of K at peak on upflow side of vortex	Convection of K to downflow side of vortex	Comments
Standard	0.045	1.5	0.01125	0.75	baseline	baseline	baseline	--
1	0.045	1.5	0.00563	0.75	impaired	impaired	slightly improved	--
2	0.045	1.5	0.0225	0.75	impaired	impaired	impaired	--
3	0.045	0.2	0.01125	0.1	impaired	impaired	impaired	--
4	0.045	4.0	0.01125	0.75	--	--	--	unstable
5	0.045	1.5	0.01125	1.5	slightly impaired	impaired	no effect	--
6	0.045	3.0	0.01125	1.5	no effect	improved	impaired	--
7	0.045	0.75	0.01125	0.375	impaired	impaired	no effect	--
8	0.035	1.5	0.01125	0.75	slightly improved	slightly improved	impaired	velocity field impaired
9	0.030	1.5	0.01125	0.75	improved	improved	much impaired	
10	0.060	1.5	0.01125	0.75	impaired	impaired	slightly improved	--
11	0.050	1.5	0.012	0.75	slightly impaired	slightly impaired	slightly improved	--
12	0.055	1.5	0.013	0.75	impaired	impaired	slightly improved	--
13	0.060	1.5	0.015	0.75	impaired	slightly improved	no effect	--

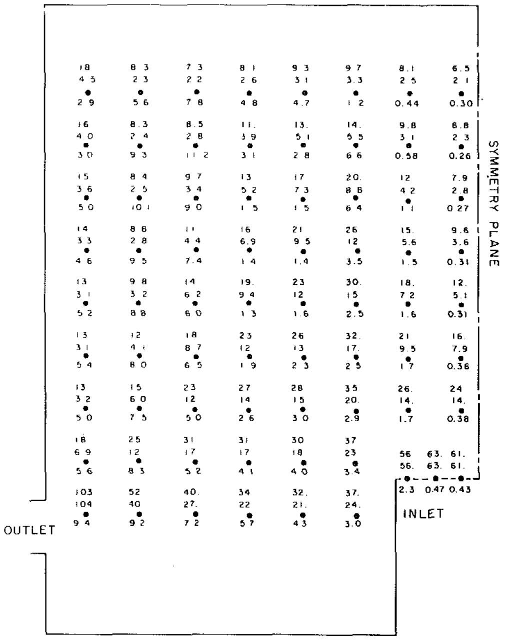

FORMAT AT EACH MEASUREMENT POINT:
K - ε PREDICTION
K - σ PREDICTION
• MEASUREMENT LOCATION
MEASURED DATA

Fig. 5 Comparison of measured and calculated turbulence kinetic energy fields, using both $K-\sigma$ and $K-\epsilon$ turbulence models, Units = $10^{-3}\ m^2/s^2$, $K_{Measured} = ½(\overline{u'^2} + \overline{v'^2})$.

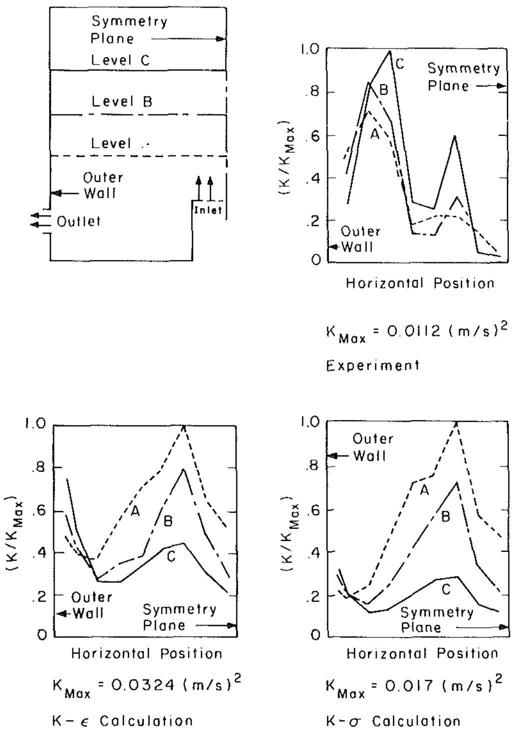

$K_{Max} = 0.0112\ (m/s)^2$
Experiment

$K_{Max} = 0.0324\ (m/s)^2$
K - ε Calculation

$K_{Max} = 0.017\ (m/s)^2$
K - σ Calculation

Fig. 6 Comparison of measured and calculated turbulence kinetic energy profiles across the flow cell at three different vertical locations, $K_{Measured} = ½(\overline{u'^2} + \overline{v'^2})$.

Figure 3 shows the calculated mean flow vector plot for the $K-\sigma$ model. The $K-\epsilon$ model result is essentially identical and is not reproduced. However, slight differences between the two models can be discerned in Fig. 4, where velocity measurements and predictions are compared graphically at two different levels in the test cell. These predictions of the steady-state flow field result from using the VARR-II code with the standard $K-\sigma$ turbulence model and the transformed $K-\epsilon$ model on a 16×24 Cartesian mesh. Only those velocities at mesh cells for which a measured velocity exists (approximately every other one) are depicted.

Comparison of the calculated fields with the experimental data shows generally good quantitative agreement. If one discounts the top row for three-dimensional effects in the experiment, the vortex center location is seen to be predicted well. The calculated vortex is elongated vertically, as in the experiment, but with a visibly milder vertical gradient of horizontal velocity near the top of the cell. The calculated upflow between the chimney entrance and the top boundary of the test cell overlies almost perfectly the experimental data, suggesting that good flow symmetry is obtained in the experiment. The steepest velocity gradients are found, in both the experiment and calculation, on the right side of the vortex adjacent to the inlet jet; however, the experimental results show a somewhat sharper gradient which persists over the top of the vortex and which is not predicted in the simulation. The gradient discrepancies are noted because they drive production of the turbulence quantities K and σ, and may explain the differences observed between the calculated and measured values of these quantities.

Turbulent Kinetic Energy (K). Figure 5 compares measured and calculated values of K throughout the test cell for both turbulence models. Significant differences are observed, even between the two calculations. A clearer picture is obtained by plotting K as a function of horizontal position at various heights in the cell. This is done at three representative locations in Fig. 6 for the data and both turbulence model predictions.

In the figure, throughout the main recirculation zone, the experimental data consistently show two characteristic peaks of K on either side of the vortex. The peaks occur in the regions where the velocity gradients are steepest, which is expected, since K can only be produced by mean flow shear. The peak in K on the inlet side increases monotonically as the fluid flows from just above the chimney to the top of the vortex. The inlet K level is significantly reduced from fully-developed flow values by screens in the entrance chimney of the test cell. Starting from this low value of K, the inlet flow is introduced into a region of high K production. As the level of K is increased by the strongly positive net production in this area of high shear, the fluid proceeds up along the inlet jet constantly increasing its K level in the same manner. The K built up in this fashion is convected along streamlines and contributes to the relatively larger K peak observed on the downflow side of the vortex. Here the velocity distribution shows a markedly reduced velocity gradient, and one expects the production of K to decrease. The data are consistent with this expectation: they show the initally high K level at the top of the vortex decreasing monotonically along the downflow streamline, indicating that the dissipation rate of K in this region has risen to the point where net production is negative.

Figure 6 also shows that the calculated K-distributions differ significantly from the experimental data: The location of the K peak on the upflow side of the vortex (in the region of high velocity shear) is predicted reliably by both models while the magnitude is overestimated somewhat. The $K-\sigma$ and $K-\epsilon$ distributions are similar, but the $K-\epsilon$ model provides a higher overestimate of magnitude and an apparent greater ability to convect K over the top of the vortex to the downflow side. The most striking disagreement between calculation and measurement is the absence of a predicted K peak on the downflow side of the vortex. A perceptible rise in K close to the wall, however, is observed in the calculations, and in fact

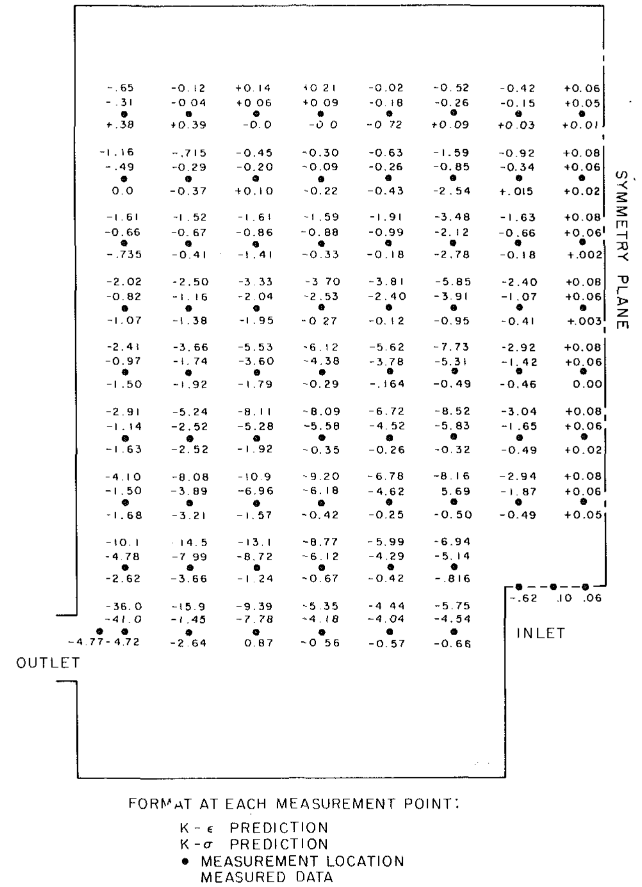

Fig. 7 Comparison of measured and calculated Reynolds stress fields, using both $K-\sigma$ and $K-\epsilon$ turbulence models, Units = kg/m s^2

decays along the downflow streamline in the same fashion as the data.

Reynolds Stress

The experimental and calculated steady-state Reynolds stress values throughout the test cell are depicted in Fig. 7. Comparison of the $K-\sigma$ and $K-\epsilon$ model estimates of Reynolds stress indicates qualitatively similar spatial distributions, with generally higher magnitudes in the $K-\epsilon$ case. Since calculated velocity gradients are approximately identical in both cases, one expects the calculated σ to be the main contributor to the differences, and this is in fact the case over most of the flow field. Reference to the K-transport equation shared by both models shows that, all other factors being equal, a higher value of σ will result in a net increase in the production rate of K. This is consistent with the overall higher levels of K obtained with the $K-\epsilon$ model. Moreover, these findings compare well with the results of similar calculations performed previously using these models in the same geometry [10]. Whether used in its original form in the TEACH-T code or in the $K-\sigma$-equivalent form in the modified VARR-II, the $K-\epsilon$ model consistently produces turbulence quantities that are higher than those predicted by the $K-\sigma$ model.

Comparison of the $K-\sigma$ Reynolds stress prediction with the data is generally poor over most of the main recirculating region with the notable exception of the downflow side of the vortex. Here data and prediction are in very good quantitative agreement. To emphasize the importance of correctly predicting σ and the Reynolds stress, note that, with the exception of the top part of the test-cell where three-dimensional flow effects are important, the major mean-flow discrepancies always correspond to points of significant disagreement between measured and calculated Reynolds stress.

Improving the Computed Predictions

The user-adjustable parameters in the $K-\sigma$ turbulence model that have the ability to change the calculated turbulence field for a given steady-state inlet flow rate are defined below:

1. Boundary conditions.
2. Inlet turbulence levels – the values of K and σ assigned to the inlet flow cells.
3. Turbulence model constants:
   α – dissipation coefficient for K,
   Γ – relative diffusivity coefficient for K,
   α_0 – dissipation coefficient for σ,
   Γ_1 = relative diffusivity coefficient for σ.

Based on physical interpretation of the data and comparison with the original calculated predictions, we have varied all of the above parameters in a systematic way to determine where the steady-state numerical prediction could be improved. Approximately 100 different combinations of the variables listed above were calculated, and an extensive discussion of this exercise is reported elsewhere [1]. As an example, a qualitative comparison of numerical predictions obtained by varying the turbulence model constants is described in Table 2. Overall, the results show that the calculated turbulence field and mean velocities are highly sensitive to changes in the boundary conditions, inlet turbulence levels, and model constants (although the mean flow is relatively insensitive to small changes in the model constants). In addition, the intricate coupling of the model transport equations is reflected in the complex response of the turbulence field to perturbations in the model constants. For example, increasing α, the K dissipation coefficient, results in higher values of K throughout the cell; decreasing α produces the opposite behavior. On the other hand, increasing α_0, the σ dissipation coefficient, decreases both σ and K; decreasing α_0 yields the opposite behavior. On balance, however, the numerical experiments indicate that no combination of revised boundary conditions, inlet turbulence levels, or turbulence model constants can improve significantly the initially-presented steady-state match between data and computation. This suggests that fundamental changes to at least some terms in the model equations are needed to improve the agreement.

It has also been suggested [11] that the disagreements in the turbulence fields predictions may be due to the use of a too-coarse computational mesh. Sensitivity analyses regarding the mesh size did not indicate that this was the case (see Appendix B); however, it was not possible to pursue this analysis to very fine-scale meshes where a different result might conceivably be obtained.

An order-of-magnitude analysis of the terms in the K-transport turbulence model equation shows that production and dissipation dominate over diffusion and advection throughout most of the flow in this problem. Further, although the data show a slight but persistent build-up of K with height above the chimney on the upflow side of the vortex, the models consistently show decay. Even when inlet K is matched to the lower experimental values (see Appendix B), the models quickly build to a high value of K that then begins to decay with height. Although it appears from the above that K-dissipation is being overestimated by the model, no tested change to the K-dissipation coefficient was able to correct this behavior. This suggests that a change in the form of the K-dissipation term may be needed.

Conclusions and Recommendations

Converting a two-equation $K-\epsilon$ turbulence model to a $K-$

σ form reveals that the two models are nearly identical in mathematical structure. Both models adequately predict the steady-state mean velocity fields. However, the general magnitudes of the scalar turbulence quantities, K and Reynolds stress, are consistently overestimated by the $K-\epsilon$ model. Both models fail to predict important features of the spatial distribution of these scalars.

The values of the scalar turbulence quantities at the inlet to the plenum strongly influence the numerical predictions. The computed turbulence field is also highly sensitive to the turbulence model constants. However, extensive adjustment of these factors does not materially improve the match between steady-state calculation and measurement.

The results of our numerical analysis suggest future work as follows: (1) examination and testing of alternative forms for the K- dissipation term, since successful prediction of the K spatial distribution is an important test of turbulence model generality; (2) use of a three-dimensional simulation to account for three-dimensional flow effects from the top part of the cell; (3) performance of numerical experiments to obtain a better understanding of the problems experienced in trying to match the inlet turbulence quantities to the experimental data; and (4) use of a finer mesh to improve the numerical simulation of the steep spatial gradients that occur in the region near the inlet.

Finally, the sensitivity of the computational predictions to small changes in the turbulence model constants is striking. The model constants are generally established in an approximate fashion from many data sources, and one would not expect the precision requirements of such constants to be high. It is possible that this sensitivity is problem-dependent, and it would be useful to know if the same sensitivity is seen in problems of larger scale.

References

1 Boyle, D. R., and Golay, M. W., "Transient Effects in Turbulence Modelling," U.S. Department of Energy Report DOE/ET/37240-83TR, MIT Nuclear Engineering Department, 1980, 275 pp.

2 Cook, J. L., and Nakayama, P. I., "VARR-II—A Computer Program for Calculating Time Dependent Turbulent Fluid Flows with Slight Density Variation," Report WARD-D-0106, Westinghouse Electric Corporation, Pittsburgh, Pa, 1975.

3 Amsden, A. A., and Harlow, F. H., "The SMAC Method: A Numerical Technique for Calculating Incompressible Fluid Flows," Report No. LA-4370, Los Alamos Scientific Laboratory, 1970.

4 Stuhmiller, J. H., "Development and Validation of a Two-Variable Turbulence Model," Report SAI-74-509-LJ, Science Applications, Inc., Palo Alto, Calif., 1974.

5 Harlow, F. H., and Nakayama, P. I., "Turbulence Transport Equations," *Physics of Fluids*, Vol. 10, 1967, pp. 2323–2332.

6 Rodi, W., and Spalding, D. B., "A Two-Equation Model of Turbulence and its Application to Free Jets," *Warme und Stoffubertragung*, Vol. 3, 1970, pp. 85–95.

7 Jones, W. P., and Launder, B. E., "The Prediction of Laminarization With a Two-Equation Model of Turbulence," *International J. Heat and Mass Transfer*, Vol. 15, 1972, pp. 301–314.

8 Launder, B. E., Reece, G. J., and Rodi, W., "Progress in the Development of a Reynolds-Stress Turbulence Closure," *J. Fluid Mech.*, Vol. 68, 1975, pp. 537–566.

9 The computer program TEACH-T, Imperial College of Science and Engineering, London, England, is reported in Notes on "Turbulent Recirculating Flow-Prediction and Measurement," College of Engineering, The Pennsylvania State University, July 28–August 1, 1975.

10 Chen, Y. B., and Golay, M. W., "Coolant Mixing in the LMFBR Outlet Plenum," U.S. Energy Research and Development Administration, Report COO-2245-44TR, MIT Nuclear Engineering Department, 1977.

11 Rodi, W., Personal Communication, 1980.

12 Wilson, E. B., Jr., *An Introduction to Scientific Research*, McGraw-Hill, New York, 1952.

13 Markatos, N. C. G., "Transient Flow and Heat Transfer of Liquid Sodium Coolant in the Outlet Plenum of a Fast Nuclear Reactor," *International Journal of Heat and Mass Transfer*, Vol. 21, 1978, pp. 1565–1579.

14 Bradshaw, P., "The Analogy Between Streamline Curvature and Buoyancy in Turbulent Shear Flow," *Journal of Fluid Mechanics*, Vol. 36, 1971, p. 1007.

15 Launder, B. E., Priddin, C. H., and Sharma, B. I., "The Calculation of Turbulent Boundary Layers on Spinning and Curved Surfaces," ASME JOURNAL OF FLUIDS ENGINEERING, Vol. 99, 1977, p. 231.

16 Launder, B. E., and Spalding, D. B., "Turbulence Models and Their Application to the Prediction of Internal Flows," Imperial College of Science and Technology (London) Report TM/TN/A/18, 1971, p. 9.

APPENDIX A

Turbulence Model Descriptions

The $K-\sigma$ and $K-\epsilon$ two-equation turbulence models are presented and the transformation of the $K-\epsilon$ model into a mathematically equivalent $K-\sigma$ model is demonstrated in this appendix.

The two-dimensional, mean-flow conservation equations solved in the numerical simulations of this work are the following:

Mass:

$$\frac{\partial U_i}{\partial x_i}=0, \text{ and} \tag{1}$$

Momentum:

$$\frac{\partial U_i}{\partial t}+U_j\frac{\partial U_i}{\partial x_j}=-\frac{\partial P}{\partial x_i}+\frac{\partial}{\partial x_j}\left(\sigma\frac{\partial U_i}{\partial x_j}\right) \tag{2}$$

subject to appropriate initial and boundary conditions. Equation (2) utilizes the assumptions that molecular diffusion may be neglected, as may the diffusional term $\partial U_j/\partial x_i \; \partial\sigma/\partial x_j$.

The turbulent viscosity, σ is obtained from either the $K-\sigma$ or $K-\epsilon$ turbulence models, which are described below.

The $K-\sigma$ Model

The $K-\sigma$ model equations are the following:

K-transport equation

$$\frac{\partial K}{\partial t}+U_j\frac{\partial K}{\partial x_j}=\frac{\sigma}{2}\left[\frac{\partial U_i}{\partial x_j}+\frac{\partial U_j}{\partial x_i}\right]^2 +\frac{\partial}{\partial x_j}\left[\Gamma\sigma\frac{\partial K}{\partial x_j}\right]-4\alpha\frac{K^2}{\sigma} \tag{3}$$

σ-transport equation

$$\frac{\partial\sigma}{\partial t}+U_j\frac{\partial\sigma}{\partial x_j}=\frac{\sigma^2}{4K}\left[\frac{\partial U_i}{\partial x_j}+\frac{\partial U_j}{\partial x_i}\right]^2+\frac{\sigma}{K}\frac{\partial}{\partial x_j}\left[\Gamma\sigma\frac{\partial K}{\partial x_j}\right] -\frac{\sigma^3}{K^2}\frac{\partial}{\partial x_j}\left[\Gamma_1 K\frac{\partial}{\partial x_j}\left(\frac{K}{\sigma}\right)\right]-4\sigma_1 K. \tag{4}$$

Here, Γ, α, Γ_1, and α_1 are the turbulence model constants, which are respectively equal to 1.5, 0.045, 0.75, and 0.01125.

The $K-\epsilon$ Model

The $K-\epsilon$ model used in this work is the version published in the program TEACH-T [9]. The $K-\epsilon$ model equations are the following:

K-transport equation

$$\frac{\partial K}{\partial t}+U_j\frac{\partial K}{\partial x_j}=\sigma\left(\frac{\partial U_i}{\partial x_j}+\frac{\partial U_j}{\partial x_i}\right)\frac{\partial U_i}{\partial x_j} +\frac{\partial}{\partial x_j}\left(\frac{\sigma}{\sigma_K}\frac{\partial K}{\partial x_j}\right)-\epsilon \tag{5}$$

$\epsilon-$transport equation

$$\frac{\partial\epsilon}{\partial t}+U_j\frac{\partial\epsilon}{\partial x_j}=\frac{C_1\sigma\epsilon}{K}\left[\frac{\partial U_i}{\partial x_j}+\frac{\partial U_j}{\partial x_i}\right]\frac{\partial U_i}{\partial x_j}+\frac{\partial}{\partial x_j}\left(\frac{\sigma}{\sigma_\epsilon}\frac{\partial\epsilon}{\partial x_j}\right) -C_2\frac{\epsilon^2}{K}. \tag{6}$$

Also, since σ as a function of time and space is the quantity of primary interest, this model requires use of the additional relation,

$$\sigma = \frac{C_\mu K^2}{\epsilon}. \tag{7}$$

Here, σ_K, C_1, σ_ϵ, C_2, and C_μ are the turbulence model constants, which are respectively equal to 1.0, 1.44, 1.3, 1.92, and 0.09.

$K-\epsilon$ to $K-\sigma$ Transformation

In order to use the $K-\epsilon$ model in the VARR-II code, we mathematically transform it into an equivalent $K-\sigma$ model. The desired transformation is obtained by using equation (7) to eliminate ϵ wherever it appears in equations (5) and (6), and by substituting the K-transport equation for the substantial derivative of K, equation (5) becomes

$$\frac{\partial K}{\partial t} + U_j \frac{\partial K}{\partial x_j} = \frac{\sigma}{2}\left(\frac{\partial U_i}{\partial x_j} + \frac{\partial U_j}{\partial x_i}\right)^2 + \frac{\partial}{\partial x_j}\left(\frac{\sigma}{\sigma_K}\frac{\partial K}{\partial x_j}\right) - C_\mu \frac{K^2}{\sigma} \tag{8}$$

and equation (6) becomes

$$\frac{\partial \sigma}{\partial t} + U_j \frac{\partial \sigma}{x_j} = \frac{\sigma^2}{K}\left(1 - \frac{C_1}{2}\right)\left(\frac{\partial U_i}{\partial x_j} + \frac{\partial U_j}{\partial x_i}\right)^2 + \frac{2\sigma}{K}\frac{\partial}{\partial x_j}\left(\frac{\sigma}{\sigma_K}\frac{\partial K}{\partial x_j}\right) - \frac{\sigma^3}{K^2}\frac{\partial}{\partial x_j}\left(\frac{2K}{\sigma_\epsilon}\right)\frac{\partial}{\partial x_j}\left(\frac{K}{\sigma}\right) - \frac{1}{\sigma_\epsilon}\left(\frac{\sigma}{K}\right)^4 \frac{\partial}{\partial x_j}\left(\frac{K^4}{\sigma^3}\frac{\partial \sigma}{\partial x_j}\right) - C_\mu(2 - C_2)K. \tag{9}$$

Equations (8) and (9) are simply reordered forms of equations (5), (6), and (7). In theory, with the exception of errors introduced by the finite difference approximations, use of equations (8) and (9) in a fluid dynamics simulation should produce the same results as use of equations (5), (6), and (7). In practice, truncation errors and differences in the treatment of boundary conditions can be expected to make the comparison less exact.

The near equivalence of the two models is demonstrated by the transformation. The two K-transport equations ((3) and (8)) are term-by-term identical, differing only in the values of the turbulence model constants. Even the more complex σ-transport equations ((4) and (9)) share identical terms with the only difference being an extra diffusionlike term, with coefficient $1/\sigma_\epsilon$, in equation (9).

APPENDIX B

Numerical Simulations

Computational Mesh. The 16 × 24 computational mesh used in this work is depicted in Fig. B.1. The experimental measurement locations are defined at the centers of the individual mesh cells.

Since the computer time requirements were very large for cases using this number of mesh cells, a series of preliminary numerical experiments were conducted using a modified 10 × 12 mesh. It was observed that the mean velocity pattern and turbulence levels obtained with this coarse mesh (10 × 12) compares well with the fine mesh (16 × 24) values. Thus, it was concluded that solutions obtained on the 16 × 24 mesh, at least with respect to the mean flow pattern, are not significantly degraded by numerical truncation errors. However, as is indicated in the boundary condition discussion, a finer mesh structure is probably needed immediately above the inlet in order to desribe the inlet jet accurately.

Boundary Conditions. The boundary conditions used in these calculations are the following:

- Free-slip on all solid boundaries (i.e., wall shear stress = 0).
- Free outflow at the exit (i.e., the horizontal velocity component on a cell exterior to the exit is matched to the horizontal velocity component of the adjacent interior cell).
- Specified profiles of mean velocity at each inlet cell.

The free-slip boundary condition was used in these calculations rather than the physically correct no-slip condition because the coarseness of the computational mesh used did not permit correct resolution of the boundary layer velocity distribution associated with the latter boundary condition. The alternative of using a "law of the wall" boundary condition treatment was not employed for reasons of computational economy. However, this was only done after comparison of results using both "law of the wall" and free-slip treatments of this flow during the initial set of experimental design calculations, in which it was seen that both treatments gave similar results (also see the results of Markatos [13] concerning this point). The free-slip boundary condition treatment of this problem provides reasonably accurate results because of the relatively small contribution of wall shear stresses to turbulence generation in comparison to the effects of flow curvature [14–16].

Inlet velocities are matched to the experimentally-observed values. Inlet turbulence kinetic energy and turbulence viscosity are each established by the code as a function of inlet velocity and mesh size. Since the inlet turbulence kinetic energy computed in this manner is significantly higher than the measured inlet values, numerical experiments were performed with the inlet K matched to measured values. Surprisingly, the spatial distribution of K produced by this matched inlet case predicts the experimental measurements more poorly than does the unmatched case. This anomaly is discussed more thoroughly in [1]; however, it is suspected that a much finer mesh is required for accurate computations in the region of the inlet jet. It is somewhat encouraging to note that, even with this large disparity between measured and computed K at the inlet, the turbulence model brings the overall K-levels into rough agreement with experiment a short distance away from the inlet.

Measurement of a Recirculating, Two-Dimensional, Turbulent Flow and Comparison to Turbulence Model Predictions. II: Transient Case

D. R. Boyle

M. W. Golay

Department of Nuclear Engineering,
Massachusetts Institute of Technology,
Cambridge, Mass. 02139

Measurements of transient water flows are performed in a 1/15-scale Fast Flux Test Facility nuclear reactor outlet plenum. During a repeated inlet-flow coastdown transient, measurements are made of the time-dependent, ensemble-averaged values of the velocity, turbulence kinetic energy, and Reynolds stress fields. These data are compared to predictions from a fluid dynamic simulation which uses a two-equation turbulence model. In general the comparison is good, and most observed transient disagreements can be attributed to errors in the calculation of the initial conditions rather than transient effects.

Introduction

To our knowledge there exist no published data obtained from transient turbulent flow measurements in cases of engineering interest. In the work reported here, such measurements have been performed. With generally satisfactory results, the data are compared to numerical predictions obtained using a two-equation turbulence model.

The purpose of this work is to provide a set of transient turbulent flow data for use in development of improved turbulence models for engineering applications, and to assess the ability of current models (which are based upon steady state experimental data) to predict the behavior observed in a case sufficiently complex and realistic to be relevant to many engineering analysis problems. This work is complementary to work reported by Boyle and Golay [1] comparing measured and numerically simulated steady-state turbulent flow fields. In both efforts the same flow cell, laser Doppler anemometer system, and flow simulation model were used.

Briefly, in this work isothermal flow coast-down transients were repetitively induced in a modeled reactor outlet plenum, and measurements were made at selected locations of the time-varying mean-flow and turbulence quantities in order to form ensemble-averages of the transient data. These data were then compared to the numerical predictions of transient turbulent flow simulations.

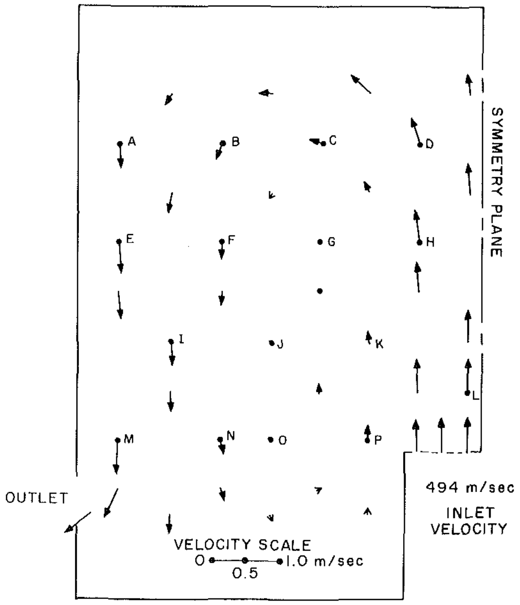

Fig. 1 Measured mean velocity field at 80 seconds into transient. The measurement error at each point of each data ensemble element is ± 5 percent of each velocity component. The uncertainty due to ensemble averaging is typically bound by ± 6 percent as illustrated in Fig. 3. The measurement stations labeled in Fig. 1 are each identified in terms of the coordinate system of Fig. B.1 of reference [1] as being at the center of the cell having coordinates I and J as follows:
Station A = Cell Coordinates (I = 20, J = 16); B = (20,12); C = (20,8); D = (20,4); E = (16,16); F = (16,12); G = (16,8); H = (16,4); I = (12,14); J = (12,10); K = (12,6); L = (10,2); M = (8,16); N = (8,12); O = (8,10); P = (8,6).

Experimental Work

Flow Geometry: The flow involved isothermal water in the two-dimensional flow cell shown in Fig. 1 of reference [1]. The cell is a 1/15 scale model of the outlet plenum of the Fast

---

Contributed by the Fluids Engineering Division and presented at the Winter Annual Meeting, Boston, Mass., November 13-18, 1983 of THE AMERICAN SOCIETY OF MECHANICAL ENGINEERS. Manuscript received by the Fluids Engineering Division, March 8, 1982. Paper No. 83-WA/FE-9.

Flux Test Facility nuclear reactor and is representative of a typical confined flow geometry of engineering design interest. The test geometry was made two-dimensional and, in the measurements, care was taken to insure that data were recorded only in an asymptotic central region of the test cell where velocity gradients in the normal (z) direction were either zero or at a minimal value. Cross-cell measurements indicated that this zone occurred at the midplane, equidistant between the two faceplates throughout most of the cell. All data were obtained in the cell midplane.

The flow was measured using a laser Doppler anemometer. The quantities measured were the mean-velocity components ($\bar{U}$ and $\bar{V}$), the turbulent kinetic energy ($K = \frac{1}{2}(\overline{u'^2} + \overline{v'^2})$), and the kinematic shear stress $(\overline{u'v'})$. The flow was carefully balanced to achieve symmetry in the test cell so that measurements and calculations need only be accomplished on one half of the cell. To obtain the steady-state flow initial conditions, measurements were made at seventy-nine regularly spaced points on a plane centered between the two Plexiglas face plates of the cell. Then during the transients, measurements were recorded at forty-two points (essentially every other one of the original seventy-nine points), while the inlet flow rate decreased in a prescribed fashion.

Flow Transients: The required flow transients were generated by a pneumatic control valve which caused the test cell inlet velocity to decrease to 34.7 percent of its initial value in 140 seconds. During this flow coast-down, the changing values of the turbulence quantities were recorded electronically. Use of repeated transients permitted computation of ensemble averages for all the measured quantities throughout the duration of the transient. The result is a series of time-sequenced "snapshot" plots of velocity vectors and a record of the values of average K and Reynolds stress over the entire test cell as a function of time during the transient. Important features of these data are discussed below; all the data and details of the electronics are reported more extensively elsewhere by Boyle and Golay [2].

Since the interest of this work concerns a transient flow, the customary approach to turbulence measurements (i.e., forming time-averages of the observed quantities) cannot be employed. Rather it is necessary to repeat the experiment a large number of times, record all variables of interest, and form ensemble-averages rather than time-averages. The number of repetitions required to form true ensemble-averages for all measurement points in this experiment is impractically large. Therefore, a unique measurement method has been developed that combines features of time and ensemble averaging to greatly reduce the number of experimental repetitions required and still provide adequate quantitative accuracy (see Appendix A).

Table 1 Flow coast-down transient percentage of measured inlet velocity versus time

Time (s)	Inlet velocity (Percent of initial full-flow value)
0	100.0 ± 5.0
10	99.4 ± 5.0
20	97.6 ± 4.9
30	94.3 ± 4.7
40	89.5 ± 4.5
50	83.1 ± 4.2
60	75.6 ± 3.8
70	67.7 ± 3.4
80	60.0 ± 3.0
90	53.2 ± 2.7
100	47.1 ± 2.4
110	41.8 ± 2.1
120	38.1 ± 2.0
130	35.6 ± 1.8
140	34.7 ± 1.8

The method is similar to that used for the measurement of transient turbulence phenomena in atmospheric and ocean flows [3]. In such cases, time-averages are formed using averaging times which are large with respect to the period of turbulent fluctuations, but small when compared to the time-scale of the diurnal or tidal variations which, strictly speaking, cause the mean values so obtained to be functions of time. The criterion to be met for successful application of this method is

$$t_{\text{turb}} << t_{\text{int}} << t_{\text{trans}}.$$

The objective in this experiment is to minimize t_{trans} so that time derivatives and their effects on the flow are enhanced. This constraint leads to a t_{int} which, though considerably larger than t_{turb}, is not large enough to produce a smooth, pseudo-constant function of time, but is small enough to follow the imposed transient to within a known small error. The characteristics of the electronic circuit used to integrate the signal determine this averaging method error. The important averaging errors are then functions of the experimental parameters and are held to less than one percent by the flow transient rate.

This averaging method error is superimposed upon steady measurement errors of 4 percent of the local mean flow

Nomenclature

C = the instantaneous local rate of convection of Q

D = the instantaneous local rate of diffusion of Q

F_j = the jth generalized transport or production term in the Q-conservation equation

K = ensemble-averaged turbulent kinetic energy

P = the instantaneous local rate of production of Q

Q = a general quantity transported in a flow

RS = ensemble-averaged Reynolds stress

S = the instantaneous local rate of destruction of Q

U = instantaneous vertical velocity

$\bar{U}$ = mean (ensemble-averaged) velocity (vertical or X direction)

$\bar{U}_i$ = mean (ensemble-averaged) velocity component in i-direction

$\bar{U}_t$ = time-averaged vertical velocity

$\bar{V}$ = mean (ensemble-averaged) velocity (horizontal or Y direction)

p = mean (ensemble-averaged) pressure

t = time

t_{int} = integration time of averaging device

t_{trans} = transient time scale

t_{turb} = turbulence time scale

$\overline{(u'v')}$ = ensemble-averaged kinematic shear stress

u', v', w' = fluctuating velocity components

x_i, x_j = general Cartesian coordinate

$\alpha, \alpha_1, \Gamma, \Gamma_1$ = constants appearing in transport equations of K-σ model

ϵ = turbulent energy dissipation rate

μ_Q = the turbulent diffusivity for Q

ρ = density of the fluid

σ = turbulent kinematic viscosity

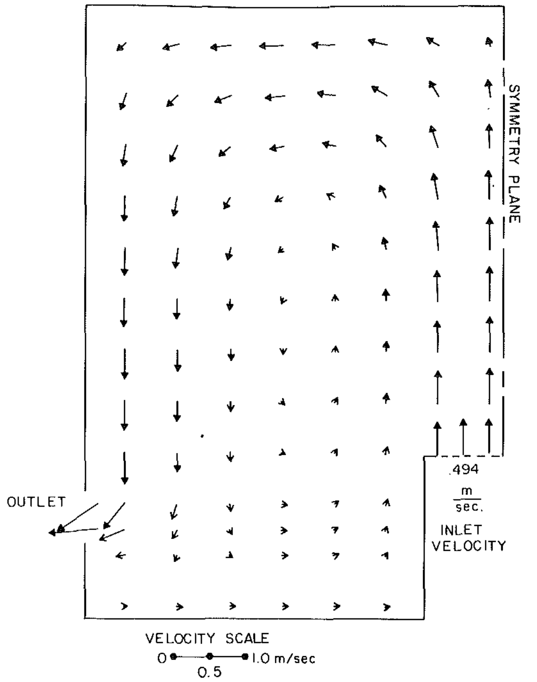

Fig. 2 Calculated mean velocity field at 80 seconds into transient

velocities, 8 percent of the local K value and 25 percent of the local Reynolds stress. The time-averaged signal so obtained is smooth enough to provide statistically useful ensemble averages from a reasonable number of repeated transients (typically ten).

Numerical Simulation Model

The transient flow predictions were obtained using the VARR-II computer program [4], which employs the K-σ (turbulent kinetic energy-turbulent viscosity) two-equation turbulence model of Stuhmiller [5]. This program uses the simplified Marker and Cell method [6] for solution of the equations of mean motion for incompressible turbulent flow in two dimensions. The K-σ model is typical of two-equation turbulence models. It is nearly mathematically equivalent to the better known K-ϵ model of Launder et al. [7, 8], and gives similar turbulence field predictions [1, 7]. The mean velocity and K-σ turbulence scalar equations of the VARR-II computer code and the boundary conditions used are summarized in Appendices A and B of reference [1].

The initial conditions are the asymptotically-steady mean-flow and turbulence field corresponding to a steady inlet flowrate. These initial values for the transient calculation were obtained at the end of a "shooting" calculation in which the flow proceeds from arbitrary initial conditions subject to prescribed steady boundary conditions. It was found that these initial conditions did not correspond exactly to those observed experimentally. While the steady-state experimental and calculated mean-velocities are in relatively close agreement, significant differences between measured and predicted spatial distributions of K and Reynolds stress exist. Accordingly, through modeling adjustments, attempts were made to improve the steady-state numerical prediction before computing the transient. This effort is described in reference [2] and produced no substantial improvement in the initial agreement between steady-state measurements and calculations.

In order to compensate for these existing initial disagreements, all graphical comparisons between measured data and numerical predictions are presented in a normalized form as the ratio $[Q(t)/Q(t=0)]_{\text{measured}}$, versus $[Q(t)/Q(t=0)]_{\text{predicted}}$, where Q is a general dependent variable. However, the nonlinear nature of the problem makes it impossible to assure that this initial normalization will compensate throughout the entire transient for the apparently fundamental inability of the model to make completely accurate steady-state (i.e., initial condition) predictions. Therefore differences in the time-varying value of a given measured and calculated quantity may not be the sole result of transient effects caused by the use of a turbulence model designed for steady flows. The measured and calculated initial velocity and turbulence data are described in reference [1].

Description of the Transient

The transient was controlled by a pneumatically-operated valve which smoothly closed off the inlet flow, leading to a flow coast-down within the cell. The measured, normalized, time-dependent inlet velocity is shown in Table 1 and follows the profile shown in the $\bar{U}$ plot in Fig. 3B (site L) which corresponds to the position directly above the chimney.

Discussion of Results

Early in the transient, the magnitudes of the characteristic time scales (see Appendix B) at site H for change in the turbulent kinetic energy via each of the important transport or net production mechanisms are the following:

Convection - 0.5 s;
Turbulence Dissipation - 0.5 s;
Turbulence Production - 5 s;
Turbulent Diffusion - 700 s.

The characteristic time scale of the flow coast-down is approximately 130 s. These time scales should also describe the instantaneous transport of other quantities since both convection and turbulent diffusion describe fluid mass transport, with the transport of other quantities (e.g., heat) being a consequence of transport of the fluid mass with which these quantities are associated.

Thus, in this relatively slow transient, the major departure from a quasi-equilibrium flow distribution would be expected to arise from the long time required for momentum diffusion throughout the flow domain. The response time scales of the other transport and net production terms are sufficiently short that they are expected to follow changes in the problem boundary conditions closely.

The initial measured steady-state flow field is shown in Fig. 2 of reference [1]. Qualitatively, this observed flow pattern is approximately observed throughout the transient; however, all of the measured quantities do not vary in direct proportion to the inlet flow rate. The measured velocity field at 80 seconds into the transient is shown in Fig. 1, which also indicates the specific locations at which the transient flow measurements are made; the corresponding simulated result is shown in Fig. 2. Measured transient data at 16 lettered sites in Fig. 1 are presented in Figs. 3 through 6. In addition, the sample standard deviation of the transient ensemble-averages shown in Figs. 3 through 6 is depicted at either the forty- or fifty-second point in each plot. While the magnitudes of the data at the various locations are different, they show a trend of monotonic decline as the transient progresses in most—but not all—cases.

Comparison of Calculations and Data

The data and calculated results at the sixteen measurement points are both presented in Figs. 3 through 6. Overall comparison of the velocity plots shows that in general the mean velocity field is predicted well. However, when the transient mean velocity results are carefully compared, some

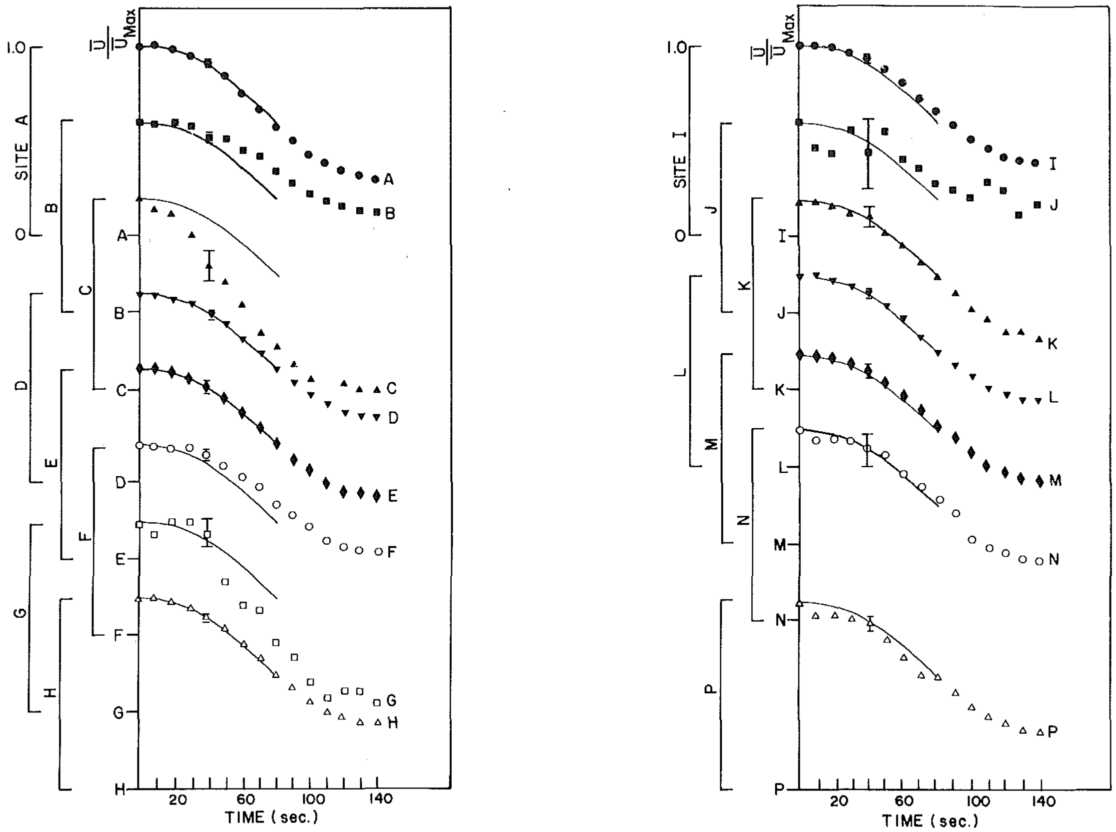

Fig. 3 Measured vertical velocity component, $\bar{U}(t)$, at various measurement sites as shown in Fig. 1 (shown as Figs. 3A and 3B). The ensemble averaging uncertainty of the data is illustrated in Figs. 3 through 6 by the ± 1.0 standard deviation error bars. The same format for data presentation is used in Figs. 3 through 6, and is shown for each figure in the uppermost set of data. The measurement station of each set of data is indicated to the right of the data stream, upon the appropriate normalized ordinate and at the origin of the ordinate for each data set. Calculated results corresponding to the data of each measurement station are shown as the solid curve which is plotted in the field of the data.

differences can be discerned. The effect is slight, but a clear trend is observed in which the calculated result moves more than the measured amount of flow to the outside of the vortex as the transient proceeds (see Figs. 1 and 2). A corresponding deficit in down-flow velocity grows with time near the center of the vortex in the calculated case.

At some sites in the data of Figs. 3 through 6, usually because a frequency tracker was unable to process a rapidly varying signal, the data for one or more measured parameters are missing. In these comparisons the plotted quantities are dimensionless, each being divided by its initial value. As discussed earlier, this is done to remove from the comparison the effects of disagreement in the initial values of the measured and calculated quantities. The calculations are terminated at 80s for reasons of computational economy and because by that time the quality of the agreement with the data is apparent.

The initial values for both the calculated and measured parameters are provided in Table 2. In most cases where data are not presented the values obtained changed sign during the transient. While the measurements were probably valid, the associated statistics at such sites were always poor.

A review of all the data plots shows that, in most cases, the measurements and calculations of mean velocity components appear to follow the general shape of the inlet velocity-versus-time curve (closely approximated by data of Site L in Fig. 3). The scalar turbulence quantities appear to vary over time as the square of these inlet velocity fractions. However, a close inspection of all the results reveals significant departures by the data and the calculation from these generalized shapes based on the inlet velocity curve. The magnitude and sign of these departures varies considerably throughout the flow domain, and the spatial "scatter" of these differences virtually eliminates the possibility that a systematic error in the measurement technique is responsible for them.

In cases where the data statistics are good, the discrepancies between measured and calculated transient behavior are on the order of ten to twenty percent. However, these differences are not solely attributable to transient effects of the turbulence model. Transient effects which occur in the computation as a result of deficient model closure assumptions are expected to manifest themselves, to first order, through the turbulence model constants. The fact that minor adjustments to the turbulence model constants produce significant variations over the entire calculated turbulence field [2] suggests that transient effects should produce a noticeable perturbation throughout the domain, no such effect is seen. More importantly, the failure of the turbulence model to predict accurately the magnitudes of the measured steady-state turbulence scalars causes the transient normalization factors $[Q(t=0)_{\text{measured}}/Q(t=0)_{\text{calculated}}]$ to vary widely throughout the plenum by as much as an order of magnitude, and more frequently by factors of two to five. These normalization factors are likely to be functions of inlet flow rate, as well as position, and therefore can cause differences to arise in the comparison of transient data with the calculations

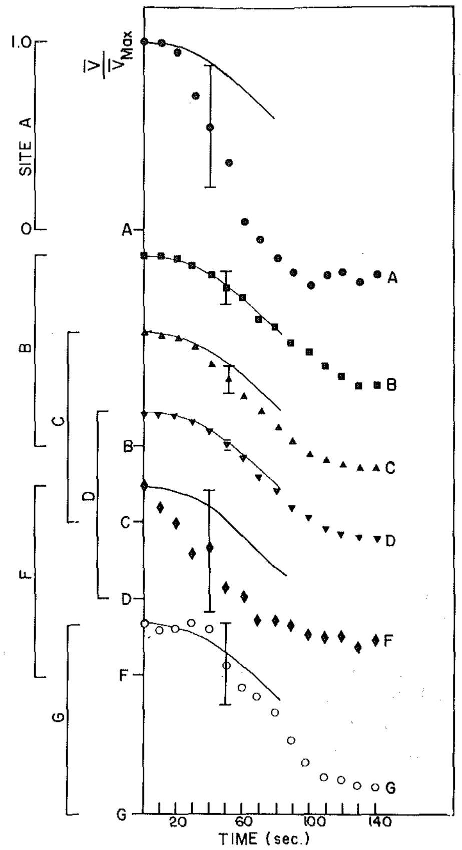

Fig. 4A

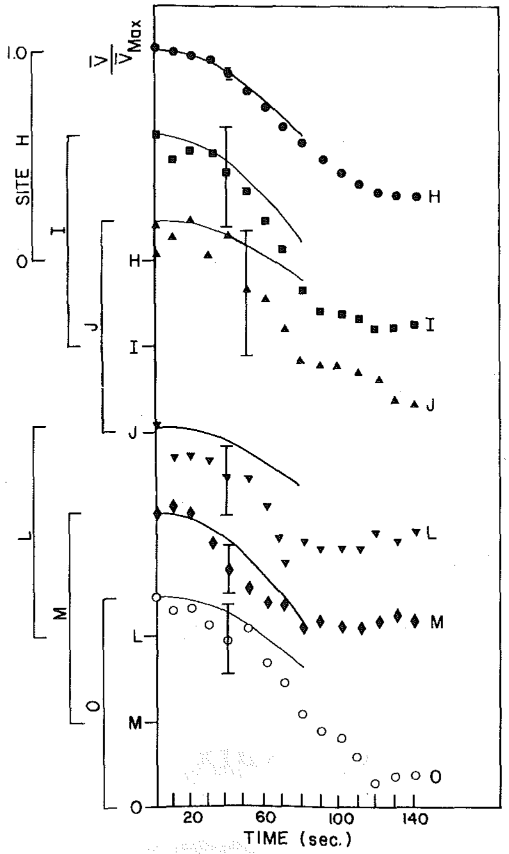

Fig. 4B

Fig. 4 Measured horizontal velocity component, $\bar{V}(t)$, at various measurement sites as shown in Fig. 1 (shown as Figs. 4A and 4B).

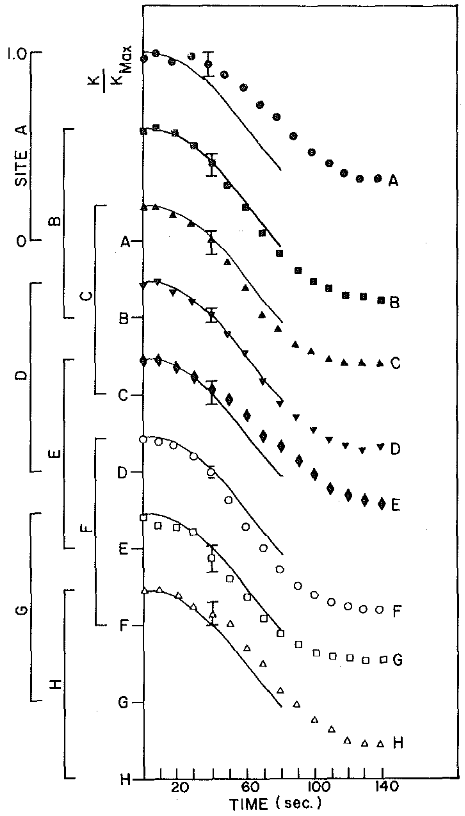

Fig. 5A

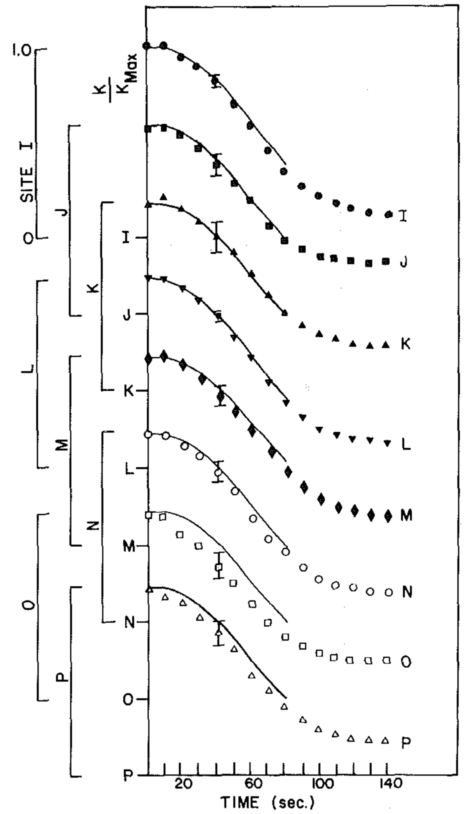

Fig. 5B

Fig. 5 Measured turbulent kinetic energy, $K(t)$, at various measurement sites as shown in Fig. 1 (shown as Figs. 5A and 5B). The measurement error at each point of each data ensemble element is ± 9 percent.

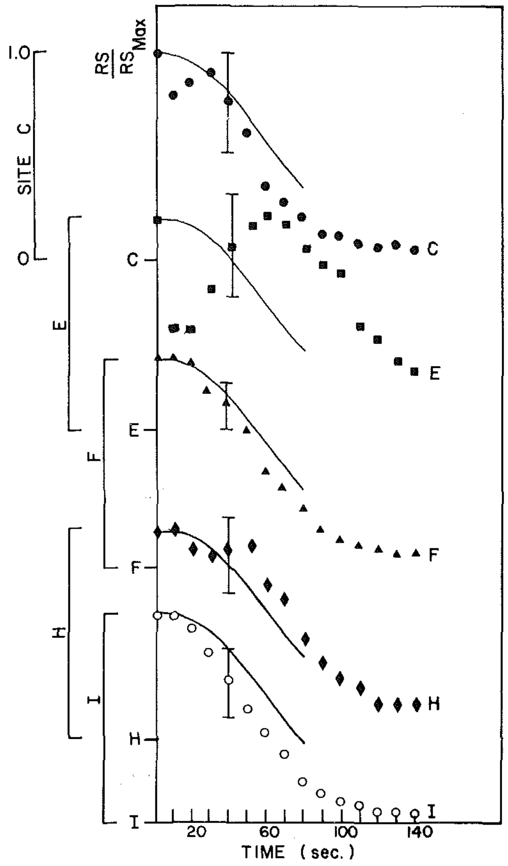

Fig. 6A

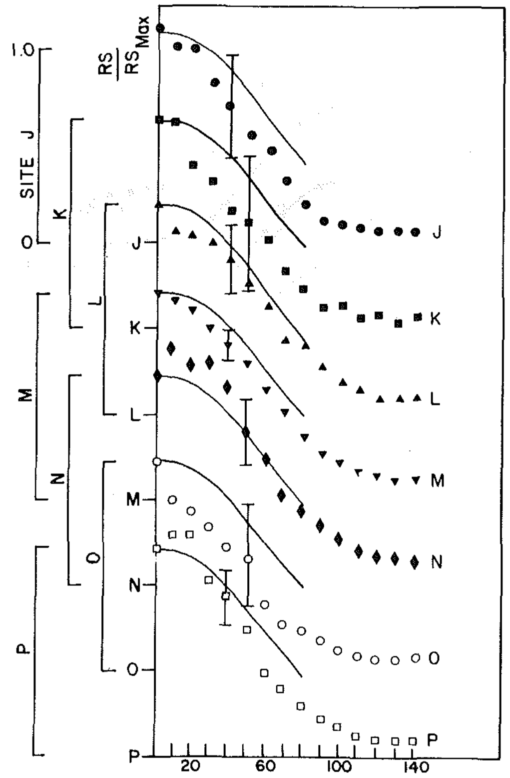

Fig. 6B

Fig. 6 Measured Reynolds stress, $RS(t) = \rho\overline{u'v'}$, at various measurement sites as shown in Fig. 1 (shown as Figs. 6A and 6B). The measurement error at each point of each data ensemble is ± 26 percent.

which are not truly transient effects. Finally, the spatial intermittency of transient discrepancies between the data and calculations is evidence that the pervasive effects expected to be caused by the steady state turbulence model's failure during a transient are not present.

Summary and Conclusions

Measurements of transient, ensemble-averaged turbulence flow data in water have been made for a case of engineering interest. In general, the data values decrease in direct relation to the inlet flowrate; however, important departures from this rule are observed. The short-term transient behavior of the turbulent kinetic energy is seen to be dominated by convective transport and local turbulent net energy dissipation, and the long-term behavior by turbulent diffusive transport.

The measured transient has been simulated numerically using a two-equation turbulence model in a two-dimensional, incompressible fluid dynamics computer program. Comparison of transient data and calculations shows some small differences in time-dependent behavior which are generally less than ten to twenty percent of the measured values. However, large initial normalization factors and the spatial irregularity of the differences suggest that adverse transient effects associated with the use of a turbulence model derived using steady state closure assumptions are not major causes of the observed discrepancies. The model's ability to follow a momentum transient of the order used in the experiment is essentially verified; however, improvements to the model's steady-state predictions are required before more comprehensive assessments can be made. Faster transients (with characteristic times on the order of 1-5 seconds) would present a more severe test of the model closure assumptions; numerical experiments examining this aspect of the problem would be worthwhile.

References

1 Boyle, D. R., and Golay, M. W., "Measurement of a Recirculating, Two-Dimensional, Turbulent Flow and Comparison to Turbulence Model Predictions. I: Steady State Case," ASME Paper No. 83-WA/FE-8.

2 Boyle, D. R., and Golay, M. W., "Transient Effects in Turbulence Modelling," U.S. Department of Energy Report No. DOE/ET/37240-83TR, MIT Nuclear Engineering Department, 1980, 275 pp.

3 White, F. M., *Viscous Fluid Flow*, McGraw-Hill, New York, 1974, p. 454.

4 Cook, J. L., and Nakayama, P. I., "VARR-II-A Computer Program for Calculating Time Dependent Turbulent Fluid Flows with Slight Density Variation," Report No. WARD-D-0106, Westinghouse Electric Corp., Pittsburgh, Pa., 1975.

5 Stuhmiller, J. H., "Development and Validation of a Two-Variable Turbulence Model," Report No. SAI-74-509-LJ, Science Applications, Inc., Palo Alto, Calif., 1974.

6 Amsden, A. A., and Harlow, F. H., "The SMAC Method: A Numerical Technique for Calculating Incompressible Fluid Flows," Report No. LA-4370, Los Alamos Scientific Laboratory, 1970.

7 Jones, W. P., and Launder, B. E., "The Prediction of Laminarization with a Two-Equation Model of Turbulence," *International J. Heat and Mass Transfer*, Vol. 15, 1972, pp. 301-314.

8 Launder, B. E., Reece, G. J., and Rodi, W., "Progress in the Development of a Reynolds-Stress Turbulence Closure," *J. Fluid Mechanics*, Vol. 68, 1975, pp. 537-566.

9 Durst, F., Melling, A., and Whitelaw, J. H., *Principles and Practices of Laser Doppler Anemometry*, Academic Press, 1975.

APPENDIX A

Outline of Experimental System

The measurements reported in this work utilized a two-channel laser Doppler anemometer, operating in the reference beam mode [9]. The chain of electronic apparatus used for data processing is shown in Fig. A.1 and the form of in-

Table 2 Initial values of both measured and calculated quantities at various measurement locations

Location	$\bar{U}$(m/s)		V(m/s)		K(m^2/s^2)		RS(kg/m-s^2)	
	Measured	Calculated	Measured	Calculated	Measured	Calculated	Measured	Calculated
A	−5.6 E-1[a]	−4.54 E-1	5.1 E-2	5.81 E-2	3.04 E-3	3.98 E-3	7.35 E-2	−4.91 E-1
B	−2.23 E-1	−2.11 E-1	1.07 E-1	2.36 E-1	1.12 E-2	2.82 E-3	3.23 E-1	−1.97 E-1
C	7.31 E-2	8.31 E-2	1.34 E-1	2.83 E-1	2.74 E-3	5.10 E-3	−4.48 E-1	−2.60 E-1
D	6.03 E-1	4.72 E-1	2.03 E-1	2.12 E-1	5.85 E-4	3.12 E-3	1.49 E-2	−3.43 E-1
E	−6.74 E-1	−6.13 E-1	−2.99 E-2	2.03 E-2	4.58 E-3	3.31 E-3	−1.07 E 0	−8.22 E-1
F	−2.97 E-1	−2.60 E-1	3.08 E-2	6.74 E-2	7.41 E-3	4.39 E-3	−2.07 E 0	−2.04 E 0
G	5.59 E-2	8.42 E-2	3.23 E-2	4.90 E-2	1.43 E-3	9.47 E-3	−1.36 E-1	−2.40 E 0
H	7.29 E-1	6.58 E-1	9.15 E-2	8.10 E-2	1.53 E-3	5.55 E-3	−4.32 E-1	−1.07 E 0
I	−5.10 E-1	−4.67 E-1	−2.24 E-2	1.35 E-2	7.73 E-3	4.14 E-3	−2.52 E 0	−2.52 E 0
J	−3.63 E-2	−4.85 E-2	2.41 E-2	−1.42 E-2	1.83 E-3	1.18 E-2	−3.85 E-1	−5.59 E 0
K	1.54 E-1	2.23 E-1	8.0 E-3	−1.73 E-2	2.44 E-3	1.73 E-2	−3.20 E-1	−5.83 E 0
L	7.98 E-1	8.13 E-1	1.37 E-2	−1.11 E-3	3.83 E-4	1.40 E-2	5.06 E-2	6.25 E-2
M	−7.59 E-1	−6.87 E-1	7.21 E-2	4.45 E-2	5.62 E-3	6.87 E-3	−2.62 E 0	−4.79 E 0
N	−1.91 E-1	−1.88 E-1	−1.00 E-2	−4.89 E-3	5.20 E-3	1.70 E-2	−1.24 E 0	−8.73 E 0
O	N.A.	−2.38 E-2	−4.73 E-2	−4.32 E-2	4.09 E-3	1.72 E-2	−6.71 E-1	−6.13 E 0
P	1.60 E-1	1.71 E-1	−7.0 E-3	−5.07 E-2	3.35 E-3	2.28 E-2	−8.17 E-1	−5.15 E 0

NA = not available.

[a] Format for the scientific notation used: 5.60 E-1 = 5.6 × 10^{-1} = 0.56.

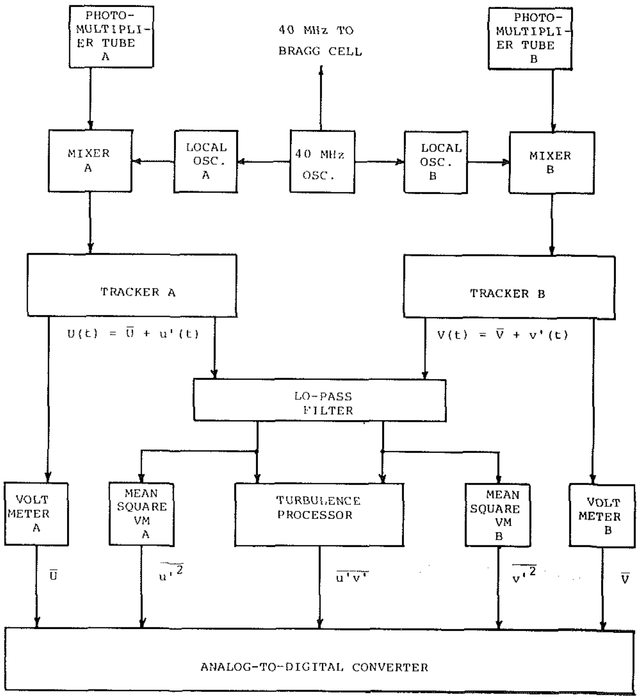

Fig. A.1 Schematic diagram of electronic signal-processing system used in measurements

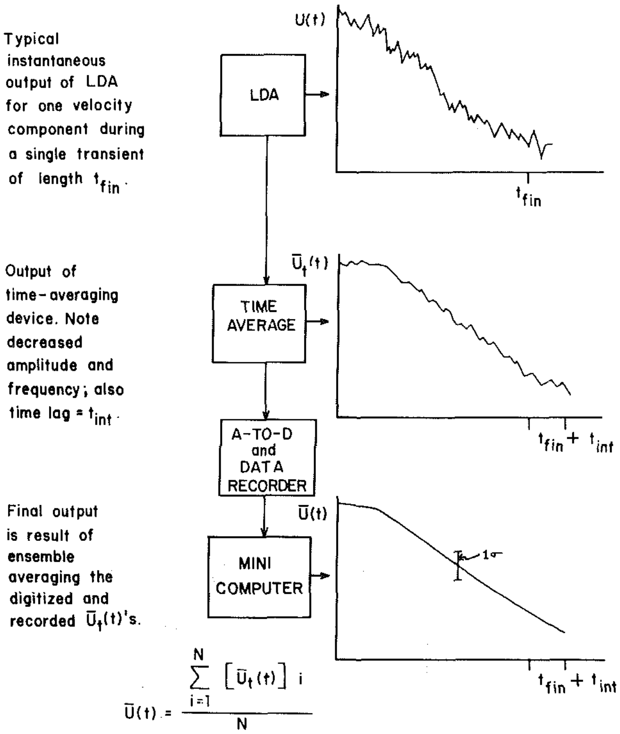

Fig. A.2 Qualitative illustration of transient velocity data obtained at a point in space, showing instantaneous data of a single transient, time-averaged data of a single transient and ensemble-averaged data from several transients. Electronic component abbreviations used are LDA: Laser Doppler Anemometer, and A-to-D: Analog-to-Digital Converter. The time- and ensemble-averaged data are displaced in time by an interval, $\tau = t_{\text{int}}$, due to the necessity to integrate instantaneous data over such an interval in order to form the time-averaged data.

stantaneous, short-term averaged, and ensemble-averaged signals obtained at a single point during a transient are illustrated qualitatively in Fig. A.2. Typically, ten transient runs would be used to form an ensemble-average of the data at a single point in space.

The capacitance of the electronic circuits used to perform the necessary signal integration imposes a time lag, t_{int}(the integration time), upon the time-averaged signal which is obtained. This time lag is apparent in the time shift shown in the illustrative data for $\bar{U}_t(t)$ and $\bar{U}(t)$ in Fig. A.2. Its effect is compensated in making all comparisons of experimental and computed results by shifting the measured data backward in time (i.e., to an earlier instant) by an amount equal to t_{int}. In all work reported here t_{int} equals 10.0 seconds.

APPENDIX B

Time Scales Characteristic of the Different Flow Transport and Net Production Phenomena

A general fluid flow conservation equation for a quantity Q (e.g., mass, momentum, heat, K) can be written as

$$\frac{\partial Q}{\partial t} = -C+D+P-S=\sum_{j=1}^{4} F_j, \qquad \text{(B-1)}$$

where

$C=-F_1=\bar{U}_i\frac{\partial Q}{\partial x_i}$ describes net convective transport,

$D=F_2=\frac{\partial}{\partial x_i}\left(\mu_Q\frac{\partial Q}{\partial x_i}\right)$ describes net diffusive transport,

and

$P=F_3$ and $S=-F_4$ describe local production and destruction of Q, respectively.

We can obtain an approximate estimate of the time scale of the contribution of each of the F_j terms to the total temporal rate of change of Q at the instant t' by treating each such term as consisting of an independent constant operator multiplied by $Q(t')$ in the form

$$F_j(t')=f_jQ(t'),$$

where $f_j = F_j(t)/Q(t)$ and $t' - t$ is small and positive. When this is done, $Q(t')$ is obtained as the solution to the equation,

$$\frac{\partial Q(t')}{\partial t'} = \sum_j f_jQ(t'), \tag{B-2}$$

as

$$Q(t')=Q(t)e^{\left[\sum_{j=1}^{4}\frac{1}{\tau_j}\right](t'-t)}, \tag{B-3}$$

where $t' > t$, and $1/\tau_j = f_j$.

The quantity $|\tau_j|$ is recognized as the instantaneous time-scale of change of Q due to the jth transport or production mechanism. These approximations are equivalent to expressing $Q(t')$ by the leading term of a temporal Taylor expansion about $t' = t$. When this is done in the case of turbulence kinetic energy, using the calculated flow field results for a rapidly-flowing region of the domain (site H) relatively early in the transient, the time scale values quoted in the text are obtained. These time scales are space- and time-dependent, and the sum $\Sigma(1/\tau_j)$ approaches zero as the flow reaches an asymptotically steady distribution.

B. R. Ramaprian
Professor in Mechanical Engineering
and Research Scientist
Iowa Institute of Hydraulic Research,
The University of Iowa,
Iowa City, Iowa.
Mem. ASME

S. W. Tu
Engineer,
Bechtel Civil and Mineral Inc.,
San Francisco, Calif.

Calibration of a Heat Flux Gage for Skin Friction Measurement

Introduction

A flush-mounted hot-film gage has very often been used for the measurement of wall shear stress in turbulent flows [1-4]. The hot film gage, as available commercially (e.g., DISA 55R45, 55R46) consists of a very thin film of nickel of about 0.75 mm length and 0.2 mm width deposited on the circular edge of a cylindrical quartz rod of about 2.5 mm diameter. The gage is mounted so that the circular surface containing the film is flush with the wall on which the shear stress is to be measured. The film sensor is operated (maintained at a constant elevated temperature) from a constant temperature anemometer, in the same manner as a velocity measuring hot-wire sensor. In the laminar *thermal* boundary layer over the film, the heat flux from the film to the air is related to the wall shear stress via the well-known Reynolds analogy. Hence, one can relate the heating current or alternately the voltage output by the anemometer to the wall shear stress τ_w.

The relationship between E and τ_w is usually assumed to be given by (see [4] for example)

$$\tau_w^{1/3} = AE^2 + B \tag{1}$$

where A and B are constants, to be determined from calibration. Such a calibration must be performed in a flow (e.g., fully developed pipeflow) where τ_w is known either from theory or from an independent measurement. Also, since equation (1) relates instantaneous values of E and τ_w, a constant voltage output can be obtained only if τ_w does not vary with time in the calibration flow. Thus, laminar flow is the ideal choice for calibration. However, it is inconvenient and often impossible to calibrate the gage in laminar flow. This is because of the difficulty of obtaining laminar flows (using air or water) and the appropriate range of shear stress values in the calibration experiment. Hence, the film gage is usually calibrated in a turbulent flow. Thus, turbulent fluctuations in the wall shear stress will be present during calibration as well as during actual measurement. This situation is unlike that during the calibration of, say a hot-film probe for velocity. In the latter case, the calibration is made in nearly turbulence-free flow. In the case of the skin friction gage, if we write $\tau_w = \bar{\tau}_w + t_w$, and $E = \bar{E} + e$, where $\bar{\tau}_w$, or $\bar{E}$ are the mean values and t_w, e are the fluctuations of wall shear stress and gage output voltage, respectively, we get

$$(\bar{\tau}_w + t_w)^{1/3} = A(\bar{E} + e)^2 + B \tag{2}$$

In practice, during the calibration and also in subsequent measurements, the (average) wall shear stress is obtained from the average output voltage, which is equivalent to using the approximation

$$\bar{\tau}_w^{1/3} = A\bar{E}^2 + B \tag{3}$$

Since τ_w depends on the sixth power of E, this procedure may lead to significant error in determining the calibration constants and the unknown wall shear stress. Sandborn [5] pointed this out in recent years. In fact, he suggested a trial and error procedure to obtain the correct wall shear stress. His method is somewhat cumbersome and not very elegant. An alternative procedure which is simple and accurate is described in this paper. The significance of this procedure is brought out from an analysis of the errors associated with the use of equation (3). The present method is especially suited for digital data acquisition.

The New Procedure

It is clear that the use of equation (3) instead of equation (1) introduces errors in two stages; first in the determination of the calibration constants A and B and subsequently in the determination of $\bar{\tau}_w$ from actual measurements. The calibration procedure can be improved in the following manner.

Equation (2) can be written as

$$\bar{\tau}_w + t_w = (AE^2 + B)^3 \tag{4}$$

Time averaging both sides of equation (4), we get

$$\bar{\tau}_w = A^3\overline{E^6} + 3A^2B\overline{E^4} + 3AB^2\overline{E^2} + B^3 \tag{5}$$

In the calibration experiment, $\bar{\tau}_w$ is obtained from an independent measurement such as pressure drop (in pipe flow) or Preston tube (in zero pressure gradient boundary layer). The instantaneous output voltage E from the gage is sampled,

---

Contributed by the Fluids Engineering Division for publication in the JOURNAL OF FLUIDS ENGINEERING. Manuscript received by the Fluids Engineering Division, January 26, 1982.

digitized and stored, using an acceptable sampling rate and sample size. These instantaneous data are then used to evaluate the time average values of the moments $\overline{E^6}, \overline{E^4}$ and $\overline{E^2}$. Equation (5), then, represents a nonlinear algebraic equation for A and B, the calibration coefficients. These can be determined, in principle, from a minimum of two calibration data points for $\bar{\tau}_w$. However, it is better to determine them from a larger number of calibration data points using a least-square fitting procedure. These values of A and B can then be used in equation (1) to obtain the instantaneous value of τ_w, corresponding to any instantaneous voltage E output by the gage.

In the actual use of the gage, the instantaneous output voltage E is again sampled, digitized and stored. The instantaneous value of τ_w can be recovered from these data using the known instantaneous calibration equation (1). The time-averaged wall shear stress $\bar{\tau}_w$ is then obtained by a simple time-averaging of these instantaneous values of τ_w. This method will give accurate values for $\bar{\tau}_w$, even when $(t_w/\bar{\tau}_w)$ is not small.

Significance of the New Procedure

One can estimate the systematic (and hence avoidable) error introduced into the measurement of $\bar{\tau}_w$ by the use of equation (3) in calibration and subsequent measurement. The procedure for doing this is routine and hence only the results will be stated here.

(*a*) Calibration Error. Rewrite equation (1) as

$$\tau_w^{1/3} = A(E^2 - C) \tag{6}$$

where

$$C = -B/A \tag{7}$$

Usually $|C| << E^2$ (as can be deduced, for example, from Fig. 1) and hence, the error in C is not significant. We shall estimate the error in A only. From the calibration data, A should be obtained as

$$A = \tau_w^{1/3}/(E^2 - C) \tag{8}$$

Neglecting terms of the order higher than the second, one gets, for the error ΔA, resulting from the use of $\bar{\tau}_w$ and $\bar{E}$ instead of τ_w and E in equation (8),

$$\frac{\Delta A}{A} \simeq \frac{1}{9} t'^2_w + e'^2 \left[\frac{1}{1 - C/\bar{E}^2}\right] \tag{9}$$

where the primed quantities denote the relative rms fluctuation intensities. Since $C/\bar{E}^2 << 1$, and $e' \sim (1/6)t_w'$ [τ_w depends on the sixth power of E, as seen from equation (6)] one can write

$$\frac{\Delta A}{A} \simeq \frac{5}{36} t_w'^2 \simeq 0.14 t_w'^2 \tag{10}$$

The ultimate relative error $(\Delta\tau_w/\bar{\tau}_w)$ in the measurement of $\bar{\tau}_w$ is, however, approximately three times the relative error $(\Delta A/A)$, since, one gets from equation (6),

$$\tau_w = A^3(E^2 - C)^3$$

and hence

$$\frac{\partial \tau_w}{\partial A} = 3A^2(E^2 - C)^3$$

or

$$\frac{\Delta\tau_w}{\bar{\tau}_w} \simeq \frac{\Delta\tau_w}{\tau_w} = \frac{3\Delta A}{A} \tag{11}$$

Hence, we have the following typical values:

t_w' (in the calibration flow)	10%	50%	70%
$\Delta A/A$	0.14%	3.5%	7%
$\Delta\tau_w/\bar{\tau}_w$	0.42%	10.5%	21%

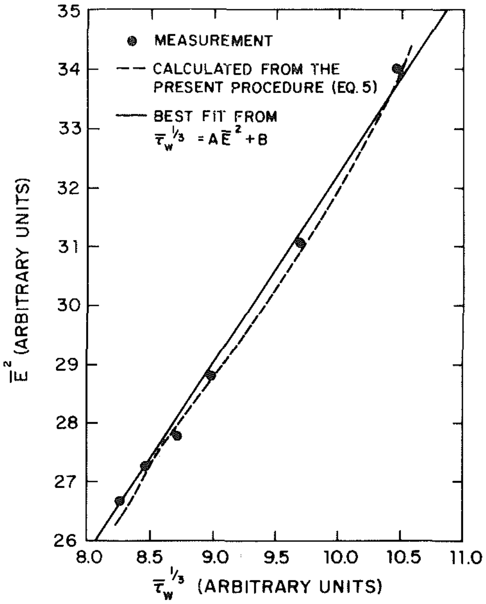

Fig. 1 Typical calibration curves for the wall shear stress gage

(*b*) Error in Measurement. Again, from an error analysis of equation (6), under similar assumptions as made earlier, one gets, for the error $\Delta\tau_w$ resulting from the use of $\bar{E}$ in place of E (for given values of A and C):

$$\frac{\Delta\tau_w}{\bar{\tau}_w} \simeq -3[1 + 4\{1/(1 - C/\bar{E}^2)\}][1 - C/\bar{E}^2]e'^2$$

$$\simeq -15e'^2 \simeq -0.4t_w'^2 \tag{12}$$

Again, we get the following typical estimates, for the error from the use of time averaged voltage, during the actual measurement.

t_w' (in the flow being measured)	10%	50%	70%
$\Delta\tau_w/\bar{\tau}_w$	−0.4%	−10%	−20%

Flows in which t_w' is 50 percent or larger are not uncommon, e.g., adverse pressure gradient boundary layers in the neighborhood of separation, unsteady boundary layers, etc. Also, note that the error (*b*) is independent of the error (*a*) estimated earlier. While the two errors appear to cancel each other, they will do so only if the turbulent intensities t_w' are the same in the calibration flow and the flow being measured.

The above procedure was successfully used by the authors in measuring wall shear stress in periodic turbulent pipeflow. In this study described in Ramaprian and Tu [6], water was used as the working fluid. A DISA quartz coated flush mounted film gage was used. The gage was calibrated "in situ" by maintaining steady pipeflow in the system at several Reynolds numbers and using Blasius friction law (See Schlichting [7]) for obtaining the wall shear stress. This law was confirmed to be valid from independent pressure drop measurements. The gage output voltage was zero-suppressed, amplified, sampled, digitized and stored in a HP-1000 minicomputer. A sampling rate of 20 Hz and a total of 3000 samples were used. The stored data were recalled and the original instantaneous voltages reconstructed. The coefficients A and B were then obtained as described earlier. In solving the nonlinear equations for A and B, approximate values computed from equation (3) were used as starting values in a trial and error process. A Newton-Raphson algorithm was used to obtain quick convergence to the correct solutions for A and B.

Figure 1 is a typical calibration result showing a comparison between the conventional and the present procedures. The graph is drawn in conventional coordinates $\bar{E}^2$ and $\bar{\tau}_w^{1/3}$. The full line is a least-square linear fit using the conventional (time-averaged) quantities, namely the measured mean voltage $\bar{E}$ and the measured wall shear stress $\bar{\tau}_w$. The dashed line, which is not a straight line, is obtained by computing the best values of A and B from the present procedure and then using these values to compute back $\bar{\tau}_w$ via the instantaneous equation (1). The dashed line seems to fit the measured data better than the conventional full line. The difference between the conventional and present procedure is however, not spectacular, in this case. This should be expected for calibration experiments performed in steady pipeflow, with t_w' of the order of 10 percent. On the other hand, the difference can be significant if the calibration flow has large wall shear stress fluctuations. Such situations may be encountered in the case of some *in situ* calibrations. For example, in experiments on an unsteady boundary layer in adverse pressure gradient, it may be necessary to calibrate the probe *in situ* in steady flow and then use it in the same location to measure the wall shear stress after switching on unsteadiness. One of the authors [BRR] is presently involved with such experiments.

Comparison With Random Errors

It is useful to compare the above systematic errors in calibration and measurement with the random errors (uncertainties) associated with these stages of the experiment. If the random (unavoidable) error is small compared to the systematic (avoidable) error, then the present procedure for removing the latter becomes significantly useful. During the calibration procedure, there is a random error δA in the determination of A, because of random errors δE and $\delta\tau_w$ in the measurement of the voltage E and the reference wall shear stress τ_w. From a simple error propagation analysis of equation (6), one gets

$$\frac{\delta A}{A} = \left[4\left(\frac{\delta E}{E}\right) + \frac{1}{9}\left(\frac{\delta\tau_w}{\tau_w}\right)^2\right]^{1/2} \tag{13}$$

With a modern digital data acquisition system, $\delta E/E \leq 0.002$. The uncertainty $\delta\tau_w$ in τ_w depends on the calibration experiment. One gets the following typical results:

$\delta\tau_w/\tau_w$	1%	5%	10%
$\delta A/A$	0.52%	1.7%	3.35%

By comparing these vlaues with the systematic calibration errors tabulated in (*a*) above, one can ascertain how significant will be the improvement in the overall accuracy of measurement, by the use of the present method.

Likewise, the random error $\delta\tau_w$ due to random error δE during the actual measurement can be estimated, again from equation (6) as

$$\frac{\delta\tau_w}{\tau_w} \sim 6\,\frac{\delta E}{E} \sim 6 \times 0.002 = 1.2\% \tag{14}$$

Comparing this with the systematic error $\Delta\tau_w/\tau_w$ listed earlier in (*b*) above, it is seen that in most practical situations, it is possible to obtain significant improvement in overall accuracy by using the present procedure for eliminating the systematic error.

Conclusions

The error estimates made above are optimistic since terms of higher than second order have been neglected. If the wall shear stress fluctuations have a probability density distribution with a long tail, the higher order terms may introduce significant additional error. Also, not much is known at present about the intensity of wall shear stress fluctuations in different flows. It seems, however, reasonable to speculate that no serious errors will be introduced by the use of a time-average relation such as equation (3) in flows like steady pipeflow and zero pressure gradient boundary layer. On the other hand, use of the instantaneous relation such as equation (1) is necessary in calibration/actual measurements in flows such as adverse pressure gradient boundary layers especially close to separation, unsteady flows, etc. The procedure described in this paper can be used with advantage when digital data acquisition and processing facilities are available. The improvement in overall accuracy obtained by the removal of the systematic errors in calibration and measurement is generally quite significant since the random errors are often much smaller than the systematic errors. Incidentally, the use of the specific form of equation (1) is only illustrative. A procedure similar to the one described in this paper can be used, in principle, with any instantaneous functional relationship between τ_w and E.

Acknowledgments

The authors wish to acknowledge the support received from the U.S. Army Research Office, via their Grant No. DAAG29-79-G-0017. The work reported here formed a part of a larger study on unsteady turbulent flows, sponsored under this Grant.

References

1 Ludwieg, H., "Instruments for Measuring the Wall Shearing Stress of Turbulent Boundary Layers," NACA TM, No. 1284, 1950.

2 Liepmann, H., and Skinner, G., "Shearing Stress Measurements by Use of a Heated Element," NACA TN, No. 3268, 1954.

3 Myers, G., Schauer, J., and Eustis, R., "Plane Turbulent Wall Jet Flow Development and Friction Factor," ASME *Journal of Basic Engineering*, Vol. 85, 1963, p. 47.

4 Bellhouse, B. J., and Schultz, D. L., "Determination of Mean and Dynamic Skin Friction, Separation and Transition in Low Speed Flow with a Thin-Film Heated Element," *Journal of Fluid Mechanics*, Vol. 24, Part 2, 1966, pp. 379–400.

5 Sandborn, V. A., "Evaluation of the Time-Dependent Surface Shear Stress in Turbulent Flows," ASME Paper 79-WA/FE-17, 1979.

6 Ramaprian, B. R. and Tu, S. W., "Periodic Turbulent Pipe Flow," IIHR Report No. 238, Iowa Institute of Hydraulic Research, The University of Iowa, Iowa City, Iowa, 1982.

7 Schlichting, H., *Boundary Layer Theory*, 6th ed., McGraw-Hill, New York, 1968, p. 561.

D. E. Stock
Department of Mechanical Engineering,
Washington State University,
Pullman, Wash. 99164-2920

K. G. Fadeff
General Electric Company,
San Jose, Calif.

Measuring Particle Transverse Velocity Using an LDA

Four problems encountered in making transverse velocity measurements with an LDA are alignment of the optical system, velocity bias correction, avoidance of incomplete signal bias, and collecting sufficient data. Each problem is discussed and the method used to overcome each is presented for the case of measuring particle transverse velocities in a laboratory-scale electrostatic precipitator.

Introduction

Many gas-particle flows (particles being solid or liquid) have larger axial velocities than transverse velocities. However, the process of interest is often related to the smaller transverse velocity of the particles. Cases where the transverse velocity is of interest include particle dispersion from a point source in the atmosphere or from a point source within pipe flow. Another example is the motion of particles in electrostatic precipitators where the transverse velocity governs the collection efficiency of the system. Measurement of particle transverse velocity and concentration can be used to determine the local effective particle turbulent diffusivity.

The laser Doppler anemometer is an ideal instrument for studying particle motion in turbulent flow fields since it produces information on particle velocity directly. Also, under the proper seeding conditions, it can give information on both the gas-phase velocity (by measuring small trace particles in the gas phase) as well as the particulate phase [1]. In this work, we were interested in the motion of the particulate phase and assumed the gas-phase was unaffected by the particle motion since the particle loading was very light.

Experiments were performed on a laboratory-scale electrostatic precipitator to determine both particle longitudinal and transverse velocities. The goal of the study was to determine the influence of the electric field on the motion of the charged particles. The longitudinal particle velocities were on the order of 2 m/s and the transverse particle velocities were 5 cm/s or less. The typical particle turbulence intensities relative to the longitudinal velocity were on the order of 2-5 percent.

In this paper, we discuss the problems encountered in trying to make the transverse velocity measurements and how the problems were overcome. Measuring transverse velocities presents four significant difficulties:

(1) alignment of the optical system relative to the flow field,
(2) velocity bias correction,
(3) avoidance of the incomplete signal bias, and
(4) collecting sufficient data to provide useful estimates for the mean and variance of the particle velocity.

Apparatus and Instrumentation

The laboratory-scale electrostatic precipitator used in this test is shown in Fig. 1. The collecting section of the precipitator was 122 cm long, 25.4 cm high, and 5 cm wide. The top and bottom were made of plexiglas to allow LDA access and the sides were aluminum. A complete description is given by Fadeff [2]. Aluminum oxide particles with a nominal size of 3 μm and mass loading of 0.1 g/m^3 were used.

The LDA system used is shown in Fig. 2 and the signal processing instrumentation in Fig. 3. The LDA was mounted vertically with the measuring volume always in the horizontal center of the duct. The LDA could be moved to any transverse or longitudinal location desired. The LDA operated in the dual beam, fringe mode using forward scattering. The measuring volume was 0.74 mm in diameter and 18.3 mm long with a fringe spacing of 7.8 μm. Figure 2 shows the laser mounted for measuring longitudinal velocity. To measure the transverse velocity, the laser and optical head were rotated 90 deg as a unit and the photomultiplier realigned.

A counting type signal processing system, coupled to a microcomputer (the computer system is described by Stock and Lentz [3]) was used. The DISA 55L90A counter operating in mode 2 validated the signal by comparing the time for five zero crossings with the time for eight crossings (5/8 comparison) and also measured the total number of fringes above the trigger level for each particle passing through the measuring volume. If the particle produced a valid signal, the counter then passed the period of the Doppler signal, the number of fringes crossed, and the time since the last valid

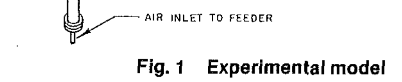

Fig. 1 Experimental model

Contributed by the Fluids Engineering Division for publication in the JOURNAL OF FLUIDS ENGINEERING. Manuscript received by the Fluids Engineering Division, September 17, 1982.

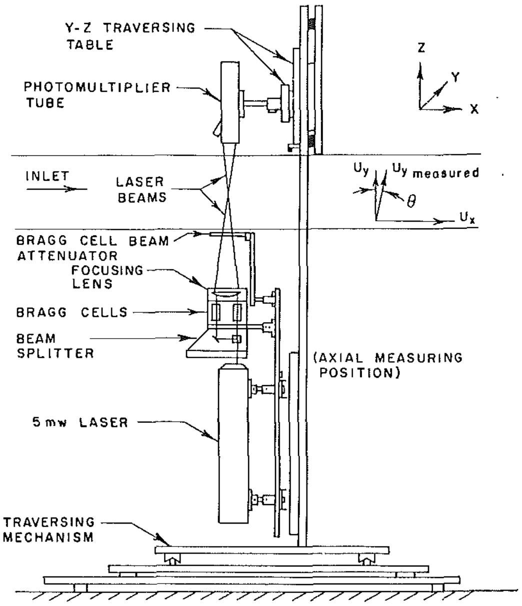

Fig. 2 Laser Doppler anemometer equipment

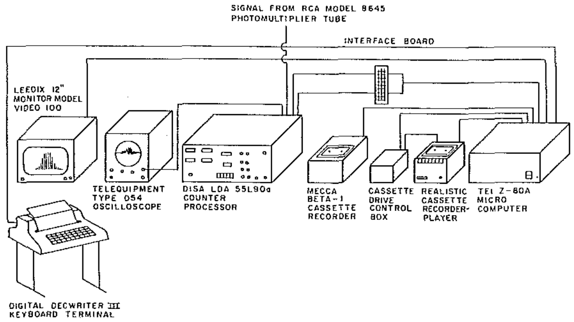

Fig. 3 Signal processing and data reduction system

signal to the computer. Data were collected in batches of either 1000 or 3000 points. Each batch of data was checked for outliers beyond 3.75 standard deviations from the mean before the final statistics were computed and the raw data was stored on tape. The counter-computer interface was capable of data rates up to 40 kHz and since the actual data rate was 15 to 25 Hz, particle arrival time controlled the data rate.

Alignment of Optical Head. Alignment of the optical head when measuring transverse velocities is extremely critical since a 1 deg misalignment could change the measured transverse velocity by ±3.5 cm/s. We found it was impossible to adjust the optical unit to make the fringes perpendicular to the transverse direction to within the tolerance required for our experiment (±0.05° for ±0.2 cm/sec). Instead, the offset angle at each location was measured and the transverse velocity corrected for the effect of the beam misalignment. The offset angle can be measured if a location can be found where the velocity has only a longitudinal component. For the model precipitator, it was assumed that the flow was only in the longitudinal direction at the center of the duct when the electric fields were turned off. Measurement of the effective longitudinal and transverse velocities were made at the center of the duct and without the electric fields. They are related by (see Fig. 2)

$$U_{x \text{ measured}} = U_x \cos\theta_x + U_y \sin\theta_x \tag{1}$$

$$U_{y \text{ measured}} = U_y \cos\theta_y + U_x \sin\theta_y \tag{2}$$

where θ is the misalignment angle. For our application, θ will be less than 1 deg and U_y will be zero at the centerline without the electric field. Therefore, equation (1) becomes

$$U_{x \text{ measured}} = U_x \tag{3}$$

and equation (2) becomes

$$\theta_y = \sin^{-1} \frac{U_{y \text{ measured}}}{U_{x \text{ measured}}} \tag{4}$$

During operation, U_y was less than 0.5 percent of U_x so the data were corrected as follows:

$$U_x = U_{x \text{ measured}} \tag{5}$$

$$U_y = U_{y \text{ measured}} - U_x \sin\theta_y \tag{6}$$

The correction angle was measured for each longitudinal location and the same correction angle used for all transverse measurement at a given longitudinal location.

Velocity Bias Correction. When using a counting (also called individual realization) type signal processing system with an LDA, the resultant velocity measurements are biased because a larger than average number of high velocity particles pass through the measuring volume [4]. The amount of bias depends on the turbulence level present in the flow and on the ratio of the particle arrival rate to the actual processor data rate (also called waiting time) [5]. We operated the processor in the free running mode (this means every particle crossing the measuring volume was interrogated by the processor). Also, our transverse turbulence intensity relative to the transverse velocity ranged from 300 percent up to infinity. The longitudinal turbulence intensity ranged from 5-35 percent relative to the longitudinal velocity. McLaughlin and Tiderman [4] suggest correcting for velocity bias (this is for a spherical measuring volume) by

$$\bar{U} = \frac{\sum_{i=1}^{m} \frac{U_i}{V_i}}{\sum_{i=1}^{m} \frac{1}{V_i}} \tag{7}$$

where $\bar{U}$ is the mean velocity, U_i is an individual velocity realization, and V_i is the magnitude of instantaneous velocity. If a component of the velocity was measured, the equation would remain the same except U_i would become U_x and $\bar{U}$ would become $\bar{U}_x$. Bias correction is unnecessary if the turbulence intensity is less than 15 percent of the total velocity vector V_i. Therefore, when measuring transverse velocity, which has high fluctuating velocities relative to the transverse velocity, bias correction is often not required since their fluctuations relative to the total velocity vector are small. In our experiments, the bias correction technique suggested by Buchhave [6], which weights the individual readings by the residence time, was used since in some cases the turbulence intensity relative to the total velocity vector was greater than 15 percent.

Incomplete Signal Bias. The DISA 55L90A counter type processor, like most counter processors, requires at least eight cycles of the Doppler burst to have an amplitude above the trigger level before the signal can be validated and used as a velocity realization. Particles crossing the probe volume at an angle can fail to cross enough fringes and therefore not become part of the sample used to calculate the mean and standard deviation. This effect is called incomplete signal bias [6, 7] and causes the measured mean velocity to be biased toward the low side. Incomplete signal bias can be overcome by frequency shifting. The amount of frequency shifting required depends on the number of fringes required to validate a signal, the magnitude of the total particle velocity

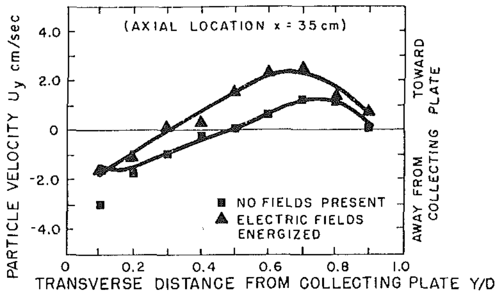

Fig. 4 Transverse particle velocity profile (uncertainty in $\bar{U}_y = \pm 0.37$ cm/s at 20:1 odds)

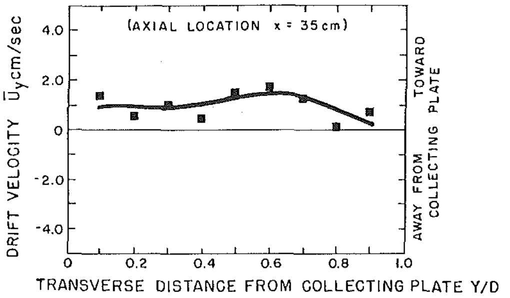

Fig. 5 Electrical field effect (uncertainty in $\bar{U}_y = \pm 0.37$ cm/s at 20:1 odds)

vector, and the angle of the particle relative to the fringes. To measure transverse velocities, the frequency shift needs to be at least twice the maximum expected velocity realization in the transverse direction. We used a shift of 75 KHz which was three times the maximum expected transverse Doppler frequency.

There also exists an upper limit to the amount of frequency shift that can be used with a counter processor. Since the counter operates in a digital mode and transfers data to a computer in digital form, there is a built-in minimum resolution. Typically, data is transferred as mantissa and exponent. The number of digits used for the mantissa sets the resolution of the measured frequency. Written in terms of frequency, the Doppler frequency is

$$f=M\times 10^E \pm \frac{1}{2^N}\times 10^E - f_s \qquad (8)$$

where M is the mantissa, E the exponent, N the number of bits of mantissa, and f_s the shift frequency. If E and f_s are large, then the uncertainty, given by

$$W_f = \pm \frac{1}{2^N}\times 10^E \qquad (9)$$

could be large. If N is equal to 7 and E is 6, then W_f would be ±7.8 KHz or, for our optical system, ±6cm/s. This is larger than the velocity we were trying to measure. The example given above corresponds to a frequency shift in the MHz range. We used a shift of 75 KHz to avoid this problem.

Sample Size Determination. The measurement of transverse velocities often involves sampling a population with a large standard deviation relative to the mean. To estimate the number of data points required to determine the mean velocity to within a given confidence interval, the t statistic

$$t=\frac{(\bar{x}-\mu)\sqrt{n}}{s} \qquad (10)$$

where $\bar{x}$ is the sample mean, s the sample standard deviation, μ the population mean, and n the number of data points, is used. One must also select a confidence level (usually 95 percent). Equation (10) can be used to define the confidence interval as

$$\mathrm{CONF}\left\{\bar{x}-\frac{ts}{\sqrt{n}} \le \mu \le \bar{x}+\frac{ts}{\sqrt{n}}\right\} \qquad (11)$$

Often the confidence interval is given as a percentage of the mean value, but in flows with very low or even zero mean it is more useful to express the confidence interval in absolute terms. Usually the confidence interval is chosen to be of the same order of magnitude or smaller than the instrumentation uncertainty. For a given uncertainty interval of $\pm W_s$, the number of data points required is [8].

$$N=\left[\frac{ts}{W_s}\right]^2 \qquad (12)$$

in our experiment, s was on the order of 0.1 m/s and W_s of ±0.002m/sec was desired. Since the sample size was large, t was equal to 1.96 for a 95 percent confidence level. Using equation (12), one finds a sample size of 10,000 is needed. For the transverse velocity measurements, we used four batches of 3000 points to give a total sample size of 12,000. A similar analysis could be applied to the confidence interval for the turbulence intensity except a chi-square distribution should be used.

Discussion

The techniques described above were used to measure the transverse velocity of particles in a laboratory-scale electrostatic precipitator using a laser Doppler anemometer. Typical results for the particle motion with and without the electric field energized are shown in Fig. 4 [2]. The profile without the fields energized is typical of developing turbulent channel flow with the fluid moving toward the centerline. The effect of the electric field on the particle motion is best shown by subtracting the particle velocity without the field energized (this represents the gas phase velocity) from the particle velocity with the field on (Fig. 5).

The measurement of transverse velocity with a laser Doppler anemometer requires careful planning to avoid problems with alignment, biasing, and sample size. We have shown how to treat one particular case, but each flow field must be considered separately.

Acknowledgments

We thank R. Lentz and M. Shook for assistance with the computer interfacing and signal processing routines. Part of the LDA used with this work was purchased under NSF grant No. ENG78-11044. The paper was written while the author was visiting at the Sibley School of Mechanical and Aerospace Engineering, Cornell University.

References

1 Stock, D. E., Jurewicz, J. T., Crowe, C. T., and Eschbach, J. E., "Measurement of Both Gas and Particle Velocity in Turbulent Two-Phase Flow," *Proceedings of the 5th Symposium on Turbulence*, Rolla, Mo., 1975.

2 Fadeff, K. G., "Particle Axial and Transverse Velocities in an Electrostatic Precipitator," M.S. thesis, Washington State University, 1981.

3 Stock, D. E., and Lentz, R. A., "Using S-100 Based Microcomputers in the Fluid Mechanics Laboratory," ASME/WAM Symposium on Computers in Flow Predictions and Fluid Dynamics Experiments, 1981.

4 McLaughlin, D. K., and Tiderman, W. G., "Biasing Correction for Individual Realization of Laser Anemometer Measurements in Turbulent Flows," *Physics of Fluids*, Vol. 16, No. 12, 1973, pp. 2082-2088.

5 Erdmann, J. C., and Tropea, C., "Turbulence-Induced Statistical Bias in Laser Anemometry," *Proceedings of the 7th Symposium on Turbulence*, Rolla, Mo., 1981.

6 Buchhave, P., "The Measurement of Turbulence with the Burst-Type Laser Doppler Anemometer—Errors and Correction Methods," Ph.D. thesis, SUNY-Buffalo, 1979.

7 Roesler, T. C., Stevenson, W. H., and Thompson, H. D., "Investigations of Bias Errors in Laser Doppler Velocimeter Measurements," AFWAL-TR-2105, Wright-Patterson Air Force Base, 1980.

8 Kreyszig, E., *Advanced Engineering Mathematics*, 3rd ed., Wiley, 1972, p. 752.

G. Bergeles
Associate Professor.

N. Athanassiadis
Professor.

Laboratory of Aerodynamics,
Department of Mechanical Engineering,
Technical University of Athens, Greece

The Flow Past a Surface-Mounted Obstacle

The length of the recirculating region past a two dimensional obstacle was investigated experimentally with a single hot wire. The width (W) of the obstacle could be changed in multiple values of obstacle height (H). The results show that upstream of the obstacle the length of the main recirculating region remains unchanged with obstacle width and equal to 0.85H; however the downstream length of the recirculating region is a strong function of the width and changes almost linearly from 11 obstacle heights for W/H = 1.0 to 3 for W/H greater than four.

Introduction

Strongly separated flows have recently become the center of intensive investigation. Despite their frequent appearance in engineering, their experimental and theoretical study is rather limited due to the difficulties encountered in the investigations. The flow around a forward facing step and also that of a backward facing step constitute two basic study cases for strongly separated flows. The flow around a two-dimensional surface mounted obstacle combines features of the above two basic engineering flows. A basic characteristic of such flow configurations is the integral parameter of the length of the recirculating region (L_R) behind the obstacle. This length depends on the ratio of the boundary layer thickness of the approaching flow to the obstacle height and also on the geometry of the obstacle itself. The flow in a backward facing step and mainly the far flow field (after reattachment) has been studied by Bradshaw and Wong [1]. In that study the flow at the edge of the backward facing step was laminar with a boundary layer thickness δ of 0.12 step heights. They found that the flow was reattaching approximately 6 step heights downstream from the step. In the experiments by Tani et al. [2], for a thicker boundary layer, the length of recirculation was 6.8 step heights while in the same study for even thicker but turbulent boundary layer this length was approximately 6.9 times the step height. The flow around a square-sectioned surface mounted obstacle has been investigated by Tillman [3] and more recently by Crabb et al. [4], Durst and Rastogi [5] and Couniham et al. [6]. In the measurements by Crabb et al., [4], Durst and Rastogi [5] for a boundary layer thickness $0.5H$, the length of recirculation was approximately 11 obstacle heights; in Tillman's measurements for a turbulent thick boundary layer ($\delta = 3.3H$) this length was found to be 12.5 times the obstacle height.

According to the author's knowledge the flow field past a surface mounted obstacle for various widths to height ratios has not been previously investigated. In this study we present measurements of the length of the recirculating region behind the obstacle as a function of the obstacle width and some velocities at one location outside the region of recirculation.

Description of the Experiment

The Flow in the Wind Tunnel. The experiments were performed in an open circuit wind tunnel of the blowdown type. The test section had dimensions 28 cm × 30 cm and a length of 120 cm. A slot of 2 cm height was located at the entrance to the test section through which the boundary layer which had developed on the bottom wall of the contraction was sucked. Therefore, a new boundary layer was developing right from the beginning of the test section floor where a sand paper of 2 cm width was also used to promote transition to turbulence. The roof of the test section could be positioned at will so that a zero streamwise pressure gradient could be imposed on the flow in the test section compensating for the blockage due to growth of the boundary layers on the walls of the test section.

The nominal air speed of the flow in the test section was 16 m/s with a turbulence level of 0.5 percent. The developing boundary layer on the bottom wall in the empty tunnel was measured with a single hot-wire and was found after 40cm from the entrance to obey a 1/6.9 power law. At the location where the obstacle was going to be installed, the boundary layer thickness (δ) was equal to 0.48 obstacle heights ($H = 25$ mm). The two dimensionality of the flow in the wind tunnel was measured without the presence of any obstruction; the maximum difference measured in the velocity was 0.4 percent of the mean velocity over the test section [7].

The Geometry of the Obstacle. The basic elements which were used in the investigation were prisms of square cross section which spanned the width of the test section (30 cm) and had a height of 25 mm (H). The prisms were made from perspex of 2 mm thickness with sharp corners so as to fix the origin of the forward separation line and were mounted on the floor of the test section. By locating similar prisms side by side the width of the obstacle could be increased in multiple values of the obstacle height. The range of obstacle width (W) to height (H) which was investigated in the present study was from $W/H = 1$ to 10. The presence of the obstacle in the test section created a blockage to the flow of 8.9 percent which could not totally be compensated by the adjustment of the top wall of the test section (obviously this ought to be a shaped roof and not a flat plate). According to the investigation of Durst and Rastogi [8] this particular blockage could have but

---

Contributed by the Fluids Engineering Division for publication in the JOURNAL OF FLUIDS ENGINEERING. Manuscript received by the Fluids Engineering Division, December 11, 1981.

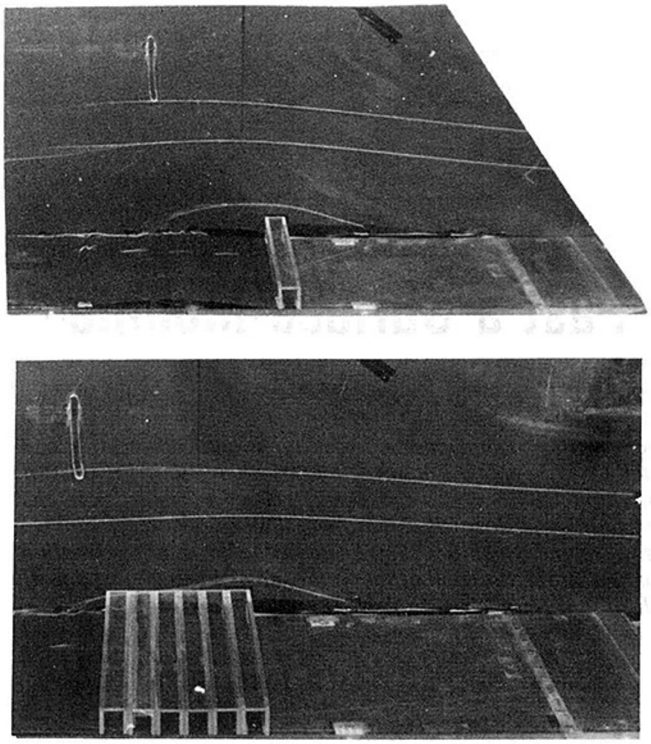

Fig. 1 Flow visualization

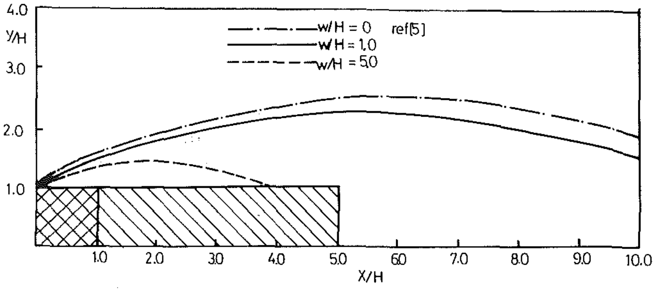

Fig. 2 Trajectory of the shear layer

a small influence on the integral length of recirculation and on the velocity measurements.

The Measurements and Their Uncertainty. The two dimensionality of the flow in the test section with the obstacle in position was checked by inspecting the movement of oil drops at various points on the bottom wall and also by inserting light tufts. Any side movement of the fluid was not observed. The length of the recirculating region for various obstacle widths was established visually by inserting in the flow light wool tufts. At the reattachment point the tufts were not very stationary. Therefore, this length could be estimated with a certainty of 0.4 obstacle heights. However, if the reattaching point is identified with the location where the output of a single hot wire is minimum in a near wall hot wire scanning (the hot wire is placed 0.2 mm from the wall), then this uncertainty in the location of the reattachment point is reduced to 0.1 H. This identification of the reattachment point maybe not precise; however the results for the integral length of recirculation should be accurate within the above stated uncertainty. Velocity measurements have been taken with a single constant temperature hot wire using a linearizer. Sample of the measurements are included in the paper and only those for which the measured turbulence intensity was less than 20 percent of the local velocity.

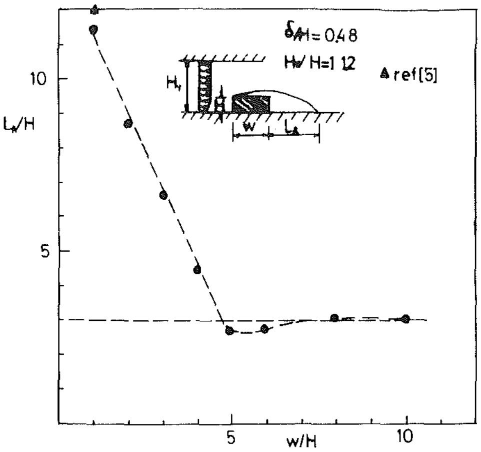

Fig. 3 Length of recirculating region

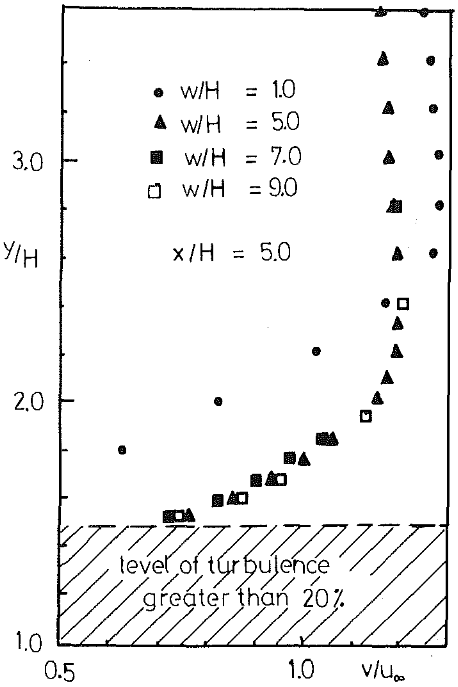

Fig. 4 Velocity measurements for various *W/H*

Presentation of Results

The Length of the Recirculating Region. The photographs in Fig. 1 show the flow around the obstacles as depicted by light threads attached to the side wall of the windtunnel. Very clearly, there is a marked difference in the flow development as the width of the obstacle becomes greater than four times the obstacle height. For the latter case the flow separates from the upstream leading edge of the obstacle and reattaches on the top surface of the obstacle where part of it is deflected upwards entering into the recirculating region located on the top of the surface while the other moves downstream.

Figure 2 shows the trajectory of the shear layer originating from the upstream edge of the square sectioned obstacle and for $W/H=4$ as it was established by flow visualization using smoke and light tufts. At the location of four heights downstream, this line (for $W/H=1.0$) is 1.15 heights above the top surface. Increasing the obstacle width it seems that the pressure on the top surface of the obstacle is reduced and the leading edge separation line is sucked towards the surface

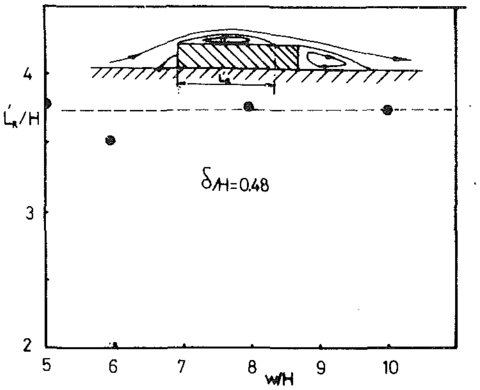

Fig. 5 Length of recirculating region of the top surface of the obstacle

resulting therefore in a quicker reattachment, as it is shown for the case of $W/H=5$. Evidently in the latter case, the angle of separation is much smaller compared to that of square-sectioned obstacle. For comparison purposes on Fig. 2 is shown the trajectory under similar experimental conditions measured by Durst and Rastogi [5]. Increasing the width of the obstacle from $W/H=1$ decreases the length of the recirculating region downstream. After the flow reattachment on the top surface, this length remains constant irrespectively of the obstacle width. The above findings by flow visualization were more accurately quantified by moving a single hot-wire along the floor of the wind tunnel. The point of reattachment was assumed to coincide with the wall location were the output of the constant temperature hot-wire was minimum. Figure 3 shows the length of the recirculating region downstream of the obstacle as a function of the obstacle width. There is an almost linear relation between the length L_R and the obstacle width. For widths greater than four obstacle heights this length remains constant and equal to 3 obstacle heights.

At this case the boundary layer type of flow which starts to develop after the reattachment point on the top surface of the obstacle has at the downstream corner of the obstacle a very thick boundary layer of the order of two obstacle heights as it is shown by hot-wire velocity measurements, Fig. 4. For such boundary layer thickness and for turbulent flow in a backward facing step, previous studies have found a reattachment length downstream of the obstacle around 6H (see Couniham et al. [16]). This considerable difference in the length of recirculation must be attributed to the flow being in a nonequilibrium state and particularly to a high level of turbulence which promotes extensive mixing and spreading of the shear layer originating at the downstream corner of the obstacle.

The length of the recirculating bubble on the top surface of the obstacle for $W/H>4$ remains constant Fig. 5. For such obstacle widths, the velocity measurements (not shown) upstream of the obstacle are almost identical indicating that the flow is similar to that past a forward-facing step.

Conclusions

The main conclusions drawn from the present experimental study is that the flow around surface-mounted obstacles depends appreciably on the width to height ratio of the obstacle. For obstacle widths smaller than 4 obstacle heights, the shear layer separating from the upstream corner reattaches at a location past the obstacle and the length of the recirculating region measured from the downstream face decreases linearly with the obstacle width. A drastic change in the flow field occurs for obstacle widths greater than four obstacle heights. In this case the flow separating from the leading corner reattaches on the top surface of the obstacle and a boundary layer type of flow starts to develop on it. In this case, the length of the recirculating region remains almost constant independently of the obstacle width.

References

1 Bradshaw, P., and Wong, F. Y. F., "The Reattachment and Relaxation of a Turbulent Shear Layer," *JFM*, Vol. 52, 1972, pp. 113–135.

2 Tani, I., Iuch, M., and Komoda, H., Aero. Res. Inst. University Tokyo Rep. no. 364.

3 Tillman, W., "Investigations of Some Particulatities of Turbulent Boundary Layers on Plates," British Ministry of Aircraft production, 1945, MAP-VGG-34-45T.

4 Crabb, D., Durao, D. F. G., and Whitelaw, J. H., "Velocity Characteristics in the Vicinity of a Two-Dimensional Rib," Fourth Brazilian Congress of Mech. Engin. 1977, paper No. B-3, pp. 415–429.

5 Durst, F., and Rastogi, A. K., "Turbulent Flow Over Two-Dimensional Fences," *Turbulent Shear Flows 1*, Springer Verlag, 1978.

6 Counihan, J., Hunt, J. C. R., and Jackson, P. S., "Wakes Behind Two-Dimensional Surface Obstacles in Turbulent Boundary Layers," *J F M*, Vol. , 1974, pp. 529–563.

7 Bergeles, G., and Athanassiadis, N., "Calibration of the 30cm × 30cm Wind Tunnel of the Laboratory of Aerodynamics NTUA," Technical Chamber of Greece, 1979, Vol. 4, pp. 24–31.

8 Durst, F., and Rastogi, A. K., "Theoretical and Experimental Investigation of Turbulence Flows With Separation," Turbulent Shear Flows II, Springer Verlag, 1980.

G. Buresti
Associate Professor,
Department of Aerospace Engineering,
Faculty of Engineering,
University of Pisa,
56100 Pisa, Italy

Appraisal of Universal Wake Numbers From Data for Roughened Circular Cylinders

An analysis was carried out to check whether certain existing universal wake numbers can characterize the cross-flow around roughened circular cylinders in transitional regimes. The results confirmed the soundness of the idea of the existence of a link between the drag coefficient of a bluff body, its pressure distribution, and the frequency of the shedding of vortices in its wake. In particular, Bearman's number and Griffin's number were shown to be able to describe this link with sufficient accuracy and to be a function of the Reynolds number based on the typical dimension of the surface roughness. A physical interpretation of Griffin's number was also given which permits to link the drag force with the velocity of the potential flow at separation and the frequency of vortex shedding.

Introduction

Vortex shedding from two-dimensional bluff bodies in cross-flow has always been one of the most intriguing problems of fluid dynamics. Researchers have been trying for a long time to fully understand the mechanisms behind this phenomenon, while engineers have been particularly concerned with the related unsteady forces and the oscillations they may induce on lightly-damped structures.

In an attempt to generalize the experimental knowledge available, several authors introduced universal wake numbers which were expected to link together the frequency of vortex shedding, the drag coefficient and the pressure distribution of bluff bodies of different cross-section. This is the case, for instance, for the numbers proposed by Roshko [1], by Bearman [2], and, separately, by Griffin [3] and Simmons [4].

Most of the proposed universal wake numbers are, essentially, modified Strouhal numbers, in which the velocity of the irrotational flow at separation, U_s, is taken as the reference velocity, while the reference lengths proposed by the various authors differ, but may still be considered to be a measure of the "width" of the wake. If it is assumed that a number so defined is an invariant of the wake, the problem is reduced to connecting the reference velocity and lengths to the body producing the wake, and the various numbers differ according to the way this connection is performed.

The idea lying behind the assumption of the universality of these numbers is that the same vortex street may originate from bodies of different "bluffness" (which may be considered to be characterized, e.g., by the ratio of the width of the wake and the transverse dimension of the body), and that this fact may be taken into account by means of the aforementioned connections between the body and the reference velocity and length. This means any effect connected to the state of the shear layers emanating from the bodies is assumed to be secondary as regards the establishment of the characteristics of the wake. Nevertheless, some dependence of the universal numbers on the parameters which determine the state of the boundary layer (such as the Reynolds number and surface roughness) may obviously be expected.

During previous research, [5, 6], a number of tests were carried out to study the influence of surface roughness on the transitional regimes around circular cylinders in cross-flow. Circumferential pressure distributions and frequencies of vortex shedding were measured, and drag coefficients and Strouhal numbers were thus obtained as a function of the Reynolds number and relative roughness.

In this paper, further analyses of the same experimental results will be described, which were performed in order to study the behavior of the universal wake numbers obtained from these data. To the author's knowledge, such an evaluation has not been carried out before for roughened circular cylinders in transitional regimes, and may probably be considered to be a stringent test of the validity of these numbers. Indeed, a roughened circular cylinder in transitional regimes is, in a certain sense, a very special bluff body, whose bluffness varies together with the movement of the boundary layer separation points on its surface. Furthermore, at the end of the subcritical and at the start of the supercritical regimes, the flow is rather unstable and particularly sensitive to even small disturbances. Lastly, different surface roughnesses give rise to different histories of the boundary layer before separation, and therefore to presumably different characteristics of the separated shear layers, even when separation takes place at similar positions.

The measurements which were used for the evaluation of

Contributed by the Fluids Engineering Division and presented at the Winter Annual Meeting, Washington, D.C., November 15-20, 1981, of THE AMERICAN SOCIETY OF MECHANICAL ENGINEERS. Manuscript received by the Fluids Engineering Division, December 18, 1981. Paper No. 81-WA/FE-23.

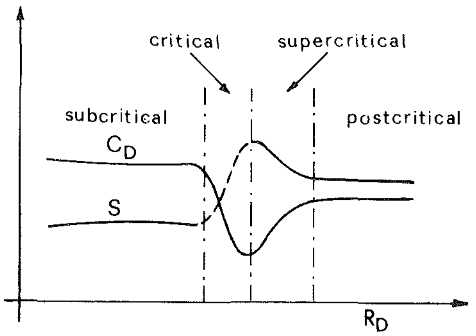

Fig. 1 Qualitative variation of C_D and S in the various flow regimes

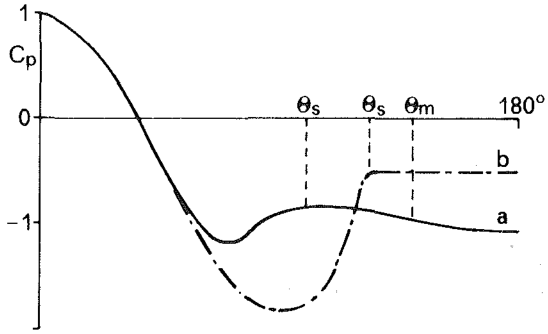

Fig. 2 Typical pressure distributions: (*a*) subcritical and postcritical; (*b*) critical and supercritical

the universal wake numbers are described in detail in [5] and [6], and refer to flow regimes varying from the end of the subcritical, to the supercritical and incipient postcritical. The explanation of this nomenclature is as follows: the critical regime is taken to be typified by the absence of regular vortex shedding, and to be followed by the supercritical regime, in which vortex shedding is again detectable, and by the postcritical regime, characterized by Strouhal numbers and drag coefficients which are virtually independent of the Reynolds number. Figure 1 shows a qualitative sketch of the variation of C_D and S in the various flow regimes.

Evaluation of Universal Wake Numbers

Roshko's Number. The number proposed by Roshko in [1] is defined as

$$S_r = fd'/U_s = S(U_0/U_s)\,(d'/d) = (S/k)(d'/d) \qquad (1)$$

where U_s is the velocity of the irrotational flow at the point of separation and is assumed to be expressed by the relationship

$$U_s = kU_0 = (1 - C_{pb})^{1/2}\,U_0 \qquad (2)$$

which may be obtained by applying Bernoulli's equation to the flow just outside the boundary layer at separation.

Wake width d' is obtained, as a function of k, from Roshko's "notched hodograph theory," [7], which is a modification of Kirchhoff's free streamline theory allowing the introduction of experimental values for the base pressure. However, this theory is applicable to circular cylinders only provided separation occurs at an angle θ which is lower than 90 deg, measured from the front stagnation point. Now, most of the vortex shedding data collected in [6] refer to supercritical and postcritical conditions, in which separation clearly occurred at larger angles, so that the evaluation of Roshko's number was not possible in these cases. Furthermore, almost all the available subcritical results were certainly influenced by their being obtained close to the transition to the critical regime, i.e., when vortex shedding starts losing its regularity. Indeed, the evaluations that were attempted in those conditions which could apparently be considered to be subcritical, did not give satisfactory results from the point of view of the constancy of S_r, and values as low as 0.133 and as high as 0.192 were found.

An important point must be made here as regards the evaluation of k, as frequently it is not clear which pressure coefficient should be assumed as the base pressure coefficient. Indeed, in many cases, and particularly in the subcritical regime, the base pressure is far from constant; in particular, the pressure just after separation is higher than the pressure at 180 deg from the stagnation point, and this difference is often significant. Roshko noticed this fact too, [1], and decided to take the pressure at about 130 deg from the stagnation point as the base pressure. A better situation is generally found in the critical and supercritical regimes, in which the base pressure is practically constant, but some variation may again be observed in the postcritical regime. The situation is qualitatively shown in Fig. 2. In the present analysis, it was decided to evaluate k in three different ways, i.e., by using the values of C_p at the end of the pressure rise leading to separation ($\theta = \theta_s$ in Fig. 2), at $\theta = 180$ deg, and at an intermediate position θ_m (generally $\theta_m \cong 140$ deg).

Roshko's universal Strouhal number was found to be largely dependent on k, and therefore on the assumed value of the base pressure coefficient. For instance, in one case S_r was found to vary from 0.144 to 0.151 and 0.183 when the values of C_p at $\theta = 180$ deg, $\theta = \theta_m$ and $\theta = \theta_s$, respectively, were assumed as base pressure coefficients. Therefore, it can be said that the nonconstancy of the pressure coefficient in the wake region of a circular cylinder in the subcritical regime is one of the main sources of doubt as to the possibility of using Roshko's number for this type of body.

Nomenclature

C_D = drag coefficient = $D/(\frac{1}{2}\rho U_0^2 d)$
C_D^* = modified drag coefficient = $D/(\frac{1}{2}\rho U_s^2 l_w)$
C_{Ds} = vortex street drag coefficient = $D_s/(\frac{1}{2}\rho U_0^2 l)$
C_{pb} = base pressure coefficient
d = cylinder diameter
d' = wake width from Roshko's hodograph theory
D = drag force acting on cylinder
D_s = vortex street drag
f = frequency of vortex shedding
G = Griffin's number = $C_D S/k^3$
h = lateral spacing of vortices
k = U_s/U_0
l = longitudinal spacing of vortices
l_w = measured wake width
R* = modified Reynolds number = $U_s l_w/\nu$
R_d = Reynolds number = $U_0 d/\nu$
R_ϵ = roughness Reynolds number = $U_0 \epsilon/\nu$
S = Strouhal number = fd/U_0
S* = modified Strouhal number = fl_w/U_s
S_b = Bearman's number = fh/U_s
S_r = Roshko's number = fd'/U_s
U_0 = free stream velocity
U_s = velocity of the irrotational flow at separation
Γ = intensity of the vortices in the wake
Γ^* = $\frac{1}{2}U_s^2/f$
ϵ = typical surface roughness dimension
θ = angular coordinate from stagnation point
λ = coefficient defined by equation (13)
ν = kinematic viscosity
ρ = fluid density
σ = standard deviation

Bearman's Number. The universal number introduced by Bearman in [2] is defined as:

$$S_b = fh/U_s = S(U_0/U_s)\,(h/d) = (S/k)\,(h/d) \qquad (3)$$

where k is given by equation (2), while h is the lateral spacing between the two rows of potential vortices of the opposite sign that may be taken as representative of the actual viscous vortex street.

Bearman proposed to evaluate h by means of Kronauer's criterion, which states that the ratio of the lateral to the longitudinal spacing of the vortices, h/l, must be such that the potential vortex street drag coefficient C_{Ds} is a minimum. C_{Ds} is defined as $C_{Ds} = D_s/(\frac{1}{2}\rho U_0^2 l)$, where D_s is the vortex street drag, and may be obtained by the following relationship:

$$C_{Ds} = \frac{4}{\pi}\left(\frac{u}{U_0}\right)^2 \left[\coth^2\frac{\pi h}{l} + \left(\frac{U_0}{u} - 2\right)\frac{\pi h}{l}\coth\frac{\pi h}{l}\right] \qquad (4)$$

where u is the velocity of the vortices relative to free stream velocity U_0. Kronauer's criterion supplies a further relationship between u/U_0 and h/l, i.e.:

$$2\cosh\frac{\pi h}{l} = \left(\frac{U_0}{u} - 2\right)\sinh\frac{\pi h}{l}\left(\cosh\frac{\pi h}{l}\sinh\frac{\pi h}{l} - \frac{\pi h}{l}\right) \qquad (5)$$

At this point the assumption is made that the vortex street drag may be equated to the cylinder drag. Thus we may write:

$$C_{Ds} l = C_D d \qquad (6)$$

which, when multiplied by f/U_0, and remembering that $fl = (U_0 - u)$, may be reduced to the following:

$$C_{Ds}\left(1 - \frac{u}{U_0}\right) = C_D S \qquad (7)$$

Equation (7), together with equations (4) and (5), allows us to assess h/l as a function of the drag coefficient and the Strouhal number. Bearman's number may then be easily calculated from:

$$S_b = S/k)(h/l)(l/d) \qquad (8)$$

where $l/d = C_D/C_{Ds}$, from (6).

The evaluation was then carried out for all the 90 different cases available from [6], and for the three values of k already mentioned, and the following mean values and standard deviations were obtained when all the data were considered together, in spite of the quite different conditions they referred to:

$k(\theta = 180\text{ deg})$: $S_b = 0.1839$, $\sigma = 0.0053$,

$\sigma/S_b = 2.9\%$

$k(\theta = \theta_s)$: $S_b = 0.1863$, $\sigma = 0.0051$,

$\sigma/S_b = 2.7\%$

$k(\theta = \theta_m)$: $S_b = 0.1851$, $\sigma = 0.0048$,

$\sigma/S_b = 2.6\%$

It is apparent that S_b is remarkably constant and that the difference between the values obtained by evaluating k from the pressures at the three different angular positions are not very large. However, this last result may be due in part to the fact that most of the data considered referred to the supercritical regime.

The aforementioned results should be compared with the value of $S_b = 0.181$ found by Bearman, [2], by using different bluff bodies, with and without base bleed and splitter plates.

To see whether some correlation between the roughness degree and Bearman's number could be found, it was decided to analyse the data with reference to the Reynolds number based on the typical surface roughness dimension, R_ϵ. To this end, the available data were divided into five groups of comparable size and the mean value of S_b and its standard deviation were evaluated for each group.

In Fig. 3 the mean values and standard deviations of S_b for the case $k = k(\theta_m)$ are shown as a function of R_ϵ (each point being plotted at the mean R_ϵ value of the corresponding group).

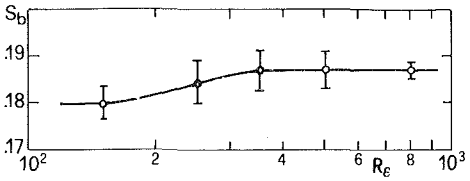

Fig. 3 Variation of the mean value and standard deviation of S_b with roughness Reynolds number for the case $k = k(\theta_m)$

As can be seen, S_b clearly increases with R_ϵ, from a value of 0.180 (which is extremely close to Bearman's suggested value) for low values of R_ϵ to a value of approximately 0.187 for $R_\epsilon > 600$. Furthermore the scatter of the data is lower for the first and, specially, for the last group, for which σ/S_b is about 1 percent. Now it must be pointed out that these two groups were composed of data relating, respectively, all to the subcritical and all to the postcritical regimes, while the other groups were composed of data corresponding to different regimes; in fact, it has been shown in [5] that the transition between the various regimes takes place in a certain range of R_ϵ, at different values for different surface conditions. Therefore, the higher scatter found in the transition range of R_ϵ is perfectly in agreement with this situation. As regards the scatter of the first group as compared to that of the last one, it must be recalled that the accuracy of the measurements of [6] was certainly lower for low than for high values of the velocity.

One of the main advantages of introducing a universal number which is approximately constant for different bodies and flow regimes, is that any one of the quantities C_D, S, and C_{pb} might be evaluated from the measured values of the other two. The accuracy of this prediction is related not only to the validity of the assumption of a constant value existing for the universal number, but also to the type of procedure leading to its evaluation. Indeed, by assuming S_b to be constant at the appropriate value corresponding to the given R_ϵ range, predictions were made by using two of the three quantities C_D, S, and C_{pb}, and the predicted values of the third were compared with the actual ones. The ratio between the standard deviation of the predicted quantity and the standard deviation of S_b was thus found to range from 3.5 to 4.0 for C_D and S, and to be about 4.5 for C_{pb}. This fact is due to the particular procedure leading to the evaluation of S_b, which causes a reduction of the fluctuation of the input parameters. In other words, equations (4) to (8) are such that a certain variation of C_D, S, and C_{pb} gives rise to a much lower variation of S_b. This fact should be borne in mind when judging the validity of Bearman's number and the results of Fig. 3.

Griffin's Number. The number introduced by Griffin, [3], and Simmons, [4], is again a modified Strouhal number, defined as:

$$S^* = fl_w/U_s = (S/k)\,(l_w/d) \qquad (9)$$

where l_w is the "measured wake width at the end of the formation region". This definition must be further clarified by pointing out that the end of the formation region is established as being that station downstream in the wake where the static pressure on the wake centerline reaches a minimum, and the width of the wake, l_w, is defined as the distance between the maxima of the rms fluctuating velocity, as measured in a traverse of the wake. All these measurements had not been taken during the experiments described in [6], so that it was not possible to evaluate S* correctly.

However, in [8] Griffin also introduced a modified drag coefficient

$$C_D^* = D/(\tfrac{1}{2}\rho U_s^2 l_w) = (C_D/k^2)(d/l_w) \tag{10}$$

and then suggested that the quantity $S^* C_D^*$ is a function of k, but that, in practice, it may be considered to be equal to a constant value of 0.073 ± 0.005, for R^* ranging from 100 to 10^7, where

$$R^* = U_s l_w/\nu = R_d k (l_w/d) \tag{11}$$

Now, from the definition of S^* and C_D^* we have:

$$S^* C_D^* = S C_D/k^3 = G \tag{12}$$

so that the quantity G, which will be called Griffin's number in what follows, is independent of l_w, and therefore could be evaluated by using the measurements of S, C_D, and C_{pb}, which were available in the present analysis. It should be noted, by the way, that G may be interpreted as the product of any universal Strouhal number and drag coefficient, provided they are evaluated by taking $U_s = kU_0$ as the reference velocity, whatever might be the reference length used to define them.

Similarly to what was done before concerning S_b, quantity G was evaluated by taking the values of C_p measured at $\theta = 180$ deg, $\theta = \theta_s$ and $\theta = \theta_m$ as the base pressure coefficients, and, when all the data were considered, the following mean values and standard deviations were obtained:

$k(\theta = 180 \text{ deg})$: $G = 0.0811$, $\sigma = 0.0074$,

$\sigma/G = 9.1\%$

$k(\theta = \theta_s)$: $G = 0.0842$, $\sigma = 0.0075$,

$\sigma/G = 8.9\%$

$k(\theta = \theta_m)$: $G = 0.0826$, $\sigma = 0.0070$,

$\sigma/G = 8.5\%$

The data were then analysed with reference to R_ϵ, as already done for Bearman's number, and the results obtained for the case $k = k(\theta_m)$ are shown in Fig. 4.

It is apparent that the behavior of G is perfectly analogous to that of S_b; again there is an increase in G from a value of 0.075, which is in remarkable agreement with that suggested by Griffin, to a value of 0.0855 which applies to high values of R_ϵ, and once again the variations in the scatter may be explained with reference to the instability of the transitional regimes.

At first glance, it might be argued that the behavior of Griffin's number is less satisfactory than that of Bearman's number, as its standard deviation is larger. In particular, σ/G is about 3 percent for $R_\epsilon > 600$. However, it is easy to establish that, if the mean value of G is used in an inverse procedure to evaluate C_D, S, and C_{pb}, the standard deviations of the predicted values of C_D and S are equal to that of G, while the standard deviation of the predicted value of C_{pb} is $\cong 1.4 - 1.5$ times larger than that of G. Therefore, from this point of view, the behavior of Griffin's number may be considered to be slightly but constantly better than that of Bearman's number, bearing in mind what has been pointed out before concerning that number.

Discussion of the Results

The results of the present analysis showed that both Bearman's and Griffin's numbers can describe with sufficient accuracy the link between frequency of vortex shedding, drag coefficient and pressure distribution for the case of roughened circular cylinders; however, to obtain such a good collapse of the data it is necessary to correlate these numbers to the Reynolds number based on the roughness degree, R_ϵ. Indeed, when such a correlation is performed, both S_b and G appear to vary with R_ϵ from the values proposed by Bearman and Griffin, respectively, to higher values which are applicable for R_ϵ larger than approximately 600.

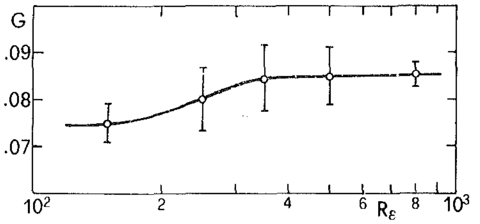

Fig. 4 Variation of the mean value and standard deviation of G with roughness Reynolds number for the case $k = k(\theta_m)$

The variation of S_b and G with R_ϵ may probably be connected to the increase in the thickness of the boundary layers separating from the cylinder when surface roughness is present; indeed, the thickness of the turbulent boundary layer separating at a certain supercritical or postcritical position on a roughened cylinder is certainly larger than the thickness of the turbulent boundary layer separating at the same position on a smooth cylinder at much higher Reynolds numbers.

As regards a comparison between Bearman's number and Griffin's number, it can be said that the apparently greater constancy of the former is due merely to the type of procedure leading to its evaluation, and therefore the predictions that may be obtained by using the mean values of both numbers are of comparable accuracy, even if Griffin's number seems to be superior on this respect.

From a physical point of view, the constancy of Bearman's number might be taken as supporting evidence of the validity of Kronauer's criterion, with its attractive minimum drag assumption, and also of the possibility of modelling the real wake by means of a double row of potential vortices. However, it has been shown by Simmons, [9], that Kronauer's criterion is applicable only provided $k < 1.5$, and even if all the data analysed in the present work fell within this range of applicability, Griffin has shown in [8] that k may reach values as high as 2.0 for bluff bodies showing regular vortex shedding.

On the other hand, Griffin's number is obtained more from an analysis of the functional relationships between C_D, S, and C_{pb}, so that its physical meaning is not immediately evident. However, if the total amount of vorticity shed from one separation point during one period, Γ, is expressed by

$$\Gamma = \tfrac{1}{2}\lambda U_s^2/f = \lambda \Gamma^* \tag{13}$$

it is then easy to show that

$$G = \tfrac{1}{2} C_D (\lambda/k)(U_0 d/\Gamma) = D/(\rho U_s \Gamma^*) \tag{14}$$

Therefore, G may be interpreted as the ratio between the drag and a force term, given by $\rho U_s \Gamma^*$, which is related to the intensity of the vortices in the wake through the velocity of the potential flow at separation and the vortex shedding frequency.

In conclusion, the present work seems to confirm the soundness of the idea of the existence of a link between the drag coefficient of a bluff body, its pressure distribution and the frequency of the shedding of vortices in its wake, but certain points still seem to deserve a deeper analysis.

First of all, the definition of the base pressure coefficient and also the possibility of correlating it to the velocity just outside the boundary layer at separation by means of equation (2), should be analysed in more detail, particularly for the case of bluff bodies without fixed points of separation and/or with significant afterbodies within the separated wake.

Secondly, it should be verified whether the correlation between Bearman's or Griffin's numbers and the roughness

Reynolds number, which was found in the present analysis, also applies to cylinders of noncircular cross-section, and to different types of surface roughness.

Finally, the constancy of Griffin's number, together with the interpretation given by equation (14), might be taken into account when trying to model the mechanism of vortex shedding and its link to the forces acting on the body. In particular, more attention should be paid to a correct modelling of the process of shedding of vorticity from the separation points. In other words, it seems that a potential model of the wake might prove useful, but only provided that the main features of the mechanism of shedding of vorticity in the near wake are correctly taken into account.

Conclusions

The behavior of certain existing universal wake numbers was analysed by utilizing a number of experimental results relating to roughened circular cylinders in cross-flow.

The problems connected to the correct definition of the base pressure for circular cylinders were pointed out; in particular, Roshko's number (which cannot be evaluated for circular cylinders in the supercritical and postcritical regimes) was found to be extremely dependent on the assumed value of the base pressure coefficient.

Both Bearman's number and Griffin's number (defined as $G = C_D S/k^3$) were found to be sensibly constant and a correlation was shown to exist between their values and the Reynolds number based on the roughness typical dimension, R_ϵ. In particular, the values proposed in the literature for these numbers closely agree with those found for $R_\epsilon < 200$ in the present analysis.

It was also shown that the procedure leading to the evaluation of Bearman's number greatly reduces the scatter of its values and that, when both numbers are used in an inverse procedure, Griffin's number gives rise to better predictions of C_D, S, or C_{pb}.

A physical interpretation of Griffin's number was devised which may serve as a guide for future modelling of the link between the drag force acting on a bluff body and the vorticity shed in its wake.

References

1 Roshko, A., "On the Drag and Shedding Frequency of Two-Dimensional Bluff Bodies," National Advisory Committee for Aeronautics, Washington, D.C., Technical Note 3169, July 1954.

2 Bearman, P. W., "On Vortex Street Wakes," *Journal of Fluid Mechanics*, Vol. 28, 1967, pp. 625-641.

3 Griffin, O. M., "A Universal Number for the 'Locking-On' of Vortex Shedding to the Vibrations of Bluff Cylinders," *Journal of Fluid Mechanics*, Vol. 85, 1978, pp. 591-606.

4 Simmons, J. E. L., "Similarities Between Two-Dimensional and Axisymmetric Vortex Wakes," *Aeronautical Quarterly*, Vol. 26, 1977, pp. 15-20.

5 Buresti, G., "The Effect of Surface Roughness on the Flow Regime Around Circular Cylinders," *Journal of Wind Engineering and Industrial Aerodynamics*, Vol. 8, No. 1/2, July 1981, pp. 105-114.

6 Buresti, G., and Martini, G., "Experimental Research on the Effects of Surface Roughness on the Cross-Flow Around Circular Cylinders," Institute of Aeronautics of the University of Pisa, AIA 80-2, May 1980.

7 Roshko, A., "A New Hodograph for Free-Streamline Theory," National Advisory Committee for Aeronautics, Washington, D.C., Technical Note 3168, July 1954.

8 Griffin, O. M., "Universal Similarity in the Wakes of Stationary and Vibrating Bluff Structures," ASME JOURNAL OF FLUIDS ENGINEERING, Vol. 103, March 1981, pp. 52-58.

9 Simmons, J. E. L., "Effect of Separation Angle on Vortex Streets," *Journal of the Engineering Mechanics Division, Proc. of ASCE*, Vol. 101, Oct. 1975, pp. 649-661.

APPENDIX

Experimental Uncertainty

The experimental procedures which were used to obtain the data of the present analysis are described in detail in [5] and [6]. Pressure distributions were measured by means of a tilting multimanometer connected to pressure tappings around the circumference of the models. The flow velocity varied from $\cong 11$ m/sec to $\cong 34$ m/sec. Drag coefficients were obtained by integration of the pressure coefficients. The frequency of vortex shedding was obtained from the measured peak in the spectra of the signals of a hot-wire placed near the cylinder; the spectra ranged from 0 to 512 Herz and had a resolution of 0.5 Herz.

The following uncertainty estimates apply to the data:

$-C_{pb}$ and C_D: uncertainty is approximately inversely proportional to U_0^2, and decreases from $\cong 5$ percent to less than 0.6 percent in the velocity range of the tests;
$-$S: uncertainty decreases from $\cong 3.5$ to 0.7 percent with increasing velocity.

Shigeo Kimura

Adrian Bejan

Department of Mechanical Engineering,
University of Colorado,
Boulder, Colo. 80309

The Buckling of a Vertical Liquid Column

This paper documents the sinuous flow of a vertical water column which impinges on a horizontal surface. It is shown experimentally that the solid obstacle buckles the column into a plane sinuous (static) shape whose wavelength scales with the local column diameter. The measured ratio (buckling wavelength)/(column diameter) is of order $\pi/2$, in agreement with the buckling theory of inviscid flow.

1 Introduction

The object of this paper is to report a series of experimental observations concerning the buckling of a vertical water column, which is a phenomenon commonly observed by placing a flat obstacle under a faucet. The observations reveal the existence of an interesting scaling law, namely, the proportionality between the diameter of the water column and its longitudinal buckling wavelength.

The flow of vertical liquid columns is a topic which draws its importance from its many engineering applications, for example, gas-to-liquid chemical processing and condensation heat transfer in heat exchanger design. As shown below, this topic has been studied extensively, however, with only one exception, all previous studies have been focused on the free-fall of the liquid column: in the free-fall regime the column remains axisymmetric. In the present study we consider a vertical column which is interrupted by an obstacle and, as a result, assumes a sinuous (nonaxisymmetric) shape.

The two-dimensional inviscid flow issuing from a very large vessel through an aperture in a solid wall is one of the classical problems in hydrodynamics, pioneered by Kirchhoff [1] and Rayleigh (see Lamb [2]) Milne-Thomson [3] considered the same phenomenon under the effect of gravity. Since, under gravity, the "infinite height of the vessel leads to an "infinite hydrostatic pressure" paradox, Conway [4] redid the problem by inserting a horizontal lid above the wall with the orifice. He was able to obtain the smooth draw-down shape of the column, employing the free surface treatment proposed by Milne-Thomson [3].

Among the numerous theoretical studies reported in the literature, the work of Scriven and Pigford [5] appears to be the first in which the liquid flow was analyzed based on a boundary layer-type approximation. Lienhard [6] chose a similar approach and included also the effects of gravity and surface tension. Matovich and Pearson [7] formulated a one-dimensional flow model and were able to obtain several closed-form solutions for symmetric column shapes in various parametric domains. A more rigorous formulation was presented by Duda and Vrentas [8]. A one-dimensional Cosserat-type theory was developed by Green [9] and Bogy [10]. The work of Bogy is concerned primarily with the condition of droplet formation at the lower end of a free-falling column. The subject of axisymmetric break-up and droplet formation has been studied extensively over the past 100 years; the core of this work was reviewed recently in the context of Hydrodynamic Stability Theory (Drazin and Reid [11]).

To our knowledge, Lienhard [12] is the only author to have analyzed the sinuous shape of a column impinging on an obstacle. Lienhard viewed the phenomenon as capillary waves which originate at the solid plane and travel upward at the same speed as the water velocity. It is interesting to note that the buckled shape of vertical water columns is sometimes accidentally photographed and published by researchers investigating an unrelated phenomenon (see, for example, Figs. 1(b) and 1(c) in Winston and Martin [13]).

2 Experiment

We carried out a series of controlled experiments in which we photographed the buckled shape of the liquid column. The purpose of this photographic record is to document the relationship between the geometry of the buckled column and physical parameters of the flow (velocity, column diameter, column height).

The experimental setup is shown schematically in Fig. 1. The apparatus consists of three basic components, the water supply reservoir, the nozzle, and the round table which interferes with the free-fall of the water column. The water reservoir is a cylindrical vessel (14 cm diameter, 60 cm height) which supplies water at a known flowrate to the nozzle section. The flowrate is known with 5 percent accuracy from preliminary calibration experiments which revealed the relationship between flowrate and reservoir water level. The reservoir and the nozzle are connected through a 1 m long vinyl tube with an inside diameter of 0.64 cm. The nozzle holder was designed to accommodate four different nozzles which produce water columns of varying diameters. As shown in the detail drawing of Fig. 1, in each nozzle the flow is first lead through a wire-mesh section in order to damp out potential disturbances originating from upstream. Water columns of different heights and diameters were established between the nozzle and the round table. Note that the table surface has a slight spherical curvature in order to prevent the irregular accumulation of water right under the column.

Contributed by the Fluids Engineering Division for publication in the JOURNAL OF FLUIDS ENGINEERING. Manuscript received by the Fluids Engineering Division, October 6, 1982.

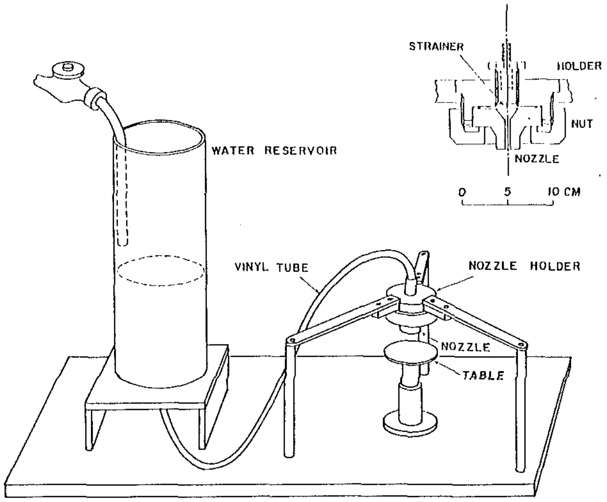

Fig. 1 Experimental apparatus

The parametric domain covered by the experiments is described in terms of two dimensionless groups,

$$W = \frac{\rho u_0{}^2 r_0}{T}, \text{ the Weber number} \tag{1}$$

$$B = \frac{\rho g r_0{}^2}{T}, \text{ the Bond number} \tag{2}$$

where ρ, g, u_0, r_0, and T represent liquid density, gravitational acceleration, liquid velocity at the nozzle exit, nozzle radius, and water-air surface tension, respectively. We varied the Weber number by changing the flow rate: although the Weber number attained in the experiment depends on nozzle size, it falls consistently in the range of 0.1-4. The Bond number was varied from 0.085 to 1.37 by changing the nozzle size (the four nozzle diameters were 0.159 cm, 0.138 cm, 0.476 cm and 0.635 cm). The Reynolds number based on conditions at the nozzle exit, $2r_0u_0/\nu$, varied from 450 to 1100. The velocity profile in the water jet immediately below the nozzle was measured recently by Yamaguchi and Takahashi [17]: their Laser-Doppler measurements showed that the velocity profile becomes flat within a longitudinal distance of order r_0 downstream from the nozzle exit. Therefore, in discussing the present experiments it is assumed that the velocity is approximately uniform in each jet cross-section.

Each experimental run was conducted as follows: first, we fixed the two parameters (W,B) by selecting a certain nozzle and by keeping the flowrate constant (note that the water reservoir level could be maintained by replenishing the water supply during the run). The table directly under the nozzle was then lowered until a new (additional) elbow was observed in the buckled shape of the column. The height of the table and the counted number of elbows were recorded and a photograph of the column shape was taken. The procedure was repeated for various Weber and Bond numbers.

Representative photographs of the buckled liquid column are shown in Fig. 2. The experimental observations are summarized in Fig. 4, as the total number of elbows vs. the dimensionless height of the column $z = z^*/r_0$. We learn that in all cases the number of elbows increases almost linearly with the height of the column. This conclusion is of fundamental importance, because it points towards the existence of a *universal proportionality* between column diameter and buckling wavelength.

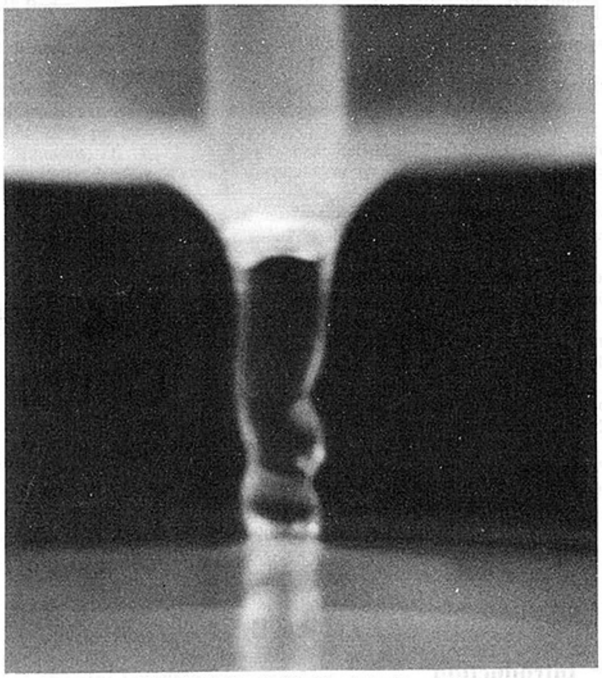

Fig. 2(*a*) $B = 0.34$, $W = 1.4$, $z/r_0 = 8.8$

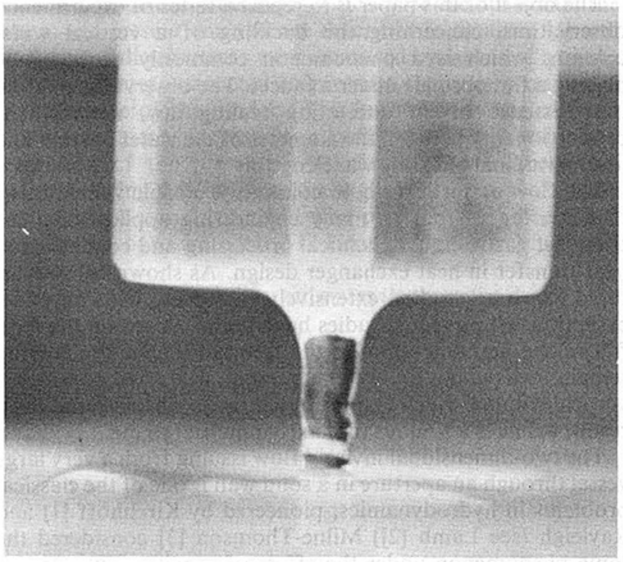

Fig. 2(*b*) $B = 0.34$, $W = 3.65$, $z/r_0 = 7.68$

Fig. 2 Photographs showing the sinuous shape of buckled liquid columns

Nomenclature

B = Bond number given by $(\rho g r_0{}^2)/T$
D = water column diameter
g = gravitational acceleration
r_0 = nozzle radius
Re = Reynolds number, $2r_0u_0/\nu$
T = water-air surface tension
u_0 = liquid velocity at the nozzle exit
W = Weber number given by $(\rho u_0{}^2 r_0)/T$
z = height of the water column
λ = buckling wavelength
ρ = density
ν = kinematic viscosity

Superscript

$*$ = dimensional quantity

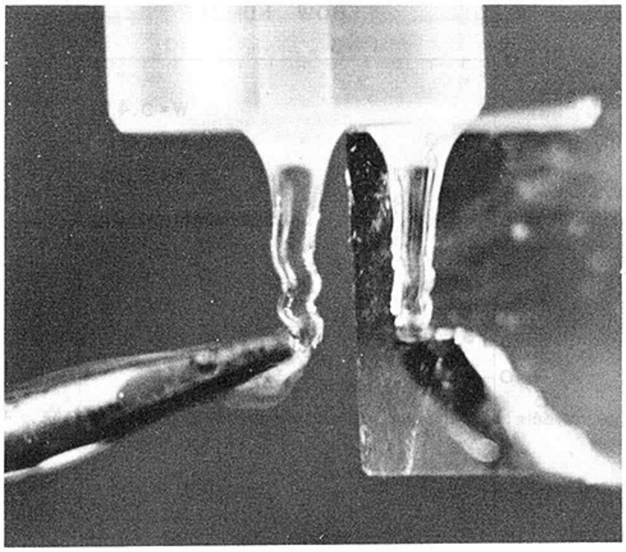

Fig. 3(*a*) $B = 0.34$, $W = 0.59$, $z/r_0 = 9.4$

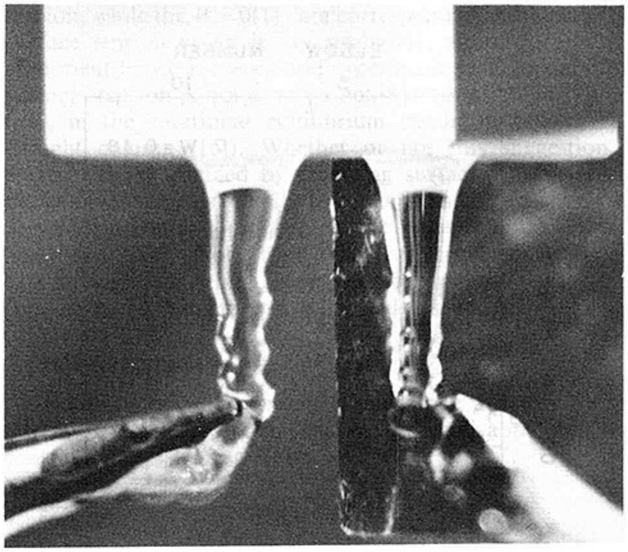

Fig. 3(*b*) $B = 0.77$, $W = 1.77$, $z/r_0 = 7.5$

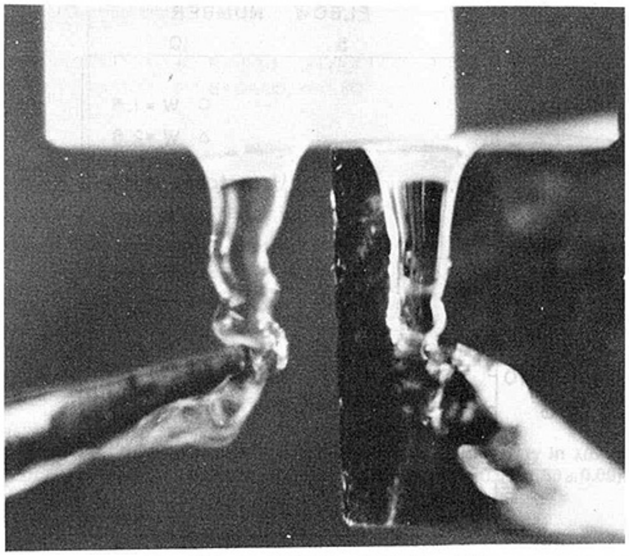

Fig. 3(*c*) $B = 0.77$, $W = 1.77$, $z/r_0 = 6.5$

Fig. 3 The plane buckled shape of the liquid column. Left side: the direct view. right side: the side view through the mirror

3 The Two-Dimensionality of the Buckled Shape

An important question arises in connection with the buckled shape of the liquid column: is this shape two-dimensional, i.e., in one plane, as the buckled shape of an elastic rod, or is it helical? In the course of photographing the columns displayed as Figs. 2(*a*, *b*), the liquid column exhibited the tendency to buckle in a way which made it visible only from a special direction. Indeed, the camera which recorded Figs. 2(*a*, *b*) had to be positioned so that the buckled shape appeared most visibly on film. However, in addition to plane buckling, tall columns showed a tendency to develop an axisymmetric (varicose) deformation at the lower end, near the round table serving as obstacle. It is important to establish whether this axisymmetric deformation is an integral part of the plane buckling phenomenon or simply a reflection of the geometric symmetry imposed by the obstacle on the liquid column.

In order to answer these questions, we conducted an additional series of experimental observations reported here via Figs. 3*a*-3*c*. The buckled column was photographed simultaneously from the front and from the side, by using a vertical mirror whose plane made a 45 deg angle with the camera-column direction. In Figs. 3*a*-3*c* the direct (front) view appears on the left side, while the mirror (side) view appears on the right side of the photographs. To focus on the column and its mirror image at the same time, the mirror had to be positioned no farther than 1 cm away from the liquid column. As the obstacle we used an asymmetric object, namely, the flat end of a screwdriver. The flat end was positioned so that is made approximately a 10-degree angle with the horizontal plane (see Figs. 3*a*-3*c*).

Figures 3*a*-3*c* show very clearly that the liquid column prefers to buckle in a plane. The view from the direction normal to this preferred plane reveals a nearly straight column.

In conclusion, the symmetric (varicose) or asymetric (sinuous) deformation of the liquid column depends on the degree of asymmetry of the obstacle. If the obstacle is from the side, as in Figs. 3*a*-3*c*, then the column buckles into a plane sinuous shape. If, on the other hand, the obstacle is symmetric (i.e., the same when seen from all directions) then the deformation tends to be symmetric also.

4 Discussion of Results

The total number of elbows measured experimentally is shown in Figs. 4*a*-4*d*. Each figure shows the total number of elbows as a function of column height z (dimensionless), for various values of B and W. In each experiment the Bond number is fixed; it was observed that below a critical Weber number the vertical column breaks up into droplets right under the nozzle, and that the buckled shape is most visible in the range where W is slightly higher than this critical value. The experimental observations summarized in Figs. 4*a*-4*d* have been performed in this optimum range of Weber numbers.

The measurements indicate that the number of elbows of the buckled column increases almost linearly with the height of the column, thus suggesting a local proportionality between buckling wavelength λ and column diameter D. The Weber number appears to have only a weak influence on the measurements of Figures 4a-4d. The Bond number effect is more noticeable, as the number of elbows for $z =$ constant increases as the Bond number B increases: This dependence is illustrated in Fig. 5.

The proportionality between λ and D is illustrated further in Figs. 6 and 7. In general, both D and λ decrease as the

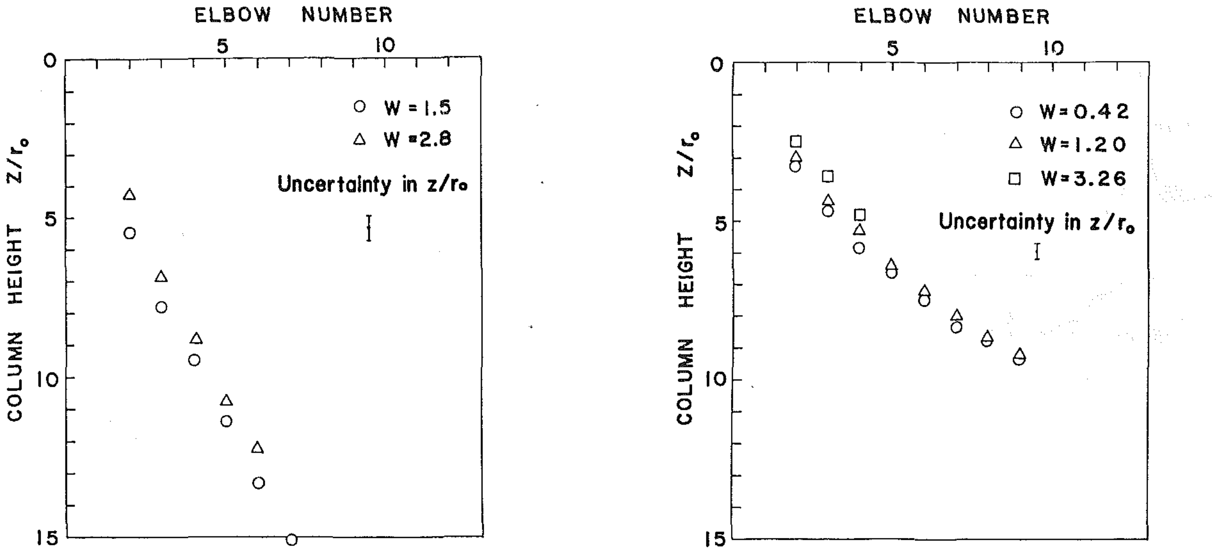

Fig. 4(*a*) $B = 0.085 \pm 0.001$ (uncertainty in $z/r_0 = \pm 0.5$, in $W = 1.5 \pm 0.2$, 2.8 ± 0.3)

Fig. 4(c) $B = 0.77 \pm 0.01$ (uncertainty in $z/r_0 = \pm 0.25$, in $W = 0.42 \pm 0.04$, 1.20 ± 0.12, 3.26 ± 0.33)

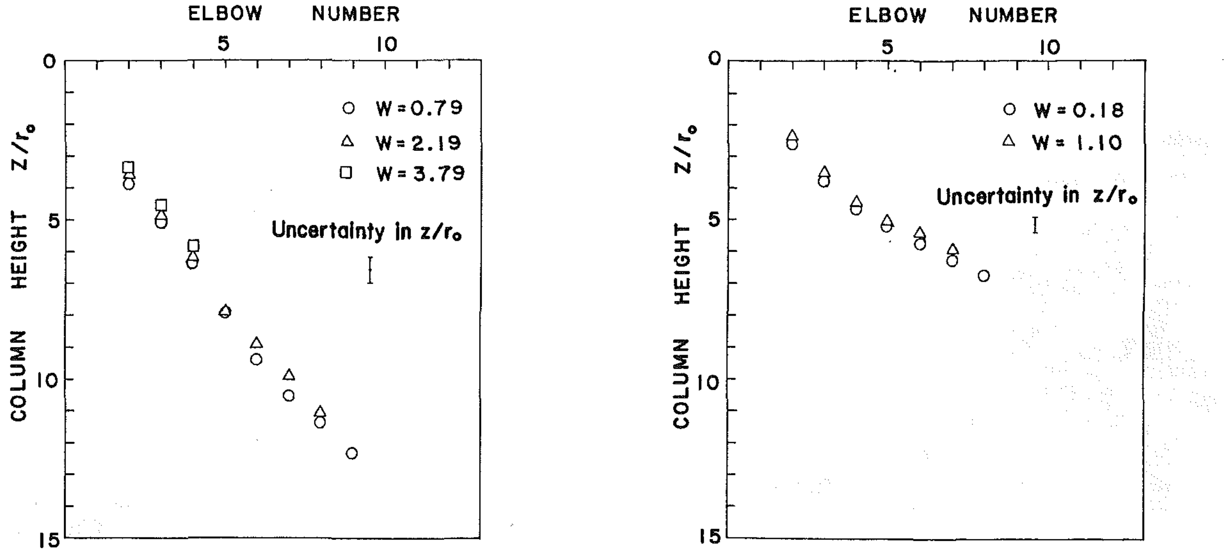

Fig. 4(*b*) $B = 0.340 \pm 0.001$ (uncertainty in $z/r_0 = \pm 0.5$, in $W = 0.79 \pm 0.08$, 2.19 ± 0.22)

Fig. 4(*d*) $B = 1.37 \pm 0.02$ (uncertainty in $z/r_0 = \pm 0.25$, in $W = 0.18 \pm 0.02$, 1.10 ± 0.11)

Fig. 4 Total number of elbows as a function of column height

water column is accelerated downward (Figs. 2, 3) however, the measured ratio λ/D appears to be independent of the vertical position along the column (Fig. 6). For this reason, in Figure 7 we show only the λ/D measurements taken from the upper section of each column, where the first buckling takes place. The λ/D ratio is largely insensitive to changes in both Weber number and Bond number. Indeed, in the *W-B* range documented by our experiments, the wavelength/diameter ratio appears to be a universal constant of order 1.5. Figure 7 shows also Lienhard's [12] theoretical curve and λ/D measurements for the axisymmetric (varicose) deformation: note that Lienhard's data merge with the present measurements in the vicinity of $W = 0(1)$, and that Lienhard's theoretical wavelength of the varicose shape appears to be consistent with both sets of data. However, Lienhard's theory does not account for the sinuous (nonaxisymmetric) shape documented by the present experiments, nor does it account for the apparent constancy of the λ/D ratio of buckled (sinuous) shapes.

We feel that the universal proportionality between buckling wavelength and column diameter is of fundamental interest for the following reasons. First, a similar $\lambda \sim D$ proportionality is also exhibited by highly viscous fluid filaments, such as honey and corn syrup falling and folding on a horizontal surface (see the photographs of Cruickshank (14) and Cruickshank and Munson [15], where the folding wavelength is greater when the filament is thicker; the same scaling is revealed while experimenting with honey filaments of increasing thickness). The present experiments demonstrate that the buckling phenomenon and the $\lambda \sim D$ scaling law are not restricted to highly viscous columns, as originally thought, rather, they are observed even when "inviscid" fluid columns impinge on an obstacle. The buckling of inviscid columns was linked theoretically to the origin of turbulence [16]. Thus, the present measurements confirm not only the possibility of "buckling" in inviscid jets, predicted theoretically [16], but also the accuracy of the theoretical buckling wavelength, $\lambda/D = \pi/2 = 1.57$ [16].

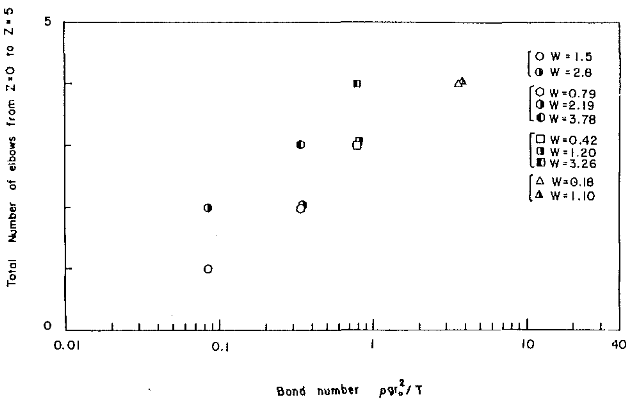

Fig. 5 The effect of Bond number on the total number of elbows over a fixed height

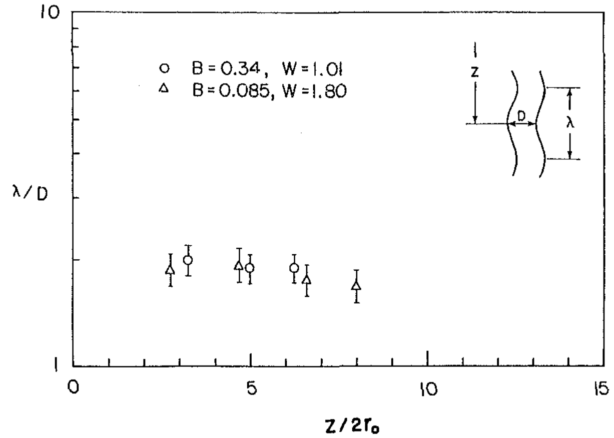

Fig. 6 Variation of λ/D with vertical position (uncertainty in $\lambda/D \simeq 10$ percent in $B = 0.34 \pm 0.004$, 0.085 ± 0.001, in $W = 1.01 \pm 0.05$, 1.80 ± 0.09)

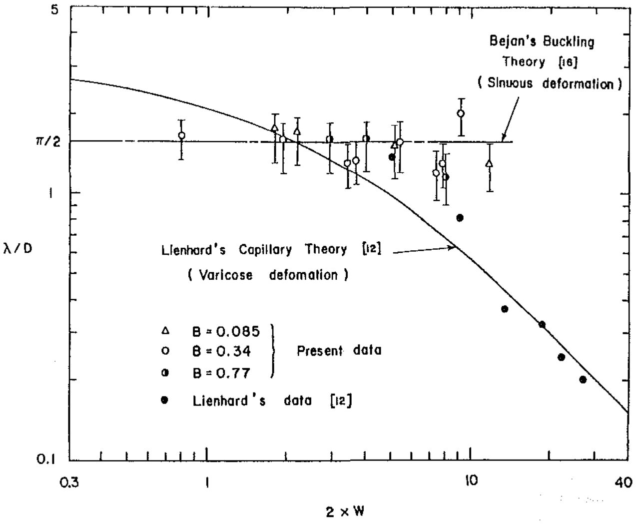

Fig. 7 Comparison of the present results with Leinhard's capillary theory. Note: In order to make the present results comparable with Lienhard's study, in this figure the Weber number is based on local jet radius and local jet velocity (uncertainty in $\lambda/D = \pm 20$ percent, in $W = \pm 20$ percent, in $B = 0.77 \pm 0.01$, 0.34 ± 0.01, 0.085 ± 0.001)

Finally, the agreement between the buckling theory of reference [16] and the λ/D data of Fig. 7 is thought-provoking, because the theory neglects the effect of surface tension, while the $W = 0(1)$ data correspond to cases where the surface tension effect is not negligible. At this stage, the agreement between theory and experiment suggests only that surfaces tension is not a major consideration in "buckling" (i.e., in the rotational equilibrium condition of a nearly straight column [16]). Whether or not this suggestion is correct can be decided by including surface tension in the buckling theory (this remains to be done) and by extending the present experiments to document the Weber number domain below $W = 0(1)$. Note that recent experiments with fast capillary jets in the high Weber number range $10^2 - 10^4$ [18] support the buckling theory of inviscid jets [16, 19].

Acknowledgment

This research was conducted under the auspices of the Office of Naval Research. The experimental apparatus was constructed by Mr. Karl Rupp.

References

1 Kirchhoff, G., "Zur Theorie freier Flussigkeitsstrahlen," *J. Grelle LXX*, 1896, pp. 289-298.

2 Lamb, Sir Horace, *Hydrodynamics*, Cambridge University Press, 1932, pp. 98-99.

3 Milne-Thomson, L. M., *Theoretical Hydrodynamics*, 5th ed. Macmillan Company, 1968.

4 Conway, W. E., "The Two-Dimensional Jet Under Gravity from an Aperture in the Lower of Two Horizontal Planes which Bounds a Liquid," PhD. thesis, University of Arizona, 1965.

5 Scriven, L. E., and Pigford, R. L., "Fluid Dynamics and Diffusion Calculations for Laminar Liquid Jets," *AIChE Journal*, Vol. 5, 1959, pp. 397-402.

6 Lienhard, J. H., "Effects of Gravity and Surface Tension upon Liquid Jets Leaving Poiseuille Tubes," ASME *Journal of Basic Engineering*, Vol. 90, 1968, pp. 262-268.

7 Matovich, M. A., and Pearson, J. R. A., "Spinning a Molten Threadline," *Industrial and Engineering Chemistry Fundamentals*, Vol. 8, 1969, pp. 512-520.

8 Duda, J. L., and Vrentas, J. S., "Fluid Mechanics of Laminar Liquid," *Chemical Engineering Science*, Vol. 22, 1967, pp. 855-869.

9 Green, A. E., "On the Non-linear Behavior of Fluid Jets," *International Journal of Engineering Science*, Vol. 14, 1976, pp. 49-63.

10 Bogy, D. B., "Steady Draw-down of a Liquid Jet under Surface Tension and Gravity," *Journal of Fluid Mechanics*, Vol. 105, 1981, pp. 157-176.

11 Drazin, P. G., and Reid, W. H., *Hydrodynamic Stability*, Cambridge University, Press, 1981.

12 Lienhard, J. H., "Capillary Action in Small Jets Impinging on Liquid Surfaces," ASME *Journal of Basic Engineering*, Vol. 90, 1968, pp. 137-138.

13 Winton, R., and Martin, H. R., "A Theoretical Model for the Transverse Impingement of Free Jets at Low Reynolds Numbers," ASME *Journal of Fluids Engineering*, Vol. 102, 1981, pp. 510-518.

14 Cruickshank, J. O., "Viscous Fluid Buckling: A Theoretical and Experimental Analysis with Extensions to General Fluid Stability," PhD thesis, Iowa State University, 1980.

15 Cruickshank, J. O., and Munson, B. R., "Viscous Fluid Buckling of Plane and Axisymmetric Jets," *Journal of Fluid Mechanics*, Vol. 113, 1981, pp. 221-239.

16 Bejan, A., "On the Buckling Property of Inviscid Jets and the Origin of Turbulence," *Letters in Heat and Mass Transfer*, Vol. 8, 1981, pp. 187-194.

17 Yamaguchi, R., and Takahashi, K., "Flow Pattern near the Outlet of a Straight Long Circular Tube," *Bull. of the JSME*, Vol. 23, No. 185, Nov. 1980, pp. 1798-1805.

18 Stockman, M. G., and Bejan, A., "The Nonaxisymmetric (Buckling) Flow Regime of Fast Capillary Jets," *Physics of Fluids*, Vol. 25(9), 1982, pp. 1506-1511.

19 Bejan, A., *Entropy Generation through Heat and Fluid Flow*, Wiley, New York, 1982, Chapter 4.

R. Friedrich[1]

N. Rudraiah

UGC-DSA Centre in Fluid Mechanics,
Department of Mathematics,
Central College,
Bangalore University,
Bangalore-560001, India

Similar Solutions of Brinkman Equations for a Two-Dimensional Plane Jet in a Porous Medium

The similar solution of the Brinkman equations for flow of a plane jet issuing into a fluid saturated porous medium is studied. The velocity field is determined in the plane of physical as well as transformed coordinates. It is shown that the jet in a porous medium is of finite length in contrast to the infinite length in the case of pure viscous flow. The difference in the volume rate of discharge and the width of the jet between the Brinkman model and the pure viscous case is brought out clearly and it is shown that the Darcy resistance tends to make the jet broader. Near the origin, the streamlines show an entrainment of fluid from infinity which results in negative transverse velocity.

1 Introduction

In recent years considerable interest has been evinced in the study of flow through porous media because of its natural occurrence and of its importance in industrial, geophysical, and biomedical applications (see Rudraiah et al. [1]). In chemical industries it has been used to achieve an effective mixing process (see De Wiest [2], Rudraiah [3], and Chandrasekhara et al. [4]). In petroleum industries porous medium is used for oil recovery (secondary), filtration, and for cleaning oil spills. In nuclear industries porous medium is used for effective insulation and for emergency cooling of nuclear reactors (Masuoka [5], Rudraiah et al. [6] and [7]). Study of flow through a porous medium is also of immense use in geothermal heat recovery (Cheng [8], Rudraiah and Srimani [9]), and in biomedical problems to understand the transport processes in lungs and kidneys. In these applications it is important that a quantitative theory be developed for describing the spreading and decay of a free jet issuing into a fluid saturated porous medium. Although much work has been done in the case of free jet issuing into a pure viscous flow (i.e., absence of porous media), the problem of free jet issuing into a fluid saturated porous medium has not been given, to our knowledge, any attention and the study of this is the object of this paper.

The free jet issuing into a pure viscous flow has been studied by Schlichting [10] and Bickley [11] and the existence of similar solutions is established. The exact solutions for laminar, axisymmetric jets emerging from a hole in a plane or conical wall have been given by Squire [12] and Morgan [13], respectively. Their solution satisfies only the slip conditions, namely, the normal velocity is continuous at the wall but not the tangential velocity. Potsch [14], reconsidered the work of Squire [12] and Morgan [13], and generalized the exact solutions for axisymmetric laminar jets with arbitrary Reynolds number. Even his solutions satisfy only the slip conditions. Recently Schneider [15] has given the exact similarity solutions for axisymmetric laminar jets and has shown that a nontrivial solution satisfying the no-slip condition at the wall exists even in the limiting case of Reynolds number tending to infinity.

We note, in the case of free jet issuing into a porous medium governed by the Darcy law, that the nontrivial solution does not exist as in the case of ordinary viscous flow ([12], [13], [14]). This Darcy law is usually valid in the case of a medium where the particles are densely packed. In many practical problems for example in the case of filtration in the bed (usually encountered in petroleum reservoirs), the particles are sparsely packed with up to 39.6 percentage of porosity. In that case the usual Darcy law is not valid and we have to consider the boundary layer nature of Brinkman model [16] which involves viscous shear in addition to the Darcy resistance.

Therefore, the main object of this paper is to study the free jet issuing into a porous medium at rest governed by the Brinkman model and to show that similarity solutions analogous to Schlichting [10] are possible even in the case of flow through a porous medium. The considerations of this model, especially in the study of efflux of a two-dimensional jet issuing from an orifice into a fluid saturated porous medium, gives a very useful physical insight into the effect of permeability, since the case of pure viscous flow can be deduced, with a proper definition of averages, in the limit as permeability tends to infinity. For this purpose the plan of the paper is as follows. In section 2 the basic equations and the required boundary conditions are discussed. The velocity distribution for Darcy flow is also given. Similar solutions are obtained in section 3. The results are discussed in section 4. It

---

[1] Present Address: Institute for Fluid Mechanics, Technical University of Munich, 8 Munchen 2, Federal Republic of Germany.

Contributed by the Fluids Engineering Division and presented at the Winter Annual Meeting, Boston, Mass., November 14–18, 1983 of THE AMERICAN SOCIETY OF MECHANICAL ENGINEERS. Manuscript received by the Fluids Engineering Division, July 20, 1982. Paper No. 83-WA/FE-11.

is shown that the jet in a porous medium is of finite length just like the vertical buoyant jet in a stably stratified fluid. The velocity field is studied in the plane of physical as well as transformed coordinates. The similar solutions of Schlichting [10] and Bickley [11] for the plane laminar incompressible jet are recovered in the case of zero Darcy resistance.

2. Formulation of the Problem

The governing equations for a two dimensional free jet issuing from an orifice into a fluid saturated porous medium using Brinkman model [16] are:

$$\frac{\partial u}{\partial x}+\frac{\partial v}{\partial y}=0, \tag{2.1}$$

$$u\frac{\partial u}{\partial x}+v\frac{\partial u}{\partial y}=\varphi\frac{\partial^2 u}{\partial y^2}-m_1 u \tag{2.2}$$

where (u,v) are the components of the filter or pore average velocity, ν the kinematic viscosity of the fluid, $m_1=\nu\epsilon/k$, ϵ the porosity and k is the permeability of a porous medium which has the dimension of length squared. The jet spreads outwards and the velocity in its center decreases in the downstream direction. Since the slit is assumed to be infinitely small, it is necessary to assume an infinite fluid velocity in the slit. The pressure gradient has been removed from equation (2.2) corresponding to the nature of a free jet. Equations (2.1) and (2.2) are solved subject to the symmetry conditions

$$v=0,\ \frac{\partial u}{\partial y}=0 \text{ at } y=0,\ u=0 \text{ at } y=\pm\infty. \tag{2.3}$$

If we consider the effect of Darcy's term alone, equation (2.2) takes the form

$$u\frac{\partial u}{\partial x}+v\frac{\partial u}{\partial y}=-m_1 u. \tag{2.4}$$

We find that, the Darcy resistance term on the right-hand side of (2.4) is responsible for a decay of the velocity field in the main flow direction. Although the free jet in the case of pure Darcy flow, governed by (2.1) and (2.4), is unrealistic, it gives some information on the length of the jet. This can be shown by applying the V. Mises transformation, with ξ, ψ as new coordinates, to the equations (2.1) and (2.4). Defining the stream function ψ through

$$u=\frac{\partial\psi}{\partial y},\ v=-\frac{\partial\psi}{\partial x} \tag{2.5}$$

and setting $\xi=\nu x$, equation (2.4) transforms to

$$\frac{\partial u}{\partial\xi}=-m_1/\nu \tag{2.6}$$

of which

$$u=u_0-\frac{m_1}{\nu}(\xi-\xi_0) \tag{2.7}$$

is the integral. The constant of integration here must be a function of ψ which has to be determined using the boundary conditions. Since the order of the equation (2.4) is reduced as in the pure viscous flow ([12], [13], [14]), it is difficult to satisfy all the conditions. Equation (2.7) shows that the jet is of finite length

$$x=x_0+\frac{u_0}{m_1} \tag{2.8}$$

and this length depends on the jet velocity u_0, measured at a distance x_0 from the slit, on the viscosity and the properties of the porous material. These properties also decide upon whether the viscous or the Darcy term plays the dominant role among the flow retarding forces.

3 Similar Solutions

We search for similar solutions of equations (2.1) and (2.2) in terms of the stream function ψ of the form

$$\psi=g(\xi,m_1)\xi^{1/3}F(\eta) \tag{3.1}$$

which is an extension of the laminar viscous case discussed by Schlichting [10] where

$$\xi=\nu x,\ \eta=\frac{1}{6}\frac{y}{\xi^p}g(\xi,m_1), p=2/3.$$

The exponent p is found to be 2/3 assuming the inertia terms in (2.2) and the viscous term to be of the same order of magnitude. This implies that the Darcy term should not exceed the order of magnitude of these terms. From (3.1) we get the following expressions for the velocity components

$$u=\frac{1}{6}g^2\xi^{-1/3}F'(\eta) \tag{3.2}$$

$$v=-\nu\left[F\left(g'\xi^{1/3}+\frac{1}{3}g\xi^{-2/3}\right)+\eta F'\left(g'\xi^{1/3}-\frac{2}{3}g\xi^{-2/3}\right)\right]. \tag{3.3}$$

Introducing ψ, the equation of motion (2.2) reads:

$$\frac{\partial\psi}{\partial y}\frac{\partial^2\psi}{\partial x\partial y}-\frac{\partial\psi}{\partial n}\frac{\partial^2\psi}{\partial y^2}=\nu\frac{\partial^3\psi}{\partial y^3}-m_1\frac{\partial\psi}{\partial y} \tag{3.4}$$

and in terms of $g(\xi,m_1)$ and $F(\eta)$ we have:

$$6gg'\xi^{-1/3}(2F'^2-FF'')-g^2\xi^{-4/3}(F''' +2(F'^2+FF''))+36\frac{m_1}{\nu}F'=0. \tag{3.5}$$

Since F is assumed to be a function of η alone, for similarity we have:

$$gg'\xi^{-1/3}=C_1=\text{const.} \tag{3.6}$$

and

$$F'''+2(F'^2+FF'')=0. \tag{3.7}$$

Hence it follows from (3.5) that

$$(2F'^2-FF'')g'g\xi^{-1/3}=-6\frac{m_1}{\nu}F'. \tag{3.8}$$

Equations (3.7) and (3.8) along with (3.6) lead to a similar solution, subject to the symmetry conditions (2.3) which imply

$$F=F''=0 \text{ at } \eta=0 \tag{3.9}$$

and

$$g(\xi,0)=1.$$

we get from (3.7) after integrating twice:

$$F'+F^2=C_3=\text{const.} \tag{3.10}$$

Since $F(0)=0$, the constant of integration C_3 is

$$C_3=F'(0)=\frac{-6m_1\xi^{1/3}}{\nu(g^2)'}. \tag{3.11}$$

Equation (3.10), being a differential equation of Riccati's type, can be integrated in closed form to give

$$F=\frac{1}{C_3{}^{1/2}}\tanh(\eta/C_3{}^{1/2}). \tag{3.12}$$

Inserting (3.12) into (3.8) we have

$$gg'\xi^{-1/3}=-3\frac{m_1}{\nu}\frac{1}{C_3} \tag{3.13}$$

and after integrating

$$g^2 = -\frac{9}{2}\frac{m_1}{\nu}\frac{1}{C_3}\xi^{4/3} + \text{const.} \tag{3.14}$$

The constant of integration is specified in such a way that the similar solution of the laminar case [10] is obtained, if Darcy's resistance is negligibly small. That is

$$g = 1 \text{ for } m_1 = 0. \tag{3.15}$$

Thus from (3.14) and (3.15) we find that

$$g = \left(1 - \frac{9}{2}\frac{m_1}{\nu}\frac{1}{C_3}\xi^{4/3}\right)^{1/2}. \tag{3.16}$$

The constant C_3 shall be determined from the total flux of momentum τ in the ξ-direction, which turns out to decay due to Darcy's resistance. It follows from (2.2) that:

$$\frac{d}{dx}\int_{-\infty}^{\infty} u^2 dy + m_1 \int_{-\infty}^{\infty} u\, dy = 0. \tag{3.17}$$

We introduce the kinematic flux of momentum K through

$$K = \tau/\rho = \int_{-\infty}^{\infty} u^2 dy \tag{3.18}$$

and assume its value K_0 to be given at the slit ($\xi = 0$). Then, according to (3.17)

$$K + m_1 \int dx \int_{-\infty}^{\infty} u\, dy = \text{const.} \tag{3.19}$$

Using (3.12) and (3.16) the velocity component in the x-direction is

$$u = \frac{1}{6}C_3\xi^{-1/3}\left(1 - \frac{9}{2}\frac{m_1}{\nu}\frac{1}{C_3}\xi^{4/3}\right)(1 - \tanh^2(\eta/C_3^{1/2})). \tag{3.20}$$

The integration in (3.19) is straightforward and yields

$$m_1 \int dx \int_{-\infty}^{\infty} u dy = 6\frac{m_1}{\nu} d\xi \frac{\xi^{2/3}}{g}\int_{-\infty}^{\infty} u d\eta$$

$$= \frac{-2}{9}C_3^{3/2}\left(1 - \frac{9}{2}\frac{m_1}{\nu}\frac{1}{C_3}\xi^{4/3}\right)^{3/2}. \tag{3.21}$$

Since the integral $K = \int_{-\infty}^{\infty} u^2 dy$ differs from (3.21) only through a minus sign, that is

$$K = \int_{-\infty}^{\infty} u^2 dy = \frac{2}{9}C_3{}^{3/2}\left(1 - \frac{9}{2}\frac{m_1}{\nu}\frac{1}{C_3}\xi^{4/3}\right)^{3/2}, \tag{3.22}$$

the constant of integration in (3.22) has to be zero and C_3 can be evaluated for $\xi = 0$, $K = K_0$ as

$$C_3 = (4.5\, K_0)^{2/3}. \tag{3.23}$$

Hence the velocity distributions in the jet take the form

$$u = 0.45428(K_0^2/\xi)^{1/3}\left(1 - 1.6509\frac{m_1}{\nu K_0{}^{2/3}}\xi^{4/3}\right)$$

$$(1 - \tanh^2(1.6509K_0^{1/3}\eta)) \tag{3.24}$$

$$v = 0.5503\frac{\nu(K_0/\xi^2)^{1/3}}{\left(1 - 1.6509\frac{m_1}{\nu K_0^{2/3}}\xi^{4/3}\right)^{1/2}} \times$$

$$\times\Big[3.3019K_0^{1/3}\eta(1 - \tanh^2(1.6509K_0{}^{1/3}\eta))$$

$$-\left(1 - 4.9528\frac{m_1}{K_0^{2/3}\nu}\xi^{4/3}\right)\tanh(1.6509K_0^{1/3}\eta)\Big]. \tag{3.25}$$

At the boundary of the jet ($\eta = \infty$) the component u vanishes and the transverse component however is

$$v_\infty =$$

$$-0.5503\nu\left(\frac{K_0}{\xi^2}\right)^{1/3}\frac{\left(1 - 4.9528\frac{m_1}{\nu K_0^{2/3}}\xi^{4/3}\right)}{\left(1 - 1.6509\frac{m_1}{\nu K_0^{2/3}}\xi^{4/3}\right)^{1/2}}. \tag{3.26}$$

We note that solution (3.25) is singular at

$1.6509\frac{m_1}{\nu K_0^{1/3}}\xi^{4/3}\xi^{4/3} = 1$ i.e., $x = l$. At $x = l$, $\eta = 0$

and hence the required solution at this singular point is

$$v = 0.1834\, m_1 y.$$

This reveals that the incoming flow will be directed in the y-direction and the axial velocity will be zero throughout the porous medium and hence at $x = l$ the porous medium behaves like an impermeable medium because of the difference in nature of the resistance offered by the solid particles to the flow in the vicinity of the slit and away from the slit at $x = l$. Therefore, the similarity solutions (3.24) and (3.25) are valid only for $x \leq l$. This is in consistance with the definition of the stream function given by equation (3.1) together with the solution (3.16) obtained on the basis of similarity analysis.

The volume rate of discharge per unit height of the slit, $Q = \rho\int_{-\infty}^{\infty} U dy$, becomes

$$Q = 3.3019\rho(K_0\xi)^{1/3}\left\{\left(1 - 1.6509\frac{m_1}{\nu K_0^{2/3}}\xi^{4/3}\right)\right\}^{1/2}. \tag{3.27}$$

The case of a purely viscous flow ($m_1 = 0$) can be easily deduced from equations (3.24) to (3.27). The effect of Darcy's term is to decrease the total amount τ in the downstream direction until it becomes zero. Thus, the jet, penetrating a porous medium, is of finite length just like a vertical free jet in a stably stratified fluid reaches a maximum height. According to equation (3.22) the length "l" of the jet is

$$l = 0.6865\frac{(k/\epsilon)^{3/4}K_0^{1/2}}{\nu}. \tag{3.28}$$

It increases with the momentum supplied to the jet and also with decreasing viscosity and increasing permeability, l can be considered as a characteristic linear dimension of the problem, suitable to define a dimensionless porous parameter P as

$$P_l = \frac{\nu}{m_1 l_{\text{ref}}^2} = \frac{k}{\epsilon l_{\text{ref}}^2}. \tag{3.29}$$

l_{ref} is the length of the jet for given reference values k_{ref}, $(k/\epsilon)_{\text{ref}}$, and K_{ref}. A Reynolds number Re can be formed, using K_0 and l_{ref} in order to define a proper velocity scale namely, $(K_0/l_{\text{ref}})^{1/2}$, as

$$\text{Re} = \frac{(K_0 l_{\text{ref}})^{1/2}}{\nu}. \tag{3.30}$$

In terms of P_l and Re, equation (3.28) takes the dimensionless form

$$\frac{l}{l_{\text{ref}}} = 0.6865\, P_l^{3/4}\text{Re} \tag{3.31}$$

with the help of which ψ, u, v, Q can be written as dimensionless quantities in terms of the transformed coordinates x/l, y/l:

$$\frac{\psi}{\nu} = 1.4564(x/l)^{1/3}(1 - (x/l)^{4/3})^{1/2}\tanh\tilde{\eta}\text{Re}P_l^{1/4}. \tag{3.32}$$

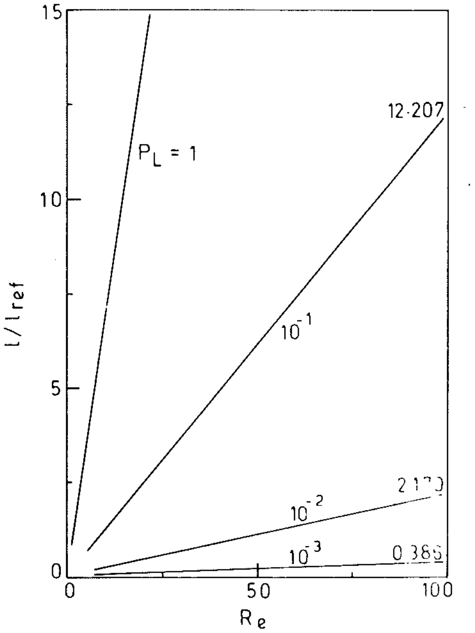

Fig. 1 Length of plane jet

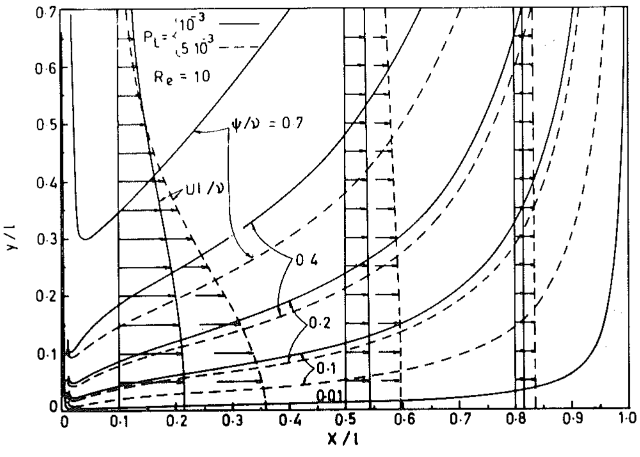

Fig. 2 Streamlines and tangential velocity distributions

$$\frac{ul}{\nu}=0.3534(l/x)^{1/3}\mathrm{Re}^2p_l^{1/2}(1-(x/l)^{4/3}(1-\tanh^2\tilde{\eta}), \qquad (3.33)$$

$$\frac{vl}{\nu}=0.4854(l/x)^{2/3}\mathrm{Re}P_l^{1/4}(1-(x/l)^{4/3})^{-1/2}$$

$$[2\tilde{\eta}(1-\tanh^2\tilde{\eta})-(1-3(x/l)^{4/3})\tanh\tilde{\eta}], \qquad (3.34)$$

$$\frac{Q}{\rho\nu}=2.9127(x/l)^{1/3}\mathrm{Re}P_l^{1/4}(1-(x/l)^{4/3})^{1/2}. \qquad (3.35)$$

The similarity variable $\tilde{\eta}$ is:

$$\tilde{\eta}=1.6509K_0^{1/3}\eta=0.2426\frac{y/l}{(x/l)^{2/3}}\mathrm{Re}P_l^{1/4}(1-(x/l)^{4/3})^{1/2}. \qquad (3.36)$$

The center line velocity, u_m, follows from (3.33) for $\tilde{\eta}=0$, is

$$\frac{u_m}{\nu}=0.3534(l/x)^{1/3}\mathrm{Re}^2P_l^{1/2}(1-(x/l)^{4/3}). \qquad (3.37)$$

It decays by a factor $(1-(x/l)^{4/3})$ faster than in the case of pure viscous flow ($P_l\rightarrow\infty$). Since U_m can be written as

$$u_m=0.4542\nu l_{\mathrm{ref}}^{-2/3}x^{-1/3}\mathrm{Re}^{4/3}(1-(x/l)^{4/3}). \qquad (3.38)$$

The ratio $u_m/(u_m)P_l\rightarrow\infty$ becomes

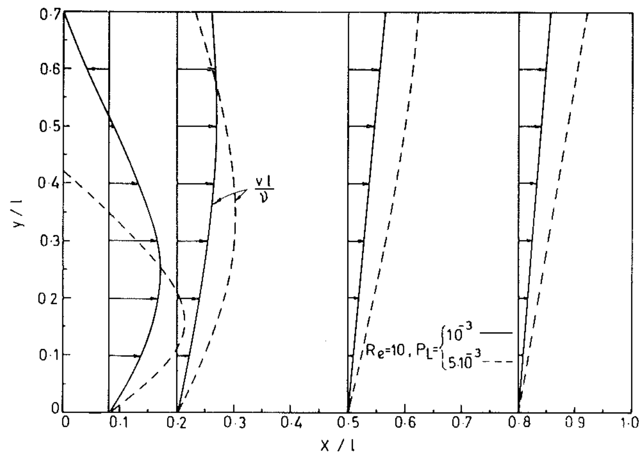

Fig. 3 Transverse velocity distributions

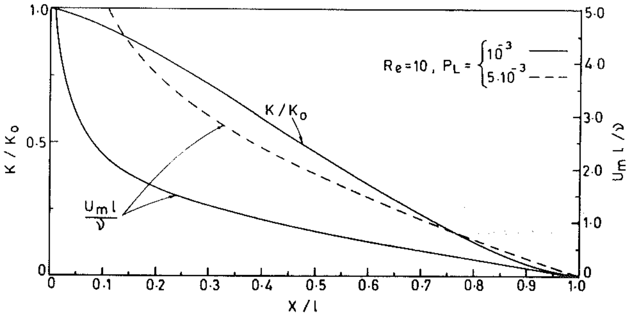

Fig. 4 Center line velocity and kinematic flux of momentum

$$\frac{u_m}{(u_m)_{P_l\rightarrow\infty}}=(1-(x/l)^{4/3}), \qquad (3.39)$$

taking into account that $(l)_{P_l\rightarrow\infty}=\infty$.

For engineering purposes it may be useful to define the width of the jet, $b_{1/2}$, as the distance from the center line at which $u/u_m=1/2$. Then we find from (3.33), (3.36), and (3.37)

$$\frac{b_{1/2}}{l}=3.6315\mathrm{Re}^{-1}P_l^{-1/4}(x/l)^{2/3}(1-(x/l)^{4/3})^{-1/2}. \qquad (3.40)$$

4 Discussion

A two-dimensional jet in a porous medium is investigated using a similarity transformation with the object of obtaining exact solutions for the velocity and the volume rate of discharge.

The dimensionless length of the jet given by equation (3.31) is numerically evaluated and the results are shown in Fig. 1. It reveals that the length of the jet depends linearly on the Reynolds number for a fixed porous parameter P_l and increases as permeability increases. The purely viscous jet ($P_l\rightarrow\infty$) does not possess a characteristic linear dimension ($l/l_{\mathrm{ref}}\rightarrow\infty$). The streamlines given by (3.32) are numerically evaluated and are drawn in Fig. 2. Streamlines (Fig. 2) become steeper as P_l decreases indicating that Darcy's resistance tends to make the jet broader as viscous resistance is able to do. The same can be concluded from the distribution of tangential velocity. Near the origin ($x/l<<1$) streamlines show an entrainment of fluid from infinity which results in negative transverse velocity (see Fig. 3). The center line velocity, in Fig. 4, increases as permeability increases. At the orifice ($x/l=0$) it is infinitely large according to the assumption of an infinitely small slit allowing there for a finite flux of kinematic momentum K_0. K/K_0 as well as U_ml/ν decay purely because of Darcy's resistance. The volume rate of discharge and the width of the jet behave differently and the former

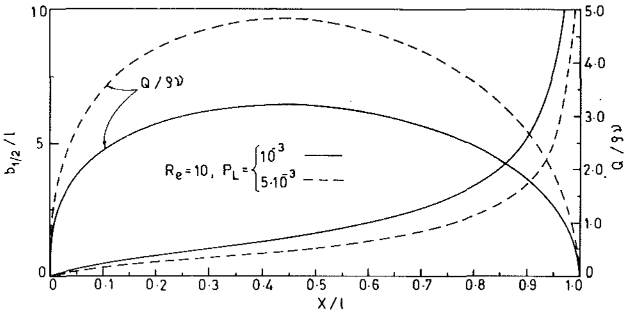

Fig. 5 Volume rate of discharge and width of the jet

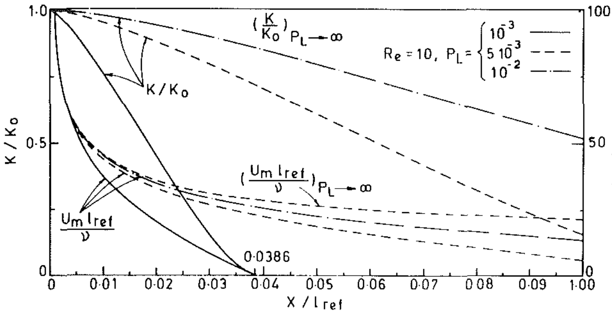

Fig. 6 Center-line velocity and kinematic flux of momentum in terms OE of the physical variable $X/l_{\rm ref}$

reaches maximum values at the position $x/l=(1/3)^{3/4}$, independent of Reynolds number and porous parameter (Fig. 5). A still better impression of the physics can be achieved, if $l_{\rm ref}$ is used as suitable length scale, instead of l. In that case equations (3.32) to (3.37) and (3.40) take the form:

$$\frac{\psi}{\nu}=1.6509(x/l_{\rm ref})^{1/3}{\rm Re}^{2/3}a(x)^{1/2}\tanh\bar{\eta}, \tag{3.41}$$

$$\frac{ul_{\rm ref}}{\nu}=0.4543(l_{\rm ref}/x)^{1/3}{\rm Re}^{4/3}a(x)(1-\tanh^2\bar{\eta}), \tag{3.42}$$

$$\frac{vl_{\rm ref}}{\nu}=0.5503(l_{\rm ref}/x)^{2/3}{\rm Re}^{2/3}a(x)^{-1/2}[2\bar{\eta}(1-\tanh^2\bar{\eta})-b(x)\tanh\bar{\eta}] \tag{3.43}$$

$$\frac{Q}{\nu\rho}=3.3019(x/l_{\rm ref})^{1/3}{\rm Re}^{2/3}a(x)^{1/2}, \tag{3.44}$$

$$\bar{\eta}=0.2752\,\frac{y/l_{\rm ref}}{(x/l_{\rm ref})^{2/3}}\,{\rm Re}^{2/3}a(x)^{1/2}, \tag{3.45}$$

$$a(x)=1-1.6509\,\frac{(x/l_{\rm ref})^{4/3}}{P_l{\rm Re}^{4/3}},$$

$$b(x)=1-4.9528\,\frac{(x/l_{\rm ref})^{4/3}}{P_l{\rm Re}^{4/3}}, \tag{3.46}$$

$$\frac{u_m l_{\rm ref}}{\nu}=0.4542(l_{\rm ref}/x)^{1/3}{\rm Re}^{4/3}a(x), \tag{3.47}$$

$$\frac{b^{1/2}}{l_{\rm ref}}=3.2038(x/l_{\rm ref})^{2/3}{\rm Re}^{-2/3}a(x)^{-1/2}. \tag{3.48}$$

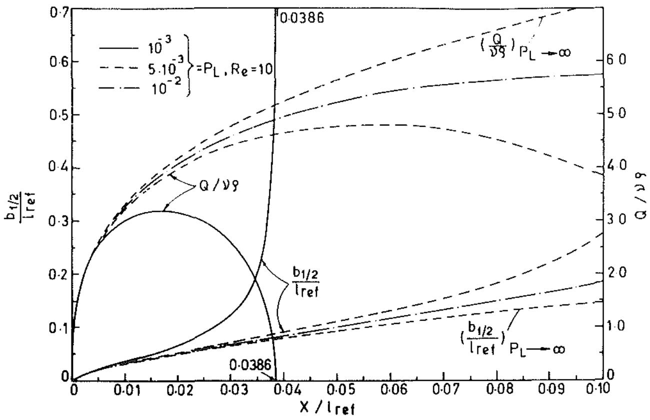

Fig. 7 Volume rate of discharge and width of the jet in terms of physical variable $X/l_{\rm ref}$

For Re = 10 and $P_l=10^{-3}$ the jet ends at $x/l_{\rm ref}=0.0386$ and for $P_l=5.10^{-3}$, 10^{-2} at $x/l_{\rm ref}=0.129$, 0.217, respectively. It can be seen from Fig. 6 that $u_m l_{\rm ref}/\nu$ is quite close to the laminar jet ($p_l\to\infty$) for $P_l=0.01$. The decay of kinematic momentum K/K_0 is still very distinct in this case. Similarly in Fig. 7 the difference in the volume rate of discharge and the width of the jet between the Brinkman model and purely viscous case is brought out clearly. Since the distribution of tangential velocity becomes more and more uniform as its magnitude tends to zero the jet becomes infinitely wide and its volume rate of discharge vanishes.

Acknowledgment

We thank the UGC for financial support under the DSA programme in Fluid Mechanics. One of us (RF) is grateful to the Technical University of Munich, for providing sabbatical leave and to the Bangalore University for offering a visiting professor's post. His thanks are also due to DFG for supporting the travel.

References

1. Rudraiah, N., et al., "Some Flow Problems in Porous Media," PGSAM Series, Bangalore University, Vol. 2, 1979.
2. De Wiest, R. J. M., *Flow Through Porous Media*, Academic Press, New York, 1969.
3. Rudraiah, N., "Dispersion of Soluble Matter in Laminar Flow Through Porous Media Between Two Parallel Plates," *Vignana Bharathi* (Bangalore University Journal) Vol. 2, No. 2, 1976, pp. 1-10.
4. Chandrasekhara, B. C., Rudraiah, N., and Nagaraj, S. T., "Velocity and Dispersion in Porous Media," *Int. J. Engng. Sci.*, Vol. 18, 1980, pp. 921-929.
5. Masuoka, T., "Convective Currents in a Horizontal Layer Divided by a Permeable Wall," *Bulletin of the JSME*, Vol. 17, 1974, pp. 225-232.
6. Rudraiah, N., et al., "Effects of Nonuniform Thermal Gradient and Adiabatic Boundaries on Convection in Porous Media," ASME *Journal of Heat Transfer*, Vol. 102, 1980, pp. 254-260.
7. Rudraiah, N. et al., "Convection in a Fluid Saturated Porous Layer With Non-Uniform Temperature Gradient," *Int. J. of Heat Mass Transfer*, 1982 (accepted for publication).
8. Cheng, P., "Heat Transfer in Geothermal Systems," *Advances in Heat Transfer*, Academic Press, Vol. 14, 1978, pp. 1-105.
9. Rudraiah, N., and Srimani, P. K., "Finite Amplitude Cellular Convection in a Fluid-Saturated Porous Layer," *Proc. Roy. Soc. Lond.*, A373, 1980, pp. 199-222.
10. Schlichting, H., *Boundary-Layer Theory*, 7th edition, McGraw-Hill, 1979.
11. Bickley, W. G., "The Plane Jet," *Phil. Mag. Ser. 7*, Vol. 23, 1939, pp. 727-731.
12. Squire, H. B., "Some Viscous Fluid Flow Problems 1: Jet Emerging From a Hole in a Plane Wall," *Phil. Mag.*, Vol. 43, 1952, pp. 942-945.
13. Morgan, A. J. A., "On a Class of Laminar Viscous Flows Within One or Two Bounding Cones," *Aero. Quart.*, Vol. 7, 1956, pp. 225-239.
14. Potsch, K., "Laminae Freistrahle im Kegelraum," *Z. Flugwiss.* Weltraumforschung, Vol. 5, 1981, pp. 44-52.
15. Schneider, W., "Flow Induced by Jets and Plumes," *J. Fluid Mech.*, Vol. 108, 1981, pp. 55-65.
16. Vafai, K., and Tien, C. L., "Boundary and Inertia Effects on Flow and Heat Transfer in Porous Media," *Int. J. Heat Mass Transfer*, Vol. 24, 1981, pp. 195-203.

Journal of Fluids Engineering Discussion

A Stall Margin Design Method for Planar and Axisymmetric Diffusers[1]

M. Nishi.[2] This paper is a welcome addition to the studies on the design of diffusers [14], [20], [21]. While the stall margin concept is interesting, there are some questions and comments raised by those who wish to use the present method.

Since planar diffusers actually used have end-walls, effects of corner and end-wall boundary layers are also important to estimate the stall margin. Thus, experimental verification is inevitable to evaluate optimum diffuser shapes designed by the present method, where the effects of wall curvature and the turbulence level on the boundary layers may be neglected, although the authors emphasized that the calculating method was accepted as of high accuracy. Do the authors have a plan to conduct an experimental study to check the method directly?

According to the experiments made by Reneau et al. [9], two-dimensional diffusers with the 7 deg divergence-angle give maximum diffuser effectiveness and maximum pressure recovery at constant area ratio regardless of inlet boundary layer blockage. Therefore, to examine the desirable value of stall margin parameter, the discusser would like to ask the authors to show the distributions of h or Λ, predicted by the present method, along the wall of 7 deg diffuser for various inlet blockages.

In the case of axisymmetric flow, there is no end-wall effect. Figure A-1 shows the relationship between δ^*/R(R:radius) and shape factor $H=\delta^*/\theta$ in the 9 deg divergence angle conical diffuser [15], which is calculated from the method proposed by Professor Senoo and the discusser [22]. It is seen that the locus of the calculated parameters is approaching the separation (or detachment) limit line of $H_s=1.8 + 7.5\ \delta^*/R$ (W is used instead of R in cases of planar diffusers) [22]. This result explains well that the 9 deg conical diffuser with area ratio $AR=3.8$ has the optimum geometry [23]. Consequently, the discusser hopes that the authors will try to examine their data in the $H-\delta^*/W$ (or $h-\delta^*/W$) plane in the cases of planar diffusers. If the $h-\delta^*/W$ plane is used, the separation (or detachment) limit relation is given by $h_s=1-1/(1.8+7.5\delta^*/W)$.

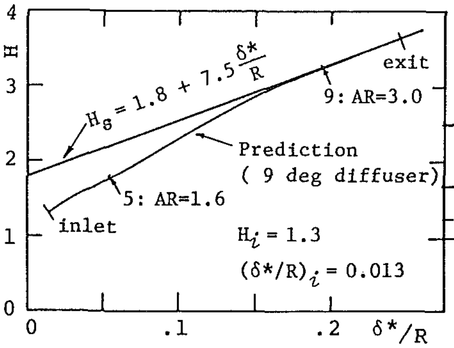

Fig. A-1 Variations of δ^*/R and H in a 9 deg conical diffuser with AR = 3.8.

Additional References

20 Senoo, Y., and Nishi, M., "Deceleration Rate Parameter and Algebraic Prediction of Turbulent Boundary Layer," ASME JOURNAL OF FLUIDS ENGINEERING, Vol. 99, No. 2, 1977, pp. 390-395.

21 Huo, S., "Optimization Based on Boundary Layer Concept for Compressible Flows," ASME *Journal of Engineering for Power*, Vol. 97, 1975, pp. 195-206.

22 Senoo, Y., and Nishi, M., "Prediction of Flow Separation in a Diffuser by a Boundary Layer Calculation," ASME JOURNAL OF FLUIDS ENGINEERING, Vol. 99, No. 2, 1977, pp. 379-389.

23 Sovran, G., and Klomp, E. D., "Experimentally Determined Optimum Geometries for Rectilinear Diffusers with Rectangular, Conical or Annular Cross Section," *Fluid Mechanics of Internal Flow*, Elsevier, New York, 1967, pp. 270-319.

Authors' Closure

The authors thank Professor Nishi for his interest in our work and wish to take this opportunity to respond to his comments and suggestions.

Direct experimental testing of contoured wall diffusers is an important part of any practical design process. As Professor Nishi points out, the effects of finite aspect ratios, diffuser wall curvature, and free-stream turbulence levels are not modeled explicitly in our design method. However, the results in our paper were obtained using a prediction method that has been directly tested against a large amount of experimental data for straight-wall planar and axisymmetric diffusers (see references [1 and 2]). We see no reason why the excellent agreement with experimental data in these straight side wall cases shouldn't also extend to the contoured-wall cases that are discussed in our paper.

Regrettably, we have no immediate plans for experimental

---

[1] By R. C. Strawn and S. J. Kline published in the March, 1983 issue of the JOURNAL OF FLUIDS ENGINEERING, Vol. 105, No. 1, pp. 28-33.

[2] Associate Professor, Mech. Engrg. Dept., Kyushu Institute of Technology, Tobata, Kitakyushu 804, Japan.

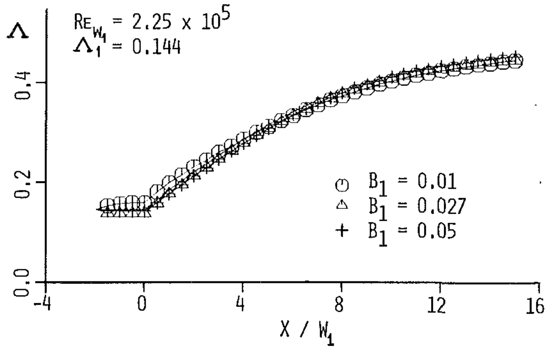

Fig. A-2 Stall margin distribution for a 2θ = 7 deg diffuser with three different boundary layer inlet blockages.

testing of the contoured wall diffusers discussed in our paper. We would, of course, be very interested in the results if such a test were to be carried out.

As suggested by Professor Nishi, we have computed a 2θ = 7 degree diffuser with several different inlet blockages. The prediction method used is that of Lyrio et al. [2]. The diffuser modeling for this method is identical to the one that us used in our paper. The results for the stall margin parameter Λ, are shown in Fig. A-2. The medium level inlet blockage case was tested in experiments by Ashjaee et al. [5]. Distributions of Λ, and *h* were not measured however. The high and low blockage cases in Fig. A-2 were not tested in the Ashjaee experiments.

The predicted results requested by Professor Nishi are shown in Fig. A-2. The stall margin values for these three cases are independent of inlet blockage. Each case shows a high performance design with incipient detachment ($0.42 \leq \Lambda \leq 0.5$) at the diffuser exit. These results are consistent with the observations of Reneau et al. [9]; however the result does no hold in general for cases with higher opening angles.

In Professor Nishi's final comment, he addresses the separation criterion that was proposed by himself and Professor Senoo [22]. Their view is that the boundary layer parameter δ^*/W is a stabilizing parameter for detachment. Our interpretation is that this stabilizing effect occurs because of a blockage/pressure gradient interaction. For interal flows, the local pressure gradient begins to relax whenever the growth of δ^* is rapid enough to affect channel blockage significantly. The direct effect of the pressure gradient acting on the boundary layer is what determines its state with respect to detachment. The effect of blockage in internal flow is related to detachment only through the way its affects the free-stream pressure gradient. Thus any direct reference to channel blockage in a criterion for boundary layer detachment is inappropriate. Reference [3] contains a more thorough verification of this point.